UNIVERSITÉ DE LYON

ÉCOLE CENTRALE LYON

Numéro d'ordre : 2021LYSEC38

THÈSE de DOCTORAT DE L'UNIVERSITÉ DE LYON

opérée au sein de

l'École Centrale de Lyon

École Doctorale 162 : Mécanique, Énergétique, Génie Civil et Acoustique

Spécialité : Mécanique des fluides et Énergétique

Soutenance publique soutenue le jeudi 28 octobre 2021, par :

Aurélien VADROT

Numerical simulation and modeling of compressible turbulence in dense gas flows

Devant le jury composé de :

Guillaume BALARAC	Maître de Conférences HDR, Grenoble-INP, LEGI	*Président et Rapporteur*
Gianluca IACCARINO	Professor, Stanford, ICME	*Rapporteur*
Luminita DANAILA	Professeur des Universités, Université de Caen, M2C	*Examinateur*
Alberto GUARDONE	Professor, Politecnico di Milano, Crealab	*Examinateur*
Christophe CORRE	Professeur des Universités, ECL, LMFA	*Directeur de Thèse*
Alexis GIAUQUE	Maître de Conférences, ECL, LMFA	*Co-encadrant de Thèse*

Remerciements

Enfin, ce moment synonyme de fin de thèse et tant attendu par tous les doctorants est arrivé ... écrire ses remerciements !

Je souhaiterais commencer par remercier l'équipe Turbomachines avec qui j'ai partagé d'agréables moments de détente au labo autour d'un café, d'un gâteau, parfois d'une Praluline et très souvent autour d'un resto U, entremêlés bien-sûr de discussions scientifiques ! L'équipe Turbomachines c'est aussi des moments d'amusement en dehors du labo autour d'une (et surtout plusieurs) bières ... Bref, je souhaiterais remercier tous les membres actuels et passés de l'équipe d'avoir égayé ces trois années ! En particulier, les anciens doctorants: Ludo, Julissa, Victor, Jeff, Thomas, Anne-Lise, Christophe, Ivo, Martin B., et les doctorants actuels (plus pour très longtemps pour certains ;)): Valdo, Martin R., Gabriel, Florent, Nicolas, Alexandra, Jean, Bertrand. Aussi, je tiens à remercier Fatima pour son aide administrative et sa disponibilité; et puis Laurent pour son aide informatique et sans qui j'aurais mis bien plus de temps à finir cette thèse !

Je souhaiterais également remercier les autres doctorants du LMFA, qui contribuent à animer cet endroit, en particulier Majid (Kheyli mamnoun ;)), Elina et Léo.

Merci aux membres du jury d'avoir accepté de relire ce manuscrit et d'avoir animer cette soutenance !

Merci à Kenta, Paolo, Corentin et Dominik pour leur contribution au projet EDGES ! Un grand merci à Pietro Congedo pour son aide précieuse sur la dernière partie de la thèse !

Je tiens tout particulièrement à remercier mes encadrants de thèse Christophe et Alexis qui m'ont énormément appris au cours de ces trois années (plus le stage). Je n'aurais pas pu espérer mieux comme encadrement et comme encadrants ! Merci pour votre disponibilité, pour vos conseils, pour votre cadrage mais aussi de m'avoir fait confiance en me laissant une bonne part d'autonomie. J'ai beaucoup apprécié votre complémentarité qui m'a permis d'être accompagné à la fois sur les difficultés du quotidien et sur les aspects de communication scientifique (article, conférence, ...). Merci beaucoup !!!

Je tiens à remercier mes amis de Lyon (Jean-Lynce, Salambo, Thomas, Bastien, Elodie, Cécile, Morgane, Clara, Hugo, Johann, Mathieu) avec qui j'ai découvert cette ville que je ne connaissais pas. Et puis finalement merci à ma famille, qui m'a accompagné au cours de ces années de thèse et bien plus, et en particulier ma mère à qui je dois une grande partie de ma réussite scolaire, merci Maman !

Résumé

Mots-clés : Gaz dense, Turbulence compressible, Couche de mélange, Simulation Numérique Directe (SND), Simulation des Grandes Echelles (SGE) *a priori* et *a posteriori*, Apprentissage Automatique.

Ce travail porte sur l'analyse et la modélisation de la turbulence dans les écoulements de **gaz denses** (GD). L'intérêt pour ces gaz provient de l'industrie des machines à cycle organique de Rankine (COR), utilisant le cycle de William Rankine largement répandu dans le monde industriel. Le fluide de travail organique utilisé de préférence à l'eau est détendu après évaporation afin de produire de l'énergie mécanique puis de l'électricité.

Au cours des 40 dernières années, les GD ont été largement utilisés par l'industrie des COR en raison de la flexibilité qu'ils apportent. Leur principal avantage est leur capacité à échanger des quantités importantes d'énergie à des températures modérées voire faibles pour la source chaude. Les GD sont des vapeurs monophasiques caractérisées par de longues chaînes d'atomes et par une masse molaire moyenne voire élevée. Leur comportement proche du point critique est très différent des gaz classiques. Nous étudierons ici une sous-famille des GD, également très répandue dans l'industrie, nommée gaz Bethe-Zel'dovich-Thompson (BZT). Ces gaz présentent une zone thermodynamique dite d'inversion où la dérivée fondamentale Γ de la dynamique des gaz est négative, autorisant les ondes de choc de détente.

L'utilisation de ces gaz pose des problèmes de modélisation lors de la conception des turbines dans les COR du fait de la nature très compressible des écoulements turbulents produits et de leur différence avec les gaz parfaits (GP). Jusqu'à présent, bien que les propriétés thermodynamiques des GD soient très différentes de celles des GP, les modèles de fermeture de la turbulence développés pour les GP ont été utilisés pour les simulations RANS et les simulations des grandes échelles (SGE) d'écoulements de GD faute de modèles dédiés disponibles. Le comportement singulier de ces gaz, en particulier les gaz BZT, remet en question ce choix qui suppose implicitement que les structures turbulentes ne sont pas modifiées par les effets GD.

Cette thèse s'intéresse au problème de la modélisation SGE pour ces gaz et comprend 3 étapes principales :

- l'analyse détaillée de simulations numériques directes (SND) de couches de mélange ;
- l'évaluation *a priori* des termes de sous-maille en utilisant des SND filtrées (une SND de turbulence homogène isotrope est également utilisée);
- la construction et la validation *a posteriori* d'une nouvelle modélisation de sous-maille en utilisant l'apprentissage automatique supervisé.

Dans le chapitre 3, les SND de couche de mélange pour l'air considéré comme un gaz parfait sont validées par comparaison avec les résultats de la littérature pour trois valeurs du nombre de Mach convectif ($M_c = 0.1 - 1.1 - 2.2$). Le chapitre 4 est consacré à l'étude des SND de GD. La comparaison avec les résultats GP montre des différences majeures pour le taux de croissance de l'épaisseur de quantité de mouvement à $M_c = 2.2$ (deux fois plus grand pour GD). Cependant, ces différences ne sont pas dues aux régions thermodynamiques BZT et GD mais plutôt aux effets gaz réels transcritiques. Plusieurs facteurs sont responsables de la réduction des effets de compressibilité dans les couches de mélange GD : le découplage entre l'énergie cinétique et l'énergie interne ; les pertes par frottement sont réduites, modifiant la distribution de la masse volumique, ce qui favorise le taux de croissance de la couche de mélange.

L'évaluation *a priori* met en évidence deux nouveaux termes de sous-maille qui doivent être modélisés pour les GD en plus des termes de sous-maille habituellement modélisés en GP : le terme associé au gradient de pression et celui associé au travail des forces de pression.

Le chapitre 6 propose donc une méthodologie afin de modéliser le terme de sous-maille de pression en utilisant des réseaux de neurones. Les résultats montrent le succès de la validation a priori. La validation a posteriori est ensuite réalisée pour des couches de mélange à $M_c = 1.1$ et $M_c = 2.2$ pour plusieurs tailles de filtrage.

Summary

Keywords : Dense Gas, Compressible Turbulence, Mixing Layer, Direct Numerical Simulation (DNS), *a priori* and *a posteriori* Large Eddy Simulation (LES), Machine Learning.

The present work is devoted to the analysis and modeling of turbulence in flows of **dense gases** (DG). The interest for these gases mainly comes from the Organic Rankine Cycles (ORC) turbine industry. ORCs rely on the so-called and widely used William Rankine's cycle. The organic working fluid (instead of water) is expanded after being evaporated so as to produce mechanical energy and then electricity.

Among organic fluids, DG have been widely used in the ORC industry over the past 40 years. Indeed, their use enables a great adaptability for ORCs. The main advantage of DG is their capacity to exchange large amount of energy at low to moderate temperatures for the heat source. DG are single-phase vapors characterized by long chains of atoms and medium to large molecular weights. In the vicinity of the critical point, DG exhibit an unusual behavior when compared with classical gases. In this study, specific DG called Bethe-Zel'dovich-Thompson (BZT) gases, also widely used in the industry, are considered. BZT gases display an "inversion zone", that is a thermodynamic region where the fundamental derivative of gas dynamics Γ becomes negative, allowing the existence of expansion shock-waves.

The use of DG in ORCs raises modeling issues when numerically designing ORC turbines since the turbulent flows at stake include both significant compressibility effects and differences with respect to perfect gases (PG). Up to now, although DG thermodynamic features strongly differ from those of PG, turbulence closure models developed for PG have been applied for RANS simulations and Large Eddy Simulation (LES) of DG flows, for lack of a better option. The peculiar thermodynamic behavior of DG, in particular BZT gases, questions the relevance of this choice, which implicitly assumes that turbulent structures are not affected by DG effects.

The present thesis tackles the DG LES modeling issue by considering 3 main steps:

- the detailed analysis of DG mixing layers direct numerical simulation (DNS);
- an *a priori* assessment of LES subgrid-scale (SGS) terms using filtered DNS (DNS of homogeneous isotropic turbulence is also used);
- the construction and *a posteriori* validation of a new LES SGS model using supervised machine learning algorithms.

DNS of mixing layers are first computed for air considered as a PG in Chapter 3 for three values of the convective Mach numbers ($M_c = 0.1 - 1.1 - 2.2$). Their comparison to reference results from the literature validates the present DNS strategy. Chapter 4 is dedicated to the

computation of DG DNS of mixing layers and the comparison with PG DNS. Results show major differences for the momentum thickness growth rates at $M_c = 2.2$, which is twice as large for DG when compared to PG. Yet, BZT effects have only a small influence on the mixing layer growth. Discrepancies between DG and PG flows are more likely related to transcritical real gas effects rather than linked to the BZT and the DG thermodynamic regions. Shocklets produce indeed only a limited effect on the mixing layer growth. Several factors tend to reduce compressibility effects in DG mixing layers: the decoupling of kinetic and internal energies reduces the effect of increasing M_c; reduced friction losses in DG flows modify the averaged density distribution, which favors the momentum thickness growth rate.

The *a priori* evaluation of SGS terms is performed from filtered DNS for the 2 above-mentioned configurations. The SGS pressure term and SGS pressure work appearing respectively in the filtered momentum and total energy equation need to be modeled in addition to the SGS terms usually modeled in PG flows.

To answer the need for a specific SGS modeling, Chapter 6 proposes a modeling methodology using artificial neural networks (ANN). The method is then applied to the SGS pressure term showing a proper a priori prediction of the term. The *a posteriori* assessment is carried out for mixing layers at $M_c = 1.1$ and $M_c = 2.2$ with several filtering sizes.

Contents

Résumé **i**

Summary **iii**

Contents **v**

List of Figures **viii**

List of Tables **xviii**

1 Introduction **1**
1.1 Context and motivation 1
1.2 Dense gas flows 3
1.3 The need for turbulence modeling in dense gas flows 6
1.4 Outline of the thesis 8

2 Governing equations and numerical tools **10**
2.1 Navier-Stokes equations 11
2.2 Thermodynamic models 12
2.2.1 Equations of state 12
2.2.2 Transport coefficients models 13
2.3 Non-dimensional formulation 14
2.3.1 General formulation 14
2.3.2 Perfect gas analysis 15
2.3.3 Dense gas analysis 16
2.4 LES governing equations 20
2.4.1 Preliminary discussion 20
2.4.2 Filter 22
2.4.3 Real gas formulation 24
2.4.4 Perfect gas formulation 25
2.4.5 A summary of SGS terms 27
2.4.6 Basic LES models 27
2.5 Numerical solver 31

3 DNS of perfect gas compressible mixing layers: verification and validation **34**
3.1 Perfect gas compressible shear layer 35
3.2 Problem formulation 37

3.2.1 Initialization . . . 37
3.2.2 Turbulent Kinetic Energy equation . . . 39
3.3 DNS verification and validation . . . 40
3.3.1 Temporal evolution and selection of the self-similar period . . . 41
3.3.2 Validation over the self-similar period . . . 45
3.3.3 Concluding remarks . . . 50

4 DNS of dense gas compressible mixing layers: analysis and comparison with perfect gas 52
4.1 Problem formulation . . . 53
4.1.1 Initialization . . . 53
4.1.2 Non-dimensional numbers in the DG context . . . 54
4.2 Dense gas effect at $M_c = 1.1$ . . . 57
4.2.1 Temporal evolution and selection of the self-similar period . . . 57
4.2.2 DG effect over the unstable growth phase at $M_c = 1.1$ . . . 58
4.2.3 DG effect over the self-similar period at $M_c = 1.1$ . . . 61
4.3 Dense gas effect: influence of the convective Mach number . . . 71
4.3.1 Temporal evolution and selection of the self-similar period . . . 71
4.3.2 DG effect over the self-similar period . . . 71
4.4 Analysis of discrepancies between DG and PG flows . . . 77
4.4.1 Shocklets influence . . . 78
4.4.2 Spatial correlations . . . 85
4.4.3 Influence of the initial thermodynamic operating point . . . 88
4.4.4 Evolution of non-dimensional terms . . . 91
4.4.5 Other influencing factors . . . 94
4.5 Concluding remarks . . . 98

5 *A priori* analysis of turbulence in dense flows: the need for (specific) modeling 100
5.1 State of the art . . . 101
5.2 Analysis of the subgrid-scale terms . . . 103
5.2.1 Filtered momentum equations . . . 103
5.2.2 Energy equation . . . 106
5.3 Concluding remarks . . . 109
5.3.1 LES equations to be solved . . . 109
5.3.2 Towards SGS modeling . . . 109

6 SGS modeling using Artificial Neural Networks 111
6.1 ANN modeling for LES . . . 113
6.1.1 State of the art . . . 113
6.1.2 ANN description . . . 115
6.1.3 Outline of the ANN-based modeling process . . . 117
6.2 Data analysis . . . 119
6.2.1 SGS pressure term . . . 119
6.2.2 Choice of inputs . . . 124
6.3 ANN tuning . . . 126
6.3.1 Data parallelism . . . 128
6.3.2 Hyperparameters optimization . . . 128
6.4 ANN training and testing . . . 147

6.4.1 Final tests for the tuned ANN . . . 147
6.4.2 Generalization tests . . . 153
6.5 Analysis of small size ANN . . . 159

7 Preliminary *a posteriori* test of the ANN-based SGS pressure model 168
7.1 Methodology . . . 169
7.2 SGS pressure contours . . . 169
7.3 Temporal evolution of the momentum thickness . . . 172
7.4 Further analysis of the SGS pressure . . . 175
7.4.1 Comparison between SGS pressure and SGS turbulent stress tensor . . . 175
7.4.2 Influence on the thermodynamic profiles . . . 177
7.4.3 Summary . . . 181

8 Conclusion and Perspectives 182

References 186

A Averaging methodology for plots using $\delta_\theta(t)$ I

B DG mixing layer: influence of domain size, resolution and initial turbulent structures size V

C Filter influence IX

D *A priori* analysis of PG mixing layers XIV

E Principal Component Analysis (PCA) XIX

F HSIC validation XXVI

List of Figures

1.1 Examples of ORC units: (left) 2 MW Turboden ORC unit using heat recovery in a cement plant and solar thermal energy (Source: Colonna *et al.* (2015)); (right) Solar ORC unit installed in Lesotho (Africa) to help local people becoming electrically self-sufficient (Source: STG international). 1

1.2 Cumulative installed capacity of commercial ORC power plants since 1995 adapted from Tartière & Astolfi (2017). 2

1.3 Evolution of the number of documents including "ORC" and "energy" (left), and "ORC", "energy", and "turbine" (right) in their title, abstract or keywords (Source: Scopus). 3

1.4 The dense gas zone ($\Gamma < 1$) and the inversion zone ($\Gamma < 0$) are plotted for our working fluid (FC-70) using the Martin-Hou equation of state. p_c and v_c are respectively the critical pressure and the critical specific volume. 4

2.1 Schematic view of the turbulence spectrum. The cut-off wavenumber $k_c = \pi/\Delta$ is associated to the filtering size Δ. It defines the limit above which turbulent scales are modeled in LES. 20

2.2 Summary of fundamental principles for the two LES approaches: the *a priori* LES and the *a posteriori* LES. 21

2.3 Filter functions are plotted in physical (left) and spectral (right) spaces for each filter given in Table 2.3. Functions in the physical space are computed using an inverse fast Fourier transform (FFT). 24

2.4 Performance of AVBP on different supercomputers (Source: CERFACS internal communication). 31

3.1 Configuration of the temporal mixing layer. The velocity magnitude is plotted for the DG DNS at $M_c = 2.2$ at $\tau = 4000$. 38

3.2 Temporal evolution of the mixing layer momentum thickness. Comparison is made between the two different grid precisions (16.8M and 134M of grid elements) to check the grid convergence and with the available literature (Pantano & Sarkar, 2002; Fu & Li, 2006; Martínez Ferrer *et al.*, 2017). 41

3.3 Temporal evolution of the mixing layer momentum thickness for $M_c = 0.1 - 1.1 - 2.2$ using air with PG EoS. Slopes are non-dimensional and standard deviations computed over the self-similar period are indicated on the plot. 42

3.4 Temporal evolution of the non-dimensional streamwise turbulent production term integrated over the whole domain $P^*_{int} = (1/(\rho_0(\Delta u)^3)) \int_{L_y} \bar{\rho} P_{xx} dy$ (with $\bar{\rho} P_{xx}(y) = -\overline{\rho u''_x u''_y} \frac{\partial \tilde{u}_x}{\partial y}$) at $M_c = 0.1$ (a), $M_c = 1.1$ (b) and $M_c = 2.2$ (c). Results are shown for the air using PG EoS. Selections of self-similar period are indicated on each plot. 43

3.5 Distributions of the normalized specific power quantities over the y direction at $M_c = 1.1$ is represented for air: P: Production, D: Dissipation and T: Transport are normalized by $\Delta u^3/\delta_\theta(t)$ and compared to Pantano & Sarkar (2002). Additional terms (R: Residuals and TD: Time Derivative) are given. The sampling space step of the averaging process is $\frac{2L_y/\delta_\theta(\tau=1700)}{N_{points}}$, with $N_{points} = 24$. Distributions have been averaged between the upper and the lower stream to get perfectly symmetrical distributions. A further explanation about the averaging process applied is given in Appendix A. 45

3.6 Streamwise specific TKE spectra computed over the centerline at $M_c = 1.1$. Comparison is made with the available literature and between the 16.8M and the 134M simulations. 46

3.7 Distribution of the xy-component of the turbulent stress tensor ($R_{xy} = \overline{\rho u''_x u''_y}/\bar{\rho}$) averaged over the self-similar period. Comparison is made between the 16.8M and the 134M simulations at $M_c = 1.1$. Distributions have been averaged between the upper and the lower stream to get perfectly symmetrical distributions. 47

3.8 Distributions of $r = L_\eta/\Delta x$ the ratio between the Kolmogorov scale and the grid cell size at $M_c = 1.1$ for several non-dimensional times inside the self-similar period ($\tau \in \{1700; 1800; 2000; 2200; 2400\}$). Results are computed from the 134M simulation. 48

3.9 Evolution of the mixing layer growth rate with respect to the convective Mach number for air using PG EoS. Comparison is made with available DNS results in literature and experimental results by Rossmann *et al.* (2001). Standard deviations are indicated on the plot. 50

4.1 The initial thermodynamic state and its evolution over time are represented in the non-dimensional $p - v$ diagram for FC-70 at $M_c = 1.1$. The dense gas zone ($\Gamma < 1$) and the inversion zone ($\Gamma < 0$) are plotted for the Martin-Hou equation of state. p_c and v_c are respectively the critical pressure and the critical specific volume. The initial value of the fundamental derivative of gas dynamics is equal to $\Gamma_{initial} = -0.284$. The normalized distribution of thermodynamic states at $\tau = 1700$ (beginning of the self-similar period) is colored along the corresponding adiabatic curve. 53

4.2 Temporal evolution of the mixing layer momentum thickness at $M_c = 1.1$. . . . 57

4.3 Temporal evolution of the non-dimensional streamwise production integrated over the whole domain, respectively $P^*_{int} = (1/(\rho_0 \Delta u^3)) \int_{L_y} \bar{\rho} P_{xx} dy$ (with $\bar{\rho} P_{xx} = -\overline{\rho u''_x u''_y} \frac{\partial \tilde{u}_x}{\partial y}$). Results are computed from the 134M simulations at $M_c = 1.1$. . . 58

4.4 Distribution of the xy-component of the turbulent stress tensor ($R_{xy} = \overline{\rho u''_x u''_y}/\bar{\rho}$) over the non-dimensional direction $y/\delta_\theta(t)$. Results are computed from the 134M simulation at $M_c = 1.1$. The curves for FC-70 and Air at $\tau = 50$ collapse. 59

4.5 Specific turbulent kinetic energy spectra in the streamwise direction computed over the centerline during the unstable growth phase. Results are computed from the 134M simulation at $M_c = 1.1$. 60

4.6 Temporal evolution of turbulent Mach number. Results are computed from the 134M simulation at $M_c = 1.1$. 60
4.7 Distribution of thermodynamic states along the initial adiabatic curve. Amplitude is normalized with the maximum value at $\tau = 1000$. Results are computed from the 134M simulation at $M_c = 1.1$. 61
4.8 Distribution of the volumetric normalized powers over the non-dimensional cross-stream direction $y/\delta_\theta(t)$ at $M_c = 1.1$. P: Production, D: Dissipation and T: Transport are normalized by $\rho_0 \Delta u^3/\delta_\theta(t)$. Results are gathered from the 134M simulation. The sampling space step for the averaging process is $\frac{2L_y/\delta_\theta(\tau=1700)}{N_{points}}$, with $N_{points} = 24$. Distributions have been averaged between the upper and the lower streams to get perfectly symmetrical distributions. 62
4.9 Distribution of the main non-dimensional volumetric power terms of the x- (top) and $y-$ (bottom) turbulent stress tensor (R_{xx} and R_{yy}) equation over the non-dimensional cross-stream direction $y/\delta_\theta(t)$ at $M_c = 1.1$. P_{xx}: Streamwise production, Π_{xx}: Streamwise pressure-strain and D_{xx}: Streamwise dissipation terms are normalized by $\rho_0 \Delta u^3/\delta_\theta(t)$. Results are computed from the 134M simulation. The sampling space step of the averaging process is $\frac{2L_y/\delta_\theta(\tau=1700)}{N_{points}}$, with $N_{points} = 24$. Distributions have been averaged between the upper and the lower stream to get perfectly symmetrical distributions. 63
4.10 Distribution of the non-dimensional mean streamwise velocity averaged over the self-similar period. Comparison is made between FC-70 and Air. Results are computed from the 134M simulation at $M_c = 1.1$. 65
4.11 Streamwise specific TKE spectra computed on the centerline at $M_c = 1.1$. 66
4.12 Dense gas / Perfect gas streamwise specific TKE spectra ratio. (PG: Perfect Gas, DG: Dense Gas). Results are computed from the 134M simulation at $M_c = 1.1$. . 66
4.13 The non-dimensional Reynolds averaged (left) and root mean square (right) values of temperature (top), density (middle) and pressure (bottom) are averaged over the self-similar period ($\tau \in [1700; 2550]$), plotted along the y direction and compared between FC-70 and Air. Results are computed from the 134M simulation at $M_c = 1.1$. 68
4.14 Temporal evolution of Reynolds number based on the momentum thickness. Results are computed from the 134M simulation at $M_c = 1.1$. 69
4.15 Distributions of the non-dimensional rms velocities (from top to bottom $xx-$, $yy-$, $zz-$ and $xy-$ components) for the dense gas (left) and the perfect gas (right) at several non-dimensional time outside ($\tau \in \{1000; 1400\}$) and inside ($\tau \in \{1800; 2200; 2500\}$) the self-similar period. Results are computed from the 134M simulation at $M_c = 1.1$. 70
4.16 Temporal evolution of the mixing layer momentum thickness for DG at $M_c = 0.1/1.1/2.2$. 72
4.17 Temporal evolution of the non-dimensional streamwise turbulent production term integrated over the whole domain $P^*_{int} = (1/(\rho_0(\Delta u)^3)) \int_{L_y} \bar{\rho} P_{xx} dV$ (with $\bar{\rho} P_{xx}(y) = -\overline{\rho u''_x u''_y} \frac{\partial \tilde{u}_x}{\partial y}$) at $M_c = 0.1$ (a), $M_c = 1.1$ (b) and $M_c = 2.2$ (c). Results are shown for the FC-70. Self-similar periods are indicated on each plot. 72
4.18 Evolution of the mixing layer growth rate over the convective Mach number for air and for FC-70. Comparison is made with available DNS results in literature and experimental results in Rossmann *et al.* (2001). 73

4.19 Distribution of the volumetric normalized powers over the non-dimensional cross-stream direction $y/\delta_\theta(t)$ at $M_c = 2.2$. P: Production, D: Dissipation and T: Transport are normalized by $\rho_0(\Delta u)^3/\delta_\theta(t)$. Distributions have been averaged between the upper and the lower stream to get perfectly symmetrical distributions. 74

4.20 Distribution of the main non-dimensional volumetric power terms of the x- (left) and y- (right) turbulent stress tensor (R_{xx} and R_{yy}) equations over the non-dimensional cross-stream direction $y/\delta_\theta(t)$. P_{xx} and P_{yy}: Streamwise and cross-stream production, Π_{xx} and Π_{yy}: Streamwise and cross-stream pressure-strain and D_{xx} and D_{yy}: Streamwise and cross-stream dissipation terms are normalized by $\rho_0(\Delta u)^3/\delta_\theta(t)$. Results are computed at $M_c = 2.2$. Distributions have been averaged between the upper and the lower stream to get perfectly symmetrical distributions. 75

4.21 Distributions of the root mean square value of pressure averaged over the self-similar period, plotted along the y direction and compared between FC-70 and air at $M_c = 1.1$ and $M_c = 2.2$. Distributions have been averaged between the upper and the lower stream to get perfectly symmetrical distributions. 76

4.22 Streamwise specific TKE spectra computed along the centerline at $M_c = 2.2$. . . 77

4.23 Temporal evolution of the turbulent Mach number M_t for the PG and DG mixing layers at $M_c = 2.2$. 78

4.24 Evolution of the density jump and the entropy increase (a) in compression shocklets for the PG flow, (b) in compression and (c) in expansion shocklets for the DG flow at the beginning of the self-similar period. 80

4.25 Thermodynamic states are represented in the non-dimensional $p-v$ diagram for BZT dense gas FC-70 at $M_c = 2.2$. The dense gas zone ($\Gamma < 1$) and the inversion zone ($\Gamma < 0$) are plotted for the Martin-Hou equation of state. p_c and v_c are respectively the critical pressure and the critical specific volume. The initial value of the fundamental derivative of gas dynamics is equal to $\Gamma_{initial} = -0.284$. The normalized distribution of the thermodynamic states is plotted at the beginning of the self-similar period ($\tau = 4000$) along the curve where the distribution of thermodynamic states is the largest. 81

4.26 Iso-surfaces of zero density laplacian ($\Delta\rho = 0$) colored by the velocity divergence at the beginning of the self-similar period: (a) for the PG flow, (b) for the DG flow with negative values of the velocity divergence, and (c) for the DG flow with negative values of the velocity divergence. 82

4.27 (Top) Iso-surfaces of zero density laplacian ($\Delta\rho = 0$) with positive values of the velocity divergence in blue and negative values of the velocity divergence in red together with the fundamental derivative Γ represented on the centerplane and (bottom) a closer view. 83

4.28 Distributions of the ratio between the compressible dissipation (ϵ_d) and the total dissipation (ϵ) (see details in Equations (3.10) and (3.11)). Results are averaged over the self-similar period. Comparison is made between FC-70 and Air at $M_c = 1.1$ and $M_c = 2.2$. Distributions have been averaged between the upper and the lower stream to get perfectly symmetrical distributions. 84

4.29 The streamwise two-point correlations of the (a) $x-$, (b) $y-$ and (c) $z-$ velocity component at the beginning of the self-similar period. Comparison is made between FC-70 and Air at $M_c = 1.1$ and $M_c = 2.2$. 85

4.30 Snapshot of the velocity magnitude normalized with Δu at the beginning of the self-similar period. Comparison is made between Air at (a) $M_c = 1.1$ and (c) $M_c = 2.2$ and FC-70 at (b) $M_c = 1.1$ and (d) $M_c = 2.2$. 86
4.31 Four different initial thermodynamic states used to perform additional DNS are represented in the non-dimensional $p - v$ diagram for BZT dense gas FC-70 at $M_c = 2.2$. The dense gas zone ($\Gamma < 1$) and the inversion zone ($\Gamma < 0$) are plotted for the Martin-Hou equation of state. p_c and v_c are respectively the critical pressure and the critical specific volume. 87
4.32 Temporal evolution of the non-dimensional streamwise turbulent production terms integrated over the whole domain $P^*_{int} = (1/(\rho_0(\Delta u)^3)) \int_{L_y} \bar{\rho} P_{xx} dV$ (with $\bar{\rho} P_{xx}(y) = -\overline{\rho u''_x u''_y} \frac{\partial \tilde{u}_x}{\partial y}$) at $M_c = 2.2$. Results are shown for the FC-70 for four different DNS: DGA, DGB, DGC and DGD. Self-similar periods are indicated on each plot: DGA ($\tau \in [4000/6000]$); DGB ($\tau \in [4000/6400]$); DGC ($\tau \in [3800/6000]$) and DGD ($\tau \in [3800/6000]$). 89
4.33 Temporal evolution of the mixing layer momentum thickness for DG at $M_c = 2.2$. Results are shown for the FC-70 for four different DNS: DGA, DGB, DGC and DGD. 90
4.34 Evolution of the non-dimensional mixing layer growth rate over the center root-mean square value of pressure normalized by $\frac{1}{2}\rho_0(\Delta u)^2$. Results are given for DG and PG at $M_c = 1.1$ and $M_c = 2.2$. 91
4.35 The mixing layer growth rate is plotted as a function of the non-dimensional terms appearing in the momentum equations (Equations (2.23) and (2.34)): the pressure gradient term (top) and the viscous term (bottom). 92
4.36 The mixing layer growth rate is plotted as a function of the non-dimensional terms appearing in the energy equation (Equations (2.23) and (2.34)): the temporal and convective derivative of the kinetic energy; the pressure work; the viscous work and the heat-flux (from top to bottom). Comparison is made between DG and PG DNS (left) and only DG DNS (right). 93
4.37 Evolution of the growth rates of the momentum thickness (δ_θ) and the velocity thickness (δ^*_θ) (see Equation (4.12)) over the convective Mach number for air and for FC-70. 96
4.38 The non-dimensional Reynolds averaged temperature (a) and density (b); and root mean squared value of the density (c) are averaged over the self-similar regime and plotted along the y direction. Comparison is made between FC-70 and Air at $M_c = 1.1$ and $M_c = 2.2$. 96
4.39 Evolution of the non-dimensional mixing layer growth rate as a function of the sound speed normalized with $\sqrt{p_c/\rho_c}$. Results are given for DG and PG at $M_c = 2.2$. 98

5.1 RMS amplitude of resolved and SGS terms in the filtered momentum equations (Equations 2.48) for the dense gas HIT case. The turbulent Mach number is equal to 0.8. 104
5.2 RMS amplitude of terms in the filtered momentum equations (Equations (2.48)) for the dense gas mixing layer at $M_c = 0.1 - 1.1 - 2.2$ (top-middle-bottom). Results are averaged over the domain and over the self-similar period growth phase of the mixing layer. The turbulent Mach numbers averaged over the centerplane are respectively equal to $0.05 - 0.38 - 0.67$. The SGS viscous terms is very small and does not appear on the plot for $M_c = 1.1$ and $M_c = 2.2$. 105

5.3 RMS amplitude of terms in the filtered total energy equation (Equation (2.48)) in the dense gas HIT configuration. The turbulent Mach is equal to 0.8. 106

5.4 RMS amplitude of terms in the filtered total energy equation (Equation (2.48)) for the dense gas mixing layer at $M_c = 0.1 - 1.1 - 2.2$ (top-middle-bottom). Results are averaged over the domain and over the self-similar period growth phase of the mixing layer. The turbulent Mach numbers averaged over the center plane are respectively equal to $0.05 - 0.38 - 0.67$. 108

6.1 Diagrams presenting the basics of ANN with (a) a simplified version and (b) a fully connected network. 116

6.2 Diagrams explaining the process to model the SGS term. 118

6.3 $z-$centerplane contours colored by $(\bar{p}-\widehat{p})$ (left) and $\widehat{p}$ (right) (Equation (6.4)) for the mixing layers at $M_c = 1.1-2.2$ ((a) and (b)) and for the forced HIT (c). The filtering length scales are respectively equal to $k/k_{min} = 18$ and $k/k_{min} = 12.5$ for the HIT and the mixing layers. 120

6.4 $z-$centerplane contours colored by $(\bar{p} - \widehat{p})$ (left) and $\|\nabla(\widehat{p})\|$ (right) (Equation (6.4)) for the mixing layers at $M_c = 1.1 - 2.2$ ((a) and (b)) and for the forced HIT (c). The filtering length scales are respectively equal to $k/k_{min} = 18$ and $k/k_{min} = 12.5$ for the HIT and the mixing layers. 121

6.5 (Top) Probability density functions (PDF) of the SGS pressure term plotted for the two different configurations: the HIT at $M_t = 0.8$ and the mixing layers at $M_c = 1.1$ ($M_t = 0.38$) and $M_c = 2.2$ ($M_t = 0.67$); and (bottom) a closer view. . 123

6.6 Diagrams explaining the process to parallelize the training step. 127

6.7 ReLU and LeakyReLU activation functions. 131

6.8 (a) Classification of HSIC and (b) representation of HSIC interactions for Grid Search 1. 135

6.9 Probability density functions among hyperparameters choices for a) the number of neurons in the first layer, b) the number of neurons in the second layer, c) the type of solver and d) the activation function. 136

6.10 r^2-scores for the 8 Layer 1-Solver combinations averaged over each 12 possible combinations encountered during GS1 varying the two other hyperparameters (Layer 2 and the activation function). 137

6.11 (a) Classification of HSIC and (b) representation of HSIC interactions for Grid Search 2 (left) and 3 (right). 138

6.12 Probability density functions among hyperparameters choices for a) the number of neurons in the first layer, b) the number of neurons in the second layer and c) the number of neurons in the third layer. 139

6.13 Probability density functions among hyperparameters choices for a) the α parameter used for L2 regression and b) the batch size. 140

6.14 Probability density functions among hyperparameters choices for a) the type of optimizer and b) the ϵ parameter used in Adam type solvers. 141

6.15 Evolution of additional computational cost related to the ANN model without using the inputs requiring Laplacian computation. 144

6.16 $z-$centerplane contours colored by (a) $\|\nabla(\widehat{p})\|$ and (b) $\Delta\widehat{p}$ for the mixing layer at $M_c = 1.1$ for (left) the *a priori* LES (filtered DNS) and for (right) the *a posteriori* LES at $\bar{\Delta}/\Delta_{\text{DNS}} = 64$. Results are plotted at $\tau = 1750$. Note that the domain length in the $y-$direction is twice larger for the *a posteriori* LES than the filtered DNS because it has been enlarged in order to obtain long enough LES simulations without reaching domain boundaries (see Chapter 7). 145

6.17 Distribution of the r^2-score as a function of the number of degrees of freedom for (top) single hidden layers ANN and (bottom) double hidden layers ANN. Networks are trained over 10 epochs. Each bar corresponds to the r^2-score of the most effective ANN for a given DoF. 146

6.18 Evolution of (a) the r^2-score and (b) the mean square error (MSE) as a function of the number of epochs. r^2-scores and MSE are evaluated on the testing partition (full partition or subset corresponding to a given flow configuration). The (15;55;55;1) ANN contains 4016 degrees of freedom and the training is performed using the Laplacians inputs as indicated by the 15 input data. 148

6.19 In red, representation of the values predicted by a (15;55;55;1) ANN model (4016 degrees of freedom) versus the true values and in black, representation of true values versus true values. Flow configuration(s) (a) mixing layer only at $M_c = 1.1$, (b) mixing layer only at $M_c = 2.2$, (c) forced HIT only, (d) full testing partition. 150

6.20 Comparison of the r^2-score evolutions between ANN with and without Laplacian inputs as a function of the number of epochs. Results are evaluated over the testing partition. 150

6.21 $z-$centerplane contours colored by $\bar{p}-\widehat{p}$ for true (left) and ANN predicted (right) values. Results are plotted for the second stored temporal solution (see Table 6.1) for each configuration: (top) the mixing layer at $M_c = 1.1$ ($\tau = 1750$), (middle) the mixing layer at $M_c = 2.2$ ($\tau = 4050$) and (bottom) the forced HIT (Solution 2). The (11;55;55;1) ANN model comprises 3796 degrees of freedom and is trained without Laplacian inputs. None of the flow solutions have been included into the ANN training. 155

6.22 $z-$centerplane contours colored by $\bar{p}-\widehat{p}$ for true (left) and ANN predicted (right) values. Results are plotted for the third stored temporal solution (see Table 6.1) for each configuration: (top) the mixing layer at $M_c = 1.1$ ($\tau = 2100$), (middle) the mixing layer at $M_c = 2.2$ ($\tau = 5000$) and (bottom) the forced HIT (Solution 8). The (11;55;55;1) ANN model comprises 3796 degrees of freedom and is trained without Laplacian inputs. None of the flow solutions have been included into the ANN training. 156

6.23 $z-$centerplane contours colored by $\bar{p}-\widehat{p}$ for true (left) and ANN predicted (right) values. Results are plotted for the mixing layers at $M_c = 2.2$: (top) DGB, (middle) DGC and (bottom) DGD. The (11;55;55;1) ANN model comprises 3796 degrees of freedom and is trained without Laplacian inputs. None of the flow solutions have been included into the ANN training. 157

6.24 **Mixing layer at $\mathbf{M_c = 1.1}$** - Four small size ANN are identically with four different Glorot initializations (Glorot & Bengio, 2010). Positive weights are colored in orange and negative ones in blue. Values of weights are only given when the absolute value is larger than 1. 163

6.25 **Mixing layer at $\mathbf{M_c = 2.2}$** - Four small size ANN are identically trained with four different Glorot initializations (Glorot & Bengio, 2010). Values of weights are only given when the absolute value is larger than 1. 164

6.26 **Forced HIT** - Four small size ANN are identically trained with four different Glorot initializations (Glorot & Bengio, 2010). Values of weights are only given when the absolute value is larger than 1. 165

7.1 Mixing layer at $M_c = 1.1$. $z-$centerplane contours colored by $\bar{p} - \widehat{p}$ for (a) predicted *a priori* values and computed *a posteriori* values with (b) $\bar{\Delta}/\Delta_{\text{DNS}} = 32$, (c) $\bar{\Delta}/\Delta_{\text{DNS}} = 16$, (d) $\bar{\Delta}/\Delta_{\text{DNS}} = 8$ and (d) $\bar{\Delta}/\Delta_{\text{DNS}} = 4$. Results are plotted at $\tau = 1750$. Note that the domain length in the $y-$direction is identical for the four LES but is twice larger than the one used for the filtered DNS. . . 170

7.2 Mixing layer at $M_c = 2.2$. $z-$centerplane contours colored by $\bar{p} - \widehat{p}$ for the (a) and (a*) predicted *a priori* values and computed *a posteriori* values with (b) $\bar{\Delta}/\Delta_{\text{DNS}} = 32$, (c) $\bar{\Delta}/\Delta_{\text{DNS}} = 16$, (d) $\bar{\Delta}/\Delta_{\text{DNS}} = 8$ and (d) $\bar{\Delta}/\Delta_{\text{DNS}} = 4$. Results are plotted at $\tau = 4050$. *A priori* results are plotted twice: (a) with the scale found in the *a priori* analysis and (a') with the scale computed in the *a posteriori* LES. Note that the domain length in the $y-$direction is identical for the four LES but is twice larger than the one used for the filtered DNS. 171

7.3 Temporal evolution of the momentum thickness. Comparison is made between DNS and *a posteriori* LES at four filtering sizes ($\bar{\Delta}/\Delta_{\text{DNS}} \in [4, 8, 16, 32]$) with and without the SGS pressure model. No difference is visible since curves overlap. Two different non-dimensional time ranges are represented for each convective Mach number: for $M_c = 1.1$, $\tau \in [1600; 2600]$ (left) and $\tau \in [1600; 3500]$ (right); for $M_c = 2.2$, $\tau \in [3500; 6500]$ (left) and $\tau \in [3500; 8000]$ (right). 173

7.4 Temporal evolution of the momentum thickness for the mixing layers at (top) $M_c = 1.1$ and (bottom) $M_c = 2.2$. Comparison is made between DNS and *a posteriori* LES at four filtering sizes ($\bar{\Delta}/\Delta_{\text{DNS}} \in [4, 8, 16, 32]$) with and without the dynamic Smagorinsky model. Two different non-dimensional time ranges are represented for each convective Mach number: for $M_c = 1.1$, $\tau \in [1600; 2600]$ (left) and $\tau \in [1600; 3500]$ (right); for $M_c = 2.2$, $\tau \in [3500; 6500]$ (left) and $\tau \in [3500; 8000]$ (right). 174

7.5 $z-$centerplane contours colored by (left) SGS pressure $\left(\frac{\partial[\bar{p}-\widehat{p}]}{\partial x_i}\right)$ and SGS turbulent stress tensor $\left(\frac{\partial \bar{\rho}[\widehat{u_i u_j} - \widetilde{u}_i \widetilde{u}_j]}{\partial x_j}\right)$ fluxes for the mixing layer at $M_c = 2.2$ and $\bar{\Delta}/\Delta_{\text{DNS}} = 8$ in (top) $x-$, (middle) $y-$ and (bottom) $z-$ directions. Results are plotted at $\tau = 6000$. The ANN model comprises 3796 degrees of freedom (11;55;55;1) and is trained without Laplacian inputs. 176

7.6 $z-$centerplane contours colored by (left) the SGS pressure $\left(\frac{\partial[\bar{p}-\widehat{p}]}{\partial x_i}\right)$ gradients and (right) the density gradients for the mixing layer at $M_c = 2.2$ and $\bar{\Delta}/\Delta = 8$ in (top) $x-$, (middle) $y-$ and (bottom) $z-$ directions. Results are plotted at $\tau = 6000$. The ANN model comprises 3796 degrees of freedom (11;55;55;1) and is trained without Laplacian inputs. 178

7.7 Mixing layer at $M_c = 1.1$. The non-dimensional Reynolds averaged (left) and root mean square (right) values of temperature (top), density (middle) and pressure (bottom) are averaged over the self-similar period ($\tau \in [1700; 2550]$), plotted along the y-direction and compared between DNS and *a posteriori* LES with and without the SGS pressure model at four different filtering sizes. Note that the bar symbol refers here to the Reynolds averaged of LES quantities and not to the LES filtering symbol. 179

7.8 Mixing layer at $M_c = 2.2$. The non-dimensional Reynolds averaged (left) and root mean square (right) values of temperature (top), density (middle) and pressure (bottom) are averaged over the self-similar period ($\tau \in [4000; 6000]$), plotted along the y-direction and compared between DNS and *a posteriori* LES with and without the SGS pressure model at four different filtering sizes. Note that the bar symbol refers here to the Reynolds averaged of LES quantities and not to the LES filtering symbol. 180

A.1 TKE budget in the self-similar turbulent region, where kC, kT, (c), (e), (d) denote respectively the convective, transport, production, pressure dilatation and dissipation terms respectively at $M_c = 0.7$. Resi denotes the residual error of TKE transport equation. Taken from Zhou *et al.* (2012). II

A.2 Figure taken from Martínez Ferrer *et al.* (2017). (a) and (b) correspond to the TKE budget terms. II

A.3 Schematic view of the averaging process applied to generate the TKE budget and thermodynamic distributions (see for instance Figures 3.5, 4.8 and 4.9). Each line corresponds to a discrete time t_i in the selected self-similar period, for which a solution is available. Each solution at $t = t_i$ contains a distribution of $N_y = 512$ points (only 17 are reported on this schematic view) distributed on the non-dimensional interval $[-L_y/\delta_\theta(t_i), L_y/\delta_\theta(t_i)]$. III

A.4 TKE budget plots at $M_c = 1.1$ with different numbers of points: first column: 24 points; second column: 39 points (used in the thesis); third column: 79 points. (a): Distributions of the PG normalized specific power quantities (see Figure 3.5); (b): Distribution of the volumetric normalized powers (see Figure 4.8); (c) $x-$turbulent stress tensor (R_{xx}) equation (see Figure 4.9(a)); (d): $y-$turbulent stress tensor (R_{yy}) equation (see Figure 4.9(b)). IV

B.1 Temporal evolution of the mixing layer momentum thickness. VII

B.2 Temporal evolution of the integral length scale l_z. VII

B.3 Temporal evolution of the non-dimensional streamwise turbulent production term integrated over the whole domain $P^*_{int} = (1/(\rho_0(\Delta u)^3)) \int_{L_y} \bar{\rho} P_{xx} dV$ (with $\bar{\rho} P_{xx}(y) = -\overline{\rho u''_x u''_y} \frac{\partial \tilde{u}_x}{\partial y}$) for the DG2 simulation. VIII

C.1 RMS amplitude of terms in the real gas filtered momentum equation (Equation (2.48)) for the DG mixing layer at $M_c = 1.1$. Results are given at the initial time of each self-similar period for the three filter types (Gaussian, top-hat and sharp filters). X

C.2 RMS amplitude of terms in the filtered energy equation (Equation (2.48)) for the DG mixing layer at $M_c = 1.1$. Results are given at the initial time of each self-similar period for the three filter types (Gaussian, top-hat and sharp filters). XI

C.3 RMS amplitude of terms in the real gas filtered momentum equation (Equation (2.48)) for the DG mixing layer at $M_c = 1.1$. Results are given at the initial time of each self-similar period for three different filter parameters $\zeta = 2-6-10$ (top-middle-bottom). XII

D.1 RMS amplitude of terms in the filtered momentum equations (Equations (2.48)) for the perfect gas mixing layer at $M_c = 0.1-1.1-2.2$ (top-middle-bottom). Results are averaged over the domain and over the self-similar period growth phase of the mixing layer. The turbulent Mach numbers averaged over the centerplane are respectively equal to $0.05 - 0.4 - 0.5$. The SGS viscous terms is very small and does not appear on the plot for $M_c = 1.1$ and $M_c = 2.2$. XVI

D.2 RMS amplitude of terms in the filtered total energy equation (Equation (2.48)) for the perfect gas mixing layer at $M_c = 0.1-1.1-2.2$ (top-middle-bottom). Results are averaged over the domain and over the self-similar period growth phase of the mixing layer. The turbulent Mach numbers averaged over the centerplane are respectively equal to $0.05 - 0.38 - 0.67$. XVIII

E.1 Cumulative variance rates are plotted for each PCA mode for the forced HIT (top) and for the mixing layers at $M_c = 1.1$ (middle) and at $M_c = 2.2$ (bottom). XX

E.2 Projection of mode 1 in the inputs space for the forced HIT (top) and for the mixing layers at $M_c = 1.1$ (middle) and at $M_c = 2.2$ (bottom). The mode 1 represents more than 40% of the information. XXI

E.3 Projection of mode 2 in the inputs space for the forced HIT (top) and for the mixing layers at $M_c = 1.1$ (middle) and at $M_c = 2.2$ (bottom). The mode 2 represents more than 22% of the information. XXII

E.4 Cumulative variance rates are plotted for each mode for the PCA performed simultaneously over the forced HIT and the mixing layers at $M_c = 1.1$ and at $M_c = 2.2$. XXIII

E.5 Projection of modes 1 (top) and 2 (bottom) in the inputs space for the PCA performed simultaneously over the forced HIT and the mixing layers at $M_c = 1.1$ and at $M_c = 2.2$. The mode 1 and 2 represents respectively about 44% and 25% of the information. XXIV

E.6 (Top) Projection of the data for the forced HIT and the mixing layers into the first two PCA modes containing more than 70% of the information. The normalized PDF is also given for each mode along axis. XXV

F.1 Representation of HSIC interactions for Exemple 2. XXIX

List of Tables

2.1 Physical parameters of FC-70 (Cramer, 1989). The critical pressure p_c, the critical temperature T_c, the boiling temperature T_b and the compressibility factor $Z_c = p_c v_c/(RT_c)$ are the input data for the Martin-Hou EoS. The critical specific volume v_c is deduced from the aforementioned parameters. The exponent n and the $c_{v_\infty}(T_c)/R$ ratio are used to compute the ideal isochoric heat capacity $c_{v_\infty}(T)$. 13

2.2 Comparison of the PG and DG non-dimensional terms appearing in the non-dimensional Navier-Stokes equations (2.23) and (2.34). The numerical values are given for air considered as a calorically perfect gas with $\gamma = 1.4$ and $Pr_0 = 0.71$. 19

2.3 Filter functions are given in physical and spectral spaces for the three classical filters used in LES. ϕ_i denotes the component of $\boldsymbol{\phi}$ in the i^{th} direction. The parameter ζ controls the selectivity of the Gaussian filter. An analysis of its influence on the *a priori* LES results is given in Appendix C. It is recommended to set this parameter to $\zeta = 6$ (Garnier *et al.*, 2009). 23

2.4 Comparison of SGS terms appearing in LES formulation, respectively for real gas (filtered system (2.48)) and perfect gas (filtered system (2.54)). In blue: terms with identical expressions in real gas and PG flows; in red: terms with different expressions in real gas and PG flows. 28

2.5 Numerical setup used in the solver AVBP. 33

3.1 Simulation parameters for Air PG DNS. L_x, L_y and L_z denote computational domain lengths measured in terms of initial momentum thickness. N_x, N_y and N_z denote the number of grid points. L_0 denotes the size of initial turbulent structures ($k_0 = 2\pi/L_0$) measured in terms of initial momentum thickness. All grids are uniform. 37

3.2 Non-dimensional parameters computed at the beginning and at the end of the self-similar period. Re_{λ_x} denotes the Reynolds number based on the longitudinal Taylor microscale $\lambda_x = \sqrt{2\overline{u'^2_x}/\overline{(\partial u'_x/\partial x)^2}}$ computed at the centerline. L_η denotes the Kolmogorov length scale computed at the centerline. 49

4.1 Simulation parameters. L_x, L_y and L_z denote computational domain lengths measured in terms of initial momentum thickness. N_x, N_y and N_z denote the number of grid points. L_0 denotes the size of initial turbulent structures ($k_0 = 2\pi/L_0$) measured in terms of initial momentum thickness. All grids are uniform. 54

4.2 Comparison of the PG and DG non-dimensional terms appearing in Equations (2.23) and (2.34). 56

4.3 Simulation parameters for additional FC-70 simulations at $M_c = 2.2$ varying the initial operating point. r, l_x/L_x and l_z/L_z are given at beginning and ending times of self-similar periods. $L_0 = L_x/8$ for all the simulations. 88
4.4 Eckert numbers and normalized momentum thickness growth rates are given for each simulation. 95

6.1 Composition of the training and testing databases used to design the ANN modeling the SGS pressure term. 119
6.2 Pearson product-moment correlation coefficients ($R_{ij} = C_{ij}/\sqrt{C_{ii}C_{jj}}$), where C is the covariance matrix) between inputs and the SGS pressure term ($\bar{p} - \widehat{p}$). Correlations whose absolute value is above 0.4 are colored in red. 125
6.3 Best r^2-scores for several ANN trained over 5.6 millions of elements randomly chosen across the database (Mixing layers $M_c = 1.1$ and 2.2 and forced HIT) for several degrees of freedom up to 10 000. 126
6.4 Overview of hyperparameters choices in the literature dedicated to the design of SGS models. Slash symbol indicates the lack of the information. 129
6.5 Recommendations to select hyperparameters (extracted from Géron (2017)). . . 130
6.6 List of performed grid searches with their corresponding parameters. 133
6.7 Appropriate hyperparameters for the present work. 143
6.8 Performance of the (15;55;55;1) ANN model (4016 degrees of freedom) trained using Laplacian inputs and with the full database training partition (80% of the data corresponding to the 3 flow configurations). r^2-scores and MSE are computed using the testing partition (remaining 20%) or subsets of the testing partition. 149
6.9 Accuracy assessment for several ANN with a different number of degrees of freedom (96-436-913-3796). r^2-scores and correlation coefficients are computed after 10 epochs using the testing partition (full or its subsets corresponding to the 3 flow configurations). All ANN are trained without Laplacian inputs. 152
6.10 Results of generalization tests for the (15;55;55;1) ANN (4016 degrees of freedom) trained with Laplacian inputs. Metrics (r^2-score and correlation coefficient) are evaluated over the full solutions after 10 epochs. 153
6.11 Performance of the (11;55;55;1) ANN model (3796 degrees of freedom) trained (without Laplacian inputs) over the full training database. r^2-scores and correlation coefficients are evaluated over the full solutions which were not included in the ANN training database (see the additional testing database in Table 6.1) 154
6.12 r^2-scores of small size ANN (of the form (11;2;2;1) yielding 33 degrees of freedom) trained over each flow configuration. Scores are evaluated over the testing partition after 10 epochs. 160
6.13 **Mixing layer at $\mathbf{M_c = 1.1}$** - Correlation coefficients are computed between the two intermediate ANN inputs (1st and 2nd inputs) at the entrance of the first hidden layer and the ANN inputs and the true value of the SGS pressure term ($\bar{p} - \widehat{p}$). Correlations with absolute values above 0.4 are colored in red. Small size ANN are trained during 10 epochs. 162
6.14 **Mixing layer at $\mathbf{M_c = 2.2}$** - Correlation coefficients are computed between the two intermediate ANN inputs (1st and 2nd inputs) at the entrance of the first hidden layer and the ANN inputs and the true value of the SGS pressure term ($\bar{p} - \widehat{p}$). Correlations with absolute values above 0.4 are colored in red. Small scale ANN are trained during 10 epochs. 166

6.15 **Forced HIT** - Correlation coefficients are computed between the two intermediate ANN inputs (1st and 2nd inputs) at the entrance of the first hidden layer and the ANN inputs and the true value of the SGS pressure term ($\bar{p} - \widehat{p}$). Correlations with absolute values above 0.4 are colored in red. Small scale ANN are trained during 10 epochs. 167

B.1 Non-dimensional parameters computed at the beginning and at the end of the self-similar period. Re_{λ_x} denotes the Reynolds number based on the longitudinal Taylor microscale $\lambda_x = \sqrt{2\overline{u'^2_x}/\overline{(\partial u'_x/\partial x)^2}}$ computed at the centerline. L_η denotes the Kolmogorov length scale computed at the centerline. VI

B.2 Simulation parameters for temporal mixing layer DNS ($Re_{\delta_{\theta,0}} = 160$) with varying domain extent, resolution and size of initial structures. L_x, L_y and L_z denote computational domain lengths measured in terms of initial momentum thickness. N_x, N_y and N_z denote the corresponding numbers of grid points. L_0 denotes the size of initial turbulent structures ($k_0 = 2\pi/L_0$) measured in terms of initial momentum thickness. All grids are uniform. VI

F.1 HSIC coefficients for Example 1 varying the number of test sets n_s. XXVII

F.2 HSIC coefficients for Example 2 varying the number of test sets n_s. XXVIII

Chapter 1

Introduction

1.1 Context and motivation

Figure 1.1: Examples of ORC units: (left) 2 MW Turboden ORC unit using heat recovery in a cement plant and solar thermal energy (Source: Colonna *et al.* (2015)); (right) Solar ORC unit installed in Lesotho (Africa) to help local people becoming electrically self-sufficient (Source: STG international).

Organic Rankine Cycles (ORCs) rely on the so-called William Rankine's cycle dating back to the 19th century (Rankine, 1873). This thermodynamic cycle is widely used in industry: refrigerator, air-conditioner, heat pump, steam engine,... It comprises two isentropic and two isobaric transformations. The working fluid (commonly water) is warmed up and evaporated through an heat source. The steam is then expanded (usually through a turbine) to produce mechanical energy. The conversion into electrical energy can be made using an alternator. An *Organic* Rankine Cycle makes use of an organic fluid (instead of water), that is a fluid belonging to the class of chemical compounds formed from carbon. Among organic fluids, **dense gases** (DG) have been widely used in the ORC industry over the past forty years.

The use of such gases enables a great adaptability of ORCs and constitutes their major asset. The first main advantage of DG is their capacity to exchange large amount of energy at low to moderate temperatures because of both their large heat capacity and their low boiling point temperature. As a result, ORCs using dense gases as working fluids cover a wide range of power (from few kW to several MW) and are well suited to enhance a wide range of heat sources whose temperature do not exceed the fluid stability limit (around 300°C to 400°C (Gaia,

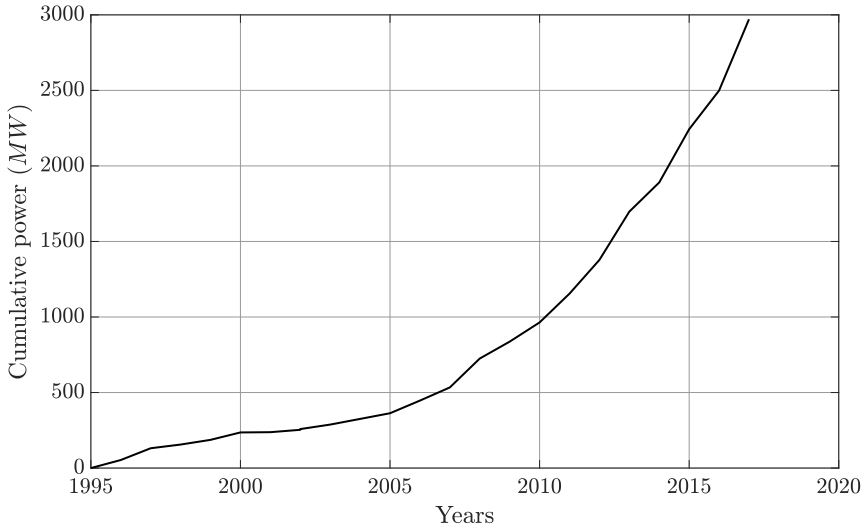

Figure 1.2: Cumulative installed capacity of commercial ORC power plants since 1995 adapted from Tartière & Astolfi (2017).

2011)). Among the most tapped heat sources, one can mention geothermal energy, biomass, heat recovery in primary engines or industrial processes, concentrated solar radiations, ocean thermal gradients, urban solid waste and landfill gas combustion, ... (see Figure 1.1 for an illustration of some different types of ORCs). Note that the most powerful ORCs use generally the geothermal energy. The previous list is far from exhaustive and the ORC potential is promising: future applications include heat recovery for automotive engines, domestic combined heat and power (CHP) or even next generation nuclear power plants. The interested reader should refer to Colonna *et al.* (2015) for a thorough review of ORCs history and applications.

Another main benefit from using DG lies in the large choice of fluids. DG can be classified into three fluid classes: hydrocarbons, fluorocarbons and siloxanes (well adapted for high-temperature ORCs). The working fluid can be selected in accordance with the operating point of the cycle, that is in particular such that the fluid thermodynamic properties match the temperature profile of heat sources (Invernizzi, 2013). ORCs are therefore very often the most appropriate technology capable to convert energy at low power with a rather good efficiency (around 15% to 20%). As a result, ORCs are usually designed for each situation so that it is rather difficult to standardize the production of their components.

Other main advantages of ORCs coming from DG properties include (Colonna *et al.*, 2015):

- A lower operating pressure inside the turbine which enables an easier design and reduces wear issues;
- A reduction of the blade corrosion;
- A lower rotational speed (around 2 to 10 times lower than a steam turbine) which dispenses from using a gearbox;
- A much lower slope of the saturation curve for some fluids which prevents condensation at the turbine exit and avoids using a regenerator to reheat the fluid;
- DG can act as lubricant unlike water for which the mixing with lubricant decreases the thermodynamic efficiency.

Because of their specific thermodynamic properties, DG are also used in other applications like Stirling engines (Invernizzi, 2010), hypersonic and supersonic wind tunnels (Wagner & Schmidt,

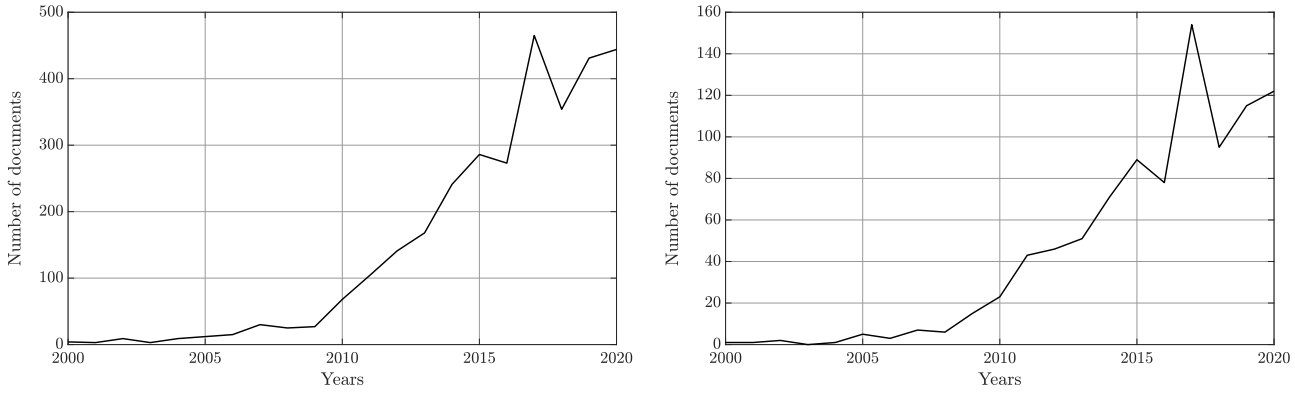

Figure 1.3: Evolution of the number of documents including "ORC" and "energy" (left), and "ORC", "energy", and "turbine" (right) in their title, abstract or keywords (Source: Scopus).

1978; Anders *et al.*, 1999) or chemical transport and processing (Kirillov, 2004).

The aforementioned advantages of the ORC technology aroused a growing interest in industry: the cumulative installed capacity of commercial ORC power plants has been multiplied by three between 2010 and 2017 (see Figure 1.2), reaching 3GW. Since the early 2000s, the market has known a significant growth correlated with the increase of oil prices. The interested reader is referred to Tartière & Astolfi (2017) for a complete overview of the ORC market.

This significant growth of the industrial market was coupled with an increasing research effort in academia, with a focus on ways to improve the overall ORC efficiency. Since the most technically advanced element of ORC is the turbine, its proper design is highly influential on ORC efficiency. Figure 1.3 illustrates the growing research interest about ORC and specifically about the turbine over the last ten years. Companies developing this technology face numerous challenges among which some come from a lack of basic knowledge regarding the turbulent flows of DG in expanders. Moreover, rotating elements are a main source of losses in turbines. Their use in transonic and supersonic regimes generates shocks associated with entropy production. However, for DG, entropy jumps through shocks are significantly reduced in specific thermodynamic regions in the vicinity of the critical point (Cinnella & Congedo, 2007). Improving knowledge about DG behavior in these specific regions could encourage ORC designers to consider turbine operating in these regions as a way to improve efficiency. Before explaining why and how the present work aims to contribute to the DG knowledge improvement, let us briefly review the current state of knowledge on DG flow physics.

1.2 Dense gas flows

DG are single-phase vapors characterized by long chains of atoms and by medium to large molecular weights. In the vicinity of the critical point, DG exhibit an unusual behavior compared with classical gases. In this study, specific DG called Bethe-Zel'dovich-Thompson (BZT) gases, also widely used in industry, are considered. The name BZT was given by Cramer (1991) to acknowledge the pioneering works of Bethe (1942), Zel'dovich (1946) and Thompson (1971) on this type of gases. BZT gases display an "inversion zone", that is a thermodynamic region where the fundamental derivative of gas dynamics becomes negative ($\Gamma < 0$).

The fundamental derivative of gas dynamics was introduced by Hayes (1958), and then

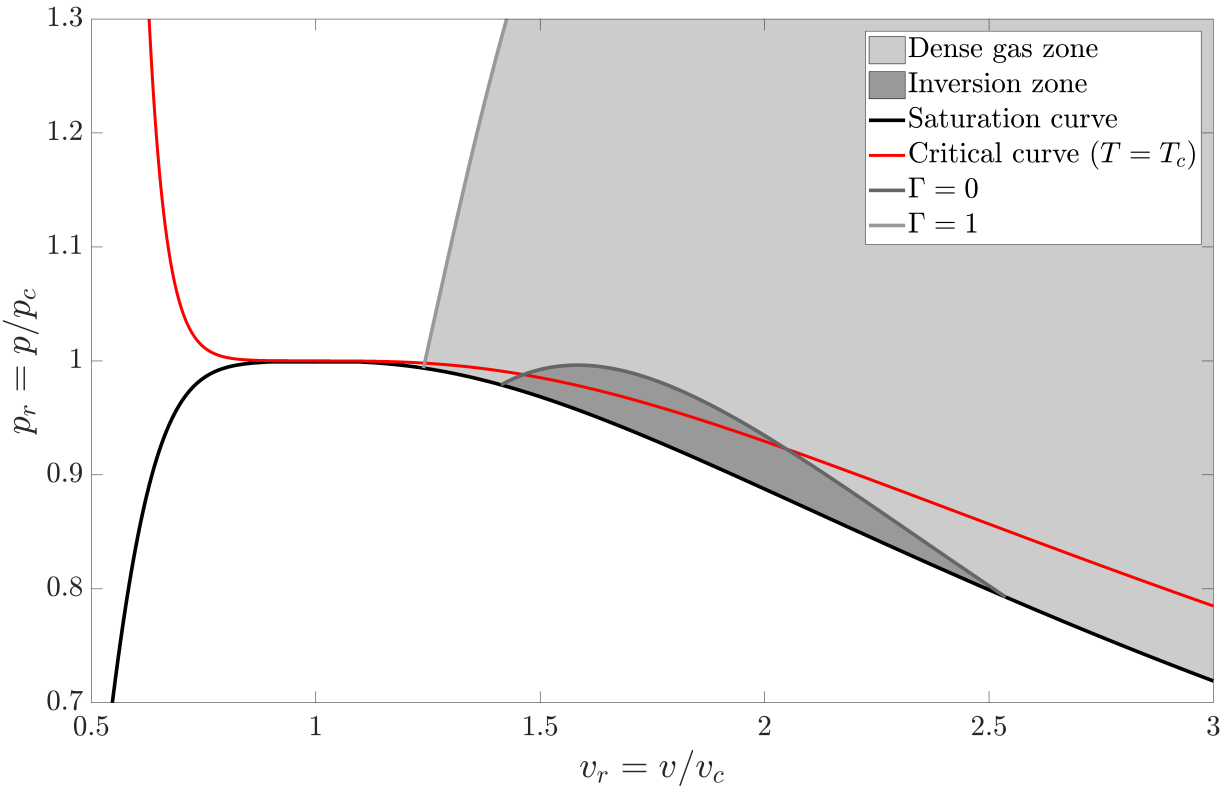

Figure 1.4: The dense gas zone ($\Gamma < 1$) and the inversion zone ($\Gamma < 0$) are plotted for our working fluid (FC-70) using the Martin-Hou equation of state. p_c and v_c are respectively the critical pressure and the critical specific volume.

rewritten by Thompson (1971) as:

$$\Gamma = \frac{v^3}{2c^2}\frac{\partial^2 p}{\partial v^2}\bigg|_s = \frac{c^4}{2v^3}\frac{\partial^2 v}{\partial p^2}\bigg|_s = 1 + \frac{\rho}{c}\frac{\partial c}{\partial \rho}\bigg|_s \tag{1.1}$$

where v is the specific volume, ρ the density, $c = \sqrt{\partial p/\partial \rho|_s}$ the speed of sound, p the pressure and s the entropy. The term "fundamental" emphasizes the importance of Γ in the determination of the non-linear behavior of dense gases. This physical quantity is a measure of the speed of sound rate of change in an isentropic transformation. It is directly related to the curvature of isentropic curves in the $p - v$ diagram $\left(\partial^2 p/\partial v^2\Big|_s\right)$.

There are three main regimes depending on the value of the fundamental derivative:

• $\Gamma > 1$ corresponds to the classical ideal gas behavior. For thermally and calorically perfect gases, the fundamental derivative is constant and given by: $\Gamma = (\gamma + 1)/2$.

• $0 < \Gamma < 1$ corresponds to the classical non-ideal gas behavior. In this regime, the speed of sound decreases in isentropic compression $\left(\partial c/\partial \rho\Big|_s < 0\right)$. It is referred as the dense gas region in Figure 1.4.

• $\Gamma < 0$ corresponds to the non-classical behavior referred to as BZT effect. It is a narrow region in the $p - v$ diagram as shown in Figure 1.4. In the inversion zone, because of the negative sign of the fundamental derivative, expansion shock-waves can occur.

For BZT DG, in the vicinity of the critical point, the isothermal curves (for example the critical one) display a negative curvature (concave), so that $\partial^2 p/\partial v^2\Big|_T < 0$ and thus $\Gamma < 0$.

Bethe (1942) and Zel'dovich (1946) were the first to justify this possible occurrence of expansion shock-waves in BZT flows. Bethe (1942) expressed the entropy jump expression across shock-waves as a function of the fundamental derivative.

$$\Delta s = s_2 - s_1 = -\left(\frac{\partial^2 p}{\partial v^2}\right)_s \frac{\Delta v^3}{12T} + O\left(\Delta v^4\right) = -\frac{c^2\Gamma}{v^3}\frac{\Delta v^3}{6T} + O\left(\Delta v^4\right) \tag{1.2}$$

with T the temperature. In the case of compression shock-waves, the specific volume variation is negative ($\Delta v < 0$), so that the fundamental derivative must be positive ($\Gamma > 0$) to ensure that the entropy jump remains positive ($\Delta s > 0$), thus satisfying the Second law of thermodynamics. Only compression shock-waves are physically admissible for classical ideal gases since $\Gamma > 1$. For BZT gases, the fundamental derivative being negative ($\Gamma < 0$), physically admissible shock-waves in the inversion region are expansion shock-waves such that the specific volume variation is positive ($\Delta v > 0$) to ensure the entropy jump remains positive. Moreover, since entropy jumps are proportional to the fundamental derivative Γ, which is of small amplitude in DG flows, intensity of shocks is significantly reduced (Cramer & Kluwick, 1984). In addition to a peculiar thermodynamic behavior, the sound speed is much lower in dense gases (up to 10 times) when compared with a usual gas such as air, which makes compressible flow regimes much more easily accessible. Another significant effect can be highlighted using one of Maxwell's relations:

$$\left.\frac{\partial T}{\partial v}\right|_s = -\left.\frac{\partial p}{\partial s}\right|_v = -\left.\frac{\partial p}{\partial T}\right|_v \left.\frac{\partial T}{\partial s}\right|_v = -\frac{\left.\frac{\partial p}{\partial T}\right|_v}{\left.\frac{\partial s}{\partial T}\right|_v} = -\frac{T}{c_v}\left(\frac{\partial p}{\partial T}\right)_v \tag{1.3}$$

If the heat capacity is large ($c_v >> 1$), which is the case for DG, the isentropic curves will follow the isothermal ones $\left(\left.\partial T/\partial v\right|_s << 1\right)$. In such fluids, because of the large heat capacity, isentropic transformations are almost isothermal. Colonna & Guardone (2006) provided further explanations using an advanced molecular study of forces at stake, depending on the molecular complexity. They showed that there exists a minimum molecular complexity that must be reached in a gas in order to fulfill DG and BZT conditions: $N > N^{DG} \approx 7.57$ and $N > N^{BZT} \approx 33.33$, with N, the molecular complexity corresponding to the number of active degrees of freedom of the molecule. The larger the complexity, the more vibrational modes absorb energy, therefore reducing the propagating energy in translational modes and thus lowering the sound speed.

Such unusual features can only be modeled when using a sufficiently complex equation of state (EoS). The simplest equation of state enabling the prediction of expansion shock-waves is the Van der Waals EoS. More complex EoS can be chosen to provide a more accurate representation of BZT DG thermodynamic behavior: Redlich-Kwong (RK) (Redlich & Kwong, 1949), Soave-Redlich-Kwong (SRK) (Soave, 1972), Peng-Robinson (PR) (Peng & Robinson, 1976) and Martin-Hou (MH) (Martin & Hou, 1955; Martin *et al.*, 1959). A comparison of these models is given in Guardone *et al.* (2004). Another popular method is based on look-up tables using NIST Refprop (Lemmon *et al.*, 2007) and CoolProp (Bell *et al.*, 2014). In the present study, because we are using FC-70 as working fluid, the first method using the MH EoS will be retained since it is considered as the reference thermodynamic model for fluorinated BZT fluids.

Many researchers have studied the non-classical phenomena occurring in (BZT) dense gases, such as rarefaction shock-waves, by considering at first the fluid as inviscid (Cramer & Kluwick, 1984; Menikoff & Plohr, 1989; Rusak & Wang, 1997; Wang & Rusak, 1999; Congedo *et al.*, 2007, 2011). Adding viscosity effects enabled the study of boundary layers and shock/boundary layers

interaction (Cramer & Crickenberger, 1991; Cramer & Park, 1999; Fergason & Argrow, 2001; Kluwick, 2004). These studies concluded on the benefits of using dense gases in ORC turbines since, when operating in the dense gas region ($0 < \Gamma < 1$) at transonic regime, dense gas effects reduce friction drag and boundary layer separation (Cinnella & Congedo, 2007). Also, when the expansion operates within the inversion region ($\Gamma < 0$), shock intensity decreases and entropy losses are reduced.

From the experimental viewpoint, it is very difficult to observe rarefaction shock-waves because of the vicinity of the critical point where physical quantities are experiencing strong variations. Borisov *et al.* (1983) and Kutateladze *et al.* (1987) claimed to have experimentally observed rarefaction shock-waves. However, their results were questioned by Cramer & Sen (1986) and Fergason *et al.* (2001) who showed that the fluid used in the experiment ($F - 13, CClF_3$) does not satisfy the Thompson & Lambrakis (1973) requirements and concluded that the observed shock-wave was not a single-phase rarefaction shock-wave.

Since then, works by Fergason *et al.* (2001), Colonna *et al.* (2008), Spinelli *et al.* (2010) and Spinelli *et al.* (2013) enabled the design of shock tubes and test rigs, such as the Test Rig for Organic VApors (TROVA) at Politecnico di Milano or the Flexible Asymmetric Shock Tube (FAST) built at Delft University of Technology (Mathijssen *et al.*, 2015). The experimental proof of rarefaction shock-waves remains an active research area. A recent review of current experimental and numerical studies on ORCs is given in Nematollahi & Kim (2020) and mentions a new test facility (ORCviP) installed in Pusan National University that consists in an ORC adapted to use visualization methods such as PIV and Schlieren methods.

1.3 The need for turbulence modeling in dense gas flows

The use of dense gases in ORCs raises modeling issues when numerically designing ORC turbines since the turbulent flows at stake include both significant compressibility effects and potential differences with respect to perfect gases (PG). Argrow (1996) was the first to perform the numerical simulation of a single-phase DG inviscid flow in a shock tube. This pioneering work was followed by contributions of Monaco *et al.* (1997), Brown & Argrow (1998), Colonna & Rebay (2004) and Cinnella & Congedo (2005) with the simulation of inviscid DG flows over airfoils or turbine cascades. Cinnella & Congedo (2007) performed for the first time DG simulations for laminar and turbulent external flows over airfoils and flat plates using Reynolds-averaged Navier-Stokes (RANS) equations with the simple algebraic model of Baldwin & Lomax in the latter case. Harinck *et al.* (2010*b*), Wheeler & Ong (2013) and From *et al.* (2017) subsequently achieved simulations of turbulent DG flows using respectively $k-\varepsilon$ and $k-\omega$ two-equation models, Spalart-Allamaras one-equation model and an Explicit Algebraic Reynolds Stress model. Recently Razaaly *et al.* (2019); Romei *et al.* (2020) performed supersonic turbine cascade RANS simulations using the $k-\omega$ Shear Stress Transport (SST).

In addition, Dura Galiana *et al.* (2016, 2017) performed Large Eddy Simulations (LES) of a turbulent dense gas flow over a turbine vane trailing-edge using the Smagorinsky-Lilly model and a wall model even though it had not been developed nor calibrated for DG flows. They noticed a strong reduction of the wake as the fundamental derivative of gas dynamics Γ decreases. A brief comparison is also made by the authors with experimental results showing much lower predicted total pressures as Γ decreases. Lately, Hoarau *et al.* (2021) achieved a coarse wall-resolved implicit LES at low supersonic conditions, using a numerical viscosity to ensure subgrid-scale dissipation.

Up to now, although the DG thermodynamic features strongly differ from those of perfect

gases, turbulence closure models developed and calibrated for perfect gases have been coupled with real-gas EoS and applied for RANS simulations and LES of dense gas flows, for lack of a better option. The peculiar thermodynamic behavior of dense gases, in particular BZT gases, questions the validity of this choice, which implicitly assumes that turbulent structures are not affected by dense gas effects. Such an assumption is not yet verified and constitutes an open-research field. Yet, the lack of reference experimental data makes the verification of the presently used turbulence models a complex task. Note the influence of the thermodynamic models (Equations of State and transport coefficient description) on the numerical prediction of dense gas flows is also an issue which has been investigated by several authors, see for instance Harinck *et al.* (2010*a*); Merle & Cinnella (2014), and also suffers from the same lack of reference experimental data. Yet, recent progress has been made on this latter topic thanks to measurements made in the TROVA facility at Politecnico di Milano. In Gori *et al.* (2020), the RANS computation of the flow in a converging-diverging nozzle was performed using a Span-Wagner EoS optimized for MDM and compared with the reference experimental results to validate the developed EoS.

The tool of choice to be used in order to assess the potential specificities of turbulence in a dense gas flow is Direct Numerical Simulation (DNS) since it enables the resolution of every turbulent scale, from the largest swirls (limited by the size of the domain) to the smallest ones (limited by the Kolmogorov scale), and thus gives access to the flow physics without resorting to any turbulent closure model. Because the number of cells needed to reach DNS resolution grows as $O(Re^{9/4})$ (Bailly & Comte-Bellot, 2003), DNS remains naturally confined to simple flow configurations. For larger and more complex systems, LES is a tool of choice since it resolves large turbulent scales and models the small ones. However, as already mentioned, it relies on subgrid models which have been tailored for turbulent flows of ideal gases so that their validity for dense gases is also questionable.

At the present time, few authors have achieved DNS of dense gas flows. Giauque *et al.* (2017) have performed a DNS of decaying homogeneous isotropic turbulence (HIT) and concluded that the standard Smagorinsky sub-grid scale model does not capture correctly the temporal evolution of the turbulent kinetic energy by comparing the LES prediction with the DNS reference results. The DNS also evidenced localized flow regions with strongly positive values for the velocity divergence that could correspond to expansion shocklets[†]. They extended their analysis by performing a forced HIT highlighting significant differences in the SGS baropycnal work and the resolved pressure-dilatation, which is reduced by a factor of 2 in the dense gas (DG) when compared to the perfect gas (PG) (Giauque *et al.*, 2020).

Sciacovelli *et al.* (2016) have also studied the large scales dynamics in decaying HIT, assuming at first an inviscid dense gas. They evidenced strong differences of the fluctuation levels for thermodynamic quantities (density, pressure, sound speed) between the perfect gas and the dense gas. They pointed out the more symmetric probability density function of the velocity divergence in the dense gas flow. Their DNS results display flow regions with strong expansions and tubular structures unlike the compression regions which are characterized by sheet-like structures. The more symmetric distribution could be explained by the presence of expansion shocklets.

Sciacovelli *et al.* (2017*b*) extended their previous decaying HIT study by considering viscous effects and focused then on the small scale dynamics. Two different initial states were selected for the dense gas : one inside the inversion region and one outside. They noticed reduced levels of thermodynamic fluctuations in dense gas flows due to the decoupling of thermal and dynamic phenomena caused by the large heat capacity. The Eckert number, which quantifies the ratio

[†]Eddy shocklets are small shocks induced by strong local fluctuating velocity events.

between the kinetic energy and the internal energy, is indeed much smaller in dense gas flows. It was also observed that the global flow dynamics is almost not influenced by local events such as expansion shock-waves. The nature of turbulent structures was also discussed based on DNS results. The formation of convergent compressed structures like compression shock-waves is strongly reduced in the BZT zone. The occurrence of non-focal convergent structures in the dense gas diminishes the vorticity and counterbalances enstrophy destruction.

Sciacovelli *et al.* (2017*a*) analyzed DG flow behavior in a supersonic turbulent channel flow. The initial thermodynamic state was chosen this time in a non-BZT DG region. Significant differences with a supersonic ideal gas channel flow were observed for some thermodynamic variables. For instance, the temperature is lower at the center line for the dense gas and the dense gas flow can actually be considered quasi-isothermal contrary to the perfect gas flow. The viscosity decreases from the wall towards the center line unlike in PG flows. They also noticed significant differences in the shape and rates of the fluctuating density and temperature distributions. Characteristics of the dense gas flow have been found to be close to those of variable-property liquid flows. Regarding the development of turbulence, the authors did not notice significant differences between the perfect gas and the dense gas for the flow configuration under study. The Reynolds stresses and the non-dimensional streamwise and spanwise lengths of the structures were found to be nearly the same. An extension of this study to the BZT DG region and to a larger Mach number would be needed to better conclude on BZT DG effects on turbulence development in a channel flow.

Gloerfelt *et al.* (2020) performed the DNS of a dense gas compressible boundary layer at Mach numbers ranging from 0.5 to 6. They confirm in particular the decoupling between dynamical and thermal effects, which leads to the suppression of friction heating. The most remarkable consequence is that the boundary layer thickness remains equal to its value in the incompressible regime as the Mach number increases.

Despite the aforementioned research effort in characterizing turbulence in DG flows, it has not yet been proven that perfect gas turbulent closure models are suitable for DG flows. This issue remains an open-research field. The present study is expected to shed some light on the specific features displayed by turbulent DG flows and which could motivate a dedicated modeling task. The method followed to address these two key questions:

- do turbulent DG flows display specific turbulent characteristics with respect to perfect gas flows ?
- if so, how should a subgrid model account for these specific characteristics ?

is described in the next section and defines the structure of the present thesis report.

1.4 Outline of the thesis

This thesis falls within the EDGES (turbulEnt Dense Gas flow modeling using large Eddy Simulation) research project funded by the National Research Agency (ANR) in France. The project is devoted to the analysis and modeling of turbulence in DG flows, with a subsequent transfer of this fundamental knowledge to the application field of ORC turbine modeling where dense gases are commonly used as working fluids. The key steps of the EDGES project are:

1. the production of a DNS database of turbulent DG flows over three classical configurations which are representative of the flow inside an ORC turbine: the Homogeneous Isotropic

Turbulence (HIT) may be seen as reflecting the turbulent behavior in a turbine inter-blade region, the mixing layer provides insight into the turbulence characteristics in the blade's wake and the channel flow provides information specific to wall bounded flows;

2. an *a priori* evaluation of LES subgrid-scale (SGS) terms and an assessment of current LES turbulent closure models using DG DNS results;

3. the construction of new LES SGS models for DG flows using supervised machine learning algorithms;

4. an *a posteriori* assessment of the relevance of these new closure models for a full ORC turbine stage.

The present thesis is organized following the key steps of the EDGES project and contributes to all these steps: the computation of a DG mixing layer is achieved (the HIT and the channel flow have been computed by other contributors of LMFA research team); the *a priori* SGS evaluation and the construction of a new SGS model are done using the HIT and the mixing layer DNS data; and the *a posteriori* validation is performed for the mixing layer configuration (the application to a full ORC turbine stage is planned in 2022, the final year of the EDGES project).

Chapter 2 references the governing equations and constitutive laws used to perform both real gas DNS and LES: instantaneous Navier-Stokes equations, thermodynamic models and LES equations. Some specific features of DG flows are also highlighted in this chapter. In addition, the numerical solver AVBP used for all the numerical simulations analyzed in the report is briefly presented.

The next two chapters are dedicated to the production of mixing layer DNS results. At first, in order to assess the quality of the present DNS, Chapter 3 is devoted to the assessment and the analysis of mixing layer DNS simulations for air (considered as a perfect gas) at three convective Mach numbers ($M_c = 0.1 - 1.1 - 2.2$). Results obtained using AVBP are in particular compared to available reference results in the literature.

Then, several DG mixing layer DNS are performed. A comparative analysis of dense gas and perfect gas mixing layers is proposed in Chapter 4 for three increasing values of the convective Mach numbers ($M_c = 0.1 - 1.1 - 2.2$). This analysis highlights and explains the differences occurring between DG and PG flows at large convective Mach numbers.

Once DG DNS results have been gathered, they can be filtered in order to study the importance of SGS terms appearing in LES equations. This task is performed in Chapter 5 for HIT and mixing layer DNS and establishes the importance of some new SGS terms, among which the SGS pressure.

To answer the need for a specific SGS modeling when dealing with DG flows, Chapter 6 proposes a modeling methodology using Artificial Neural Network (ANN). The method is then applied to the new SGS pressure term.

The closing Chapter 7 is dedicated to the *a posteriori* validation of the novel ANN-based SGS model for compressible DG mixing layers at several filtering sizes.

Chapter 2

Governing equations and numerical tools

THIS chapter is devoted to the description of the governing equations and the numerical solver (AVBP) ensuring their discrete solution, that will be employed in the next chapters. The (instantaneous) Navier-Stokes equations given in Section 2.1 are used for DNS computations in chapters 3 and 4. Their filtered version given in Section 2.4 is used for both *a priori* and *a posteriori* LES respectively in chapters 5 and 7. These governing equations are completed in Section 2.2 with the description of the specific thermodynamic modeling dedicated to dense gases, comprising the equations of state (EoS) (both thermal and caloric) and the transport coefficients models. DG peculiarities and their influence on the mathematical framework are underlined. In particular, Section 2.3 emphasizes the differences between PG and DG flows regarding the non-dimensional numbers involved in the set of governing equations. Finally, Section 2.5 introduces the numerical setup used in the AVBP solver and justifies its relevance for the DNS and LES performed in this work.

2.1 Navier-Stokes equations

Only few experimental results being available for compressible DG flows (Dura Galiana *et al.*, 2016, 2017), one needs to use DNS to accurately describe their turbulent behavior. The unsteady, three-dimensional, compressible Navier-Stokes equations are thus solved in the single-phase context for DNS. They represent the conservation of mass, momentum and total energy.

$$\begin{cases} \dfrac{\partial \rho}{\partial t} + \dfrac{\partial (\rho u_i)}{\partial x_i} = 0 \\ \dfrac{\partial (\rho u_i)}{\partial t} + \dfrac{\partial (\rho u_i u_j)}{\partial x_j} = -\dfrac{\partial p}{\partial x_i} + \dfrac{\partial \tau_{ij}}{\partial x_j} \\ \dfrac{\partial (\rho E)}{\partial t} + \dfrac{\partial [(\rho E + p) u_j]}{\partial x_j} = \dfrac{\partial (\tau_{ij} u_i - q_j)}{\partial x_j} \end{cases} \tag{2.1}$$

with ρ the density, p the pressure, u_i the i^{th} component of the flow speed ($i \in 1, 2, 3$) and $E = E_{int} + \frac{1}{2} u_i u_i$ the specific total energy (E_{int} the specific internal energy). The heat flux q_j is given by Fourier's law:

$$q_j = -\kappa \frac{\partial T}{\partial x_j} \tag{2.2}$$

with κ the thermal conductivity and T the temperature. τ_{ij} represents the viscous stress tensor. In the following, since only Newtonian fluids will be considered, the viscous stress tensor is aligned with the strain-rate tensor $\left(S_{ij} = \frac{1}{2} \left[\frac{\partial u_i}{\partial x_j} + \frac{\partial u_j}{\partial x_i} \right] \right)$. In the compressible formulation, the strain-rate tensor can be decomposed into a traceless symmetric part (the deviatoric part: S_{ij}^D), which is associated to a constant volume deformation, and a purely diagonal component (the isotropic part: S_{ij}^I), which is related to the volumetric distortion.

$$S_{ij} = \underbrace{\frac{1}{3} S_{kk} \delta_{ij}}_{S_{ij}^I} + \underbrace{\left[S_{ij} - \frac{1}{3} S_{kk} \delta_{ij} \right]}_{S_{ij}^D} \tag{2.3}$$

with $\delta_{ij} = \begin{cases} 1, & \text{if } i = j. \\ 0, & \text{otherwise.} \end{cases}$, the Kronecker delta. In the most general formulation, the viscous stress tensor is expressed as a combination of both deviatoric and isotropic parts of the strain-rate tensor.

$$\tau_{ij} = 2\mu S_{ij}^D + 2\mu_b S_{ij}^I \tag{2.4}$$

where μ and μ_b denote respectively the dynamic viscosity and the bulk viscosity. Following Stokes' hypothesis, the bulk viscosity can be usually neglected with respect to the dynamic viscosity. Very few experimental data containing the bulk viscosity are actually available for dense gases and none for FC-70, the BZT DG fluid used in this analysis. Yet, Sciacovelli *et al.* (2017*a*) roughly estimate its value for another BZT DG fluid (PP-11) and show that its effect is negligible on their results. As done in Gloerfelt *et al.* (2020), the bulk viscosity is neglected in this analysis. The viscous stress tensor becomes therefore:

$$\tau_{ij} = \mu \left(\frac{\partial u_i}{\partial x_j} + \frac{\partial u_j}{\partial x_i} - \frac{2}{3} \frac{\partial u_k}{\partial x_k} \delta_{ij} \right) \tag{2.5}$$

2.2 Thermodynamic models

The above-mentioned equations (2.1) need to be completed with a thermodynamic modeling, which is composed of both the equations of state (EoS) and the transport coefficients models.

2.2.1 Equations of state

In their general form, EoS are composed of the thermal EoS, which expresses the pressure as a function of the density (or the specific volume $v = 1/\rho$) and the temperature, and the caloric EoS, which expresses the internal energy as a function of the density (or the specific volume) and the temperature:

$$p = \mathcal{F}_t(\rho, T) \tag{2.6}$$

$$E_{int} = \mathcal{F}_c(\rho, T) \tag{2.7}$$

where $\mathcal{F}_t$ and $\mathcal{F}_c$ denote respectively the thermal and the caloric EoS. In this study, DNS are both performed for air considered as a perfect gas and for FC-70, which is a BZT dense gas. Since these two different types of gases do not have the same level of complexity, their thermodynamic description requires two different EoS formulations: the perfect gas EoS for air and the Martin-Hou EoS for FC-70.

Perfect Gas EoS

Air is thermodynamically described with the perfect gas EoS:

$$\begin{cases} p = \rho R T \\ \\ E_{int} = E_{int,ref} + \displaystyle\int_{T_{ref}}^{T} c_v(T')dT' \end{cases} \tag{2.8}$$

where $(.)_{ref}$ denotes a reference state, $R = \mathcal{R}/M$ is the specific gas constant (M, the molar mass and $\mathcal{R} = 8.314$ J.mol^{-1}.K^{-1}, the universal gas constant) and c_v, the specific heat capacity at constant-volume conditions. The specific heat capacity (c_v) is defined as the slope of the sensible energy $\left(c_v = \frac{\partial E_s}{\partial T}\big|_v\right)$. The sensible energy ($E_s$) is computed using the JANAF tables (Stull & Prophet, 1971). Specific heats are thus not constant. The relation $\Gamma = (\gamma+1)/2$ expressed in Section 1.2 is no longer suitable, since it is only valid for a thermally and calorically perfect gas.

Martin-Hou EoS

For DG simulations, perfluorotripentylamine (FC-70, $C_{15}F_{33}N$) is chosen similarly as Fergason *et al.* (2001) in their shock tube simulations, where they evidence rarefaction shock-waves. This almost non-toxic gas is particularly used as heat transfer fluid but has also been evaluated as synthetic blood (Costello *et al.*, 2000). Physical parameters useful for the thermodynamic description of FC-70 are given in Table 2.1, as taken from Cramer (1989).

In order to provide an accurate representation of FC-70 thermodynamic behavior, the Martin-Hou (MH) EoS is retained since it is considered as the reference thermodynamic model

	T_c (K)	p_c (atm)	Z_c	T_b (K)	$m\ (= c_{v_\infty}(T_c)/R)$	n
FC-70	608.2	10.2	0.270	488.2	118.7	0.493

Table 2.1: Physical parameters of FC-70 (Cramer, 1989). The critical pressure p_c, the critical temperature T_c, the boiling temperature T_b and the compressibility factor $Z_c = p_c v_c/(RT_c)$ are the input data for the Martin-Hou EoS. The critical specific volume v_c is deduced from the aforementioned parameters. The exponent n and the $c_{v_\infty}(T_c)/R$ ratio are used to compute the ideal isochoric heat capacity $c_{v_\infty}(T)$.

for fluorinated BZT fluids (Guardone *et al.*, 2004). The MH EoS are given by the following fifth-order equations:

$$\begin{cases} p = \dfrac{RT}{v-b} + \displaystyle\sum_{i=2}^{5} \frac{A_i + B_i T + C_i e^{-kT/T_c}}{(v-b)^i} \\ \\ E_{int} = E_{int,ref} + \displaystyle\int_{T_{ref}}^{T} c_{v_\infty}(T')dT' + \sum_{i=2}^{5} \frac{A_i + C_i(1+kT/T_c)e^{-kT/T_c}}{(i-1)(v-b)^{i-1}} \end{cases} \tag{2.9}$$

where c_{v_∞} denotes here the isochoric specific heat capacity in the ideal gas limit (i.e. $c_{v_\infty}(T) = \lim_{v\to\infty} c_v(T,v)$, namely the ideal isochoric specific heat capacity), $b = v_c(1 - (-31,883Z_c + 20.533)/15)$, $k = 5.475$ and the coefficients A_i, B_i and C_i are numerical constants determined by Martin & Hou (1955) and Martin *et al.* (1959) from the physical parameters summarized in Table 2.1.

The caloric EoS is transformed by approximating the form of the ideal heat capacity with a power law (see Guardone & Argrow (2005)):

$$E_{int} = E_{int,ref} + \frac{c_{v_\infty}(T_c)T_c}{n+1}\left(\frac{T}{T_c}\right)^{n+1} + \sum_{i=2}^{5} \frac{A_i + C_i(1+kT/T_c)e^{-kT/T_c}}{(i-1)(v-b)^{i-1}} \tag{2.10}$$

where the exponent n is given in Table 2.1.

2.2.2 Transport coefficients models

The thermodynamic description needs to be completed with models of transport coefficients (dynamic viscosity and thermal conductivity) for both air and FC-70.

Perfect gas

For air, the dynamic viscosity follows Sutherland's law (Sutherland, 1893):

$$\mu(T) = \mu(T_{ref})\left(\frac{T}{T_{ref}}\right)^{3/2}\frac{T_{ref}+S}{T+S} \tag{2.11}$$

where S is the Sutherland temperature and μ_{ref} is the dynamic viscosity at T_{ref}. The selected constants for Sutherland's law are the ones given in White (1998), which are valid for the range of temperature met in the present study (Grieser & Goldthwaite, 1963). In addition, a constant

Prandtl number is set equal to 0.71. The Prandtl number is defined as the ratio between the kinematic viscosity and the thermal diffusivity:

$$Pr = \frac{\nu}{\alpha} \tag{2.12}$$

with $\alpha = \kappa/(\rho c_p)$, the thermal diffusivity (c_p is the heat capacity at constant-pressure conditions). A large Prandtl number indicates that the viscous diffusivity is faster than the thermal diffusivity. Setting this parameter enables the computation of thermal diffusivity and thus of thermal conductivity.

Dense gas

For FC-70, Chung's model is used to compute dynamic viscosity and thermal conductivity from density and temperature (Chung *et al.*, 1988). This modeling yields satisfactory results for dense gases. In our case, FC-70 is assumed to behave as a nonpolar gas, its dipole moment is neglected.

2.3 Non-dimensional formulation

This section seeks to give a non-dimensional formulation of the governing equations for both PG and DG flows. This non-dimensional framework will be used in Chapter 4 to explain some of the differences observed between PG and DG mixing layers. The governing equations are first normalized in their most general form before focusing on each type of flow.

2.3.1 General formulation

A general normalization of the Navier-Stokes equations is provided in the following paragraphs. Thermal and caloric EoS are investigated in the next two sections (Sections 2.3.2 and 2.3.3). To that end, $\breve{\phi} = \phi/\phi_R$ denotes the non-dimensional variable associated to the flow variable ϕ where ϕ_R corresponds to a reference (dimensional) value for ϕ. It is assumed that $t_R = x_R/u_R$, choosing $\breve{t} = t/t_R$, $\breve{x} = x/x_R$ and $\breve{u} = u/u_R$. For the sake of clarity, the same reference values are chosen for each direction of the flow. Introducing these non-dimensional quantities into the Navier-Stokes equations (2.1) yields:

$$\begin{cases} \dfrac{\partial \breve{\rho}}{\partial \breve{t}} + \dfrac{\partial(\breve{\rho}\breve{u}_i)}{\partial \breve{x}_i} = 0 \\ \dfrac{\partial(\breve{\rho}\breve{u}_i)}{\partial \breve{t}} + \dfrac{\partial(\breve{\rho}\breve{u}_i\breve{u}_j)}{\partial \breve{x}_j} = -\dfrac{p_R}{\rho_R u_R^2}\dfrac{\partial \breve{p}}{\partial \breve{x}_i} + \dfrac{\mu_R}{\rho_R u_R x_R}\dfrac{\partial}{\partial \breve{x}_j}\left(\breve{\mu}\breve{S}_{ij}^D\right) \\ \left[\dfrac{\partial(\breve{\rho}\breve{E}_{int})}{\partial \breve{t}} + \dfrac{\partial(\breve{\rho}\breve{E}_{int}\breve{u}_j)}{\partial \breve{x}_j}\right] + \dfrac{u_R^2}{(E_{int})_R}\left[\dfrac{\partial(\breve{\rho}\breve{u}_i\breve{u}_i)}{\partial \breve{t}} + \dfrac{1}{2}\dfrac{\partial(\breve{\rho}\breve{u}_i\breve{u}_i\breve{u}_j)}{\partial \breve{x}_j}\right] = -\dfrac{p_R}{\rho_R(E_{int})_R}\dfrac{\partial \breve{p}\breve{u}_j}{\partial \breve{x}_j} \\ + \dfrac{\mu_R u_R}{\rho_R(E_{int})_R x_R}\dfrac{\partial}{\partial \breve{x}_j}\left(\breve{\mu}\breve{u}_i\breve{S}_{ij}^D\right) + \dfrac{\kappa_R T_R}{\rho_R(E_{int})_R u_R x_R}\dfrac{\partial}{\partial \breve{x}_j}\left(\breve{\kappa}\dfrac{\partial \breve{T}}{\partial \breve{x}_j}\right) \end{cases} \tag{2.13}$$

where $\breve{S}_{ij}^D = \left(\frac{\partial \breve{u}_i}{\partial \breve{x}_j} + \frac{\partial \breve{u}_j}{\partial \breve{x}_i} - \frac{2}{3}\frac{\partial \breve{u}_k}{\partial \breve{x}_k}\delta_{ij}\right)$ denotes the non-dimensional deviatoric strain-rate tensor. Equations (2.13) can be further simplified introducing non-dimensional numbers. To that

end, some logical choices are made for the reference quantities. Initial values are retained for length (L_0, for instance the initial characteristic length of a developing shear layer), density (ρ_0), pressure (p_0), temperature (T_0), viscosity (μ_0) and conductivity (κ_0). Because of the compressible context, the reference velocity is chosen equal to the initial sound speed c_0. The reference value of the internal energy is different between DG and PG flows. At this stage, its expression is kept fixed to $(E_{int})_R$.

Let us define the three non-dimensional numbers appearing in the aforementioned equations. The initial Reynolds number is defined as the ratio between the inertial forces and the viscous forces at initial conditions:

$$Re_0 = \frac{\rho_0 u_0 L_0}{\mu_0} \tag{2.14}$$

where u_0 denotes the initial velocity. The initial Mach number represents the ratio between the initial flow velocity and the initial speed of sound:

$$M_0 = \frac{u_0}{c_0} \tag{2.15}$$

The initial Prandtl number is such that:

$$Pr_0 = \frac{\mu_0 \left(c_p\right)_0}{\kappa_0} \tag{2.16}$$

The non-dimensional Navier-Stokes equations (2.13) can be expressed as:

$$\begin{cases} \dfrac{\partial \breve{\rho}}{\partial \breve{t}} + \dfrac{\partial (\breve{\rho} \breve{u}_i)}{\partial \breve{x}_i} = 0 \\ \dfrac{\partial (\breve{\rho} \breve{u}_i)}{\partial \breve{t}} + \dfrac{\partial (\breve{\rho} \breve{u}_i \breve{u}_j)}{\partial \breve{x}_j} = -\dfrac{\boldsymbol{p_0}}{\boldsymbol{\rho_0 c_0^2}} \dfrac{\partial \breve{p}}{\partial \breve{x}_i} + \dfrac{\boldsymbol{M_0}}{\boldsymbol{Re_0}} \dfrac{\partial}{\partial \breve{x}_j} \left(\breve{\mu} \breve{S}_{ij}^D \right) \\ \left[\dfrac{\partial (\breve{\rho} \breve{E}_{int})}{\partial \breve{t}} + \dfrac{\partial (\breve{\rho} \breve{E}_{int} \breve{u}_j)}{\partial \breve{x}_j} \right] + \dfrac{\boldsymbol{c_0^2}}{\boldsymbol{(E_{int})_R}} \left[\dfrac{\partial (\breve{\rho} \breve{u}_i \breve{u}_i)}{\partial \breve{t}} + \dfrac{1}{2} \dfrac{\partial (\breve{\rho} \breve{u}_i \breve{u}_i \breve{u}_j)}{\partial \breve{x}_j} \right] = -\dfrac{\boldsymbol{p_0}}{\boldsymbol{\rho_0 (E_{int})_R}} \dfrac{\partial \breve{p} \breve{u}_j}{\partial \breve{x}_j} \\ + \dfrac{\boldsymbol{M_0}}{\boldsymbol{Re_0}} \left[\dfrac{\boldsymbol{c_0^2}}{\boldsymbol{(E_{int})_R}} \dfrac{\partial}{\partial \breve{x}_j} \left(\breve{\mu} \breve{u}_i \breve{S}_{ij}^D \right) + \dfrac{\boldsymbol{1}}{\boldsymbol{Pr_0}} \dfrac{\boldsymbol{(c_p)_0 T_0}}{\boldsymbol{(E_{int})_R}} \dfrac{\partial}{\partial \breve{x}_j} \left(\breve{\kappa} \dfrac{\partial \breve{T}}{\partial \breve{x}_j} \right) \right] \end{cases} \tag{2.17}$$

Bold expressions are further specified depending on the thermodynamic modeling in the following sections.

2.3.2 Perfect gas analysis

For a calorically perfect gas, additional relations come into play:

$$\left(c_p\right)_0 = c_p = \gamma c_v \tag{2.18}$$

$$c_0^2 = \frac{\gamma p_0}{\rho_0} = \gamma R T_0 \tag{2.19}$$

$$\left(E_{int}\right)_R = \left(E_{int}\right)_0 = \eta_0 c_v T_0 \tag{2.20}$$

where γ denotes the heat capacity ratio and $\eta_0 = 1 + \frac{E_{int,ref}}{c_v T_0}$. For a given perfect gas, for instance air, $\gamma = 1.4$ is fixed and the initial thermodynamic state only appears through the initial temperature T_0 and the parameter η_0. Essentially, the problem is fully defined through

the choice of the Mach number and the Reynolds number (the Prandtl number is set to 0.71). It can be also noticed the non-dimensional EoS do not introduce new parameters. Thermal and caloric EoS become:

$$\breve{p} = \breve{\rho}\breve{T} \tag{2.21}$$

$$\breve{E}_{int} = \frac{\breve{T}}{\eta_0} + \left(1 - \frac{1}{\eta_0}\right) \tag{2.22}$$

Assuming $\eta_0 \approx 1$, the caloric equation becomes $\breve{e} = \breve{T}$. Finally, using this assumption yields to the following non-dimensional equations for a calorically perfect gas flow:

$$\begin{cases} \dfrac{\partial \breve{\rho}}{\partial \breve{t}} + \dfrac{\partial(\breve{\rho}\breve{u}_i)}{\partial \breve{x}_i} = 0 \\ \dfrac{\partial(\breve{\rho}\breve{u}_i)}{\partial \breve{t}} + \dfrac{\partial(\breve{\rho}\breve{u}_i\breve{u}_j)}{\partial \breve{x}_j} = -\dfrac{1}{\gamma}\dfrac{\partial \breve{p}}{\partial \breve{x}_i} + \dfrac{M_0}{Re_0}\dfrac{\partial}{\partial \breve{x}_j}\left(\breve{\mu}\breve{S}^D_{ij}\right) \\ \left[\dfrac{\partial(\breve{\rho}\breve{E}_{int})}{\partial \breve{t}} + \dfrac{\partial(\breve{\rho}\breve{E}_{int}\breve{u}_j)}{\partial \breve{x}_j}\right] + \gamma(\gamma-1)\left[\dfrac{\partial(\breve{\rho}\breve{u}_i\breve{u}_i)}{\partial \breve{t}} + \dfrac{1}{2}\dfrac{\partial(\breve{\rho}\breve{u}_i\breve{u}_i\breve{u}_j)}{\partial \breve{x}_j}\right] = -(\gamma-1)\dfrac{\partial \breve{p}\breve{u}_j}{\partial \breve{x}_j} \\ + \dfrac{M_0}{Re_0}\left[\gamma(\gamma-1)\dfrac{\partial}{\partial \breve{x}_j}\left(\breve{\mu}\breve{u}_i\breve{S}^D_{ij}\right) + \dfrac{\gamma}{Pr_0}\dfrac{\partial}{\partial \breve{x}_j}\left(\breve{\kappa}\dfrac{\partial \breve{T}}{\partial \breve{x}_j}\right)\right] \end{cases} \tag{2.23}$$

Blue and red colors enable to distinguish respectively between similarities and differences when comparing PG and DG flows. To obtain the full non-dimensional problem for PG flow, one needs to complete the Navier-Stokes equations (2.23) with the non-dimensional thermal and caloric EoS, the non-dimensional transport coefficients models and non-dimensional initial conditions.

2.3.3 Dense gas analysis

There are several ways to normalize the Martin-Hou thermal and caloric EoS. In this study, we introduce the compressibility factor based on the initial thermodynamic state:

$$Z_0 = \frac{p_0}{\rho_0 R T_0} \tag{2.24}$$

The MH thermal EoS chosen for dense gas flows (Equation (2.9)) can be transformed as:

$$\breve{p} = \frac{1}{Z_0}\left[\frac{\breve{T}}{\breve{v} - \breve{b}} + \sum_{i=2}^{5}\frac{\breve{A}_i + \breve{B}_i\breve{T} + C_i e^{-k\breve{T}(T_0/T_c)}}{(\breve{v} - \breve{b})^i}\right] \tag{2.25}$$

where $\breve{A}_i = A_i/(RT_0 v_0^{i-1})$, $\breve{B}_i = B_i/(R v_0^{i-1})$ and $\breve{C}_i = C_i/(RT_0 v_0^{i-1})$. Moreover, $\breve{b} = b/v_0 = (b/v_c) \times (v_c/v_0)$, where the non-dimensional coefficient b/v_c depends on the critical compressibility factor, which is itself dependent on the gas. It can thus be considered that:

$$\breve{p} = \frac{1}{Z_0} f\left(\breve{v}, \breve{T}, \frac{v_c}{v_0}, \frac{T_0}{T_c}\right) \tag{2.26}$$

Equation (2.26) evidences the role played by the initial compressibility factor and the initial thermodynamic state. For the caloric EoS (initially written in Equation (2.10)), instead of

choosing the reference value for the internal energy as $(E_{int})_R = (E_{int})_0 = E_{int}(v_0, T_0)$, one can define $(E_{int})_R = \frac{c_{v_\infty}(T_c)T_c}{n+1}\left(\frac{T_0}{T_c}\right)^{n+1}$ †:

$$\breve{E}_{int} = \breve{T}^{n+1} + \frac{RT_0}{(E_{int})_R}\left[\sum_{i=2}^{5}\frac{\breve{A}_i + \breve{C}_i(1 + k\breve{T}(T_0/T_c))e^{-k\breve{T}(T_0/T_c)}}{(i-1)(\breve{v}-\breve{b})^{i-1}}\right] \tag{2.27}$$

It can thus be considered that:

$$\breve{E}_{int} = \breve{T}^{n+1} + f\left(\breve{T}, \breve{v}, \frac{v_c}{v_0}, \frac{T_0}{T_c}\right) \tag{2.28}$$

Since both thermal and caloric EoS are non-dimensional, bold expressions appearing in Equations (2.17) can now be expressed for the DG flow. We will proceed one term at a time.

With the definition introduced for the reference internal energy, the ratio $\boldsymbol{(c_p)_0 T_0/(E_{int})_R}$ becomes:

$$\frac{(c_p)_0 T_0}{(E_{int})_R} = \underbrace{\frac{(n+1)}{c_{v_\infty}(T_c)/R}}_{\text{fluid dependent}} \times \underbrace{\left(\frac{T_c}{T_0}\right)^n \frac{(c_p)_0}{R}}_{\text{initial state and fluid dependent}} = K_0\frac{(c_p)_0}{R} \tag{2.29}$$

where $K_0 = \frac{(n+1)}{c_{v_\infty}(T_c)/R} \times \left(\frac{T_c}{T_0}\right)^n$ depends on the fluid properties and on the initial thermodynamic state.

In a real gas context, the ratio $\boldsymbol{p_0/(\rho_0 c_0^2)}$ can no longer be simplified into $1/\gamma$. It is possible to rewrite the ratio as follows:

$$\frac{p_0}{(\rho_0 c_0^2)} = Z_0 M_0 \frac{RT_0}{u_0} \tag{2.30}$$

The non-dimensional number rT_0/u_0 can be thoroughly transformed. The initial Eckert number is defined as the ratio between the kinetic energy and the enthalpy:

$$Ec_0 = \frac{u_0^2}{(c_p)_0 T_0} \tag{2.31}$$

Using the Eckert number enables the transformation of the ratio $\boldsymbol{p_0/(\rho_0 c_0^2)}$:

$$\frac{p_0}{(\rho_0 c_0^2)} = \frac{Z_0 M_0^2}{Ec_0}\frac{r}{(c_p)_0} \tag{2.32}$$

Finally, the ratio $\boldsymbol{c_0^2/(E_{int})_0}$ takes the form:

$$\frac{c_0^2}{(E_{int})_0} = K_0\frac{(c_p)_0}{R}\frac{Ec_0}{M_0^2} \tag{2.33}$$

The new non-dimensional quantities defining the problem in the dense gas context are therefore the initial compressibility factor Z_0, the initial Eckert number Ec_0, the parameter K_0 computed from fluid properties and from the ratios T_0/T_c and $r/(c_p)_0$ and the initial Mach and Reynolds numbers. The ratios T_0/T_c and v_c/v_0 (or ρ_0/ρ_c) also appear in the thermal and

†The reference value $E_{int,ref}$ which appears in Equation (2.10) can be set to zero.

caloric EoS. The non-dimensional Navier-Stokes equations for compressible DG flows read:

$$\begin{cases} \dfrac{\partial \breve{\rho}}{\partial \breve{t}} + \dfrac{\partial(\breve{\rho}\breve{u}_i)}{\partial \breve{x}_i} = 0 \\ \dfrac{\partial(\breve{\rho}\breve{u}_i)}{\partial \breve{t}} + \dfrac{\partial(\breve{\rho}\breve{u}_i\breve{u}_j)}{\partial \breve{x}_j} = -\dfrac{Z_0 M_0^2}{Ec_0}\dfrac{R}{(c_p)_0}\dfrac{\partial \breve{p}}{\partial \breve{x}_i} + \dfrac{M_0}{Re_0}\dfrac{\partial}{\partial \breve{x}_j}\left(\breve{\mu}\breve{S}_{ij}^D\right) \\ \left[\dfrac{\partial(\breve{\rho}\breve{E}_{int})}{\partial \breve{t}} + \dfrac{\partial(\breve{\rho}\breve{E}_{int}\breve{u}_j)}{\partial \breve{x}_j}\right] + \dfrac{K_0 Ec_0}{M_0^2}\dfrac{(c_p)_0}{R}\left[\dfrac{\partial(\breve{\rho}\breve{u}_i\breve{u}_i)}{\partial \breve{t}} + \dfrac{1}{2}\dfrac{\partial(\breve{\rho}\breve{u}_i\breve{u}_i\breve{u}_j)}{\partial \breve{x}_j}\right] = -Z_0 K_0 \dfrac{\partial \breve{p}\breve{u}_j}{\partial \breve{x}_j} \\ + \dfrac{M_0}{Re_0}\left[\dfrac{K_0 Ec_0}{M_0^2}\dfrac{(c_p)_0}{R}\dfrac{\partial}{\partial \breve{x}_j}\left(\breve{\mu}\breve{u}_i\breve{S}_{ij}^D\right) + \dfrac{K_0}{Pr_0}\dfrac{(c_p)_0}{R}\dfrac{\partial}{\partial \breve{x}_j}\left(\breve{\kappa}\dfrac{\partial \breve{T}}{\partial \breve{x}_j}\right)\right] \end{cases} \tag{2.34}$$

To complete the full definition of the non-dimensional problem (2.34) for DG flows, one needs to add the non-dimensional thermal and caloric EoS given in Equations (2.25) and (2.27), the non-dimensional transport coefficients models and initial conditions. Non-dimensional numbers at stake in both DG and PG formulations are summarized and compared in Table 2.2. They will be further used in Chapter 4 to contribute to explain the physical differences observed between DG and PG mixing layers.

Momentum equations	PG	DG
$\dfrac{\partial p}{\partial x_i}$	$\dfrac{1}{\gamma} \approx 0.71$	$\dfrac{Z_0 M_0^2}{Ec_0}\dfrac{R}{c_{p_0}}$
$\dfrac{\partial}{\partial x_j}\left(\mu S_{ij}^D\right)$	$\dfrac{M_0}{Re_0}$	$\dfrac{M_0}{Re_0}$
Energy equation	**PG**	**DG**
$\left[\dfrac{\partial(\rho u_i u_i)}{\partial t} + \dfrac{1}{2}\dfrac{\partial(\rho u_i u_i u_j)}{\partial x_j}\right]$	$\gamma(\gamma-1) = 0.56$	$\dfrac{K_0 Ec_0}{M_0^2}\dfrac{(c_p)_0}{R}$
$\dfrac{\partial(p u_j)}{\partial x_j}$	$(\gamma-1) = 0.4$	$Z_0 K_0$
$\dfrac{\partial}{\partial x_j}\left(\mu u_i S_{ij}^D\right)$	$\gamma(\gamma-1)\dfrac{M_0}{Re_0} = 0.56\dfrac{M_0}{Re_0}$	$\dfrac{K_0 Ec_0}{M_0^2}\dfrac{(c_p)_0}{R}\dfrac{M_0}{Re_0}$
$\dfrac{\partial}{\partial x_j}\left(\kappa\dfrac{\partial T}{\partial x_j}\right)$	$\dfrac{\gamma}{Pr_0}\dfrac{M_0}{Re_0} \approx 1.97\dfrac{M_0}{Re_0}$	$\dfrac{K_0}{Pr_0}\dfrac{(c_p)_0}{R}\dfrac{M_0}{Re_0}$

Table 2.2: Comparison of the PG and DG non-dimensional terms appearing in the non-dimensional Navier-Stokes equations (2.23) and (2.34). The numerical values are given for air considered as a calorically perfect gas with $\gamma = 1.4$ and $Pr_0 = 0.71$.

2.4 LES governing equations

This section is devoted to the presentation of the LES mathematical framework. LES fundamentals are briefly introduced, followed by a presentation of the filtering process. The emphasis is then put on specificities induced by the thermodynamic modeling. A summary helps to identify and classify the different subgrid scale terms. Finally, standard models later used in Chapter 7 are introduced.

2.4.1 Preliminary discussion

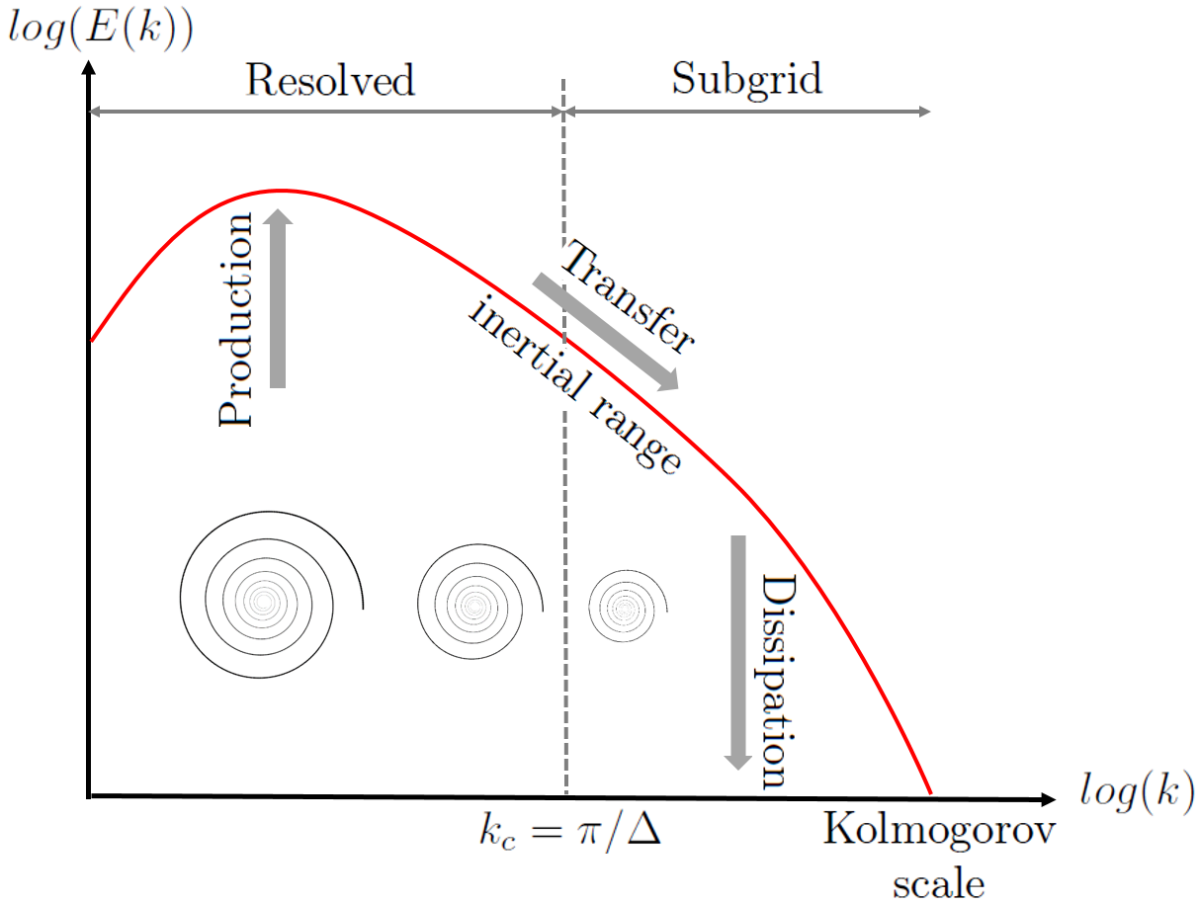

Figure 2.1: Schematic view of the turbulence spectrum. The cut-off wavenumber $k_c = \pi/\Delta$ is associated to the filtering size Δ. It defines the limit above which turbulent scales are modeled in LES.

Large Eddy Simulation (LES) finds its origins in the turbulence cascade. In 1922, Richardson writes "*Big whirls have little whirls that feed on their velocity, and little whirls have lesser whirls and so on to viscosity*" (Richardson, 1922). He was the first to describe interactions between large and small scales. In tribute to its work, the turbulent cascade is often named the Richardson cascade. The concept of a viscous limit preventing the propagation of energy over swirls was thoroughly developed by Kolmogorov in 1941. He made significant advances introducing the existence of a scale from which "*the effect of viscosity on the pulsations of the order n finally prevents the formation of pulsations of the order n+1*" (Kolmogorov, 1941). Yet, Kolmogorov major contribution is certainly the universal form for the energy spectrum arising from the hypothesized existence of an isotropic intermediate range of length scales: the

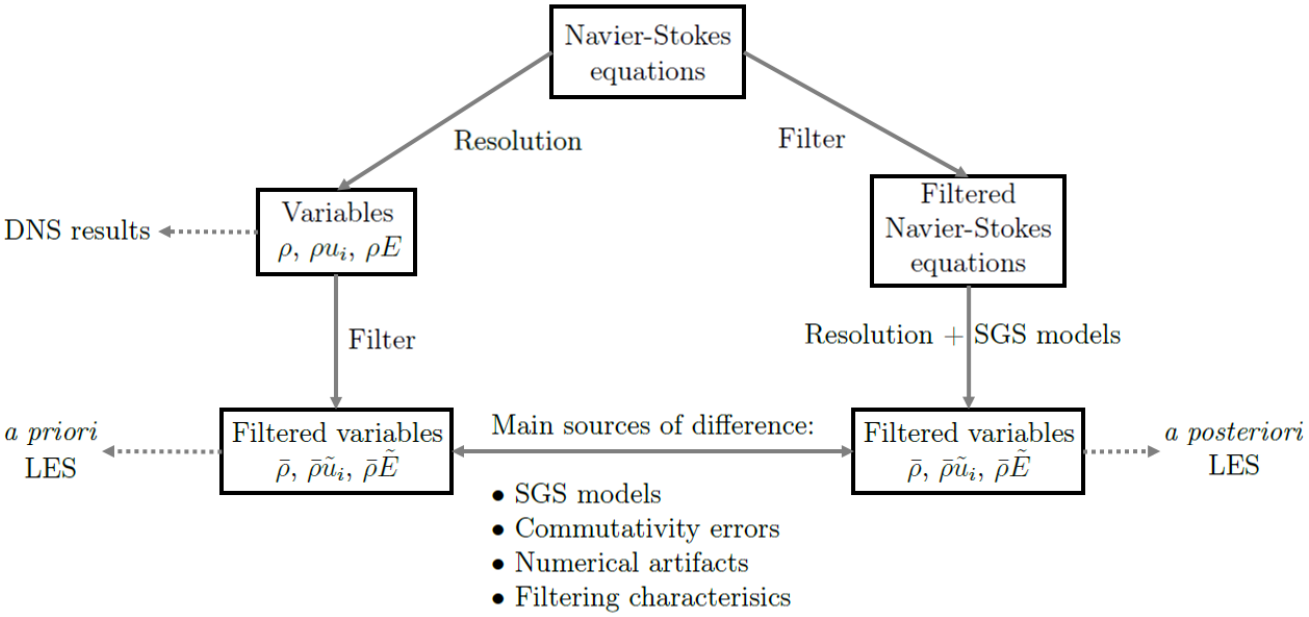

Figure 2.2: Summary of fundamental principles for the two LES approaches: the *a priori* LES and the *a posteriori* LES.

so-called inertial range in which the turbulent kinetic energy spectrum $E(k)$ associated to the wavenumber k satisfies

$$E(k) = C_K \epsilon^{2/3} k^{-5/3} \tag{2.35}$$

where $C_K \approx 1.5$ is the Kolmogorov constant and $\epsilon = 2\nu \int_0^\infty k^2 E(k) dk$ is the dissipation rate ($\nu = \mu/\rho$ denotes the kinematic viscosity). Note that this result is not verified for compressible flows in which case the energy decreases slightly faster (Kritsuk *et al.*, 2007; Wang *et al.*, 2013).

A schematic view of the turbulent spectrum is represented in figure 2.1. Energy, which can either be a forcing term (for example in forced homogeneous isotropic turbulence) or comes from flow conditions, is injected at the largest scales generating a turbulent production. The turbulent energy is then transferred to the smallest ones through an inertial zone in which the turbulent kinetic energy spectrum decreases following the Kolmogorov law ($E(k) \propto k^{-5/3}$). Finally, the turbulent kinetic energy is dissipated at the smallest scales down to the Kolmogorov scale. Note that there exists an opposite energy transfer mechanism named backscatter from the small scales to the large ones. Its intensity is much weaker and occurs in specific flow conditions like compressible, rotating flows (Garnier *et al.*, 2009) or 2D turbulence (Grooms *et al.*, 2015).

In LES, the turbulent spectrum is decomposed in two parts: resolved scales and subgrid scales, which are modeled. The smallest scales are assumed to be isotropic and independent of the largest ones. These two hypothesis are at the origin of the universal feature of the smallest scales and at the core of subgrid-scales (SGS) models. The separation between resolved and unresolved scales is called the cut-off wavenumber (k_c). It is located in the inertial range implying scale similarity of energy flux. It defines the limit above which turbulent structures need to be modeled.

In Sections 2.4.4 and 2.4.3, filtered Navier-Stokes equations are derived. These equations are used in Chapter 5 and Chapter 7 in two contexts: the *a priori* LES and the *a posteriori* LES. In *a priori* LES, one starts from DNS results. A filtering operator is then applied to flow variables giving the filtered variables. In *a posteriori* LES, Navier-Stokes equations are filtered before being solved. The SGS terms, which are not computable in this approach, are modeled.

The *a posteriori* LES is the default approach when applying LES in general. The whole process for both approaches is described in figure 2.2.

For both approaches, one could expect to obtain the same filtered variables. Yet, there are four main sources of difference between filtered variables provided by *a priori* and *a posteriori* LES: the SGS models that do not perfectly describe SGS terms, the commutativity errors occurring between filtering and differentiation operators, some numerical artifacts like artificial viscosity used to stabilize the computation, and the filtering characteristics like the type of filter or the choice of selectivity parameters. This last point is discussed in the next section.

2.4.2 Filter

The filtering operation is mainly applied in *a priori* LES in order to obtain filtered flow variables. Yet, it can also be used in *a posteriori* LES to compute SGS models using dynamic procedures. In both approaches, a flow variable (denoted for instance ϕ) is decomposed into a resolved large-scale component ($\bar{\phi}$) and a small-scale component (ϕ') such that:

$$\phi = \bar{\phi} + \phi' \tag{2.36}$$

The large-scale component ($\bar{\phi}$) is formally defined from the flow variable (ϕ) using a low-pass filter:

$$\bar{\phi}(\boldsymbol{x}, t) = \int_{\Omega} G_{\boldsymbol{\Delta}}(\boldsymbol{x} - \boldsymbol{\xi}, t)\phi(\boldsymbol{\xi}, t)d\boldsymbol{\xi} \tag{2.37}$$

where $\boldsymbol{x}$ and $\boldsymbol{\xi}$ are vectors in the flow domain Ω, and $G_{\boldsymbol{\Delta}}$ is the convolution kernel associated to the filter size $\boldsymbol{\Delta}$ (Note that $\boldsymbol{\Delta}$ is not necessarily identical in each direction, that is why it is defined as a vector). It satisfies the following normalization condition:

$$\int_{\Omega} G_{\boldsymbol{\Delta}}(\boldsymbol{x} - \boldsymbol{\xi})d\boldsymbol{\xi} = 1 \tag{2.38}$$

Following the formulation of the Favre filtering (Favre *et al.*, 1971) dedicated to compressible flows, large-scale and small-scale components can be weighted by density:

$$\widetilde{\phi} = \frac{\overline{\rho\phi}}{\overline{\rho}} \tag{2.39}$$

The flow variable can thus be split instead as:

$$\phi = \widetilde{\phi} + \phi'' \tag{2.40}$$

The following relations can be obtained:

$$\overline{\rho\phi''} = 0 \tag{2.41}$$

$$\overline{\phi''} = -\frac{\overline{\rho'\phi'}}{\overline{\rho}} \neq 0 \tag{2.42}$$

There are three main filters used in LES: the box (or top-hat) filter, the Gaussian filter and the sharp cut-off (or spectral cut-off) filter. Table 2.3 gives filter functions in spectral and physical spaces for each filter in 3D. Since the filtering operation can have a significant effect on the LES results (see Appendix C), it has to be chosen carefully. In order to choose the filter, one needs to find an acceptable compromise between physical and spectral selectivity, keeping in mind the more selective a filter is in physical space, the less selective it is in spectral space.

Filter	Filter function in the physical space $G_{\boldsymbol{\Delta}}(\boldsymbol{x}-\boldsymbol{\xi})$	Filter function in the spectral space $\hat{G}_{\boldsymbol{\Delta}}(k)$
Box or top-hat	$\begin{cases} \dfrac{1}{\prod_{i=1}^{3}\Delta_i}, & \text{if } \lvert x_i-\xi_i\rvert \leq \frac{\Delta_i}{2}. \\ 0, & \text{otherwise.} \end{cases}$	$\displaystyle\prod_{i=1}^{3}\operatorname{sinc}\left(\frac{k_i\Delta_i}{2}\right)$
Gaussian	$\displaystyle\prod_{i=1}^{3}\left[\left(\frac{\zeta}{\pi\Delta_i^2}\right)^{\frac{1}{2}}\exp\left(\frac{-\zeta(x_i-\xi_i)^2}{\Delta_i^2}\right)\right]$	$\displaystyle\prod_{i=1}^{3}\left[\exp\left(\frac{-\Delta_i^2k_i^2}{4\zeta}\right)\right]$
Sharp or spectral cut-off	$\displaystyle\prod_{i=1}^{3}\left[\frac{1}{\Delta_i}\operatorname{sinc}(k_{c_i}(x_i-\xi_i)\right]$ with $k_{c_i}=\frac{\pi}{\Delta_i}$	$\begin{cases} 1, & \text{if } \lvert k_i\rvert \leq k_{c_i}. \\ 0, & \text{otherwise.} \end{cases}$

Table 2.3: Filter functions are given in physical and spectral spaces for the three classical filters used in LES. ϕ_i denotes the component of $\boldsymbol{\phi}$ in the i^{th} direction. The parameter ζ controls the selectivity of the Gaussian filter. An analysis of its influence on the *a priori* LES results is given in Appendix C. It is recommended to set this parameter to $\zeta = 6$ (Garnier *et al.*, 2009).

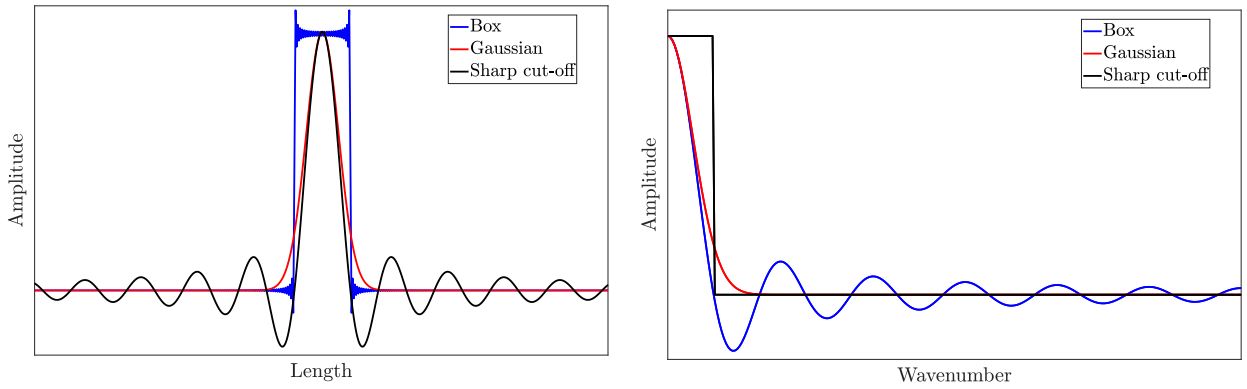

Figure 2.3: Filter functions are plotted in physical (left) and spectral (right) spaces for each filter given in Table 2.3. Functions in the physical space are computed using an inverse fast Fourier transform (FFT).

To illustrate this statement, each filter function is plotted in both spaces (see Figure 2.3).

The sharp cut-off filter is very selective in the frequency domain but it is not selective at all in the physical one. The sinc function introduces secondary lobes, which makes this filter non-local in space. It is thus not representative of the mesh filtering in *a posteriori* LES. On the contrary, the box (or top-hat) filter is very selective in space but it is not in the spectral domain. These two filters display strong discontinuities either in spectral or spatial domains. These discontinuities are a source of oscillations, when using direct or inverse fast Fourier transform (FFT) algorithm. One can notice here that the inverse FFT of the box filter shows some oscillations close to the discontinuities. This can artificially increase local spatial values. The Gaussian filter offers a good compromise between spatial and spectral selectivity as long as the parameter ζ is well set. For these reasons, preference will be given to the Gaussian filter in Chapter 5 to filter DNS results. An analysis of the influence of ζ on the result is provided in Appendix C.

2.4.3 Real gas formulation

Since the PG formulation is a particular case of the real gas one, the filtered Navier-Stokes equations and EoS are first expressed for the general real gas case. This formulation is then used for the DG *a priori* LES in Chapter 5. The specific PG case is formulated in Section 2.4.3. In order to obtain the filtered Navier-Stokes equations, it is assumed that the filtering operator commutes with temporal and spatial differentiations. This assumption is valid if the domain is not bounded and if the filtering size Δ_i is constant and homogeneous. Filtering the Navier-Stokes equations (2.1) yields the following set of equations:

$$\begin{cases} \dfrac{\partial \bar{\rho}}{\partial t} + \dfrac{\partial \bar{\rho}\widetilde{u}_j}{\partial x_j} = 0 \\ \dfrac{\partial \bar{\rho}\widetilde{u}_i}{\partial t} + \dfrac{\partial \bar{\rho}\widetilde{u_i u_j}}{\partial x_j} = -\dfrac{\partial \bar{p}}{\partial x_i} + \dfrac{\partial \bar{\tau}_{ij}}{\partial x_j} \\ \dfrac{\partial \bar{\rho}\widetilde{E}}{\partial t} + \dfrac{\partial \bar{\rho}\widetilde{E u_j}}{\partial x_j} = -\dfrac{\partial \overline{p u_j}}{\partial x_j} + \dfrac{\partial \overline{\tau_{ij} u_i}}{\partial x_j} - \dfrac{\partial \bar{q}_j}{\partial x_j} \end{cases} \tag{2.43}$$

Regardless of the type of flow of interest, filtered temperature and pressure are unknown

quantities. Without assumptions on the form of the EoS, one can not use the commutativity between the filtering operator and the thermal and caloric EoS. In *a posteriori* LES, the only available pressure and temperature are the ones computed from the filtered variables. From now on, the computable quantities will be denoted $\widehat{\phi}$. Let $\mathcal{F}_t$ and $\mathcal{F}_c$ denote respectively the thermal and caloric EoS. The differences between filtered pressure $\bar{p}$ and temperature $\bar{T}$ and computable pressure $\hat{p}$ and temperature $\hat{T}$ can be summarized as:

$$\bar{T} = \overline{\mathcal{F}_c(\rho, \rho u_i, \rho E)} \tag{2.44}$$
$$\bar{p} = \overline{\mathcal{F}_t(T, \rho)} \tag{2.45}$$
$$\widehat{T} = \mathcal{F}_c(\bar{\rho}, \bar{\rho}\widetilde{u}_i, \bar{\rho}\widetilde{E}) \neq \bar{T} \tag{2.46}$$
$$\widehat{p} = \mathcal{F}_t(\bar{\rho}, \widehat{T}) \neq \bar{p} \tag{2.47}$$

The transport coefficients are also influenced by these differences. $\widehat{\kappa}$ and $\widehat{\mu}$ denote respectively the thermal conductivity and the viscosity computed from the filtered density $\bar{\rho}$ and the available temperature $\widehat{T}$. These observations lead to the following set of equations where all subgrid-scale terms are in bold type and labeled while resolved terms are in light type:

$$\begin{cases} \dfrac{\partial \bar{\rho}}{\partial t} + \dfrac{\partial \bar{\rho}\widetilde{u}_j}{\partial x_j} = 0 \\ \dfrac{\partial \bar{\rho}\widetilde{u}_i}{\partial t} + \dfrac{\partial \bar{\rho}\widetilde{u}_i\widetilde{u}_j}{\partial x_j} = -\dfrac{\partial \widehat{p}}{\partial x_i} + \dfrac{\partial \widehat{\tau}_{ij}}{\partial x_j} \\ \qquad \underbrace{-\dfrac{\boldsymbol{\partial}\left[\bar{\boldsymbol{p}} - \widehat{\boldsymbol{p}}\right]}{\boldsymbol{\partial x_i}}}_{\text{Pressure}} \underbrace{+\dfrac{\boldsymbol{\partial}\left[\bar{\boldsymbol{\tau}}_{\boldsymbol{ij}} - \widehat{\boldsymbol{\tau}}_{\boldsymbol{ij}}\right]}{\boldsymbol{\partial x_j}}}_{\text{Viscous}} \underbrace{-\dfrac{\boldsymbol{\partial \bar{\rho}}\left[\widetilde{\boldsymbol{u_i u_j}} - \widetilde{\boldsymbol{u}}_{\boldsymbol{i}}\widetilde{\boldsymbol{u}}_{\boldsymbol{j}}\right]}{\boldsymbol{\partial x_j}}}_{\text{Turbulent stress}} \\ \dfrac{\partial \bar{\rho}\widetilde{E}}{\partial t} + \dfrac{\partial \bar{\rho}\widehat{E}_{int}\widetilde{u}_j}{\partial x_j} + \dfrac{\partial \bar{\rho}\widehat{K}\widetilde{u}_j}{\partial x_j} = -\dfrac{\partial \widehat{p}\widetilde{u}_j}{\partial x_j} + \dfrac{\partial \widehat{\tau}_{ij}\widetilde{u}_i}{\partial x_j} - \dfrac{\partial \widehat{q}_j}{\partial x_j} \\ \qquad \underbrace{-\dfrac{\boldsymbol{\partial}\left[\overline{\boldsymbol{pu_j}} - \widehat{\boldsymbol{p}}\widetilde{\boldsymbol{u}}_{\boldsymbol{j}}\right]}{\boldsymbol{\partial x_j}}}_{\text{Pressure work}} \underbrace{+\dfrac{\boldsymbol{\partial}\left[\overline{\boldsymbol{\tau_{ij}u_i}} - \widehat{\boldsymbol{\tau}}_{\boldsymbol{ij}}\widetilde{\boldsymbol{u}}_{\boldsymbol{i}}\right]}{\boldsymbol{\partial x_j}}}_{\text{Viscous work}} \underbrace{-\dfrac{\boldsymbol{\partial}\left[\bar{\boldsymbol{q}}_{\boldsymbol{j}} - \widehat{\boldsymbol{q}}_{\boldsymbol{j}}\right]}{\boldsymbol{\partial x_j}}}_{\text{Heat Flux}} \\ \qquad \underbrace{-\dfrac{\boldsymbol{\partial \bar{\rho}}\left[\widetilde{\boldsymbol{E_{int}u_j}} - \widehat{\boldsymbol{E}}_{\boldsymbol{int}}\widetilde{\boldsymbol{u}}_{\boldsymbol{j}}\right]}{\boldsymbol{\partial x_j}}}_{\text{Internal energy flux}} \underbrace{-\dfrac{\boldsymbol{\partial \bar{\rho}}\left[\widetilde{\boldsymbol{Ku_j}} - \widehat{\boldsymbol{K}}\widetilde{\boldsymbol{u}}_{\boldsymbol{j}}\right]}{\boldsymbol{\partial x_j}}}_{\text{Kinetic energy flux}} \end{cases} \tag{2.48}$$

where K stands for the specific kinetic energy ($K = E - E_{int}$). Note that $\widehat{K} = \frac{1}{2}\widetilde{u}_i\widetilde{u}_i$, $\widehat{E}_{int} = \widetilde{E} - \widehat{K}$, $\widehat{\tau}_{ij} = \widehat{\mu}\left(\frac{\partial \widetilde{u}_i}{\partial x_j} + \frac{\partial \widetilde{u}_j}{\partial x_i} - \frac{2}{3}\frac{\partial \widetilde{u}_k}{\partial x_k}\delta_{ij}\right)$ and $\widehat{q}_i = -\widehat{\kappa}\frac{\partial \widehat{T}}{\partial x_i}$. All bold terms in brackets are unknown and potentially need modeling.

2.4.4 Perfect gas formulation

Now that the general real gas formulation has been established, the particular PG case can be formulated for the filtered Navier-Stokes equations and the EoS. This set of equations is used

as a comparison with the DG formulation in the next section and in Appendix D where an *a priori* analysis of mixing layer DNS results obtained in Chapter 3 is conducted. The calorically perfect gas assumption leads to the following set of filtered EoS:

$$\begin{cases} \bar{p} = (\gamma-1)\bar{\rho}\widetilde{E}_{int} \\ \\ \bar{T} = \dfrac{(\gamma-1)}{R}\bar{E}_{int} \end{cases} \tag{2.49}$$

For PG flows, at every time step, temperature and pressure are determined using the filtered internal energy ($\widetilde{E}_{int}$). However, the filtered internal energy is computed from the filtered total energy ($\widetilde{E}$) and the unfiltered kinetic energy as:

$$\bar{\rho}\widetilde{E}_{int} = \bar{\rho}\widetilde{E} - \frac{1}{2}\bar{\rho}\widetilde{u_i u_i} = \bar{\rho}\widetilde{E} - \frac{1}{2}\bar{\rho}\widetilde{u}_i\widetilde{u}_i - \frac{t_{ii}}{2} \tag{2.50}$$

where $t_{ij} = \bar{\rho}(\widetilde{u_i u_j} - \widetilde{u}_i\widetilde{u}_j)$ denotes the SGS turbulent stress tensor. It is unknown in *a posteriori* LES. Yet, at this step already, most solvers describe the filtered internal energy by means of filtered quantities only, assuming that the contribution of $t_{ii}/2$ is negligible. The relevance of this assumption is thoroughly investigated in Appendix D. Without using this hypothesis, the filtered internal energy and therefore the filtered pressure and the filtered temperature remain unknown quantities. For PG flows, SGS terms associated to the filtered pressure and the filtered internal energy can be simplified using the following equations.

$$\bar{\rho}\widehat{E}_{int} = \bar{\rho}\widetilde{E} - \frac{1}{2}\bar{\rho}\widetilde{u}_i\widetilde{u}_i \tag{2.51}$$

$$\widehat{p} = (\gamma-1)\bar{\rho}\widehat{E}_{int} = \underbrace{(\gamma-1)\bar{\rho}\widetilde{E}_{int}}_{\bar{p}} + \frac{(\gamma-1)}{2}t_{ii} \tag{2.52}$$

$$\widehat{T} = \frac{(\gamma-1)}{R}\widehat{E}_{int} = \underbrace{\frac{(\gamma-1)}{R}\widetilde{E}_{int}}_{\bar{T}} + \frac{(\gamma-1)}{2R\bar{\rho}}t_{ii} \tag{2.53}$$

Finally, the filtered Navier-Stokes equations for a calorically perfect gas read:

$$\begin{cases} \dfrac{\partial\bar{\rho}}{\partial t} + \dfrac{\partial\bar{\rho}\widetilde{u}_j}{\partial x_j} = 0 \\ \\ \dfrac{\partial\bar{\rho}\widetilde{u}_i}{\partial t} + \dfrac{\partial\bar{\rho}\widetilde{u}_i\widetilde{u}_j}{\partial x_j} = -\dfrac{\partial\widehat{p}}{\partial x_i} + \dfrac{\partial\widehat{\tau}_{ij}}{\partial x_j} + \dfrac{(\gamma-1)}{2}\dfrac{\partial t_{ii}}{\partial x_i} + \dfrac{\partial\left[\bar{\tau}_{ij} - \widehat{\tau}_{ij}\right]}{\partial x_j} - \dfrac{\partial t_{ij}}{\partial x_j} \\ \\ \dfrac{\partial\bar{\rho}\widetilde{E}}{\partial t} + \dfrac{\partial\bar{\rho}\widehat{E}_{int}\widetilde{u}_j}{\partial x_j} + \dfrac{\partial\bar{\rho}\widehat{K}\widetilde{u}_j}{\partial x_j} = -\dfrac{\partial\widehat{p}\widetilde{u}_j}{\partial x_j} + \dfrac{\partial\widehat{\tau}_{ij}\widetilde{u}_i}{\partial x_j} - \dfrac{\partial\widehat{q}_j}{\partial x_j} - \dfrac{\gamma}{(\gamma-1)}\dfrac{\partial\left[\overline{pu_j} - \bar{p}\widetilde{u}_j\right]}{\partial x_j} + \dfrac{(\gamma-1)}{2}\dfrac{\partial t_{ii}\widetilde{u}_j}{\partial x_j} \\ \qquad\qquad + \dfrac{\partial\left[\overline{\tau_{ij}u_i} - \widehat{\tau}_{ij}\widetilde{u}_i\right]}{\partial x_j} - \dfrac{\partial\left[\bar{q}_j - \widehat{q}_j\right]}{\partial x_j} - \dfrac{\partial\bar{\rho}\left[\widetilde{Ku_j} - \widehat{K}\widetilde{u}_j\right]}{\partial x_j} \end{cases} \tag{2.54}$$

SGS terms are colored in blue if their expression is similar between PG and real gas formulation (used for DG flows) and in red if their expression is different. All these SGS terms potentially request modeling. The SGS turbulent stress tensor has been the center of attention in the LES community. A summary of usually modeled and neglected terms is given in Table 2.4. Note that formulation (2.54) is equivalent to the system II in Vreman *et al.* (1995).

2.4.5 A summary of SGS terms

SGS terms are often associated to the SGS turbulent stress tensor only. However, in the formulation of the filtered compressible Navier-Stokes equations, several SGS terms are present both in the filtered momentum equation and in the filtered energy equation, even for the PG formulation. A comparison of real gas (used for DG flows) and PG formulations is summarized in Table 2.4. These SGS terms are all extracted either from Equations (2.48) or from Equations (2.54). SGS terms are colored in blue if their expression is similar between real gas and PG formulations and in red if their expression is different. Differences appear for the SGS pressure term and the SGS internal energy term because of the complexity of thermal and caloric EoS used for DG. Note that the SGS heat flux and the SGS internal energy are distinguished in Table 2.4. The SGS heat flux term refers here to the Fourier heat flux. The SGS internal energy is often named SGS heat flux because of its link with the temperature, which is valid in the PG case only.

For PG flows, most of the SGS terms are neglected following Vreman *et al.* (1995)'s and Martin *et al.* (2000)'s analysis. An evaluation and a discussion of these terms is conducted in Appendix D for the compressible PG mixing layers introduced in Chapter 3. Note that SGS terms neglected for PG flows (for instance SGS pressure terms) might be of importance for real gas flows. Besides the important work of Bellan's group (see for example (Selle *et al.*, 2007)), which addresses the case of the mixing layer in a real gas flow, no such evaluation of SGS terms for real gases has been undertaken yet. This will be the purpose and original contribution of Chapter 5. Moreover, even for modeled terms, available models for PG flows might not be relevant for real gas flows. The assessment of available SGS models is not carried out in this study. SGS models commonly used for PG flows are used in the *a posteriori* LES (Chapter 7) conducted to assess a new model designed for SGS pressure (Chapter 6) for which no accurate model exists[†]. To that end, the next section 2.4.6 introduces the SGS models that will be used in Chapter 7: for SGS convective terms, the Smagorinsky model and its dynamic counterpart; for SGS internal energy, a model based on a SGS Prandtl number.

2.4.6 Basic LES models

Functional and structural modeling

The filtered compressible Navier-Stokes equations (2.48) show the entanglement of SGS terms in both the momentum and energy conservation equations. Two main strategies are followed to model these terms: **functional modeling** or **structural modeling**.

Functional modeling seeks to faithfully reproduce the turbulent energy transfer mechanism from the large scales to the small ones. It is based on the assumption that subgrid scales have mainly an energetic effect on the resolved scales. This approach does not try to describe the topology of coherent vortices, which contains in particular the structural information related to the turbulence anisotropy. Among functional models, the most popular one is the Smagorinsky model (Smagorinsky, 1963). Its dynamic counterpart was first developed by Germano *et al.* (1991). These models are introduced in the following paragraphs. Energy transfer can also be partly reproduced using the numerical scheme if its truncation error mimics the SGS dissipation.

[†]With the exception of the model proposed by Selle *et al.* (2007), which is based on a Taylor series but the use of which is not advised by the authors when the filter size becomes too large.

[†]$t_{ij}^D = t_{ij} - \frac{1}{3}t_{kk}\delta_{ij}$ and $t_{ij}^I = \frac{1}{3}t_{kk}\delta_{ij}$ are respectively the deviatoric and the isotropic parts of the turbulent SGS stress tensor.

Momentum equations	Real gas	PG	PG modeling
Pressure	$-\frac{\partial\left[\bar{p}-\widehat{p}\right]}{\partial x_i}$	$\frac{(\gamma-1)}{2}\frac{\partial t_{ii}}{\partial x_i}$	neglected
Viscous	$+\frac{\partial\left[\bar{\tau}_{ij}-\widehat{\tau}_{ij}\right]}{\partial x_j}$	$+\frac{\partial\left[\bar{\tau}_{ij}-\widehat{\tau}_{ij}\right]}{\partial x_j}$	neglected
Convective	$-\frac{\partial t_{ij}}{\partial x_j}$	$-\frac{\partial t_{ij}}{\partial x_j}=-\frac{\partial\left(t_{ij}^D+t_{ij}^I\right)}{\partial x_j}$ †	t_{ij}^D: modeled t_{ij}^I: generally neglected
Energy equation	**Real gas**	**PG**	**PG modeling**
Pressure work	$-\frac{\partial\left[\overline{pu_j}-\widetilde{p}\widetilde{u}_j\right]}{\partial x_j}$	$-\frac{\partial\left[\overline{pu_j}-\bar{p}\widetilde{u}_j\right]}{\partial x_j}$ $+\frac{(\gamma-1)}{2}\frac{\partial t_{ii}\widetilde{u}_j}{\partial x_j}$	neglected
Viscous work	$+\frac{\partial\left[\overline{\tau_{ij}u_i}-\widehat{\tau}_{ij}\widetilde{u}_i\right]}{\partial x_j}$	$+\frac{\partial\left[\overline{\tau_{ij}u_i}-\widehat{\tau}_{ij}\widetilde{u}_i\right]}{\partial x_j}$	neglected
Heat Flux	$-\frac{\partial\left[\bar{q}_j-\widehat{q}_j\right]}{\partial x_j}$	$-\frac{\partial\left[\bar{q}_j-\widehat{q}_j\right]}{\partial x_j}$	neglected
Internal energy flux	$-\frac{\partial\bar{\rho}\left[\widetilde{E_{int}u_j}-\widehat{E}_{int}\widetilde{u}_j\right]}{\partial x_j}$	$-\frac{1}{(\gamma-1)}\frac{\partial\left[\overline{pu_j}-\bar{p}\widetilde{u}_j\right]}{\partial x_j}$	modeled
Kinetic energy flux	$-\frac{\partial\bar{\rho}\left[\widetilde{Ku_j}-\widehat{K}\widetilde{u}_j\right]}{\partial x_j}$	$-\frac{\partial\bar{\rho}\left[\widetilde{Ku_j}-\widehat{K}\widetilde{u}_j\right]}{\partial x_j}$	partially modeled

Table 2.4: Comparison of SGS terms appearing in LES formulation, respectively for real gas (filtered system (2.48)) and perfect gas (filtered system (2.54)). In blue: terms with identical expressions in real gas and PG flows; in red: terms with different expressions in real gas and PG flows.

This approach is called implicit LES (ILES).

On the contrary, structural modeling seeks to reproduce the unfiltered field from the filtered field. Since structural models do not focus on SGS dissipation, they can raise stability issues. An additional functional modeling term is generally added to a structural model, which is then called a mixed model. Structural (or mixed) models are known to give better correlations between real and predicted terms than purely functional models. Among the most popular structural models, one can mention the scale-similarity model (Bardina *et al.*, 1980) and the gradient model (Clark *et al.*, 1979). Readers should refer to Garnier *et al.* (2009) for more details about functional and structural approaches applied to LES modeling.

Smagorinsky model

The Smagorinsky model developed in 1963 (Smagorinsky, 1963) is without any doubt the most popular turbulent closure in LES because of its simplicity. It is based on the Boussinesq hypothesis (Boussinesq, 1897)[†] which assumes that the SGS energy transfer is analogous to a molecular dissipation. The molecular viscosity is replaced by a subgrid viscosity denoted ν_{sgs}. The deviatoric part of the turbulent SGS stress tensor is aligned with the deviatoric part of the strain-rate tensor as:

$$t_{ij}^D = t_{ij} - \underbrace{\frac{1}{3}t_{kk}\delta_{ij}}_{t_{ij}^I} = -2\bar{\rho}\nu_{\text{sgs}}\underbrace{\left(\widetilde{S}_{ij} - \frac{1}{3}\widetilde{S}_{kk}\delta_{ij}\right)}_{\widetilde{S}_{ij}^D} \tag{2.55}$$

where $\widetilde{S}_{ij} = \frac{1}{2}\left(\frac{\partial \widetilde{u}_i}{\partial x_j} + \frac{\partial \widetilde{u}_j}{\partial x_i}\right)$ is the strain-rate tensor associated to the resolved velocity. The isotropic part of the turbulent SGS stress tensor represents the SGS turbulent kinetic energy. It is generally neglected for PG flows following Erlebacher *et al.* (1992)'s recommendation even though Yoshizawa (1986) proposes a model based on an analogy with the Smagorinsky model. This assumption is investigated in Appendix D.

The Smagorinsky model is based upon a dimensional analysis which gives the following expression for the subgrid viscosity:

$$\nu_{\text{sgs}} = C_s^2\Delta^2\sqrt{2\tilde{S}_{ij}\tilde{S}_{ij}} \tag{2.56}$$

where Δ denotes the filtering size and C_s is the Smagorinsky constant, the value of which depends on flow conditions. Assuming that the filtering frequency is located inside the inertial part of the spectrum leads to $C_s \approx 0.18$. This model is generally too dissipative in strong strain-rate regions like near walls regions. Some damping can be added to limit this effect. The Smagorinsky model effect is also entirely dissipative: the model is not able to predict local backward energy transfer events (from the small scales to the resolved ones).

Dynamic eddy-viscosity model

Although the Smagorinsky model is simple, its predictions are not always satisfactory. In order to improve it, Germano *et al.* (1991) and Lilly (1992) developed a dynamic approach to transform the Smagorinsky constant into a time and space dependent field; the dynamic constant will be denoted C_d. Its use allows some local backward energy transfers (Germano *et al.*, 1991). Yet, its implementation is costly. Negative values of the subgrid viscosity can

[†]Prandtl was the first to express it as the Boussinesq's hypothesis in 1904 (Prandtl, 1904).

deteriorate the numerical stability of the computation. The subgrid viscosity field is often averaged over space in order to avoid abrupt changes.

This dynamic procedure implies a double filtering operation. In *a posteriori* LES, the first filtering operator corresponds to the inherent filtering of the mesh associated to the filter size Δ. In *a priori* LES, the filtering has been already introduced in Equation (2.39). The same notation $\widetilde{\phi}$ is used to denote the filtered field for both *a priori* and *a posteriori* LES. The second filtering operator is applied at a larger filtering size $\widehat{\Delta} > \Delta$[†]. The associated filtered field is denoted $\widehat{\phi}$. The double filtering of the turbulent SGS stress tensor $\widehat{t}_{ij}$ takes the form:

$$\widehat{t}_{ij} = \widehat{\overline{\rho}\widetilde{u_i}\widetilde{u_j}} - \widehat{\overline{\rho}\widetilde{u}_i}\widehat{\widetilde{u}_j} = \underbrace{\widehat{\overline{\rho}\widetilde{u_i}\widetilde{u_j}} - \widehat{\left(\frac{1}{\overline{\rho}}\right)}\widehat{\overline{\rho}\widetilde{u}_i}\widehat{\overline{\rho}\widetilde{u}_j}}_{\mathcal{T}_{ij}} + \underbrace{\widehat{\left(\frac{1}{\overline{\rho}}\right)}\widehat{\overline{\rho}\widetilde{u}_i}\widehat{\overline{\rho}\widetilde{u}_j} - \widehat{\overline{\rho}\widetilde{u}_i}\widehat{\widetilde{u}_j}}_{-\mathcal{L}_{ij}} \tag{2.57}$$

where $\mathcal{T}_{ij}$ is the turbulent SGS tensor at the combination of the two filtering levels and $\mathcal{L}_{ij}$ is the Leonard tensor. Since it is only expressed from resolved quantities, the Leonard tensor can be directly computed. The two deviatoric parts of the turbulent SGS stress tensor $\mathcal{T}_{ij}$ and t_{ij} are modeled with the Smagorinsky model. The same dynamic constant C_d is used for both SGS tensors assuming that the slope of turbulent kinetic energy spectrum is constant:

$$t_{ij}^D = t_{ij} - \frac{1}{3}t_{kk}\delta_{ij} = -2\overline{\rho}C_d\Delta^2\widetilde{s}\widetilde{S}_{ij} \tag{2.58}$$

$$\mathcal{T}_{ij}^D = \mathcal{T}_{ij} - \frac{1}{3}\mathcal{T}_{kk}\delta_{ij} = -2\overline{\rho}C_d\left(\widehat{\Delta}\right)^2\widehat{\widetilde{s}}\widehat{\widetilde{S}}_{ij} \tag{2.59}$$

where $\widetilde{s} = \sqrt{2\widetilde{S}_{ij}\widetilde{S}_{ij}}$ and $\widehat{\widetilde{s}} = \sqrt{2\widehat{\widetilde{S}}_{ij}\widehat{\widetilde{S}}_{ij}}$. Combining Equations (2.57), (2.58) and (2.59) yields the following relationship:

$$\mathcal{L}_{ij}^D = \mathcal{L}_{ij} - \frac{1}{3}\mathcal{L}_{kk}\delta_{ij} = \mathcal{T}_{ij}^D - \widehat{t}_{ij}^D = -2C_d\underbrace{\left[\left(\widehat{\Delta}\right)^2\widehat{\widetilde{s}}\widehat{\widetilde{S}}_{ij} - \Delta^2\widehat{\widetilde{s}\widetilde{S}}_{ij}\right]}_{\mathcal{M}_{ij}} \tag{2.60}$$

From Equation (2.60), the dynamic constant can be computed in several ways. Germano *et al.* (1991) express C_d as:

$$C_d = -\frac{\mathcal{L}_{ij}^D\tilde{S}_{ij}}{2\mathcal{M}_{ij}\tilde{S}_{ij}} \tag{2.61}$$

The following modified expression developed by Lilly (1992) avoids problems arising when the denominator of (2.61) cancels:

$$C_d = -\frac{\mathcal{M}_{ij}\mathcal{L}_{ij}^D}{2\mathcal{M}_{kl}\mathcal{M}_{kl}} \tag{2.62}$$

This relation is obtained using the least squares method by minimizing $\mathcal{L}_{ij}^D + 2C_d\mathcal{M}_{ij}$ as:

$$\frac{\partial}{\partial C_d}\left[\mathcal{L}_{ij}^D + 2C_d\mathcal{M}_{ij}\right]^2 = 0 \tag{2.63}$$

[†] $\widehat{\Delta} = 2\Delta$ is a good compromise.

SGS internal energy model

The most common way to model the SGS internal energy term is to follow the assumption of Eidson (1985) who considers that the internal energy transfer from resolved scales to subgrid scales is proportional to the gradient of the resolved temperature. The SGS conductivity is linked to the SGS viscosity as follows:

$$\kappa_{\text{sgs}} = \frac{\bar{\rho}\nu_{sgs}c_p}{Pr_{\text{sgs}}} \tag{2.64}$$

where Pr_{sgs} is the SGS Prandtl number. It is set to 0.6 in the present work (Lesieur, 2012). The SGS internal energy is thus expressed as:

$$\frac{\partial \bar{\rho}\left[\widetilde{E_{int}u_j} - \widehat{E}_{int}\widetilde{u}_j\right]}{\partial x_j} = -\frac{\partial}{\partial x_j}\left(\kappa_{\text{sgs}}\frac{\partial \widehat{T}}{\partial x_j}\right) \tag{2.65}$$

2.5 Numerical solver

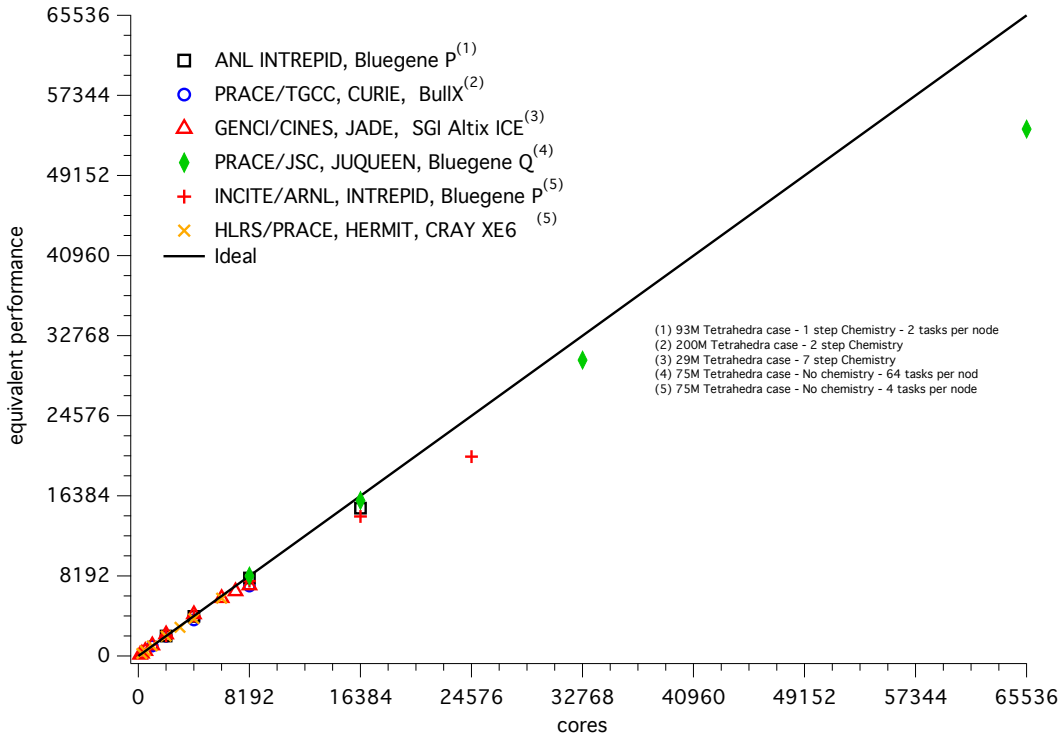

Figure 2.4: Performance of AVBP on different supercomputers (Source: CERFACS internal communication).

General features of AVBP This section is devoted to a brief presentation of the numerical solver AVBP and the setup used in the present work. The AVBP project started in 1993 at CERFACS upon an initiative of Michael Rudgyard and Thilo Schönfeld. AVBP is now co-owned by CERFACS and IFP Energies Nouvelles. It is widely used in industry (Safran Group, Airbus, Air Liquide, Total, GRTgaz, Renault, Alstom, Siemens Power Generation,...) and in laboratories (LMFA, EM2C, IMFT, IRPHE, CORIA, UPPA,...). It is considered as a reference

code in fluid mechanics. AVBP is designed for massively parallel computation. Its very high scalability has been proven over some of the most powerful supercomputers (Marenostrum, Ter@10, IBM eServer BlueGene, Cray XT3/XT4 Oakridge) (see Figure 2.4). This key feature is essential in order to perform simulations on complex configurations within a reasonable time. Most of the code is coded in Fortran and some parts (like allocation, deallocation) are coded in C.

Numerical methods AVBP solves reactive multi-species 3D unsteady compressible Navier-Stokes equations using an explicit formulation. The code can work with unstructured and hybrid grids composed of triangles and quadrilaterals in 2D and tetrahedra, prims, pyramids and hexahedra in 3D. In order to handle this type of grids, AVBP is based on a cell vertex formulation.

The code uses two types of numerical methods associated to specific numerical schemes for the hyperbolic terms (convection) of the governing equations:

• For the finite volume method, the Lax Wendroff scheme (Ni, 1982) ensures a second-order accuracy in space and in time. Because of its low order of accuracy combined with its low computational cost, it is generally used to obtain a preliminary solution.

• For the finite element method, the two-steps Taylor Galerkin schemes (TTGC [†] or TTG4A) ensure a third order accuracy in space and respectively third or fourth order in time.

The computational cost of the aforementioned Taylor-Galerkin schemes is about 1.9 times larger than the one of the Lax-Wendroff scheme (Lamarque, 2007). The cost remains very reasonable for these higher order accurate schemes. In AVBP, diffusive terms can be discretized using FV4Δ (Finite Volume with a 4Δ stencil) or FE2Δ (Finite Element with a 2Δ stencil) operators. Readers should refer to Lamarque (2007) for further details. The scheme is completed with a shock capturing method. In regions where strong gradients exist, an additional dissipation term is added following the approach of Cook & Cabot (2004). Its impact on the resolution of the smallest scales has been analyzed in Giauque *et al.* (2020).

Application to DNS and LES AVBP can be used to perform LES as well as DNS simulations (Desoutter *et al.*, 2009; Cadieux *et al.*, 2012). Its adaptability and its performance are fundamental assets for the present work where both DNS and LES are performed over large computational grids. It is essential to keep the same code for DNS and LES in order to reduce the sources of differences between *a priori* and *a posteriori* LES. Table 2.5 summarizes the parameters used in AVBP to perform DNS (Chapters 3 and 4) and LES (Chapter 7). The implementation of the Martin-Hou EoS is validated using the shock tube simulation of Fergason *et al.* (2001).

In the next chapter, the AVBP numerical setup is assessed on the DNS of a PG compressible mixing layer using the results of Pantano & Sarkar (2002) as reference. The validation for this PG case paves the way for the computation of new results in Chapter 4 with the DNS of a DG compressible mixing layer.

[†]The TTGC was built to answer LES and DNS requirements. It combines the benefits of the Taylor-Galerkin schemes but it is much less dissipative on small wave lengths (Colin & Rudgyard, 2000).

[†]The Courant-Friedrichs-Lewy (CFL) number controls the numerical stability of the convection scheme.

[†]The Fourier number controls the numerical stability of the diffusion scheme.

Convection scheme	TTGC
Diffusive scheme	FV4Δ
CFL number†	0.8
Fourier number†	0.8

Table 2.5: Numerical setup used in the solver AVBP.

Chapter 3

DNS of perfect gas compressible mixing layers: verification and validation

Contents

1.1 Context and motivation **1**
1.2 Dense gas flows **3**
1.3 The need for turbulence modeling in dense gas flows **6**
1.4 Outline of the thesis **8**

STATING that AVBP is a tool of choice to perform DNS (and LES) of compressible flows is not sufficient to demonstrate the relevance of the choice made in the present thesis to apply this solver to the comparison of dense gas and perfect gas compressible mixing layers using DNS. While dense gas mixing layers were still *terra incognita* at the start of the present thesis, perfect gas mixing layers and in particular air mixing layers have been already studied both experimentally and numerically by previous authors. Therefore this chapter is devoted to the assessment of AVBP for the DNS of an air (considered as a perfect gas) compressible mixing layer. A review of the literature is proposed in the first section in order to select a reference ideal gas compressible mixing layer and also to identify some key results regarding the compressible mixing layer of an ideal gas, to which the dense gas DNS results will be next confronted in Chapter 4. The next section describes the flow configuration and the main physical and numerical parameters of the study. Finally, the DNS results produced in the present work are analyzed and compared to available results from the literature. Note this chapter gathers PG results which have been published in Vadrot *et al.* (2020) and Vadrot *et al.* (2021).

3.1 Perfect gas compressible shear layer

Mixing layer studies belong to a long-term research program on the characterization of turbulence. Turbulent mixing layers appear in many physical domains and industry problems. The very first investigation of turbulent mixing layers was performed by Liepmann & Laufer (1947) who demonstrated the self-preserving property of such flows. Subsequently, many experimental investigations were led on turbulent mixing layers, especially for aeronautic purposes, such as scram-jet engines and abatement of supersonic jet noise.

Convective Mach number M_c and other parameters Quickly, compressibility effects proved to be a key point in high-speed mixing layer flows. Bogdanoff (1983) introduced the concept of convective Mach number, taking into account not only the velocity and sound speed of each stream of the mixing layer but a combination of them. Denoting U_i, c_i respectively the flow speed and the sound speed of stream i (upper or lower stream) of the mixing layer, the convective Mach number is defined as :

$$M_c = \frac{U_1 - U_2}{c_1 + c_2} = \frac{\Delta u}{c_1 + c_2} \tag{3.1}$$

The convective Mach number provided the community with a similar comparative scale when discussing different configurations. A consensus appeared on the reduction of the mixing layer growth rate when increasing the convective Mach number (Bradshaw, 1977; Papamoschou & Roshko, 1988).

Further studies were conducted in order to capture the key parameters allowing to better understand the fundamental mechanisms at stake, such as for instance the initial density ratio between the upper and lower streams. Brown & Roshko (1974) investigated density effects using two different gases and thoroughly analyzed turbulent structures to conclude that density effects are far less prominent than compressibility effects. Although the mixing layer flow configuration appears rather simple, Bradshaw (1966) showed that initial conditions and technical difficulties with the experimental realization of the flow are a main source of the discrepancies observed between published results.

Direct Numerical Simulations The first DNS of a compressible mixing layer was performed by Sandham & Reynolds (1990), followed by Luo & Sandham (1994), Vreman *et al.* (1996*a*), Freund *et al.* (2000), Pantano & Sarkar (2002), Fu & Li (2006), Zhou *et al.* (2012), Martínez Ferrer *et al.* (2017), Dai *et al.* (2018) and recently Matsuno & Lele (2020). These DNS of compressible mixing layers assume the fluid behaves like an ideal gas. They all confirm that the spreading rate decay is due to a lower turbulent production (Sarkar, 1995). The compressible turbulent kinetic energy equation includes additional terms with respect to its incompressible formulation, namely compressible dissipation (ϵ_d) and pressure-dilatation (Π_{ii}) terms. Key questions, seemingly related, are why is the turbulent production decreasing and how do these additional terms evolve with an increasing convective Mach number.

Zeman (1990) and Sarkar *et al.* (1991) predicted that the dilatational part of the dissipation increases with the turbulent Mach number ($M_t = \sqrt{\overline{u_i' u_i'}}/c$, where $u_i{}'$ represents the fluctuating velocity in direction i) because of the occurrence of eddy shocklets. They proposed a modeling of this term that captures the growth rate reduction as the Mach number increases. However, Vreman *et al.* (1996*a*) and Freund *et al.* (2000) suggested that the proposed model

is not realistic since eddy shocklets at that time had not yet been observed in 3D DNS with a convective Mach number below one. Since then, Zhou *et al.* (2012) observed shocklets in their 3D simulation for a convective Mach number of 0.7. Although eddy shocklets may occur in the compressible mixing layer for a convective Mach number as low as 0.7, the compressible dissipation term remains small as shown by Pantano & Sarkar (2002) for a convective Mach number of 1.1 and below. This observation is confirmed by the present simulations (see Chapter 4). Considering a dense gas instead of an ideal gas should even further lessen this dissipation term since entropy jumps across shocklets are reduced within the inversion region (Giauque *et al.*, 2020).

Pressure strain correlations and mixing layer growth rate The pressure-dilatation term (Π_{ii}) is formed from the sum of the pressure-strain rate correlations (Π_{ij}). It is negligible if compared with the most important terms of the turbulent kinetic energy equation (Vreman *et al.*, 1996*a*; Freund *et al.*, 2000; Pantano & Sarkar, 2002). However, each pressure-strain correlation is far from being negligible and the decrease of these correlations with an increasing Mach number is likely to explain the decay of the growth rate (Vreman *et al.*, 1996*a*) and Freund *et al.* (2000). Vreman *et al.* (1996*a*) noticed thanks to DNS that this reduction of the growth rate was mainly due to the decrease of pressure fluctuations normalized by the dynamic pressure ($p_{rms}/(\frac{1}{2}\rho_0(\Delta u)^2)$). Freund *et al.* (2000) confirm this observation and propose a model to predict this abatement based on the concept of sonic-eddy developed by Breidenthal (1992). Pantano & Sarkar (2002) later demonstrated analytically the aforementioned observation. Hamba (1999) performed the DNS of an homogeneous shear flow varying the turbulent Mach number M_t from 0.1 to 0.3. The author identifies a dissipative term, responsible for the normalized pressure fluctuations diminution, in the transport equation for $p^{'2}$ called pressure-variance dissipation and which depends on the thermal conductivity. Several turbulence models were next proposed, based on the normalized pressure fluctuations reduction (Fujiwara *et al.*, 2000; Park & Park, 2005; Huang & Fu, 2008).

Since pressure-strain correlations are composed of pressure fluctuations and strain-rate fluctuations, Martínez Ferrer *et al.* (2017) suggested that the reduction of pressure fluctuations may not be the only reason for the pressure-strain rate decay. Their 3D DNS simulations at convective Mach numbers between 0.35 and 1.1 suggest that the strain-rate fluctuations also decrease with an increasing Mach number.

Case of high convective Mach number Few experiments and DNS have been achieved at high M_c. Rossmann *et al.* (2001) have experimentally studied higher compressibility regimes until $M_c = 2.25$ and Matsuno & Lele (2020) recently performed DNS of temporal mixing layers up to $M_c = 2.0$. In the following, several 3D DNS of compressible perfect gas mixing layers are performed up to $M_c = 2.2$. These DNS are thoroughly compared to the available results from the literature in particular to the results of Pantano & Sarkar (2002) used as reference. The comparison with their dense gas counterparts will be performed in the next chapter.

M_c	ρ_1/ρ_2	$Re_{\delta_{\theta,0}}$	$L_x \times L_y \times L_z$	$N_x \times N_y \times N_z$	Δu $(m.s^{-1})$	$\delta_{\theta,0}$ (nm)	L_0
0.1	1.0	160	$344 \times 344 \times 86$	$1024 \times 1024 \times 256$	34.11	135.8	$L_x/48$
1.1	1.0	160	$344 \times 172 \times 86$	$512 \times 256 \times 128^{\dagger}$	375.18	12.348	$L_x/48$
1.1	1.0	160	$344 \times 172 \times 86$	$1024 \times 512 \times 256^{\dagger\dagger}$	375.18	12.348	$L_x/48$
2.2	1.0	160	$688 \times 688 \times 172$	$1024 \times 1024 \times 256$	753.0	6.153	$L_x/8$

Table 3.1: Simulation parameters for Air PG DNS. L_x, L_y and L_z denote computational domain lengths measured in terms of initial momentum thickness. N_x, N_y and N_z denote the number of grid points. L_0 denotes the size of initial turbulent structures ($k_0 = 2\pi/L_0$) measured in terms of initial momentum thickness. All grids are uniform.

3.2 Problem formulation

3.2.1 Initialization

Several DNS up to $M_c = 2.2$ are performed for air considered as a perfect gas. The initial conditions of the mixing layer require the choice of an initial operating thermodynamic point in the $p-v$ diagram. Since the key objective of this DNS analysis is to compare perfect and dense gases in identical initial conditions, the same values of reduced specific volume and reduced pressure are selected for the initial thermodynamic state for both types of gases. This choice is thoroughly explained in the next chapter (see Section 4.1.1). Critical values used for air are the critical pressure $p_c = 3.7663 \times 10^6$ Pa and the specific volume $v_c = 3.13 \times 10^{-3}$ $\mathrm{m}^3.\mathrm{kg}^{-1}$ (Stephan & Laesecke, 1985).

Key non-dimensional parameters are the convective Mach number (Equation (3.1)) and the Reynolds number based on the initial momentum thickness $\delta_{\theta,0}$:

$$Re_{\delta_{\theta,0}} = \frac{\Delta u \delta_{\theta,0}}{\nu} \tag{3.2}$$

where ν denotes the kinematic viscosity and the momentum thickness at time t is defined as:

$$\delta_\theta(t) = \frac{1}{\rho_0(\Delta u)^2} \int_{-\infty}^{+\infty} \bar{\rho} \left(\frac{(\Delta u)^2}{4} - \widetilde{u}_x^2 \right) dy \tag{3.3}$$

with $\rho_0 = (\rho_1 + \rho_2)/2$ the averaged density and $\widetilde{u}_x$ the Favre averaged streamwise velocity defined in Eq. 3.9.

This study aims at validating the present DNS results first at $M_c = 1.1$ using the results of Pantano & Sarkar (2002) as reference. DNS at other convective Mach numbers are then validated using in particular the recent results of Matsuno & Lele (2020). Following the reference work of Pantano & Sarkar (2002), the Reynolds number based on the initial momentum thickness is set equal to 160 for all simulations and the initial density ratio ρ_1/ρ_2 between the upper and lower streams is equal to unity. Table 3.1 summarizes the computational parameters for PG simulations performed for different M_c (domain size, number of grid elements, dimensional values of velocity, initial momentum thickness and initial turbulent structures sizes).

†Referred to as the $16.8M$ simulation. $16.8M$ corresponds to the number of grid cells.
††Referred to as the $134M$ simulation. $134M$ corresponds to the number of grid cells.

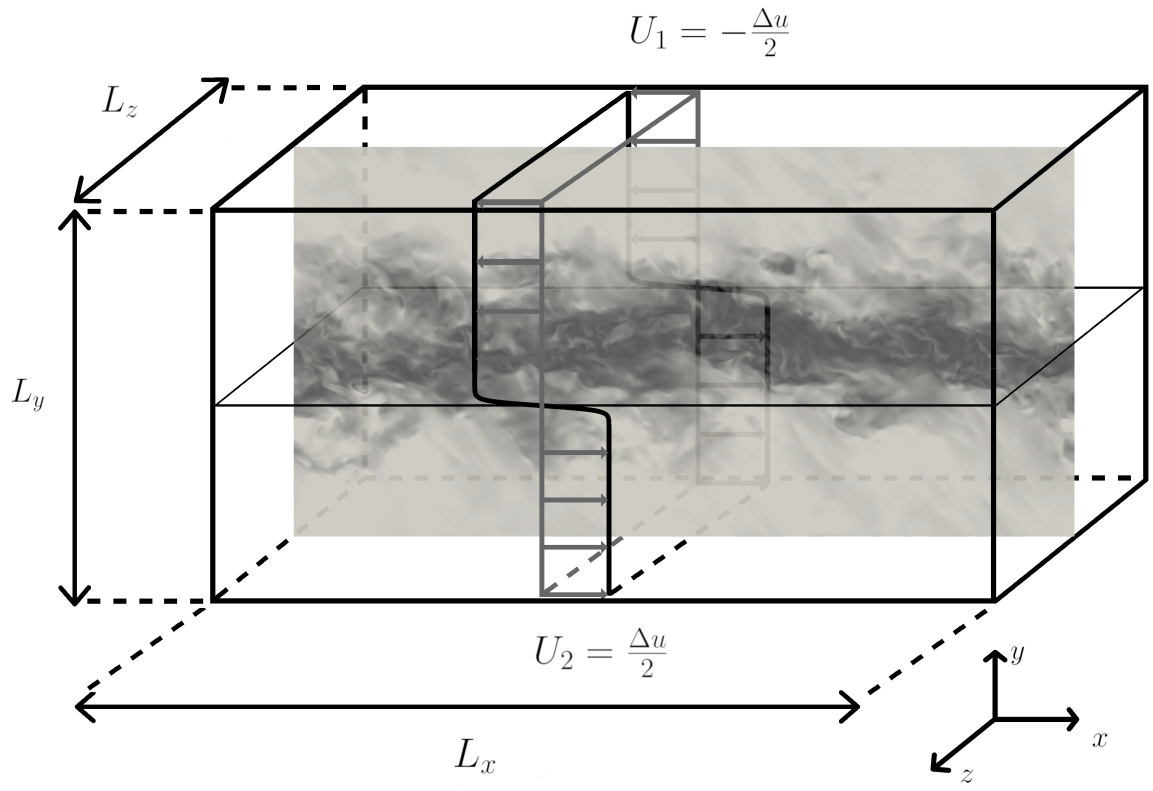

Figure 3.1: Configuration of the temporal mixing layer. The velocity magnitude is plotted for the DG DNS at $M_c = 2.2$ at $\tau = 4000$.

The ratio r between the Kolmogorov scale and the grid cell size (L_η/Δ_x) is about 0.52 for the least refined mesh ($16.8M$ simulation) at the centerline during the selected self-similar range (see Section 3.3.1). To check grid convergence and because the value $r = 0.52$ corresponding to the baseline mesh is not very large for a DNS, a second DNS is performed with a refined mesh obtained by doubling the number of grid cells in each direction ($134M$ simulation) yielding a ratio r equal to 1.03 (see figure 3.8). Details about the numerical setup (choice of numerical methods and associated tuning parameters) have been previously provided in Section 2.5.

In the present study, the temporal mixing layer is chosen instead of the spatially developing mixing layer because it is less computationally expensive and will ease the exploration of various configurations (different values of the convective Mach number but also, for DG flows, different choices for the initial thermodynamic state). There are slight differences between these two configurations. For the temporal mixing layer, the two streams flow in opposite directions, which enables to increase the differential speed with a smaller absolute speed for each stream. A representation of the computational domain is provided in Figure 3.1. For the spatial mixing layer, both streams flow in the same direction and a speed gap which corresponds to the differential speed is imposed. The transition from one configuration to the other is a change of Galilean reference frame given by (de Bruin, 2001):

$$t\Delta u_{\text{temporal}} = \frac{x\Delta u_{\text{spatial}}}{u_c} \tag{3.4}$$

where t denotes the time scale of the temporal configuration, $\Delta u_{\text{temporal}}$, the differential speed of the temporal evolution, $\Delta u_{\text{spatial}}$, the differential speed of the spatial evolution, $u_c = (U_1 + U_2)/2$, the convective speed and x, the streamwise position scale of the spatial configuration.

The temporal mixing layer requires periodic boundary conditions in the x and z directions. A non-reflective boundary condition (the NSCBC model proposed by Poinsot & Lele (1992)) is imposed in the y direction to prevent the reflection of acoustic waves inside the computational domain.

The streamwise velocity field is initialized using an hyperbolic tangent profile:

$$\bar{u}_x(y) = \frac{\Delta u}{2} \tanh\left(-\frac{y}{2\delta_{\theta,0}}\right) \tag{3.5}$$

The complete streamwise velocity field is obtained by adding fluctuations to the average velocity. For the y and z components, the average velocity is set equal to zero. A Passot-Pouquet spectrum is imposed for the initial velocity fluctuations:

$$E(k) = (k/k_0)^4 exp(-2(k/k_0)^2) \tag{3.6}$$

where k denotes the wavenumber. The peak wavenumber k_0 controls the size of the initial turbulent structures. It corresponds to the integral scale for which the turbulent kinetic energy is maximum inside the initial mixing layer. Its influence on the mixing layer growth is investigated in Appendix B for the DG mixing layer. It is observed that a larger value of k_0 accelerates the transition to the unstable growth. Its value for each DNS is given in Table 3.1. The velocity field is then filtered to initialize turbulence only inside the initial momentum thickness. This is done by multiplying the velocity field by an exponential decay over the y-direction in the same way as Pantano & Sarkar (2002) :

$$f(y) = \frac{1}{\sigma\sqrt{2\pi}} exp\left(-\frac{(y - L_y/2)^2}{2\sigma^2}\right) \tag{3.7}$$

where the full width at half maximum of the peak is set equal to the initial momentum thickness $\delta_{\theta,0} = 2\sigma\sqrt{2ln(2)}$. Also, the Gaussian distribution is normalized to reach a maximum value of 1 at the center $y = L_y/2$.

3.2.2 Turbulent Kinetic Energy equation

The unsteady, three-dimensional, compressible Navier-Stokes equations (Equations (2.1)) are solved to describe the temporally evolving mixing layer. In addition, the thermal perfect gas and the caloric EoS (Equations (2.8)) are used for air. To complete the thermodynamic description of the PG, the Sutherland's model is used associated to a constant Prandtl number set equal to 0.71 to compute transport coefficients (see Section 2.2.2).

For the sake of the physical analysis of the mixing layer, the turbulent kinetic energy equation (TKE equation) can be derived from the Navier-Stokes equations (Equations (2.1)). Density, pressure and velocity are decomposed into a mean and fluctuating component as follows :

$$\begin{cases} \rho = \bar{\rho} + \rho' \\ p = \bar{p} + p' \\ u_i = \widetilde{u}_i + u_i'' \end{cases} \tag{3.8}$$

where $\bar{\phi}$ denotes the Reynolds average for a flow variable ϕ while the Favre average $\widetilde{\phi}$ is defined as :

$$\widetilde{\phi} = \frac{\overline{\rho\phi}}{\bar{\rho}} \tag{3.9}$$

Reynolds fluctuations are denoted ϕ' while Favre fluctuations are denoted ϕ''. For the temporal mixing layer, Reynolds averaging is equivalent to plane averaging along x and z directions because of the use of periodic boundary conditions. Reynolds and Favre averages must not be confused with their LES filtering counterparts presented in Section 2.4.2. In the first case, the fluctuating field is separated from the Reynolds-averaged one and in the second case, the resolved field is separated from the subgrid-scale field.

Introducing the relationships (3.8) into the instantaneous Navier-Stokes equations, applying the Reynolds averaging and combining the resulting equations (see details for instance in Bailly & Comte-Bellot (2003)) allow to obtain the turbulent kinetic energy equation (TKE equation) :

$$\begin{aligned}\frac{\partial \bar{\rho}\widetilde{k}}{\partial t}+\frac{\partial \bar{\rho}\widetilde{k}\widetilde{u}_j}{\partial x_j} =& \underbrace{-\overline{\rho u_i'' u_j''}\frac{\partial \tilde{u}_i}{\partial x_j}}_{\text{Production}} \underbrace{-\overline{\tau_{ij}'\frac{\partial u_i''}{\partial x_j}}}_{\text{Dissipation}} \\ & \underbrace{-\frac{1}{2}\frac{\partial \overline{\rho u_i'' u_i'' u_j''}}{\partial x_j}}_{\text{Turbulent transport}} \underbrace{-\frac{\partial \overline{p' u_i''}}{\partial x_i}}_{\text{Pressure transport}} \underbrace{+\frac{\partial \overline{u_i'' \tau_{ij}'}}{\partial x_j}}_{\text{Viscous transport}} \\ & \underbrace{+\overline{p'\frac{\partial u_i''}{\partial x_i}}}_{\text{Pressure dilatation}} \underbrace{-\overline{u_i''}\left(\frac{\partial \bar{p}}{\partial x_i}-\frac{\partial \bar{\tau}_{ij}}{\partial x_j}\right)}_{\text{Mass-flux term}}\end{aligned} \tag{3.10}$$

where $\widetilde{k}=\frac{1}{2}\widetilde{u_i'' u_i''}$ denotes the specific turbulent kinetic energy. The TKE equation allows to assess the contribution of the significant turbulent terms. The main terms of (3.10) are the production, dissipation and transport terms. Pressure dilatation and mass-flux term (the later includes the baropycnal work) are equal to zero in the incompressible case. The dissipation term can be decomposed into a solenoidal (or incompressible), a low-Reynolds number and a dilatational component. The latter is associated to losses occurring in eddy shocklets. Lee *et al.* (1991) express the dilatational dissipation also called the compressible dissipation as:

$$\epsilon_d=-\frac{4}{3}\overline{\nu\left(\frac{\partial u_k''}{\partial x_k}\right)^2}-2\overline{u_k''\frac{\partial \nu'}{\partial x_k}\frac{\partial u_k''}{\partial x_k}} \tag{3.11}$$

This expression takes into account the effect of viscosity variations unlike Sarkar & Lakshmanan (1991) and Zeman (1990) who express it as $\epsilon_d=-\frac{4}{3}\overline{\bar{\nu}\left(\frac{\partial u_k''}{\partial x_k}\right)^2}$, neglecting viscosity variations. For decaying compressible turbulence, Lee *et al.* (1991) found that Sarkar & Lakshmanan (1991) and Zeman (1990)'s expression overestimates by about 15% the compressible dissipation.

3.3 DNS verification and validation

This section is devoted to the assessment of the quality of the perfect gas DNS performed for air at three different convective Mach numbers ($M_c=0.1-1.1-2.2$). The validation starts with the study of the temporal evolution of the momentum thickness and with the selection of the self-similar period. Once this period is selected, the present work is first compared with the

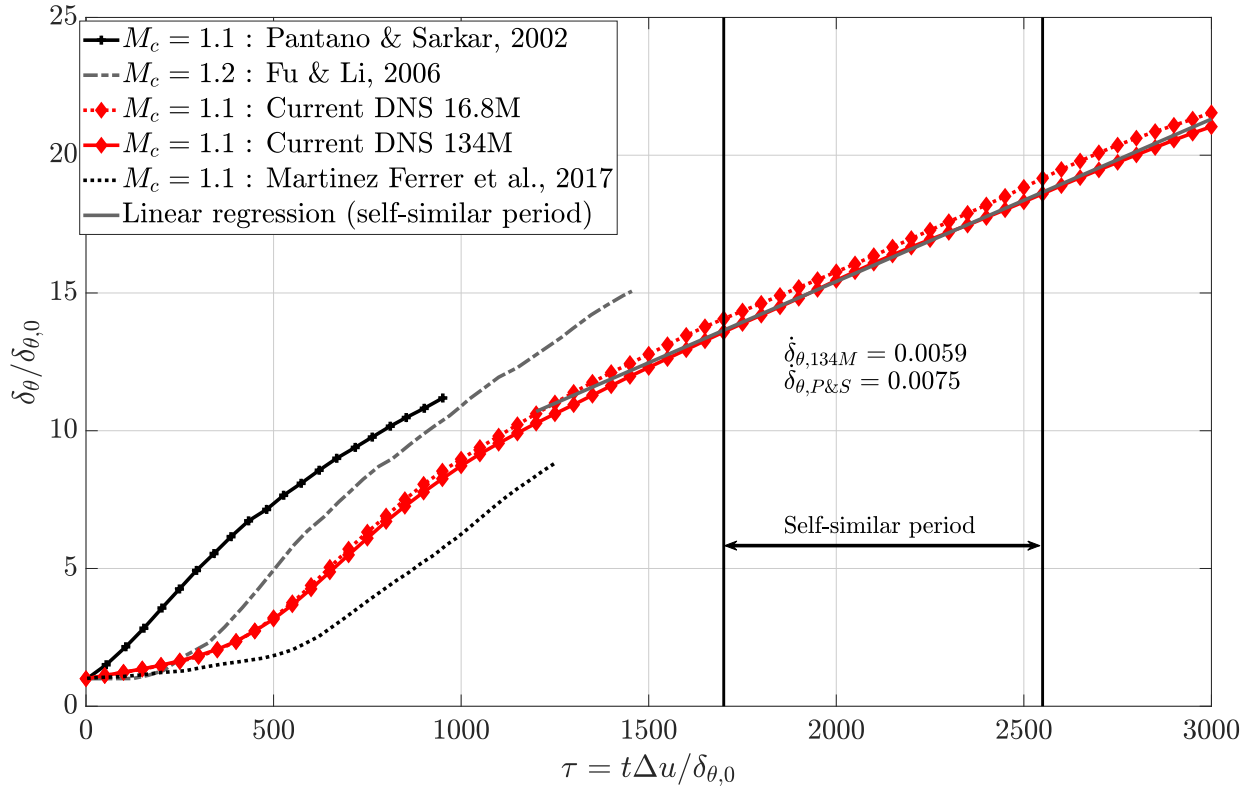

Figure 3.2: Temporal evolution of the mixing layer momentum thickness. Comparison is made between the two different grid precisions (16.8M and 134M of grid elements) to check the grid convergence and with the available literature (Pantano & Sarkar, 2002; Fu & Li, 2006; Martínez Ferrer *et al.*, 2017).

results of Pantano & Sarkar (2002) at $M_c = 1.1$ and then to other available results in literature at $M_c = 0.1$ and $M_c = 2.2$.

3.3.1 Temporal evolution and selection of the self-similar period

Temporal evolution

Results for the case $M_c = 1.1$ are analyzed first. Figure 3.2 shows the temporal evolution of the mixing layer momentum thickness computed for the two levels of grid refinement, along with results from the available literature (Martínez Ferrer *et al.*, 2017; Fu & Li, 2006; Pantano & Sarkar, 2002). The time is non-dimensional ($\tau = t\Delta u/\delta_{\theta,0}$) and the momentum thickness (δ_θ) is normalized by its initial value ($\delta_{\theta,0}$). Grid convergence seems well achieved since the mixing layer growth rates are very close between both simulations (16.8M and 134M). Additional proofs of grid convergence are provided in the next Section 3.3.2 during the self-similar period. The momentum thickness temporal evolution is composed of three main sequences:

- The first one is a kind of delay, observed in the present work and also in the results of Martínez Ferrer *et al.* (2017), Fu & Li (2006), but which appears rather short for Pantano & Sarkar (2002). This delay is likely to be a transition of modes. The energy is initially injected inside the mixing layer through a Passot-Pouquet spectrum. Afterwards, the energy is distributed over the whole spectrum and some unstable modes are amplified leading to the unstable growth.

- The second step of the development of the mixing layer consists in an unstable growth which eventually turns into an over-linear growth rate.

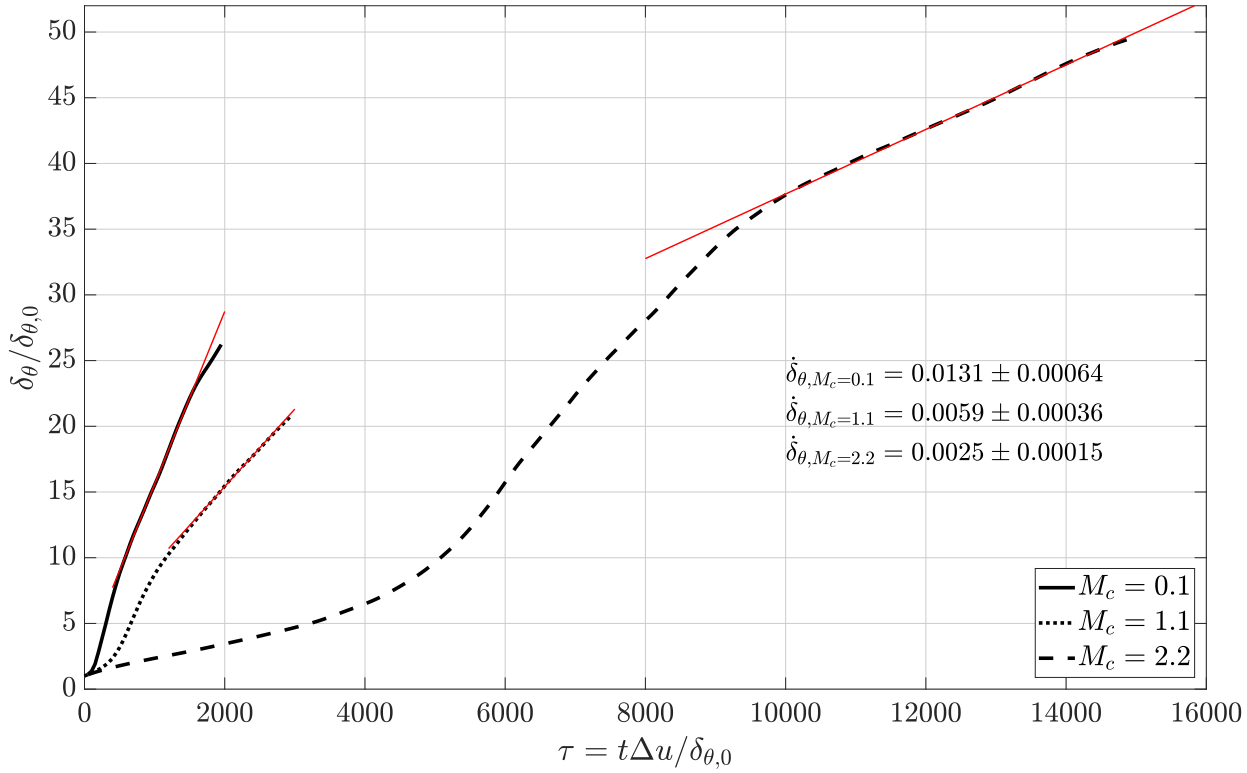

Figure 3.3: Temporal evolution of the mixing layer momentum thickness for $M_c = 0.1 - 1.1 - 2.2$ using air with PG EoS. Slopes are non-dimensional and standard deviations computed over the self-similar period are indicated on the plot.

- Finally, the system reaches a saturation point. At this time, a self-similar state is developing until the turbulent structures exit the computational domain above and below the mixing layer. Self-similarity is characterized by a linear evolution of the momentum thickness over time.

The computed time evolution of the momentum thickness shows a rather good match with the available literature even though the mixing layer momentum thickness growth rate computed for the current $134M$ simulation is smaller (a difference of about 20% is observed) than the one of Pantano & Sarkar (2002). Since the computation of the growth rate depends on the chosen self-similar period and since the self-similar period of the current simulation is chosen late enough to achieve a complete convergence, the computed growth rate is smaller.

The study is extended to two other convective Mach numbers ($M_c = 0.1$ and $M_c = 2.2$). The first one ($M_c = 0.1$) is considered as the reference incompressible case. The second one ($M_c = 2.2$) enables the study of highly compressible regimes. Figure 3.3 gathers the temporal evolution of the momentum thickness for the three convective Mach numbers ($M_c = 0.1 - 1.1 - 2.2$). One can identify the three main aforementioned phases.

At $M_c = 2.2$, one notices that the mixing layer takes a much longer time to develop. This is consistent with observations of Pantano & Sarkar (2002) who noticed that the time required to reach a self-similar regime increases with compressibility. Self-similarity is reached around $\tau \approx 11500$ after a long unstable growth phase. As a comparison, at $M_c = 0.1$ and $M_c = 1.1$, self-similarity is reached respectively at $\tau = 700$ and $\tau = 1700$.

A long time delay is observed at the beginning of the simulation, associated to the transition of modes. Turbulent kinetic energy is initially injected at a given integral length set equal to $L_x/8$. Afterwards, energy is distributed over the whole spectrum and some unstable modes

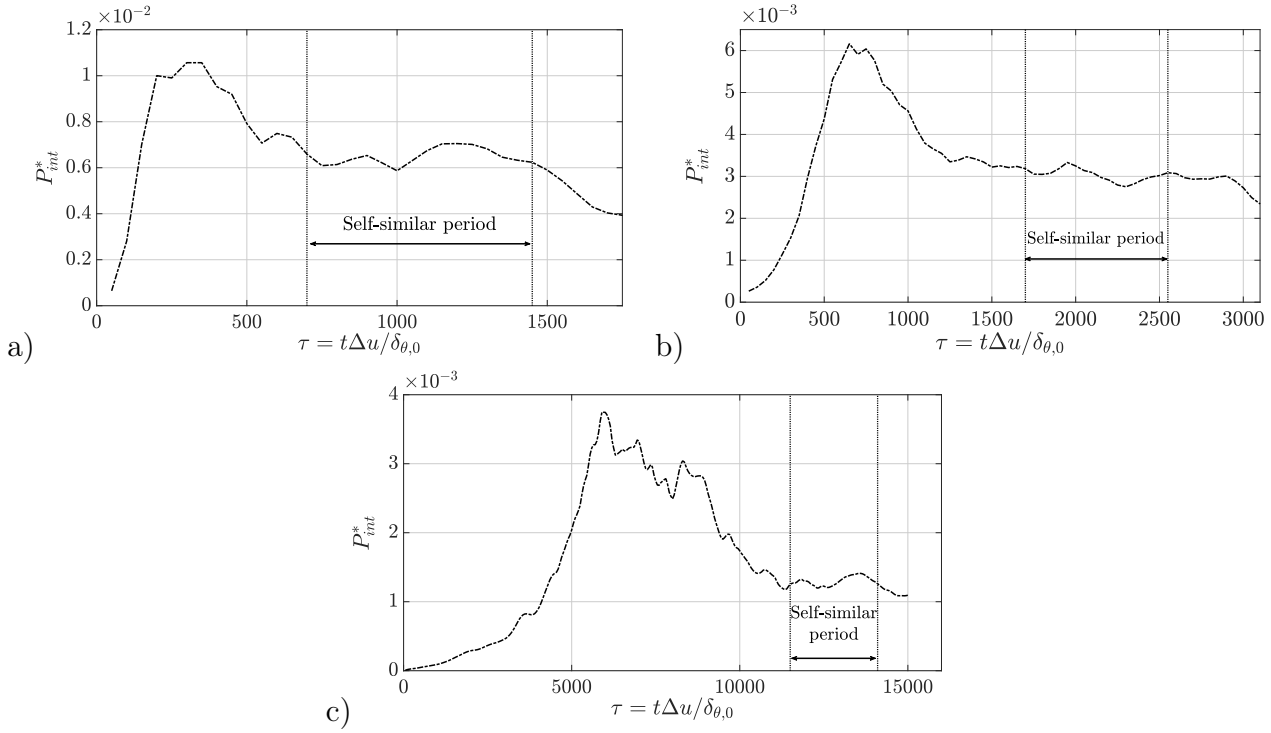

Figure 3.4: Temporal evolution of the non-dimensional streamwise turbulent production term integrated over the whole domain $P^*_{int} = (1/(\rho_0(\Delta u)^3)) \int_{L_y} \bar{\rho} P_{xx} dy$ (with $\bar{\rho} P_{xx}(y) = -\overline{\rho u''_x u''_y} \frac{\partial \tilde{u}_x}{\partial y}$) at $M_c = 0.1$ (a), $M_c = 1.1$ (b) and $M_c = 2.2$ (c). Results are shown for the air using PG EoS. Selections of self-similar period are indicated on each plot.

are amplified leading to the unstable growth phase. In order to reduce this time delay, initial turbulent structures have been chosen larger in proportion to the initial momentum thickness at $M_c = 2.2$ (Table 3.1). This modification of initial turbulent structures size does not impact the growth rate over the self-similar regime. This is verified for DG flows in Appendix B.

In addition, for this $M_c = 2.2$ calculation, domain lengths are doubled in x and z directions and multiplied by four in the y direction when compared to DNS at $M_c = 1.1$. Note that all lengths are normalized by the initial momentum thickness. This extension of the computational domain for $M_c = 2.2$ enables the mixing layer to develop until larger values of $\delta_\theta(t)/\delta_{\theta,0}$ and to obtain a long enough self-similar period without reaching the domain boundaries. Note that other simulations performed without this extension of the computational domain did not allow the flow to reach self-similarity.

Slopes and standard deviations reported in Figure 3.3 are computed over the self-similar period. One can observe that the growth rate is divided by a factor of about two between DNS at $M_c = 2.2$ and at $M_c = 1.1$. Indeed, compressibility effects tend to reduce mixing layer development as the convective Mach number increases.

The DNS performed at $M_c = 0.1$ provides the reference incompressible case used to plot $\dot{\delta}_\theta/\dot{\delta}_{\theta,inc} = f(M_c)$. The computed "incompressible" growth rate is about 0.0131 which is relatively close to the empirical value of 0.016 given by Pantano & Sarkar (2002). One can notice for this case a short unstable growth phase when compared to larger convective Mach number cases.

How to select the self-similar period ?

Self-similarity is a major characteristic of mixing layers: during the self-similar period, flow development can be described using single length and velocity scales. The momentum thickness evolves linearly with time over this period. This particular state in the development of mixing layers is widely used to extract key features of mixing layers. The well known chart giving the evolution of the mixing layer growth rate as a function of the convective Mach number (Papamoschou & Roshko, 1988) is plotted during the self-similar regime (see Section 3.3.2). This period is also used to investigate the balance of the TKE equation, because temporal solutions can be averaged during self-similarity since the flow is in a statistically stable state. The objective of the present paragraph is to determine an appropriate self-similar range, which is actually not a trivial task since several criteria to characterize the self-similar period are proposed in the literature, not all of them precisely defined.

Barre & Bonnet (2015) define their flow as self-similar when they obtain superposition of the mean velocity profiles. Rogers & Moser (1994) conclude that they reach self-similarity because of the linear evolution of the momentum thickness, the collapse on a single curve of the mean velocity profiles and the collapse on a single curve of the Reynolds stress profiles. However, the determination of the proper superposition of several curves is sometimes difficult and may be subjective. The same remarks apply to the determination of the linear evolution of the momentum thickness. Analysis of data obtained by Pantano & Sarkar (2002), Rogers & Moser (1994) and Zhou *et al.* (2012) show that the growth rate is probably sub-linear, as also stated by Pirozzoli *et al.* (2015). Many authors confirmed the difficulty encountered to reach a perfect self-similar state (Pantano & Sarkar, 2002; Pirozzoli *et al.*, 2015). The diversity of results found in the literature for the well-known growth rate vs convective Mach number graph (see Section 3.3.2) comes in part from this difficulty to accurately define the growth rate.

Another method to determine self-similarity is used in this study. It consists in computing the streamwise production term integrated over the whole domain. Vreman *et al.* (1996*a*) indeed demonstrate the following relation between the volumetric streamwise production power ($\bar{\rho}P_{xx} = -\overline{\rho u_x'' u_y''}\frac{\partial \tilde{u}_x}{\partial y}$) and the momentum thickness growth rate:

$$\delta_\theta' = \frac{d\delta_\theta}{dt} = \frac{2}{\rho_0 \Delta u^2}\int \bar{\rho}P_{xx}dy \tag{3.12}$$

Figure 3.4 shows the temporal evolution of the non-dimensional streamwise production integrated over the whole domain for the three DNS at M_c ranging from 0.1 to 2.2 performed for air using the PG EoS. The selected self-similar periods are given on each graph and correspond to a converged state of the mixing layer. At $M_c = 1.1$, a long period has been chosen (about 900τ) in comparison with the available literature. Pantano & Sarkar (2002) and Rogers & Moser (1994) respectively selected in their study a period of 257 and 45 non-dimensional times.

The temporal evolution of the production is consistent with the temporal evolution of the momentum thickness. The three steps mentioned earlier can be identified. During the unstable growth, the production quickly increases, until it reaches a maximum. Afterwards, the mixing layer converges to a self-similar state. A constant integrated production is directly related to a self-similar regime according to Eq. (3.12). As the convective Mach number increases, the maximum peak of integrated turbulent production decreases, which is consistent with the decrease of the momentum thickness growth rate. Time required to achieve self-similarity lengthens.

Difficulties can be encountered to get a fully stable plateau with an almost constant integrated turbulent production. Domain lengths have a major influence on self-similarity. Influence of the domain size on self-similarity is thoroughly investigated in Appendix B for dense

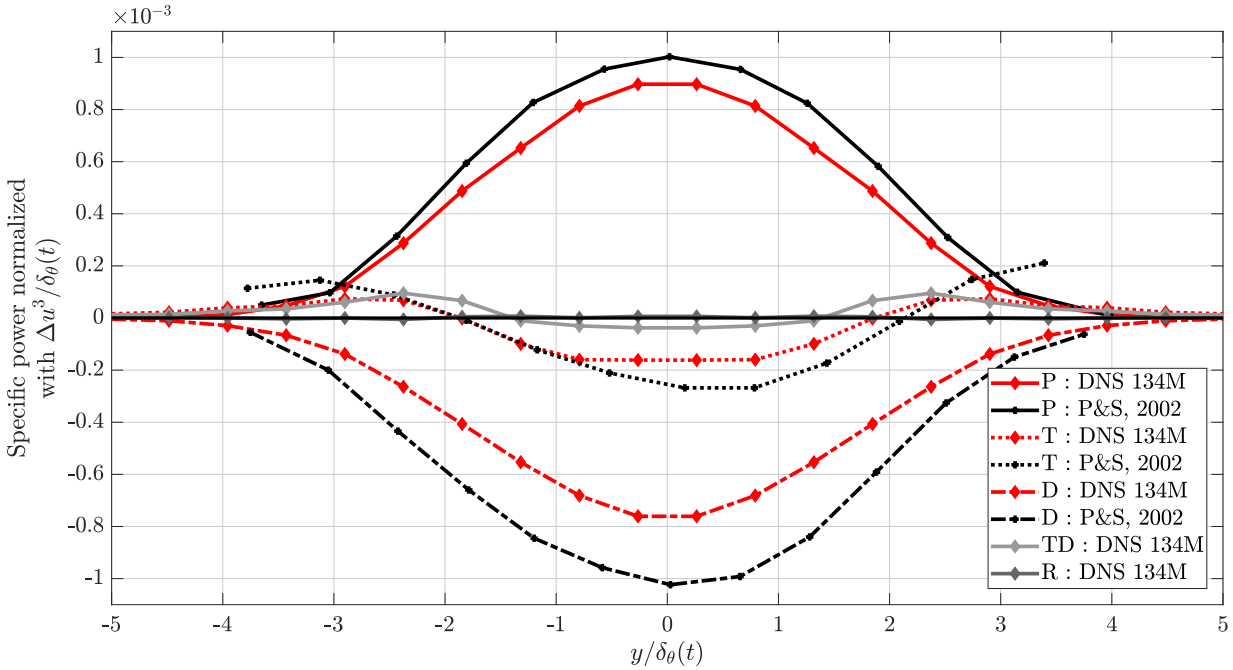

Figure 3.5: Distributions of the normalized specific power quantities over the y direction at $M_c = 1.1$ is represented for air: P: Production, D: Dissipation and T: Transport are normalized by $\Delta u^3/\delta_\theta(t)$ and compared to Pantano & Sarkar (2002). Additional terms (R: Residuals and TD: Time Derivative) are given. The sampling space step of the averaging process is $\frac{2L_y/\delta_\theta(\tau=1700)}{N_{points}}$, with $N_{points} = 24$. Distributions have been averaged between the upper and the lower stream to get perfectly symmetrical distributions. A further explanation about the averaging process applied is given in Appendix A.

gas flows and correlations with integral length scales are analyzed.

3.3.2 Validation over the self-similar period

Validation at $M_c = 1.1$

Once a relevant time interval selected to consider the mixing layer to be self-similar, one can focus on the study of the turbulent kinetic power balance. This equation evaluates terms at stake in the development of turbulence. It also helps to validate our simulation by comparing present DNS results with those of Pantano & Sarkar (2002) at $M_c = 1.1$. In Figure 3.5, quantities are integrated over the two periodic directions (x and z), normalized by $\Delta u^3/\delta_\theta(t)$ and drawn versus the non-dimensional cross-stream direction $y/\delta_\theta(t)$. Solutions are averaged over time during the self-similar period ($\tau \in [1700; 2550]$). A further explanation about the averaging process applied to generate the plot of Figure 3.5 is given in Appendix A.

The present DNS results agree reasonably well with Pantano & Sarkar (P&S) results, especially the production and the transport terms : shapes as well as intensities are close. The discrepancies between the dissipation terms could be explained by the difference in the choice or definition for the self-similar period.

Two additional quantities are also analyzed in Figure 3.5: the residuals and the time derivative of the turbulent kinetic energy. Residuals are almost zero, thus demonstrating the proper closure of the balance. The time derivative is far from being negligible and has almost the same intensity as the transport term. This term is rarely reported in the literature maybe because of the difficulties encountered when extracting it, especially for the temporal mixing layer. Also,

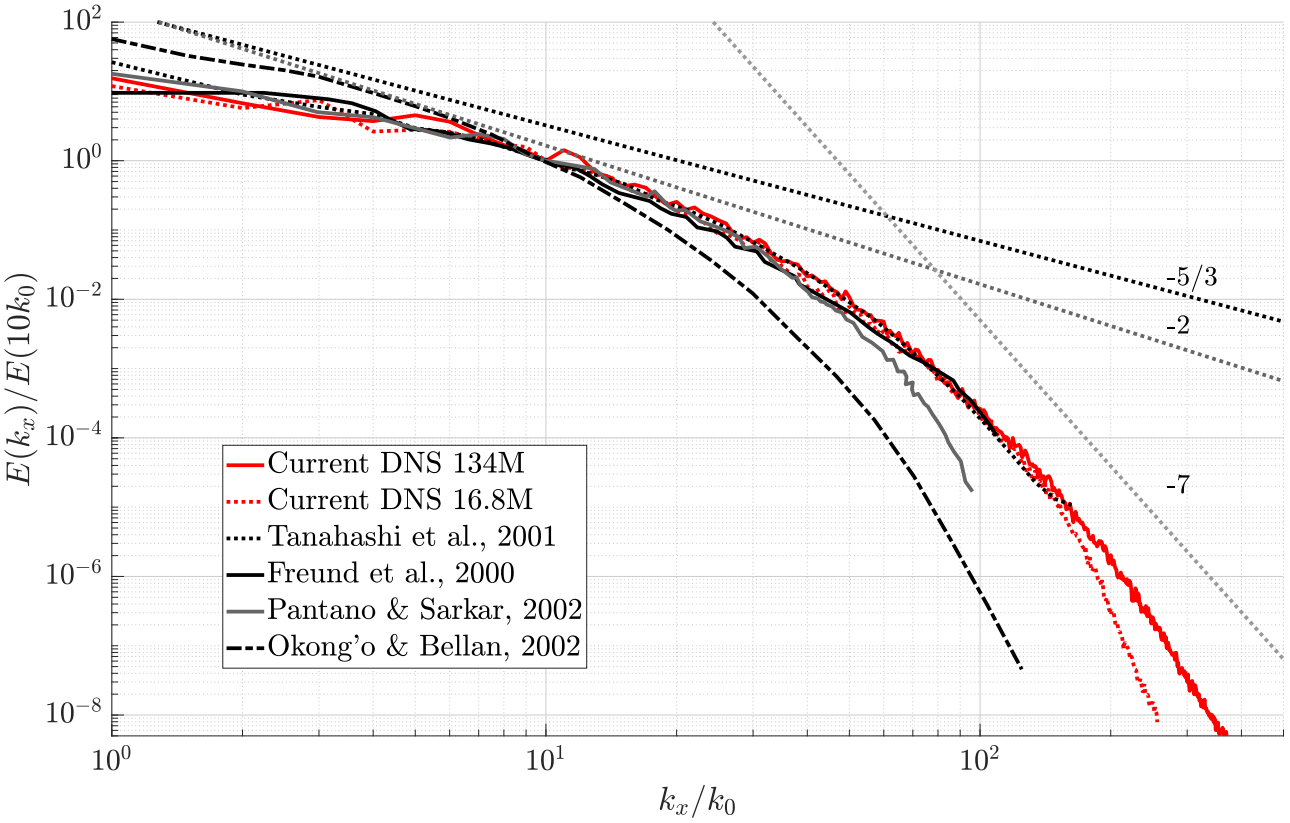

Figure 3.6: Streamwise specific TKE spectra computed over the centerline at $M_c = 1.1$. Comparison is made with the available literature and between the 16.8M and the 134M simulations.

the convective derivative is negligible, in contrast with Zhou *et al.* (2012) who study a spatial mixing layer. In fact, the time derivative of the kinetic energy in a temporal mixing layer and the convective derivative of the kinetic energy in a spatial mixing layer play a symmetric role since the two configurations are linked by a change of Galilean reference frame (see (3.4)). It is thus expected that the time derivative in the temporal mixing layer is non negligible in the same way that the convective derivative in the spatial mixing layer is significant.
Finally, it is noticed that the compressible dissipation, the pressure-dilatation, the mass-flux coupling term including the velocity pressure gradient, and the convective derivative are negligible in the present study and are thus not shown. Similar observations have been consistently made by several authors as previously mentioned in Section 3.1.

The turbulent kinetic energy balance computed over the whole range of turbulent scales is not the only tool available to highlight the influence of the main terms of the TKE equation. Spectra are very useful to compare turbulent kinetic energy scale by scale. At this stage, we wish to validate the spectrum computed for air. To this end, the present DNS results are compared in Figure 3.6 with results from the literature (Tanahashi *et al.*, 2001; Freund *et al.*, 2000; Pantano & Sarkar, 2002; Okong'o & Bellan, 2002). The current spectrum is computed over the centerline and averaged over the self-similar period ($\tau \in [1700; 2550]$). Because the spectra from the literature display different large scale values, they are normalized by their value at $10k_0$. This value is indeed a good threshold to compare spectra at small scales without being subjected to geometrical differences. The present results are found to compare favorably with the current literature and the expected reference slopes. The -7 slope in the logarithmic scale has been established by Batchelor (1953) to describe the evolution of kinetic energy at

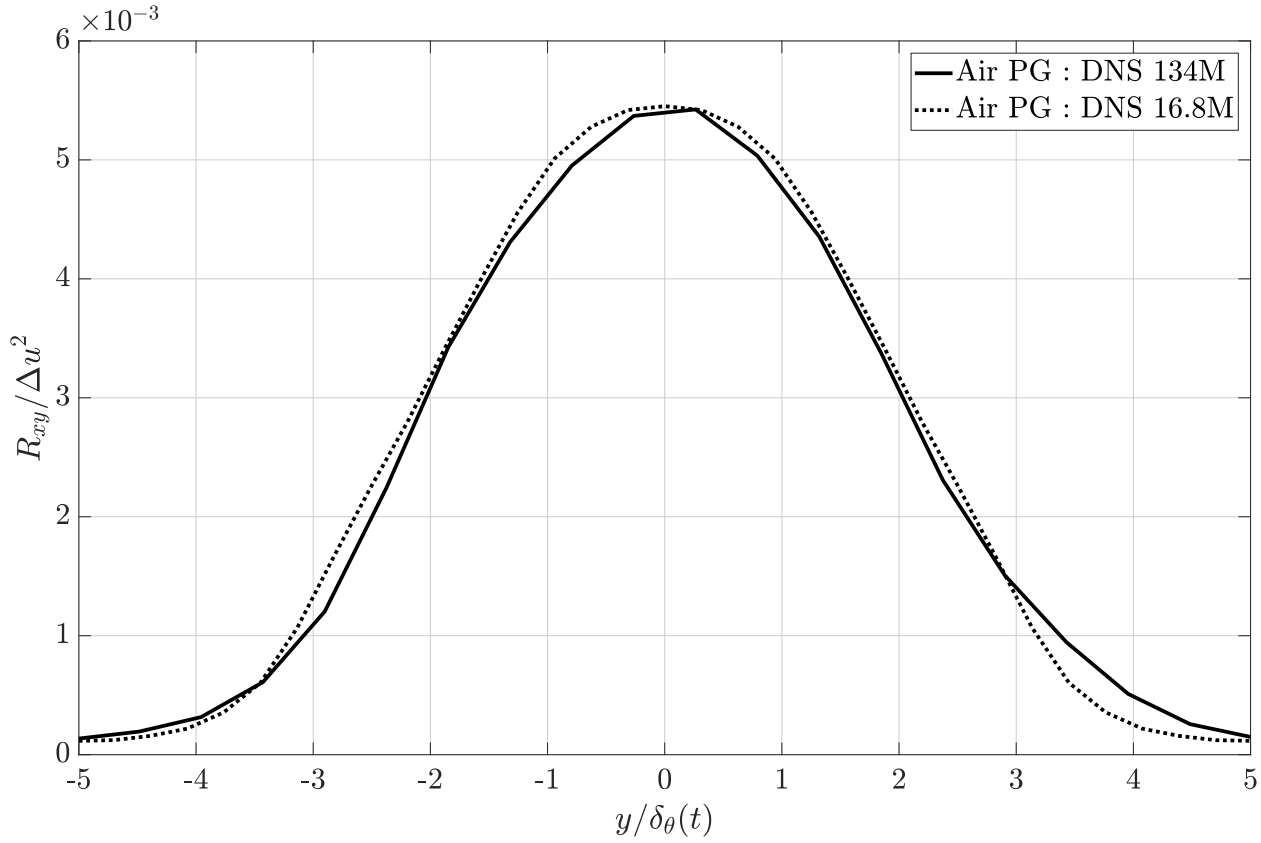

Figure 3.7: Distribution of the xy-component of the turbulent stress tensor ($R_{xy} = \overline{\rho u_x'' u_y''}/\bar{\rho}$) averaged over the self-similar period. Comparison is made between the 16.8M and the 134M simulations at $M_c = 1.1$. Distributions have been averaged between the upper and the lower stream to get perfectly symmetrical distributions.

small scales and is consistent with the present spectrum at high wavenumbers. This indicates a proper resolution of the small scales. The $-5/3$ and -2 slopes are the slopes of isothermal homogeneous isotropic turbulence inertial ranges respectively for incompressible and compressible flows (Kritsuk *et al.*, 2007). Moreover, the 16.8M and the 134M simulations spectra are very close. Discrepancies occur at very small scales only, where energy is very low. This shows that the energy decrease for the 16.8M simulations starts at $k_x/k_0 \approx 150$, corresponding to about 1/2 to 1/3 of the Nyquist–Shannon sampling frequency. This observation appears very reasonable, given the third-order spatial accuracy of the numerical scheme.

Figures 3.7 and 3.8 additionally confirm the quality of the present DNS. The $xy-$ components of the turbulent stress tensor computed for the 134M and for the 16.8M simulations during the self-similar period are found very close, demonstrating a proper grid convergence of the results. Figure 3.8 displays the vertical distribution of $r = L_\eta/\Delta x$ at different non-dimensional times within the self-similar range. The ratio r characterizes the resolution of simulations. The larger the ratio, the better the resolution. At the center of the mixing layer, the Kolmogorov length scale is at its minimum value since the turbulent activity is maximum. Values of r stay above unity, which is enough for DNS resolution. As a comparison Pantano & Sarkar (2002)'s ratio is close to 0.38.

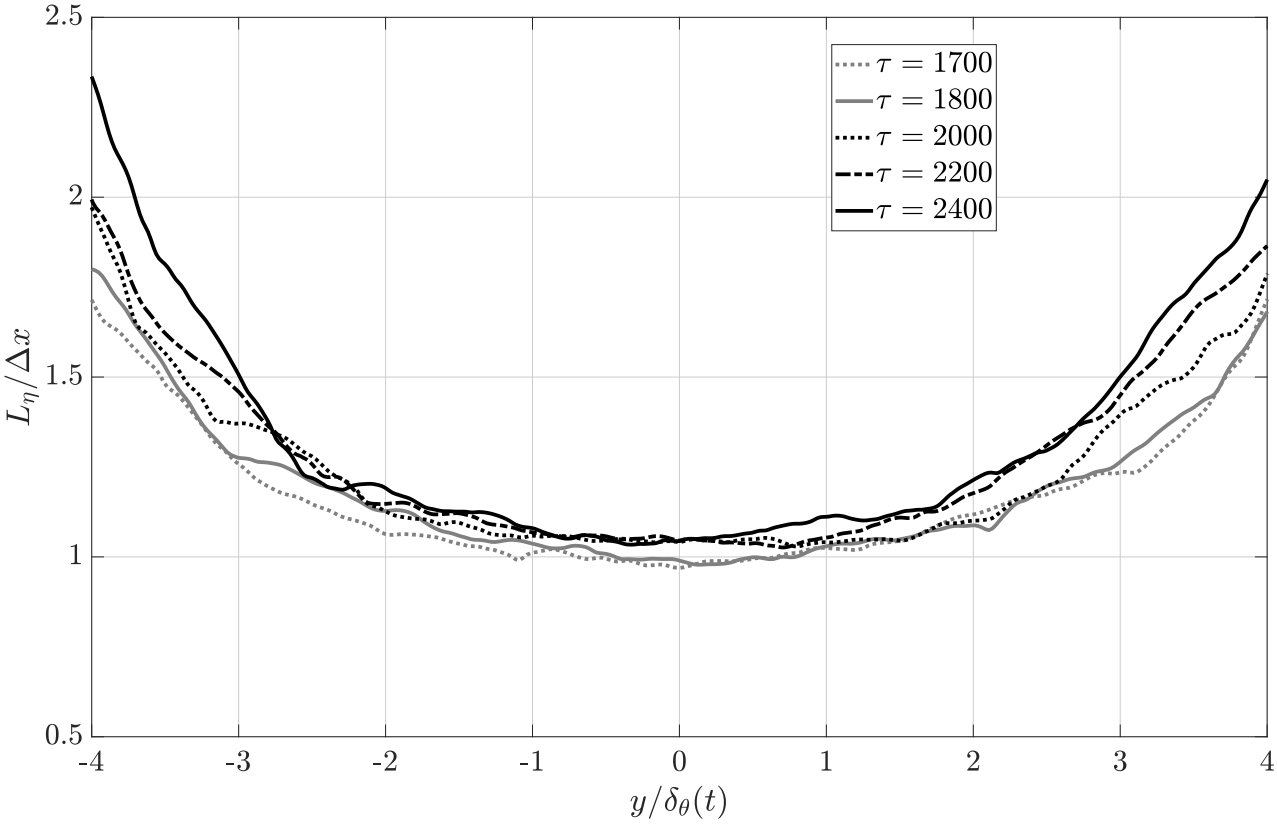

Figure 3.8: Distributions of $r = L_\eta/\Delta x$ the ratio between the Kolmogorov scale and the grid cell size at $M_c = 1.1$ for several non-dimensional times inside the self-similar period ($\tau \in \{1700; 1800; 2000; 2200; 2400\}$). Results are computed from the 134M simulation.

	M_c	Re_{δ_θ}	Re_{λ_x}	$r = L_\eta/\Delta x$	l_x/L_x	l_z/L_z
Air ($\tau = 700$)	0.1	1879	209	0.63	0.10	0.04
Air ($\tau = 1450$)	0.1	3444	194	0.81	0.11	0.13
Air ($\tau = 1700$)	1.1	1874	143	0.97	0.07	0.06
Air ($\tau = 2550$)	1.1	2413	156	1.09	0.12	0.08
Air ($\tau = 11500$)	2.2	3487	146	1.44	0.12	0.07
Air ($\tau = 14100$)	2.2	3700	191	1.64	0.11	0.10

Table 3.2: Non-dimensional parameters computed at the beginning and at the end of the self-similar period. Re_{λ_x} denotes the Reynolds number based on the longitudinal Taylor microscale $\lambda_x = \sqrt{2\overline{u'^2_x}/\overline{(\partial u'_x/\partial x)^2}}$ computed at the centerline. L_η denotes the Kolmogorov length scale computed at the centerline.

Validation at other convective Mach numbers

Results obtained in the present work using AVBP are validated thanks to available results from the literature at $M_c = 1.1$. At highly compressible regimes, the lack of numerical results makes the validation process more complex. Yet, numerical parameters given in Table 3.2 allow to assess the quality of the present DNS. The integral lengths l_x and l_z are computed using the streamwise velocity field:

$$l_x = \frac{1}{2\overline{u'^2_x}} \int_{-L_x/2}^{L_x/2} \overline{u'_x(\boldsymbol{x}) u'_x(\boldsymbol{x} + r\boldsymbol{e_x})} dr \tag{3.13}$$

$$l_z = \frac{1}{2\overline{u'^2_x}} \int_{-L_z/2}^{L_z/2} \overline{u'_x(\boldsymbol{x}) u'_x(\boldsymbol{x} + r\boldsymbol{e_z})} dr \tag{3.14}$$

Integral length scales show that the domain is chosen sufficiently large. Values do not exceed 0.12 in the streamwise direction and 0.13 in the z direction. As a comparison, Pantano & Sarkar (2002)'s integral length scale reaches 0.178 in the streamwise direction for a configuration with $M_c = 0.7$ and a density ratio of 4.

The ratio $r = L_\eta/\Delta x$ characterizes the resolution of the simulations. The larger the ratio, the better the resolution. Minimum value is about 0.63, computed for the DNS at $M_c = 0.1$. For other simulations, values are larger than 0.97 and the maximum value is 1.64 at $M_c = 2.2$ because of the smaller dissipation found in high compressible regimes. As a comparison, Matsuno & Lele (2020) recently performed a DNS at $M_c = 2.0$ with a L_η/dx ratio equal to 0.41. One can thus consider that turbulent scales are adequately resolved for all simulations presented in this paper since in addition the turbulent kinetic energy is very low close to the Kolmogorov scale (Moin & Mahesh, 1998*a*).

Since self-similar periods are well defined for each DNS, it is possible to plot the evolution of the mixing layer growth rate with respect to the convective Mach number. Figure 3.9 shows a comparison between current PG results and available numerical (Freund *et al.*, 2000; Pantano & Sarkar, 2002; Kourta & Sauvage, 2002; Fu & Li, 2006; Zhou *et al.*, 2012; Martínez Ferrer

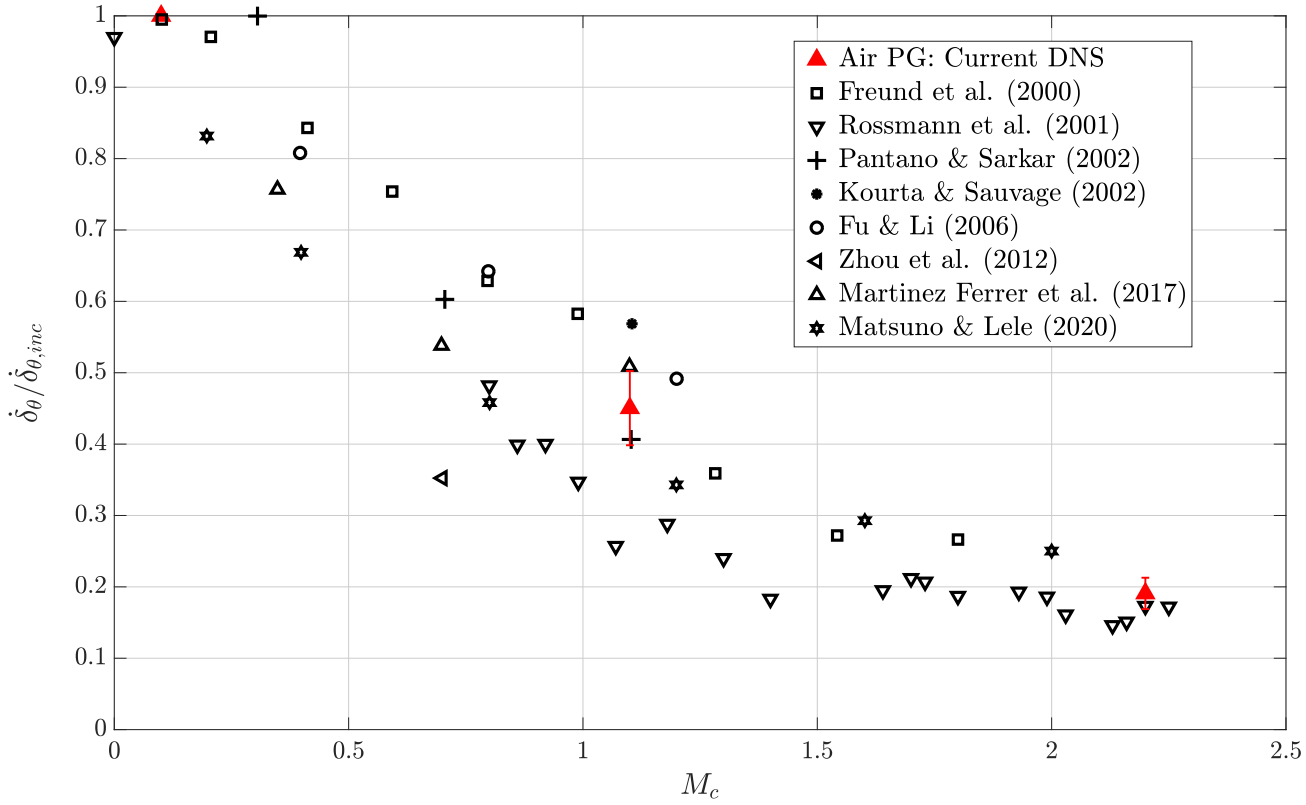

Figure 3.9: Evolution of the mixing layer growth rate with respect to the convective Mach number for air using PG EoS. Comparison is made with available DNS results in literature and experimental results by Rossmann *et al.* (2001). Standard deviations are indicated on the plot.

et al., 2017; Matsuno & Lele, 2020)] and experimental results (Rossmann *et al.*, 2001) from the literature. The current DNS follow the tendency observed and described in the literature, namely the well-known compressibility-related reduction of the momentum thickness growth rate as M_c increases. From the incompressible case to $M_c = 2.2$, the mixing layer growth rate is divided by a factor of about five. Standard deviations are computed and reported on the plot. It represents about 5% of the computed growth rates. It is rather difficult to reduce this uncertainty because of difficulties encountered in reaching perfect self-similarity. This is also illustrated by the scattering of the results from the literature, which might be a consequence of this phenomenon.

3.3.3 Concluding remarks

DNS of compressible mixing layers at convective Mach numbers $M_c = 0.1 - 1.1 - 2.2$ have been achieved for air described as a perfect gas. Results are compared with available results from the literature in order to demonstrate the quality of the present DNS before moving to the perfect versus dense gas comparison and the identification of dense gas turbulence specificities (see Chapter 4).

The selection of the self-similar period is a key point in the study of mixing layers: this choice remains complex and the diversity of the criteria used for the selection process contributes to the diversity of the results obtained in the literature (also translating into the scattering of $\dot{\delta}_\theta = f(M_c)$ results). Care has been taken in the present study to reach a well-justified selection of this self-similar period, based on the analysis of the integrated streamwise production over

time, which is proportional to the momentum thickness growth rate under certain conditions (Vreman *et al.*, 1996*a*).

The sensitivity of the results to mesh refinement is also investigated. The comparison of the present results obtained for air with the previous DNS of Pantano & Sarkar (2002) shows a good agreement and validates the present DNS of a compressible mixing layer in air described with the perfect gas EoS at $M_c = 0.1 - 1.1 - 2.2$. In addition to the validation of the present DNS using PG EoS, an analysis of the influence of the domain size, the resolution and the size of initial turbulent structures is provided for the DG mixing layer in Appendix B.

Chapter 4

DNS of dense gas compressible mixing layers: analysis and comparison with perfect gas

Contents

2.1 Navier-Stokes equations 11
2.2 Thermodynamic models 12
2.2.1 Equations of state 12
2.2.2 Transport coefficients models 13
2.3 Non-dimensional formulation 14
2.3.1 General formulation 14
2.3.2 Perfect gas analysis 15
2.3.3 Dense gas analysis 16
2.4 LES governing equations 20
2.4.1 Preliminary discussion 20
2.4.2 Filter 22
2.4.3 Real gas formulation 24
2.4.4 Perfect gas formulation 25
2.4.5 A summary of SGS terms 27
2.4.6 Basic LES models 27
2.5 Numerical solver 31

THE present chapter investigates the effects of a BZT dense gas (FC-70) on the development of turbulent compressible mixing layers at three different convective Mach numbers $M_c = 0.1$, 1.1 and 2.2. The first section completes the problem formulation presented in the previous chapter for PG: the choice of initial conditions for DG is explained and non-dimensional numbers introduced in Section 2.3 are computed for PG and DG and compared between both types of gases. The next two sections are dedicated to the comparison between PG and DG mixing layers: first, at $M_c = 1.1$ and then extended to a larger compressibility regime at $M_c = 2.2$. Finally, discrepancies between both types of gases are thoroughly analyzed in Section 4.4. The DG results presented in this chapter have been published in (Vadrot *et al.*, 2020) and (Vadrot *et al.*, 2021).

4.1 Problem formulation

4.1.1 Initialization

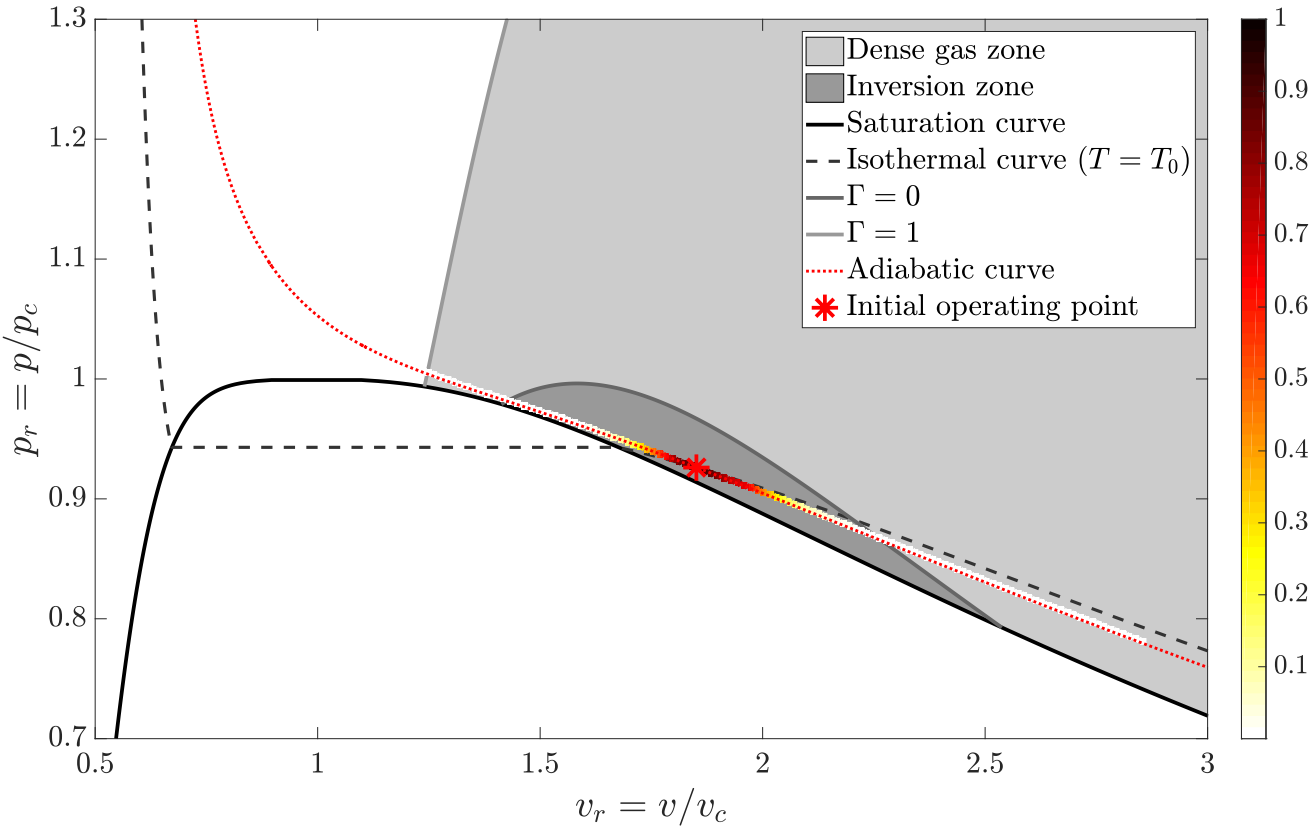

Figure 4.1: The initial thermodynamic state and its evolution over time are represented in the non-dimensional $p - v$ diagram for FC-70 at $M_c = 1.1$. The dense gas zone ($\Gamma < 1$) and the inversion zone ($\Gamma < 0$) are plotted for the Martin-Hou equation of state. p_c and v_c are respectively the critical pressure and the critical specific volume. The initial value of the fundamental derivative of gas dynamics is equal to $\Gamma_{initial} = -0.284$. The normalized distribution of thermodynamic states at $\tau = 1700$ (beginning of the self-similar period) is colored along the corresponding adiabatic curve.

The initial conditions of the mixing layer require the choice of the initial operating thermodynamic point in the $p-v$ diagram. In order to compare DG and PG mixing layers in identical initial conditions, the same values of reduced specific volume and reduced pressure defining the initial thermodynamic state are selected for both gases. As described in Figure 4.1, this initial state is chosen within the inversion zone of FC-70 in order to favor the occurrence of expansion shocklets and to maximize dense gas effects on turbulence. This is also in that region that compressibility effects are the largest since the sound speed is reduced (Colonna & Guardone, 2006), which maximizes the Mach number. Figure 4.1 also shows the adiabatic curve on which the initial operating point is lying in the non-dimensional $p - v$ diagram. The corresponding initial value of the fundamental derivative of gas dynamics is equal to $\Gamma_{initial} = -0.284$. During the development of the mixing layer, the thermodynamic conditions stay within a close range around the adiabatic curve as shown in Figure 4.1, because shocklet entropy losses and mechanical dissipation are weak at $M_c = 1.1$. Also, almost all the thermodynamic states stay within the inversion zone throughout the dense gas simulation. The evolution of thermodynamic states is investigated during the unstable growth phase in Section 4.2.2.

Like for PG flow, the Reynolds number based on the initial momentum thickness is set equal to 160 for all the DNS. Table 3.1 summarizes the computational parameters of simulations performed for different M_c (domain size, number of grid elements, dimensional values of velocity, initial momentum thickness and initial turbulent structures sizes). Domains lengths are identical between air and FC-70 at $M_c = 0.1$ and $M_c = 1.1$. At $M_c = 2.2$, the domain length is doubled in the y direction for air compared with FC-70 in order to let the flow evolve long enough to reach self-similarity without interference effects of the lower and upper boundaries. For both types of gas, the size of initial turbulent structures is increased at $M_c = 2.2$ in order to shorten the simulation time. At $M_c = 1.1$, two simulations have been computed for both gases in order to study grid convergence. Additional DG simulations given in Appendix B have been performed for other domain sizes and resolutions to validate the current DNS. The impact of these numerical parameters on the self-similar period selection is also analyzed in Appendix B.

	M_c	$L_x \times L_y \times L_z$	$N_x \times N_y \times N_z$	Δu $(m.s^{-1})$	$\delta_{\theta,0}$ (nm)	L_0
Air	0.1	$344 \times 344 \times 86$	$1024 \times 1024 \times 256$	34.11	135.8	$L_x/48$
FC-70	0.1	$344 \times 344 \times 86$	$1024 \times 1024 \times 256$	5.665	2070	$L_x/48$
Air	1.1	$344 \times 172 \times 86$	$512 \times 256 \times 128$	375.2	12.35	$L_x/48$
Air	1.1	$344 \times 172 \times 86$	$1024 \times 512 \times 256$	375.2	12.35	$L_x/48$
FC-70	1.1	$344 \times 172 \times 86$	$512 \times 256 \times 128^{\dagger}$	62.32	188.2	$L_x/48$
FC-70	1.1	$344 \times 172 \times 86$	$1024 \times 512 \times 256^{\dagger\dagger}$	62.32	188.2	$L_x/48$
Air	2.2	$688 \times 688 \times 172$	$1024 \times 1024 \times 256$	753.0	6.153	$L_x/8$
FC-70	2.2	$688 \times 344 \times 172$	$1024 \times 512 \times 256$	125.1	93.77	$L_x/8$

Table 4.1: Simulation parameters. L_x, L_y and L_z denote computational domain lengths measured in terms of initial momentum thickness. N_x, N_y and N_z denote the number of grid points. L_0 denotes the size of initial turbulent structures ($k_0 = 2\pi/L_0$) measured in terms of initial momentum thickness. All grids are uniform.

4.1.2 Non-dimensional numbers in the DG context

The non-dimensional formulations of the governing equations have been presented in Section 2.3 for both PG and DG flows. The reference values used in these formulations are now adapted to the mixing layer problem: the reference length is the initial momentum thickness, $L_0 = \delta_{\theta,0}$; the reference density, pressure, temperature, viscosity and sound speed correspond to the initial values ρ_0, p_0, T_0, μ_0 and c_0; the reference velocity is also the initial velocity $u_0 = \Delta u/2^{\dagger}$. The

†Referred to as the $16.8M$ simulation. $16.8M$ corresponds to the number of grid cells.
††Referred to as the $134M$ simulation. $134M$ corresponds to the number of grid cells.
†The subscript ϕ_0 for a given variable ϕ denotes the initial value.

non-dimensional numbers appearing in the governing equations are therefore such that:

$$M_0 = \frac{u_0}{c_0} = \frac{\Delta u}{2c_0} = M_c \tag{4.1}$$

$$Re_0 = \frac{\rho_0 u_0 L_0}{\mu_0} = \frac{\rho_0 \Delta u \delta_{\theta,0}}{2\mu_0} = \frac{Re_{\delta_{\theta,0}}}{2} \tag{4.2}$$

Table 4.2 compares non-dimensional coefficients appearing in Equations (2.23) and (2.34) modified using the relationships (4.1) and (4.2). These coefficients are computed for each mixing layer, with varying convective Mach number but constant Reynolds number. Note that non-dimensional momentum equations are written in such a way that the coefficients related to the temporal variation and the transport of the momentum are equal to unity (see Equations (2.23)). For the energy equation, the coefficients related to the temporal variation and the transport of the internal energy are equal to unity (see Equations (2.23)) and are not provided in Table 4.2.

For momentum equations, ratios between non-dimensional terms are very close between DG and PG flows unlike the energy equation. Differences between both types of gases are indeed expected to appear in compressible flows where the energy equation gains in influence. In the energy equation, all terms except the heat flux are reduced for DG with respect to PG. Since DG are characterized by long chains of atoms and by medium to large molecular weights, their internal energy is much larger than the kinetic energy when compared to PG flows. This difference is responsible for the strong reduction of the transport and temporal variation of the kinetic energy, the pressure work and the viscous work with respect to the temporal and convective derivatives of the internal energy. This phenomenon and its consequences on the mixing layer turbulence characteristics are further analyzed in Section 4.4. Note that for some terms (especially the ones depending on the ratio M_c^2/Ec_0), because the initial thermodynamic operating points are identical, no difference is observed between the three DNS computed at $M_c = 0.1 - 1.1 - 2.2$. That will not remain true when modifying the initial thermodynamic operating point like in Section 4.4.3.

Momentum equations	PG ($M_c = 0.1 - 1.1 - 2.2$)	DG ($M_c = 0.1 - 1.1 - 2.2$)
$\frac{\partial p}{\partial x_i}$	$\frac{1}{\gamma}$ (0.71)	$\frac{Z_0 M_c^2}{Ec_0}\frac{R}{c_{p_0}}$ (0.89)
$\frac{\partial}{\partial x_j}\left(\mu S_{ij}^D\right)$	$\frac{2M_c}{Re_{\delta_\theta}}$ $(0.125 - 1.38 - 2.75) \times 10^{-2}$	$\frac{2M_c}{Re_{\delta_\theta}}$ $(0.125 - 1.38 - 2.75) \times 10^{-2}$
Energy equation	**PG ($M_c = 0.1 - 1.1 - 2.2$)**	**DG ($M_c = 0.1 - 1.1 - 2.2$)**
$\left[\frac{\partial(\rho u_i u_i)}{\partial t} + \frac{1}{2}\frac{\partial(\rho u_i u_i u_j)}{\partial x_j}\right]$	$\gamma(\gamma - 1)$ (0.56)	$\frac{K_0 Ec_0}{M_c^2}\frac{(c_p)_0}{R}$ (0.0066)
$\frac{\partial(p u_j)}{\partial x_j}$	$(\gamma - 1)$ (0.4)	$Z_0 K_0$ (0.0059)
$\frac{\partial}{\partial x_j}\left(\mu u_i S_{ij}^D\right)$	$\gamma(\gamma - 1)\frac{2M_c}{Re_{\delta_\theta}}$ $(0.07 - 0.77 - 1.54) \times 10^{-2}$	$\frac{K_0 Ec_0}{M_c^2}\frac{(c_p)_0}{R}\frac{2M_c}{Re_{\delta_\theta}}$ $(0.08 - 0.91 - 1.82) \times 10^{-4}$
$\frac{\partial}{\partial x_j}\left(\kappa\frac{\partial T}{\partial x_j}\right)$	$\frac{\gamma}{Pr_0}\frac{2M_c}{Re_{\delta_\theta}}$ $(0.25 - 2.71 - 5.42) \times 10^{-2}$	$\frac{K_0}{Pr_0}\frac{(c_p)_0}{R}\frac{2M_c}{Re_{\delta_\theta}}$ $(0.16 - 1.81 - 3.65) \times 10^{-2}$

Table 4.2: Comparison of the PG and DG non-dimensional terms appearing in Equations (2.23) and (2.34).

4.2 Dense gas effect at $M_c = 1.1$

4.2.1 Temporal evolution and selection of the self-similar period

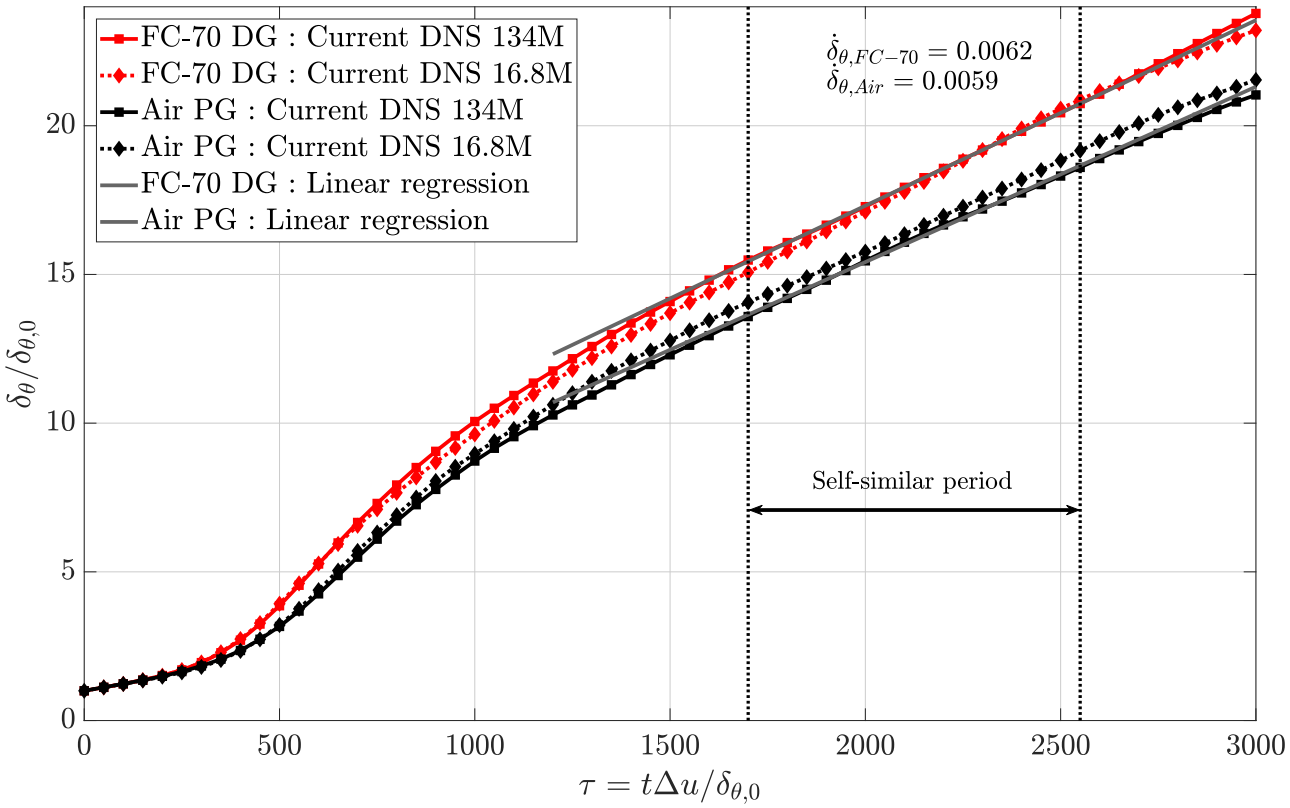

Figure 4.2: Temporal evolution of the mixing layer momentum thickness at $M_c = 1.1$.

As done for the perfect gas validation process, the computation of the turbulent kinetic energy balance requires first the selection of the self-similar range. This is achieved through the combined investigation of the momentum thickness evolution and the integrated production evolution over time. Figure 4.2 displays the momentum thickness temporal evolution: perfect gas (PG) and dense gas (DG) results show a similar evolution. The curves are initially ($\tau \leq 200$) very close, with a different evolution for PG and DG mixing layers taking place in the second phase of the mixing layer development (approximately $200 \leq \tau \leq 1500$), when the unstable growth is governed by instability modes. The DG unstable growth is faster than the PG one, likely because instability modes and their amplification factor evolve differently for PG and DG mixing layers (Gloerfelt *et al.*, 2020). Figure 4.2 also displays the evolution of the DG momentum thickness for the 16.8M simulation, which is very close to the 134M simulation, showing a proper resolution.

Figure 4.3 displays the integrated production. The DG turbulent production is found to be larger than the PG production, consistently with the larger DG momentum thickness growth rate. Although the unstable evolution is faster for the dense gas mixing layer, both mixing layers reach a self-similar stage almost at the same time as confirmed in Figure 4.3. It seems that the DG mixing layer displays an extended converged self-similar state compared with the PG mixing layer. The choice has however been made in the current study to select a common self-similar range, namely $\tau \in [1700; 2550]$. The growth rate slopes calculated during the self-similar stage are reported in Figure 4.2: the slope is slightly larger for the DG than for the PG

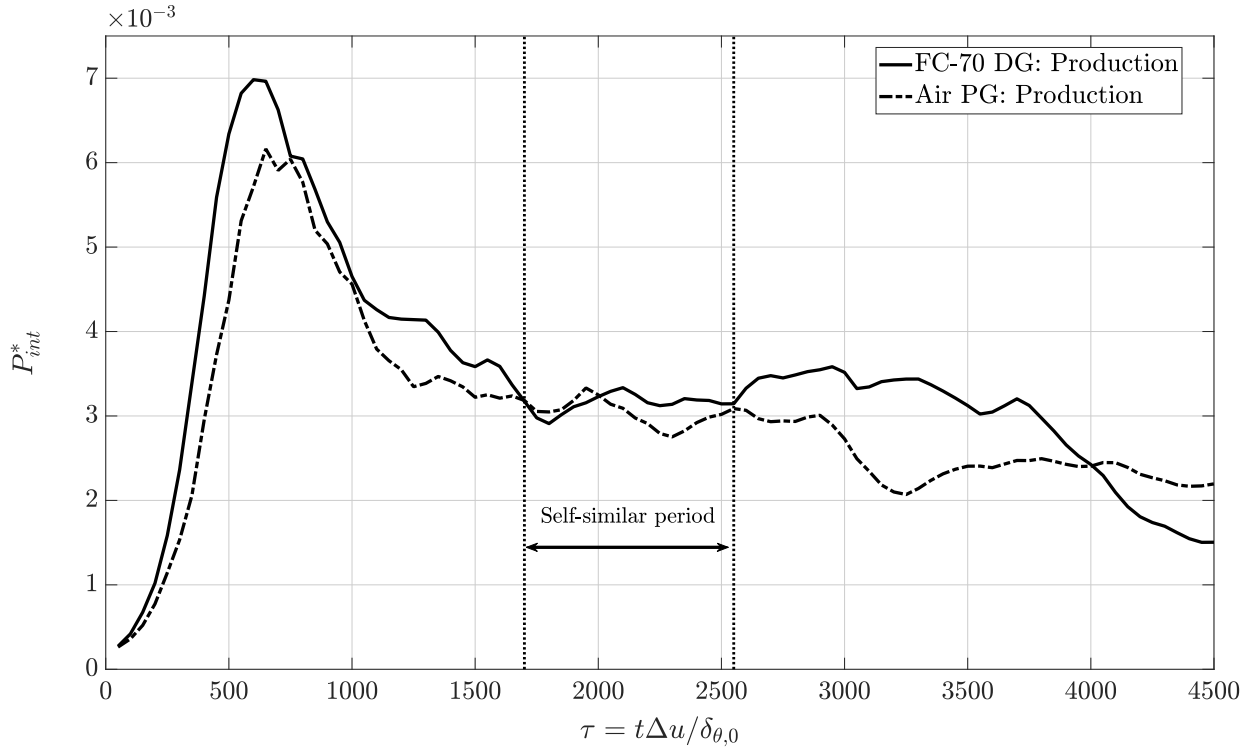

Figure 4.3: Temporal evolution of the non-dimensional streamwise production integrated over the whole domain, respectively $P^*_{int} = (1/(\rho_0 \Delta u^3)) \int_{L_y} \bar{\rho} P_{xx} dy$ (with $\bar{\rho} P_{xx} = -\overline{\rho u''_x u''_y} \frac{\partial \tilde{u}_x}{\partial y}$). Results are computed from the 134M simulations at $M_c = 1.1$.

with a typical 5% difference between DG and PG mixing layers.

From the above analysis, the comparison between the DG and the PG mixing layers at $M_c = 1.1$ can be divided into two main parts: the initial unstable growth during which differences between the two mixing layers are significant and the self-similar range, where the mixing layers dynamic seems rather close.

4.2.2 DG effect over the unstable growth phase at $M_c = 1.1$

During the unstable growth, the momentum thickness evolution is governed by instability modes and their amplification mechanism. A larger growth is directly related to a larger production term according to Vreman *et al.* (1996*a*). The streamwise production term is composed of the Favre averaged velocity gradient and the turbulent stress tensor. The comparison of the first term does not show significant differences between DG and PG, unlike the second term. Figure 4.4 displays the distributions of the $xy-$ component of the turbulent stress tensor $R_{xy} = \overline{\rho u''_x u''_y}/\bar{\rho}$ normalized by Δu^2 along the normalized cross-stream direction $y/\delta_\theta(t)$ during the initial growth. The DG $xy-$ component of the turbulent stress tensor increases much faster than the PG one until $\tau \approx 500$. Afterwards, both tensors reach the same level at $\tau \approx 1000$. This observation is consistent with the temporal evolution of the integrated streamwise production term.

In order to better understand the difference of dynamics between PG and DG, the comparison of PG and DG mixing layers during the unstable growth is investigated thanks to the specific TKE spectra. Spectra reported in Figure 4.5 are computed along the centerline in the streamwise direction. One can notice the sudden increase of the specific turbulent kinetic

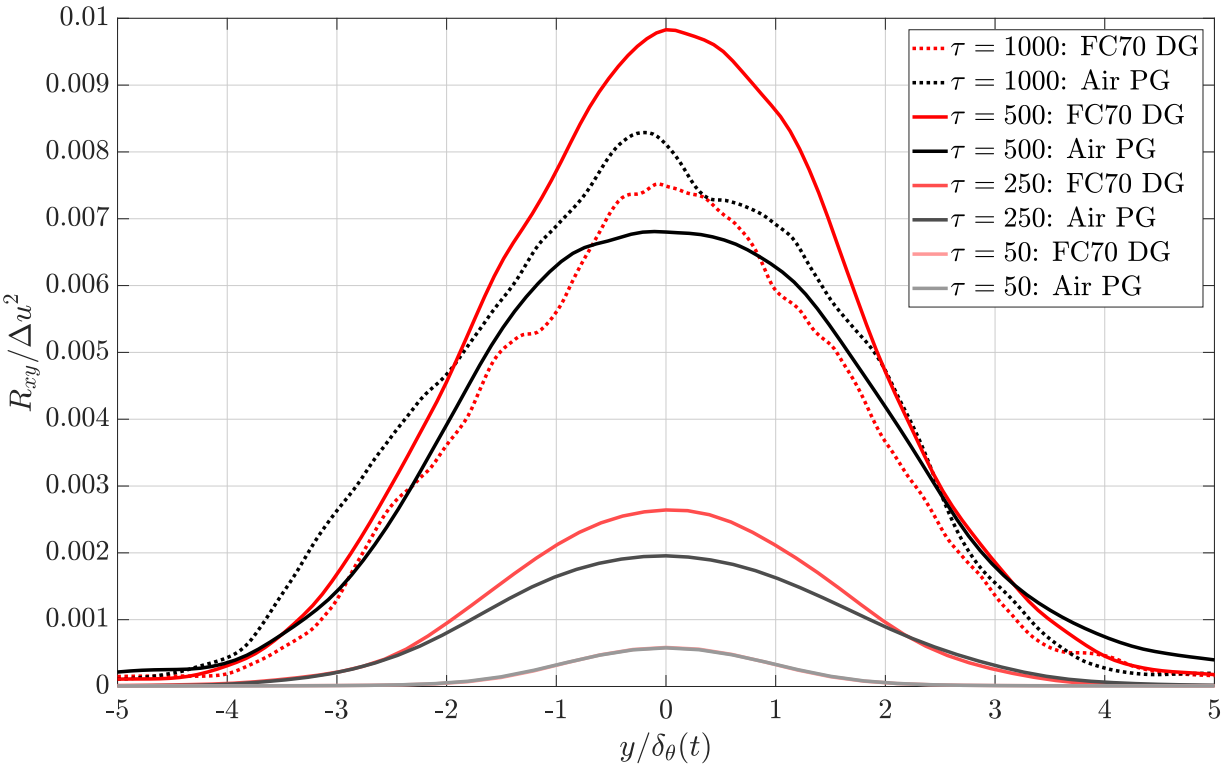

Figure 4.4: Distribution of the xy-component of the turbulent stress tensor ($R_{xy} = \overline{\rho u_x'' u_y''}/\bar{\rho}$) over the non-dimensional direction $y/\delta_\theta(t)$. Results are computed from the 134M simulation at $M_c = 1.1$. The curves for FC-70 and Air at $\tau = 50$ collapse.

energy at the smallest scales for the dense gas. Consistently with observations made for DNS of forced homogeneous isotropic turbulence (Giauque *et al.*, 2020) in a dense gas, the dynamic at the smallest scales is different between PG and DG.

This increase is not likely to explain the different unstable growth phase between dense and perfect gases because this region of the spectrum corresponds to low-energy modes. However, in the approximate range $k_x/k_0 \in [10; 22]$, energy is much larger for the DG when compared to the PG (a factor between 2 and 3 is found). These modes are high-energy modes and are responsible for the difference between the DG and the PG during the unstable growth phase.

Moreover, since it is known that shocklets generation is different between DG and PG flows (see Section 1.2), another explanation can be found using the evolution of the turbulent Mach number M_t[†], displayed in Figure 4.6 for FC-70 and air. Turbulent Mach numbers increase during the unstable growth phase until $M_t \approx 0.53$. Evolutions for DG and PG are very close during this first phase, with a slightly larger value for the dense gas, which is consistent with the evolutions of the turbulent production (see Figure 4.3). Turbulent Mach numbers then decrease and reach an approximately constant value during the self-similar period. Average values are almost equal for dense gas and perfect gas ($M_{t_{av,DG}} \approx 0.38 < M_{t_{av,PG}} \approx 0.39$).

Shocklets might be observed for a short period of time during the unstable growth phase ($\tau \in [500; 750]$), which corresponds to the period of time during which discrepancies appear between DG and PG (see Figure 4.2). During this short period of time, even though the values of the turbulent Mach number are almost the same for DG and PG, their effect on the mixing layer growth is different. Since the majority of the thermodynamic states lie inside the inversion region (see Figures 4.1 and 4.7), expansion shocklets could be one reason for discrepancy

[†]The expression of the turbulent Mach number is given in Section 3.1.

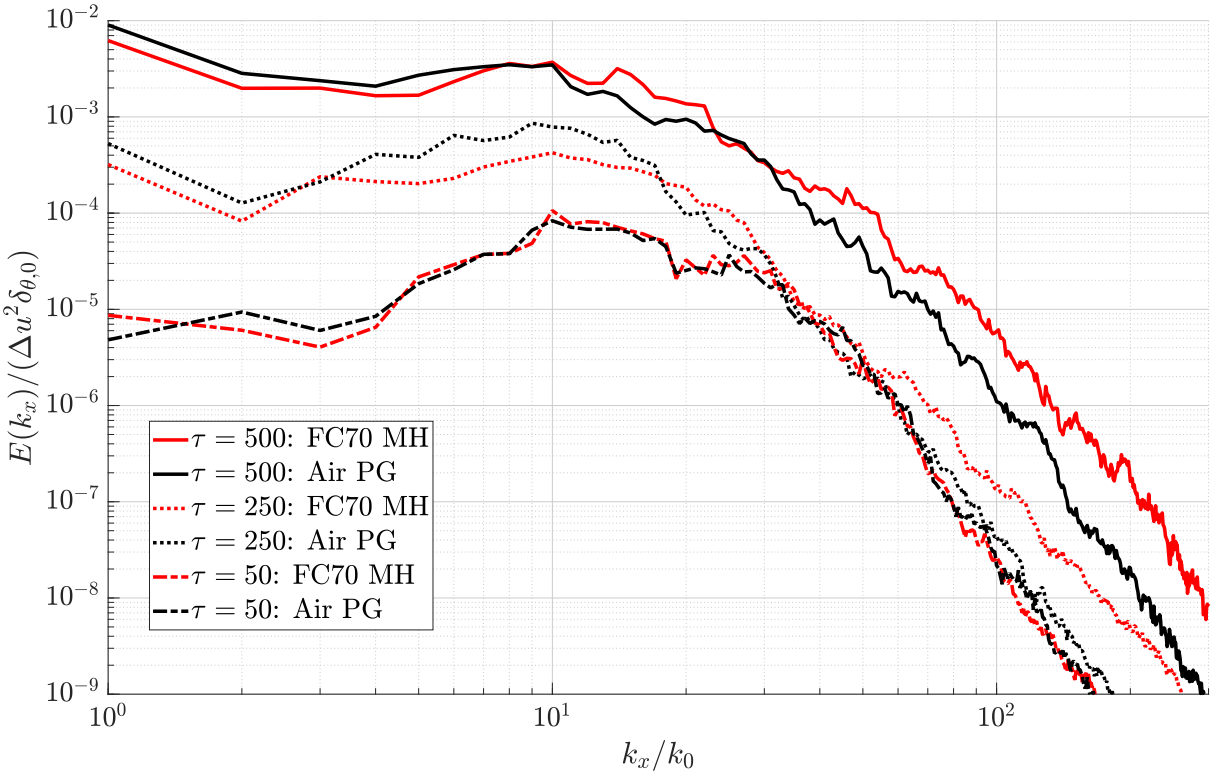

Figure 4.5: Specific turbulent kinetic energy spectra in the streamwise direction computed over the centerline during the unstable growth phase. Results are computed from the 134M simulation at $M_c = 1.1$.

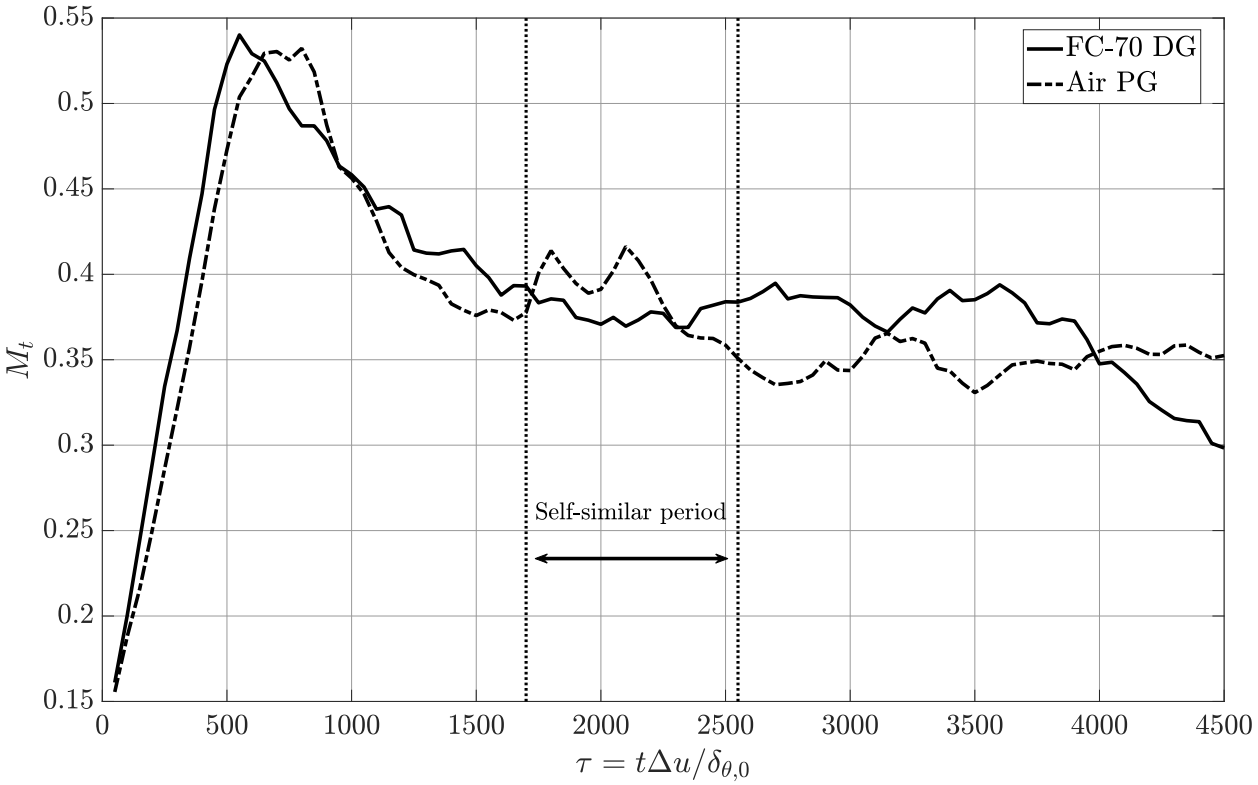

Figure 4.6: Temporal evolution of turbulent Mach number. Results are computed from the 134M simulation at $M_c = 1.1$.

between DG and PG. However, since it represents a very short period of time after which M_t decreases well below the range of values for which shocklets are expected, it is not likely to influence the self-similar period. In order to study the shocklet effect over the mixing layer growth, additional DNS are performed at larger M_c and for other operating thermodynamic point in Section 4.4.1.

4.2.3 DG effect over the self-similar period at $M_c = 1.1$

Distribution of thermodynamic states

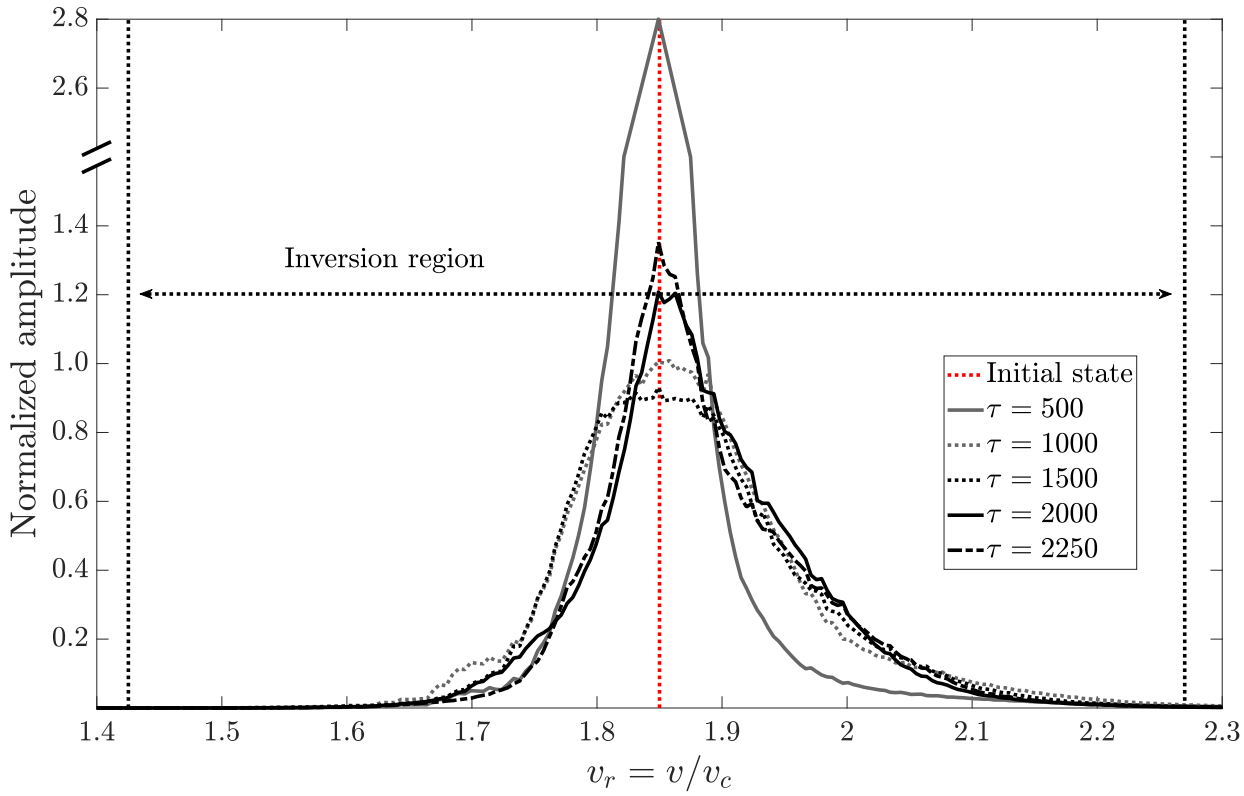

Figure 4.7: Distribution of thermodynamic states along the initial adiabatic curve. Amplitude is normalized with the maximum value at $\tau = 1000$. Results are computed from the 134M simulation at $M_c = 1.1$.

Before analyzing the TKE equation, it can be checked, in order to maximize the differences between dense and perfect gases, that the dense gas mixing layer thermodynamic states stay inside the inversion region in the $p - v$ diagram. Figure 4.7 represents the thermodynamic states distributions on the adiabatic curve normalized by the maximum value at $\tau = 1000$. One can note that almost all the thermodynamic states stay indeed inside the inversion region all along the development of the mixing layer. Also, the distributions seem to become asymmetric towards larger reduced molar volumes (v_r) which corresponds to a decrease of the reduced pressures (p_r) in Figure 4.1.

Turbulent kinetic energy balance computed over the self-similar period

During the self-similar period ($\tau \in [1700; 2550]$), both DG and PG mixing layers are in a statistically stable state and the terms of the TKE equation can be averaged. Consistently with the

evolution of the integrated production shown in Figure 4.3 and with the formulation of Vreman *et al.* (1996*a*), powers reported in Figure 4.8 are volumetric unlike in Figure 3.5 which shows the comparison with Pantano & Sarkar (2002). Using the volumetric or the specific power formulation influences the comparison between DG and PG. The difference between the two formulations can be more easily expressed by a normalization with either ρ_0 or $\bar{\rho}$, respectively for the volumetric and for the specific powers. For the DG, the difference between both formulations is reduced compared with the PG. The decrease of the Reynolds averaged density over the y direction is indeed lower for the DG than for the PG. It is likely that the large heat capacity of the DG reduces the temperature increase related to the viscous dissipation, which also reduces the density decrease and thus the difference between the volumetric and specific power formulations (see the thermodynamic distributions in Figure 4.13).

Figure 4.8 displays the comparison of the main volumetric turbulent kinetic energy budget

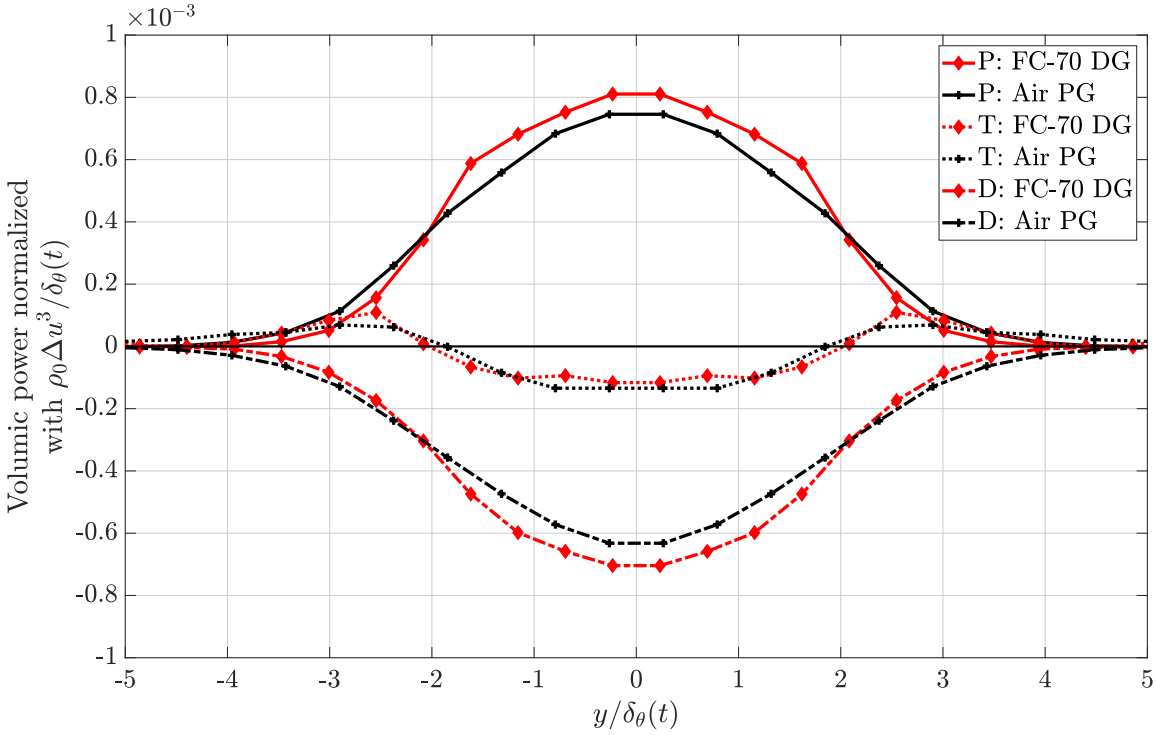

Figure 4.8: Distribution of the volumetric normalized powers over the non-dimensional cross-stream direction $y/\delta_\theta(t)$ at $M_c = 1.1$. P: Production, D: Dissipation and T: Transport are normalized by $\rho_0\Delta u^3/\delta_\theta(t)$. Results are gathered from the 134M simulation. The sampling space step for the averaging process is $\frac{2L_y/\delta_\theta(\tau=1700)}{N_{points}}$, with $N_{points} = 24$. Distributions have been averaged between the upper and the lower streams to get perfectly symmetrical distributions.

terms between the perfect gas and the dense gas mixing layers. Production, dissipation and transport terms are averaged during corresponding self-similar ranges. The production term (denoted P) is always positive and is responsible for the growth of the mixing layer. Viscous dissipation (denoted D) is always negative and counterbalances the production term. The transport term (denoted T) enables the propagation of TKE from the center to the edges of the mixing layer. It is thus negative at the center and positive close to the edges. Results are close between the two types of gases. The production term is slightly larger for the DG when compared to the PG, which is consistent with Figure 4.3 and with the 5% larger momentum growth rate. The dissipation is also greater for the DG in order to counterbalance the turbulent production. The transport term is almost identical between DG and PG. The pressure

transport and turbulent transport terms (not shown) are close between both types of gases (the viscous transport is negligible). The dense gas seems to have a limited effect on these turbulent quantities at $M_c = 1.1$. However, one can highlight a slower propagation of the TKE terms at the boundaries of the mixing layer as a visible effect induced by the dense gas: the curves are slightly wider for the PG with respect to the DG. The observation of this effect is confirmed by the distributions of the mean axial velocity in Figure 4.10.

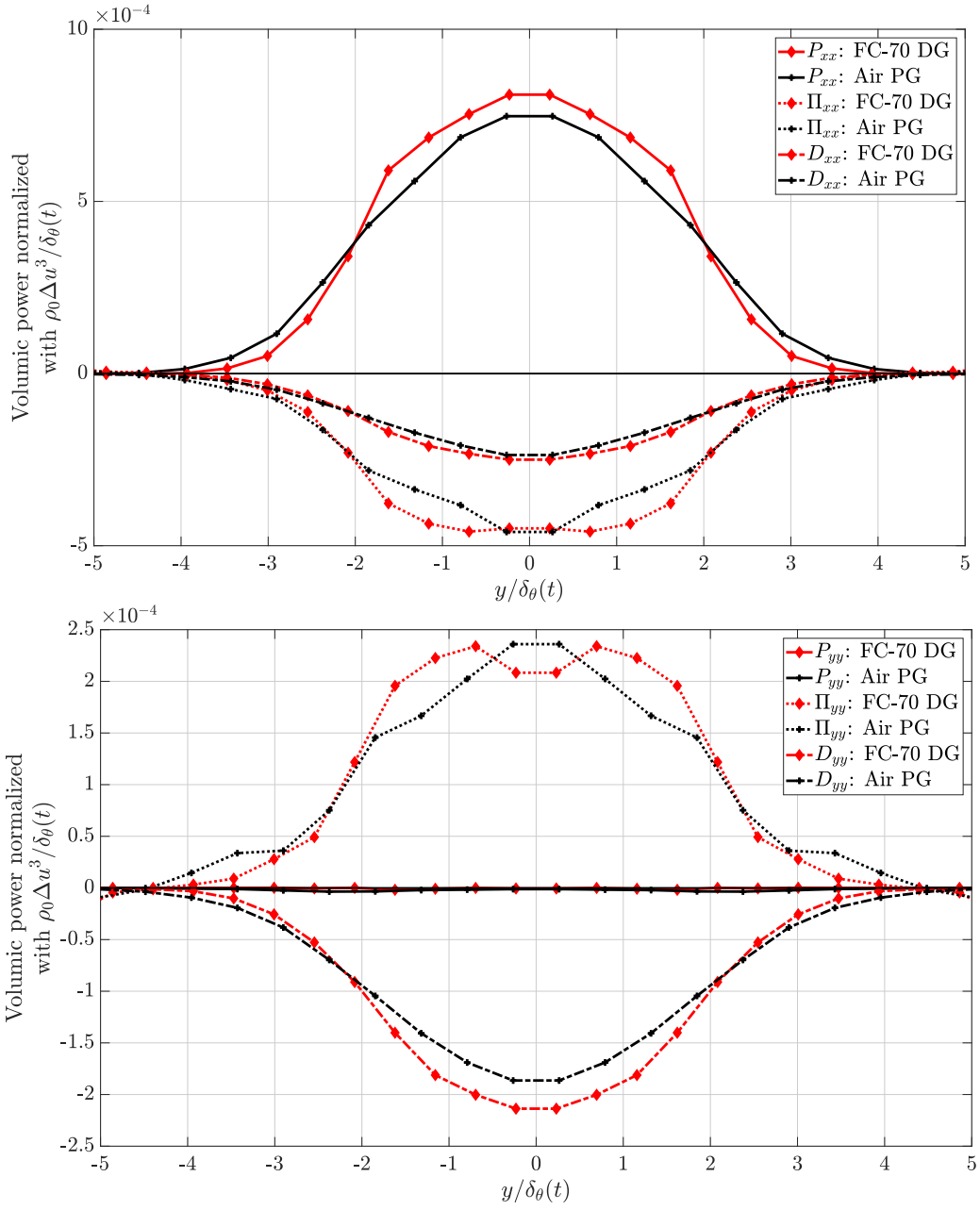

Figure 4.9: Distribution of the main non-dimensional volumetric power terms of the x- (top) and $y-$ (bottom) turbulent stress tensor (R_{xx} and R_{yy}) equation over the non-dimensional cross-stream direction $y/\delta_\theta(t)$ at $M_c = 1.1$. P_{xx}: Streamwise production, Π_{xx}: Streamwise pressure-strain and D_{xx}: Streamwise dissipation terms are normalized by $\rho_0\Delta u^3/\delta_\theta(t)$. Results are computed from the 134M simulation. The sampling space step of the averaging process is $\frac{2L_y/\delta_\theta(\tau=1700)}{N_{points}}$, with $N_{points} = 24$. Distributions have been averaged between the upper and the lower stream to get perfectly symmetrical distributions.

Concerning the other terms of the TKE equation, it is found that the compressible dissipation, the pressure-dilatation, the mass-flux coupling term and the convective derivative of the turbulent kinetic energy are negligible in both PG and DG. Residuals and time derivative agree well between both gases.

As mentioned in the introduction, Pantano & Sarkar (2002) demonstrate that the compressibility related reduction of the momentum thickness growth rate is induced by the reduction of pressure-strain terms Π_{ij}, which causes a reduction of turbulent production. In the TKE equation, which is obtained from the sum R_{ii}, the pressure-strain terms *per se* do not appear. Their sum Π_{ii}, which constitutes the pressure-dilatation term, appears in the TKE equation but is negligible. In order to study pressure-strain terms, one needs to plot turbulent stress tensor equations terms. Figure 4.9 gives the turbulent stress tensor budget terms over respectively the x and y directions. In the streamwise direction, the pressure-strain term counterbalances the streamwise production, whereas in the cross-stream directions, pressure-strain term is positive and is balanced by viscous dissipation. In the cross-stream direction, turbulent production term can be neglected unlike in the streamwise direction for which it is maximal. In the same way as for the perfect gas, the pressure-strain terms are not negligible for the DG, but no significant difference is observed between DG and PG. The dense gas mixing layer experiences the same reduction of the pressure-strain terms at $M_c = 1.1$, which is due to both (i) the reduction of the pressure fluctuations and (ii) the reduction of the gradient of velocity fluctuations.

At $y/\delta_\theta(t) = 0$, a non-monotonic behavior is observed for DG, which is due to the difference in the thermodynamic behavior illustrated in Figure 4.13. Density fluctuations are larger at the center of the mixing layer for DG, unlike PG for which peaks of rms density are located at the borders of the layer. This larger density fluctuations rate at the center is likely to disturb the distributions of production since this term is calculated using Favre-averaging.

In the vertical direction, production terms are even more non-monotonic both for DG and PG because they involve the vertical gradient of the mean vertical velocity. Since this gradient is calculated in the vertical direction, which corresponds to the direction of the mixing layer growth, it induces more disturbed distributions.

Figure 4.10 displays the distribution of the mean streamwise velocity for the DG and the PG shear layers. These profiles confirm the effect highlighted when looking at the TKE distributions (Figures 4.8 and 4.9) and at the thermodynamic profiles (Figure 4.13), namely a slower propagation at the boundaries of the mixing layer for DG compared with PG. At first sight, that seems contradictory with the larger momentum thickness growth rate for DG with respect to PG (see Figure 4.2). Yet, the momentum thickness is proportional to the integral of volumetric streamwise production power which reflects the turbulent mixing inside the layer (see Equation (3.12)). It is therefore possible for the momentum thickness growth rate to be smaller with a wider distribution as long as the turbulent mixing inside the mixing layer is less intense. That is the case for the PG mixing layer when compared to the DG one. Note that the density distribution comes also into play since the production power is computed using the Favre average.

Specific turbulent kinetic energy (TKE) spectra computed during the self-similar period

The aforementioned results do not exhibit significant differences between DG and PG, but that does not imply there is no difference at all: a turbulent quantity may appear to be the same for PG and DG when looked at as a global quantity over the whole wavenumbers range but

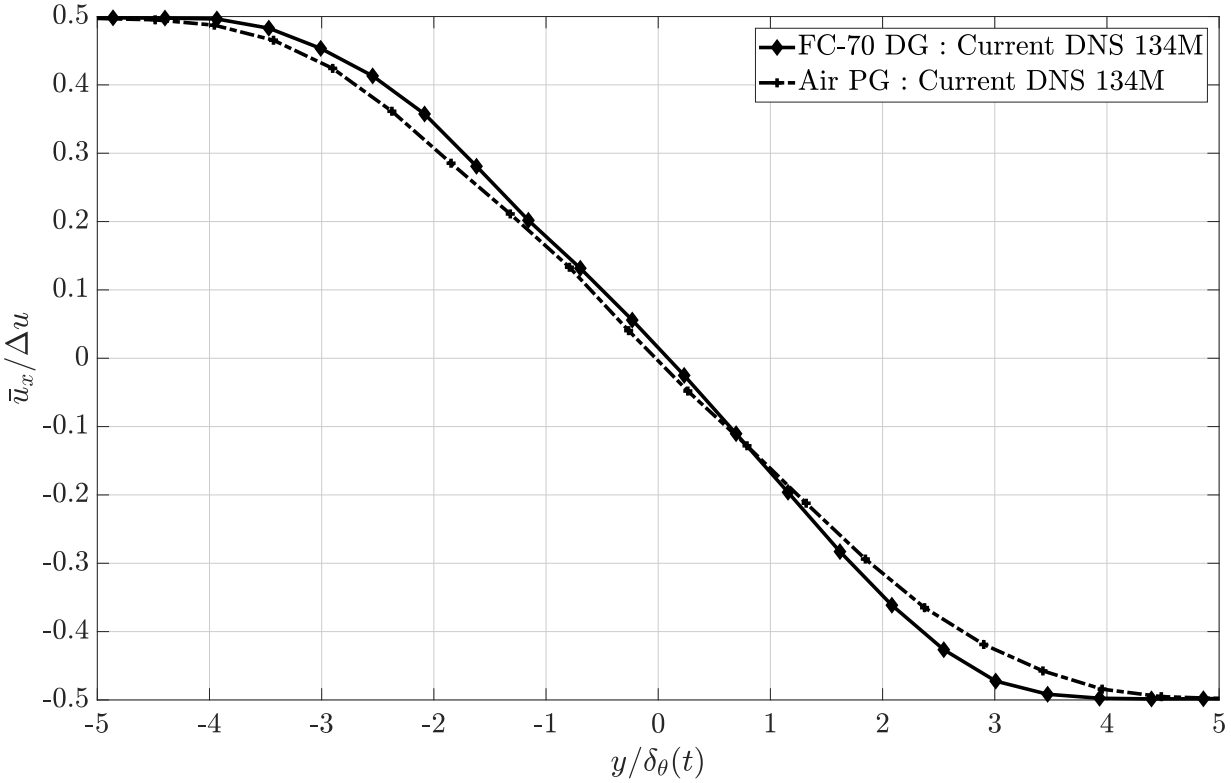

Figure 4.10: Distribution of the non-dimensional mean streamwise velocity averaged over the self-similar period. Comparison is made between FC-70 and Air. Results are computed from the 134M simulation at $M_c = 1.1$.

may actually behave differently for some specific turbulent scales. Since our final objective is to assess the need for new LES sub-grid models in the case of turbulent dense gas flows, it is important to take a closer look at each quantity in the spectral domain. The streamwise specific turbulent kinetic energy spectra computed on the centerline are thus drawn in Figure 4.11 for DG and PG. Spectra are normalized by $\Delta u^2 \delta_\theta(t)$ following Pirozzoli *et al.* (2015). The longitudinal Taylor microscale λ_x is also reported in Figure 4.11, computed as (see Bailly & Comte-Bellot (2003)):

$$\lambda_x = \sqrt{\frac{2\overline{u'^2_x}}{\overline{\left(\frac{\partial u'_x}{\partial x}\right)^2}}} \tag{4.3}$$

Note the following simplified equation, often used in the literature :

$$\lambda_x = \sqrt{\frac{30\nu\overline{u'^2}}{\epsilon}} \tag{4.4}$$

does not apply here since it is only valid for an incompressible and homogeneous turbulence (Kolmogorov, 1941).

The evolution of turbulent kinetic energy is similar for both PG and DG flows at the largest scales. However, at small scales, the perfect gas TKE is decreasing faster than the dense gas TKE, an observation reminiscent of the one made for the unstable growth phase. The dense gas effect therefore increases small scales energy. The dissipation term, which is the main term at these scales, is reduced. Figure 4.12 displays the ratio of the DG over PG spectra and enables to precisely focus on the quantities at stake. At scales smaller than the Taylor microscale, the

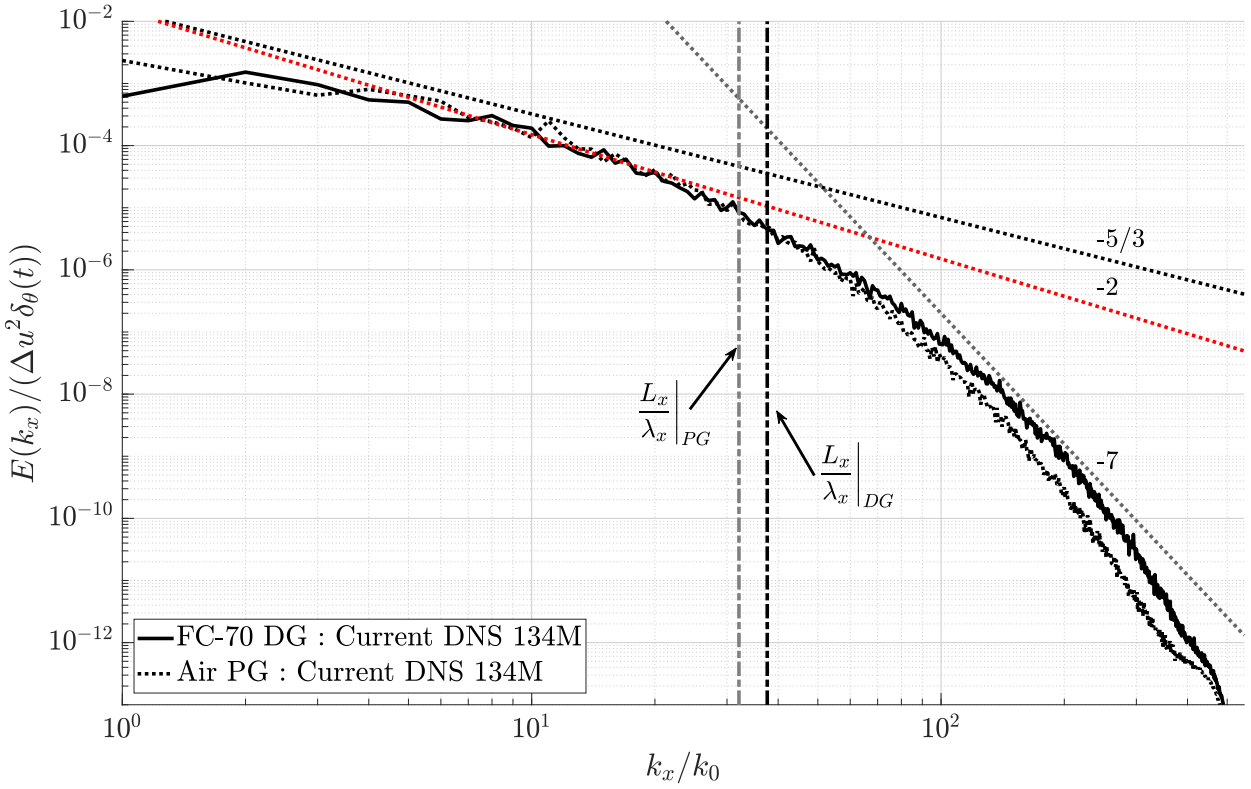

Figure 4.11: Streamwise specific TKE spectra computed on the centerline at $M_c = 1.1$.

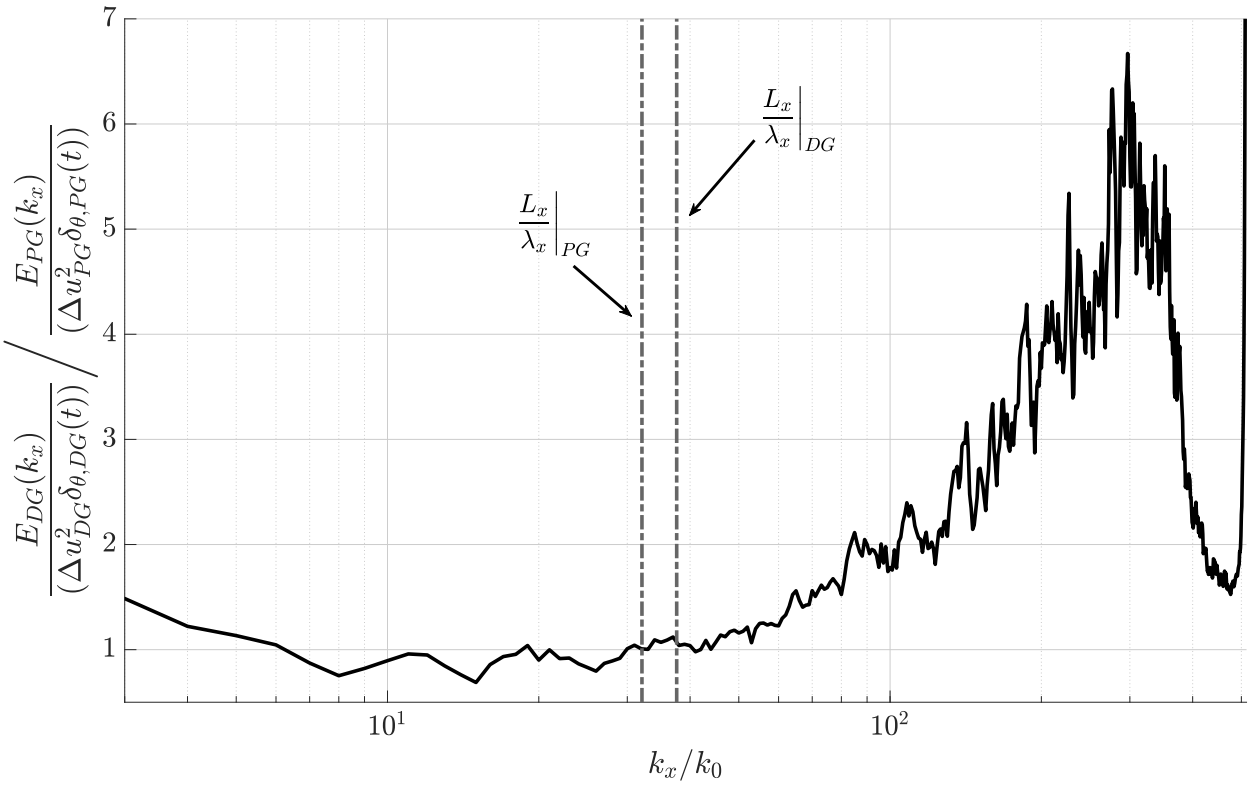

Figure 4.12: Dense gas / Perfect gas streamwise specific TKE spectra ratio. (PG: Perfect Gas, DG: Dense Gas). Results are computed from the 134M simulation at $M_c = 1.1$.

dense gas to perfect gas energy ratio increases up to a factor of six.

Note that, the L_x/λ_x ratio is slightly smaller for the DG. The turbulent structures for which dissipation plays an important role are smaller for the DG than for the PG.

Mean and fluctuating thermodynamic quantities in the self-similar stage

Figure 4.13 provides a comparison of pressure, temperature and density between DG and PG flows over the self-similar period. For PG, when looking at the Reynolds averaged values, one can notice an increase of about 16% of the temperature at the center of the mixing layer, due to viscous dissipation. Density decreases in similar proportions unlike pressure which is less influenced (4.5% decrease). For DG, the temperature is almost not affected by the viscous dissipation. Due to the large heat capacity of dense gas flows, the thermodynamic evolution is almost isothermal as already observed by Sciacovelli *et al.* (2017*b*) and therefore averaged density and pressure are much less influenced by the development of the mixing layer when compared to the PG flow.

When looking at the root mean square values of the fluctuations for PG (Figure 4.13 right), significant temperature fluctuations occur at the edges of the mixing layer due to turbulent mixing, leading to significant density variations. Pressure fluctuations are maximum at the center of the mixing layer. For DG, temperature fluctuations are almost suppressed. Pressure fluctuations in the dense gas mixing layer are very close to fluctuations observed in the perfect gas mixing layer, which is consistent with the same pressure-strain levels found in Figure 4.9. Thermodynamic distributions are thoroughly discussed at a larger compressibility regime ($M_c = 2.2$) in Section 4.4.5 in order to analyze discrepancies between DG and PG flows.

Additional comparison during the self-similar period

Figure 4.14 provides a comparison between FC-70 and air for the Reynolds numbers based on the momentum thickness (Re_{δ_θ}). These Reynolds numbers are computed using the domain averaged viscosity. Results show a much larger increase of the Reynolds number during the whole evolution for DG compared to PG. During the unstable growth phase, this seems consistent with Section 4.2.2 showing for instance a stronger increase of the xy-component of the turbulent stress tensor for DG with respect to PG. However, during the self-similar period, the gap between DG and PG becomes larger and tends to increase. This behavior is explained by an increase of the viscosity for PG due to the increase of the temperature absent in the DG flow, for which the thermodynamic evolution is almost isothermal (see Figure 4.13). Since the flows are significantly turbulent, this difference in the Reynolds number evolution between DG and PG does not influence the mixing layers growth rates.

Figure 4.15 shows the profiles of $xx-$, $yy-$, $zz-$ and $xy-$ rms velocities for PG and DG. The self-similar period selected ($\tau \in [1700; 2550]$) is well confirmed by these distributions which collapse relatively well in this time interval. At $\tau = 1000$, the profiles are clearly not self-similar. At $\tau = 1400$, it is less obvious to decide whether self-similarity is already achieved or not. In order to define the self-similar period from the rms velocities distributions, one can follow the method given in Almagro *et al.* (2017) computing the temporal mean and standard deviation of the Reynolds stresses for several time intervals. In this paper, another methodology is retained to define the self-similar period (see Section 4.2.1). The comparison between DG and PG in Figure 4.15 shows a similar evolution for the four computed components. The peak value averaged over the self-similar period is about 0.14 and 0.09 respectively for the $xx-$ and $yy-$ components, which is in good agreement with (Pantano & Sarkar, 2002) where these values are

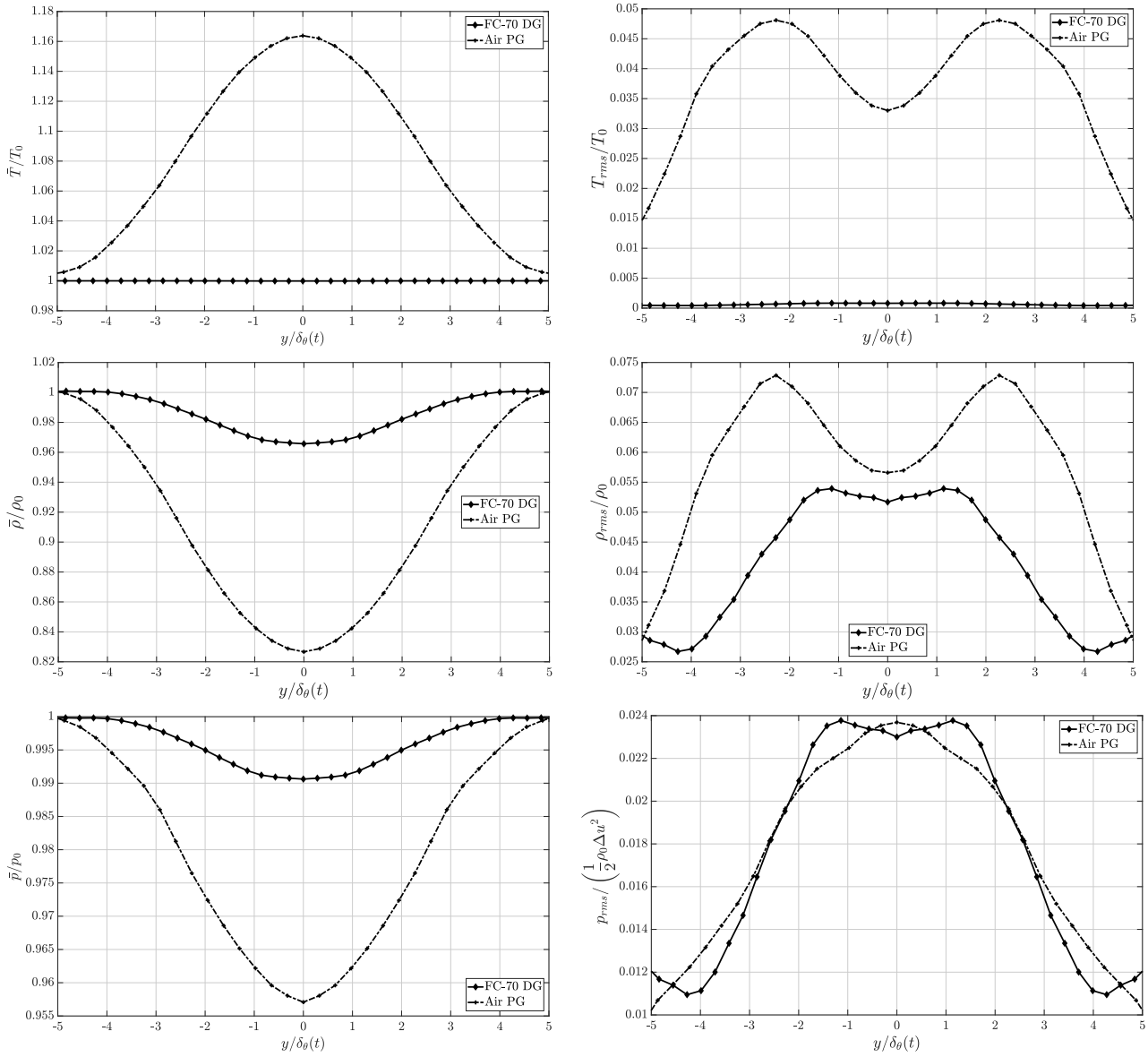

Figure 4.13: The non-dimensional Reynolds averaged (left) and root mean square (right) values of temperature (top), density (middle) and pressure (bottom) are averaged over the self-similar period ($\tau \in [1700; 2550]$), plotted along the y direction and compared between FC-70 and Air. Results are computed from the 134M simulation at $M_c = 1.1$.

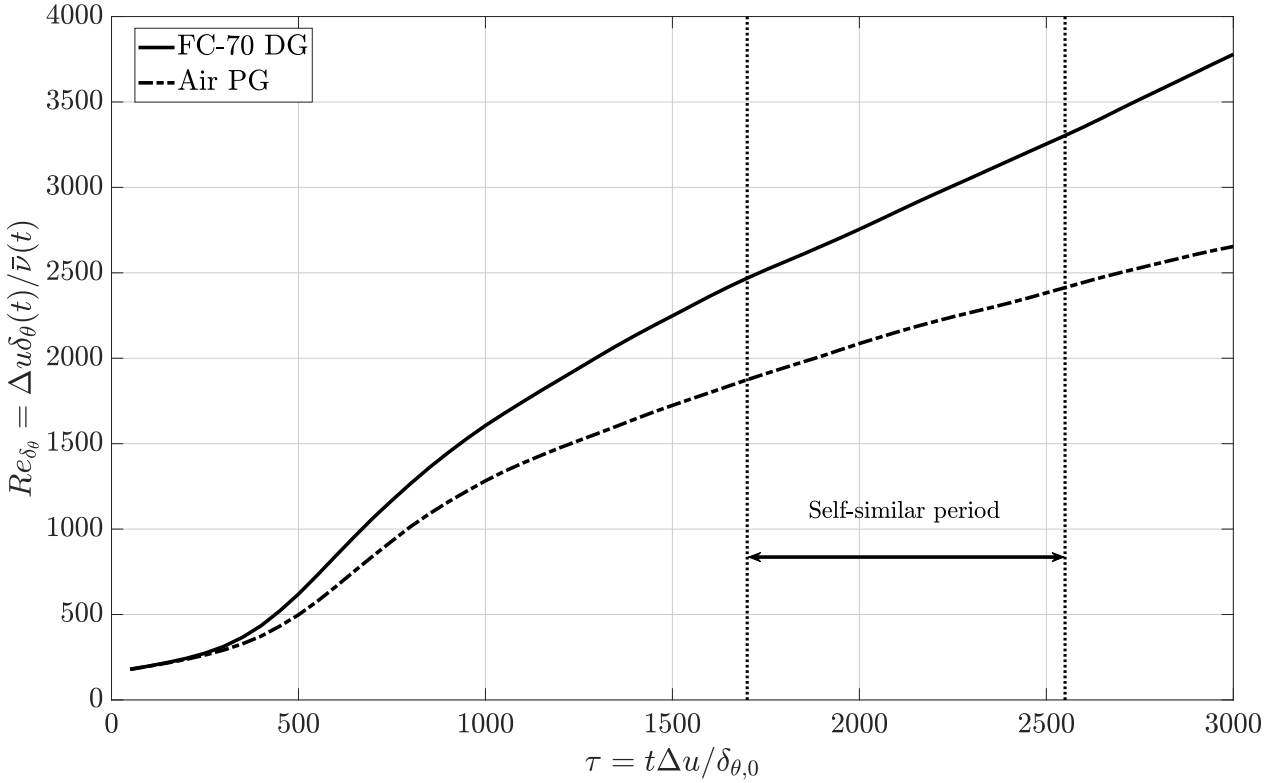

Figure 4.14: Temporal evolution of Reynolds number based on the momentum thickness. Results are computed from the 134M simulation at $M_c = 1.1$.

reported as 0.14 and 0.10.

Concluding remarks

The comparison between perfect and dense gases at $M_c = 1.1$ does not show major differences for the momentum thickness growth rates. The dense gas seems to face the same well-known compressibility-related reduction of the momentum thickness growth rate, caused by the reduction of both pressure fluctuations and the gradient of the velocity fluctuations leading to the reduction of the pressure-strain terms. However, when these quantities are analyzed across turbulent scales, distributions over the wavenumbers slightly differ between PG and DG. Results suggest that the dense gas effect yields an increase of the turbulent kinetic energy at small scales.

Because of a significant decrease in the speed of sound, very large turbulent Mach numbers are expected to be observed experimentally when using dense gases for thermodynamic states located in the vicinity of the critical point. At $M_c = 1.1$, the turbulent Mach number is limited to approximately 0.4 on the centerline during the self-similar period and only briefly increases beyond 0.5 during the unstable growth phase. In order to expand the present conclusion to highly supersonic flows, the next section is dedicated to the analysis of the DG shear layer at $M_c = 2.2$.

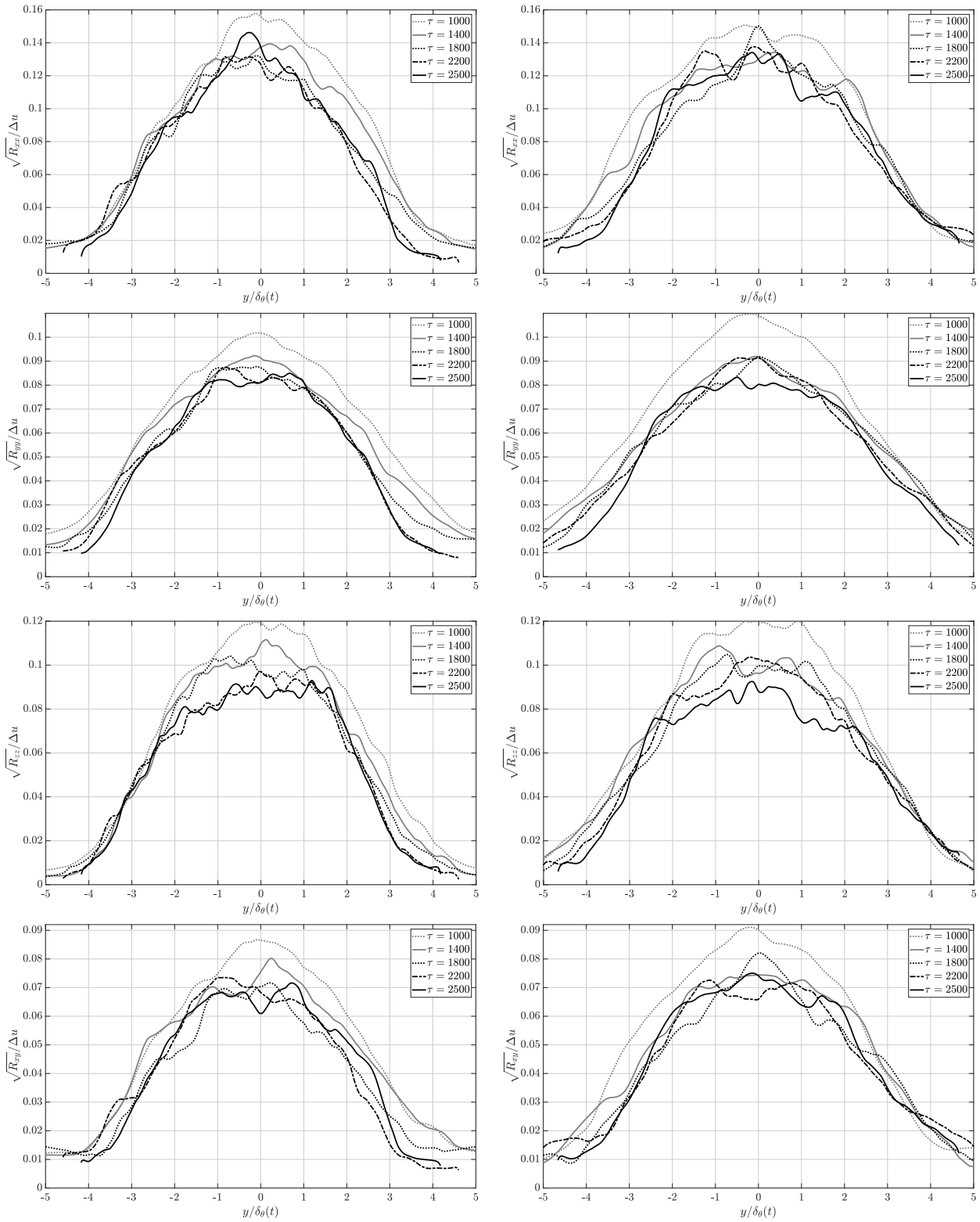

Figure 4.15: Distributions of the non-dimensional rms velocities (from top to bottom $xx-$, $yy-$, $zz-$ and $xy-$ components) for the dense gas (left) and the perfect gas (right) at several non-dimensional time outside ($\tau \in \{1000; 1400\}$) and inside ($\tau \in \{1800; 2200; 2500\}$) the self-similar period. Results are computed from the 134M simulation at $M_c = 1.1$.

4.3 Dense gas effect: influence of the convective Mach number

4.3.1 Temporal evolution and selection of the self-similar period

As previously done at $M_c = 1.1$, it is required to precisely define the self-similar range at other convective Mach numbers ($M_c = 0.1 - 2.2$). This is done through both the analysis of the momentum thickness (Figure 4.16) and the turbulent production (Figure 4.17). Figure 4.16 compares the normalized DG momentum thickness over time at three different convective Mach numbers : $M_c = 0.1 - 1.1 - 2.2$. Details about the simulation parameters are given in Table 4.1. At $M_c = 0.1$, similarly to PG mixing layer, the domain length is doubled in the y direction to get a long enough self-similar period. At $M_c = 2.2$, the domain length is divided by two in the y direction when compared to PG flow. The domain is therefore large enough to reach a self-similar period which lasts 4000τ. Initial turbulent structures are chosen six times larger at $M_c = 2.2$ when compared to other M_c to be consistent with PG simulation. It is nevertheless shown that the size of these initial turbulent structures does not influence the growth rate during self-similarity (see Appendix B). This choice was motivated by the will to shorten the simulation time. Enlarging the size of initial turbulent structures reduces the unstable growth phase. As a consequence, in Figure 4.16, $M_c = 1.1$ and $M_c = 2.2$ curves overlap after $\tau \approx 2500$.

Slopes and standard deviations computed over the self-similar range are given in Figure 4.16. At $M_c = 0.1$, because of the absence of compressibility effects, growth rate is very close to that of PG flow: the difference is about 1.5% and is below the standard deviation range. Like for PG, the DNS at $M_c = 0.1$ is considered as the reference incompressible case and is used to plot the dependence of the normalized momentum thickness growth rate with respect to M_c.

Figure 4.16 shows that the momentum thickness growth rates are very close between $M_c = 2.2$ and $M_c = 1.1$ unlike in the perfect gas case (Figure 3.3). The well-known decrease of the growth rate with the convective Mach number is modified by dense gas effects. Despite $FC-70$ being a highly compressible fluid, compressibility effects decrease in this dense gas. Tentative explanations for this effect are given in Section 4.4.

Slopes provided in Figure 4.16 are determined using the temporal evolution of the non-dimensional integrated turbulent production term P^*_{int}, as done for PG mixing layers. One can notice that, at $M_c = 2.2$, the initial phase corresponding to an energy transfer to the most unstable modes, is much shorter for DG flow with respect to PG flow (Figures 4.16 and 3.3), likely because unstable modes are different between the two types of gas (Gloerfelt *et al.*, 2020). After this phase, turbulent production reaches a maximum which decreases as M_c increases. Finally, self-similar periods are defined selecting the range during which turbulent production is almost constant. One notices that integrated production terms in DG flows are consistent with momentum thickness growth rates: the values of P^*_{int} are very close between $M_c = 2.2$ and $M_c = 1.1$ and the value of P^*_{int} at $M_c = 0.1$ is twice as large as the one at $M_c = 1.1$. This observation confirms the relevance of Vreman *et al.* (1996*a*) relationship between the growth rate ($\dot{\delta}_\theta$) and the integrated production $\left(\int \bar{\rho} P_{xx} dV\right)$ (Equation (3.12)). Beginning and ending times for each DNS self-similar periods are provided in Table B.1.

4.3.2 DG effect over the self-similar period

Now that self-similar temporal spans have been selected for both types of gas and all convective Mach numbers, it is possible to plot the evolution of self-similar growth rates as a function of

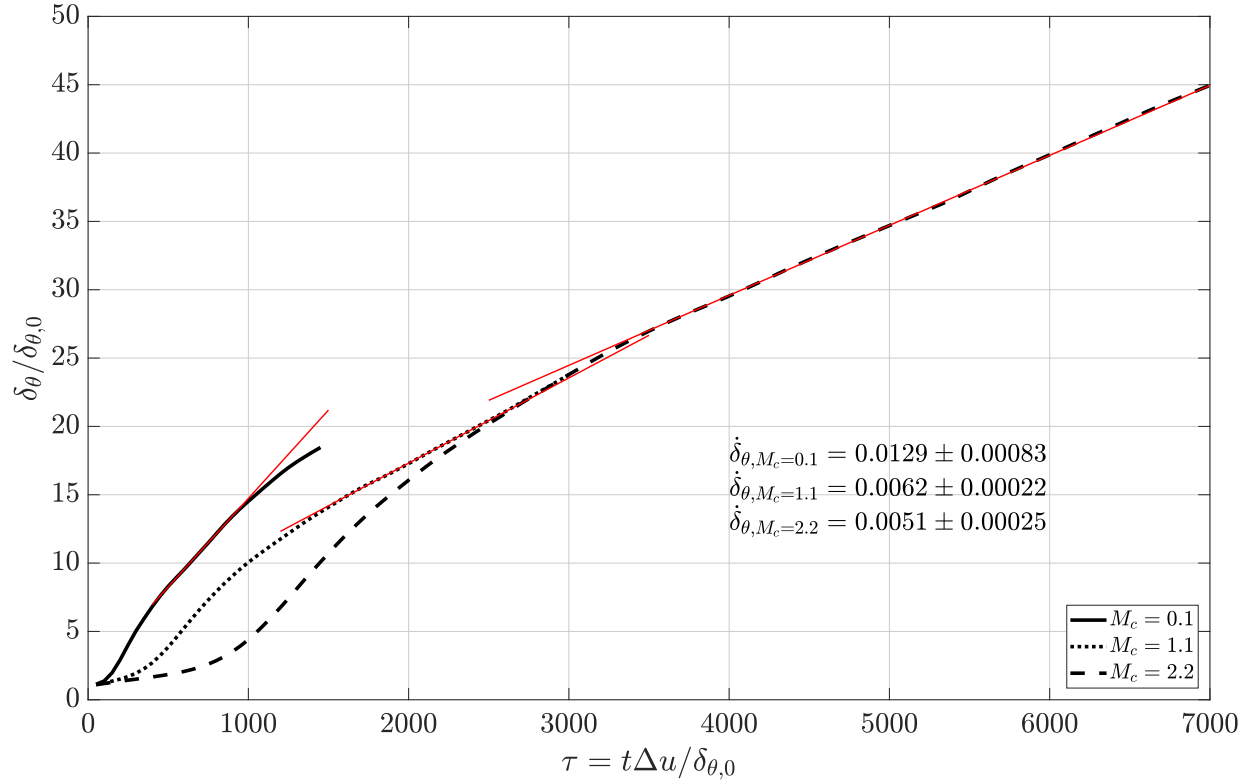

Figure 4.16: Temporal evolution of the mixing layer momentum thickness for DG at $M_c = 0.1/1.1/2.2$.

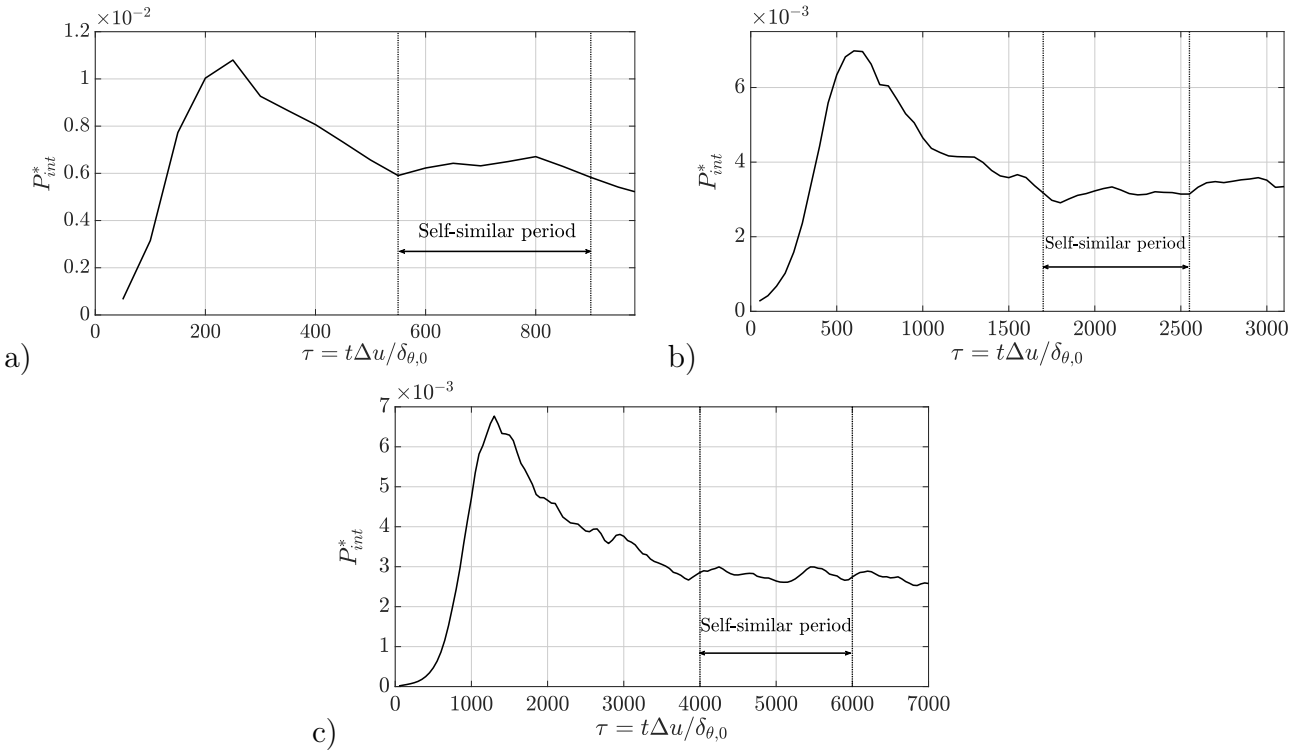

Figure 4.17: Temporal evolution of the non-dimensional streamwise turbulent production term integrated over the whole domain $P^*_{int} = (1/(\rho_0(\Delta u)^3)) \int_{L_y} \bar{\rho} P_{xx} dV$ (with $\bar{\rho} P_{xx}(y) = -\overline{\rho u''_x u''_y} \frac{\partial \tilde{u}_x}{\partial y}$) at $M_c = 0.1$ (a), $M_c = 1.1$ (b) and $M_c = 2.2$ (c). Results are shown for the FC-70. Self-similar periods are indicated on each plot.

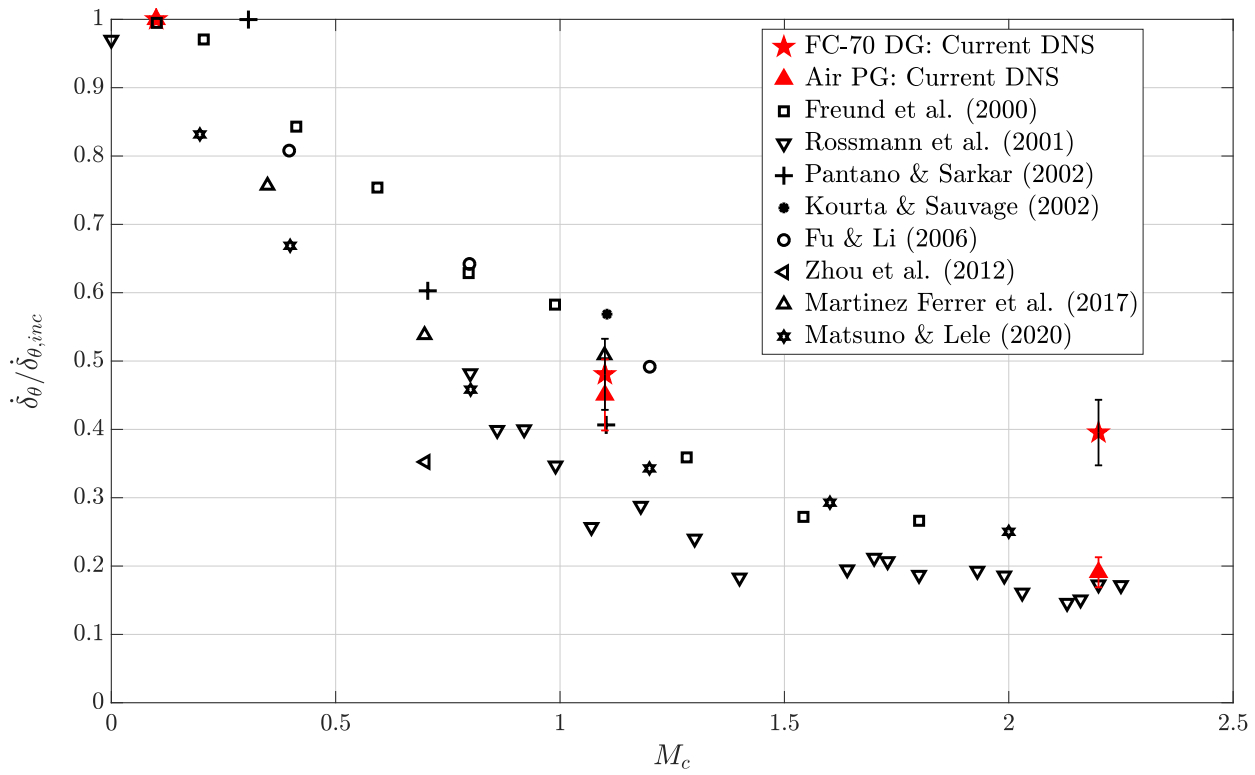

Figure 4.18: Evolution of the mixing layer growth rate over the convective Mach number for air and for FC-70. Comparison is made with available DNS results in literature and experimental results in Rossmann *et al.* (2001).

the convective Mach number. Slopes are normalized using an incompressible reference case at very low convective Mach number for which compressibility effects can be neglected. DNS at $M_c = 0.1$ is considered here as the reference incompressible case. For example, Pantano & Sarkar (2002) use a simulation at $M_c = 0.3$ as a reference case. There is no consensus on this choice, which can partly explain the spreading of PG results observed in Figure 4.18 - where the same literature results previously used in Figure 3.9 are reported. DG mixing layer results are plotted with error bars colored in black. They represent the standard deviation of the normalized growth rate over the self-similar range. Unlike the PG mixing layer which shows a fairly abrupt decrease of its growth rate as M_c increases, the DG mixing layer seems to be much less influenced by compressibility effects as M_c increases beyond 1.1. Differences between DG and PG mixing layers are large enough when compared to standard deviations to reveal that turbulence development is actually modified by dense gas effects in mixing layer flows above $M_c = 1.1$.

In order to analyze the impact of compressibility effects, Pantano & Sarkar (2002) study the TKE equation and particularly the importance of the turbulent production term. They find that this term is decreasing in consistent proportion with the growth rate as the convective Mach number increases. The computation of TKE equation terms requires to statistically average the terms. This can only be done during the self-similar period during which both mixing layers are in a statistically stable state. Figure 4.19 shows the comparison between DG and PG mixing layers of the normalized main terms of the TKE equation over the non-dimensional cross-stream direction $y/\delta_\theta(t)$. Consistently with the comparison of slopes between DG and PG flows, all main terms and particularly the production term are two to three times larger for DG.

Another noticeable feature which was highlighted in the analysis at $M_c = 1.1$ (see Figure

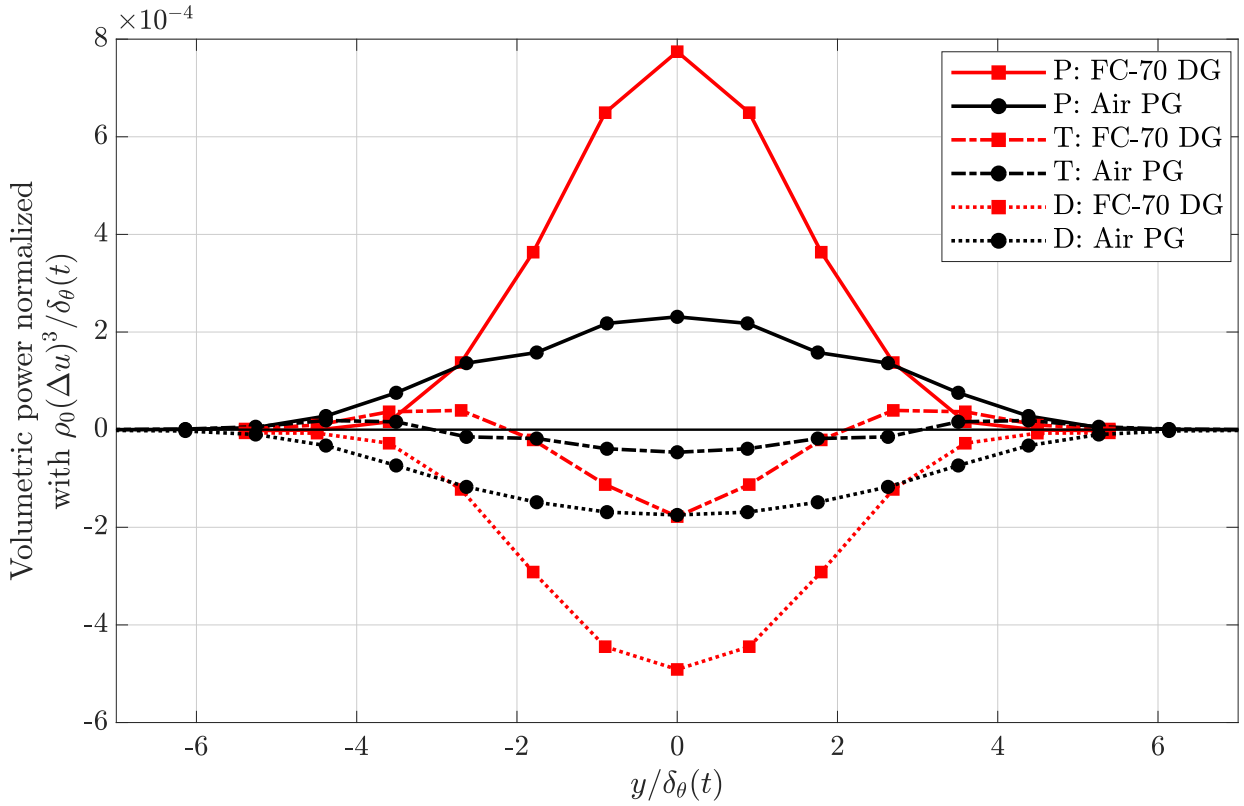

Figure 4.19: Distribution of the volumetric normalized powers over the non-dimensional cross-stream direction $y/\delta_\theta(t)$ at $M_c = 2.2$. P: Production, D: Dissipation and T: Transport are normalized by $\rho_0(\Delta u)^3/\delta_\theta(t)$. Distributions have been averaged between the upper and the lower stream to get perfectly symmetrical distributions.

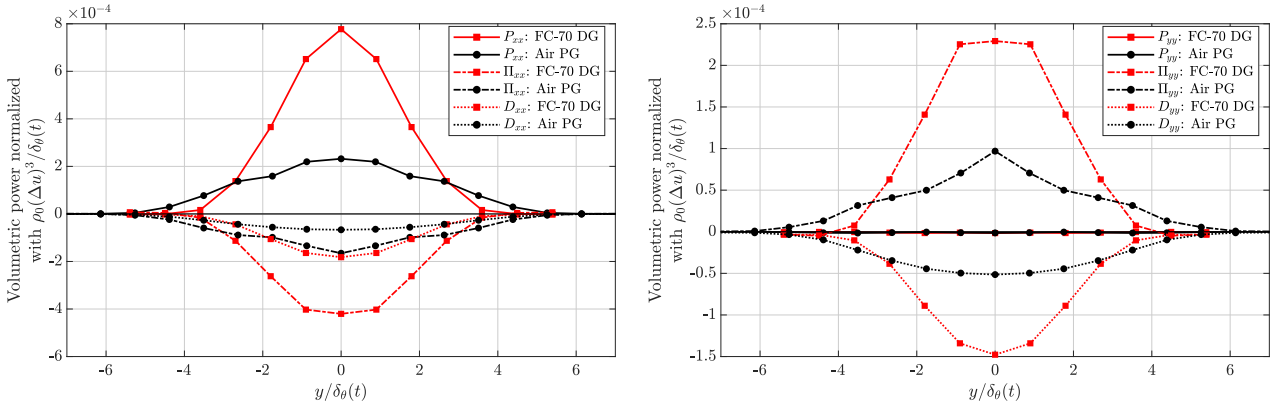

Figure 4.20: Distribution of the main non-dimensional volumetric power terms of the x- (left) and y- (right) turbulent stress tensor (R_{xx} and R_{yy}) equations over the non-dimensional cross-stream direction $y/\delta_\theta(t)$. P_{xx} and P_{yy}: Streamwise and cross-stream production, Π_{xx} and Π_{yy}: Streamwise and cross-stream pressure-strain and D_{xx} and D_{yy}: Streamwise and cross-stream dissipation terms are normalized by $\rho_0(\Delta u)^3/\delta_\theta(t)$. Results are computed at $M_c = 2.2$. Distributions have been averaged between the upper and the lower stream to get perfectly symmetrical distributions.

4.10) is confirmed here: distributions are wider for the PG mixing layer, when compared to the DG mixing layer. For the DG mixing layer, the TKE is more localized at the center. This is directly linked to the thermodynamic profiles, which are wider for PG mixing layer (see Figure 4.38).

Other terms of the TKE equation, namely the compressible dissipation, the mass-flux coupling term, the convective derivative of the TKE and even the pressure dilatation are negligible for both types of gas.

As mentioned in Section 3.1, the well-known compressibility-related reduction of the momentum thickness growth rate is explained by a reduction of the pressure-strain terms (Π_{ij}). Figure 4.20 confirms this effect showing the main terms of the $x-$ and $y-$ components of the turbulent stress tensor equations at $M_c = 2.2$. Pressure-strain terms are significantly reduced for PG flows when compared to DG flows: the streamwise pressure strain term is twice as large for DG when compared to PG. PG pressure-strain terms strongly decrease at $M_c = 2.2$ with respect to $M_c = 1.1$ (see Figure 4.9) unlike DG pressure-strain terms which are of the same magnitude. It is consistent with the comparison of momentum thickness growth rates. For both types of gas, growth rates are closely linked to their pressure-strain terms. Compressibility effects influence the same terms for both DG and PG.

It remains to verify the last step in Pantano & Sarkar (2002)'s explanation, which is that the reduction of pressure-strain terms is caused by a reduction of normalized pressure fluctuations. Figure 4.21 shows the cross-stream distribution of the root-mean square value of pressure normalized by the dynamic pressure $\frac{1}{2}\rho_0(\Delta u)^2$. Comparison is made between DG and PG flows at $M_c = 1.1$ and $M_c = 2.2$.

At $M_c = 1.1$, DG and PG distributions are very close as are their corresponding momentum thickness growth rates. As the convective Mach number increases, DG non-dimensional pressure fluctuations experience a 20% decrease also consistent with the observed decrease in the growth rate. This decrease is yet much smaller than that of the PG mixing layer, in which normalized pressure fluctuations are approximately divided by a factor of two. One can conclude that although the same mechanism is responsible for the growth rate decrease in both types

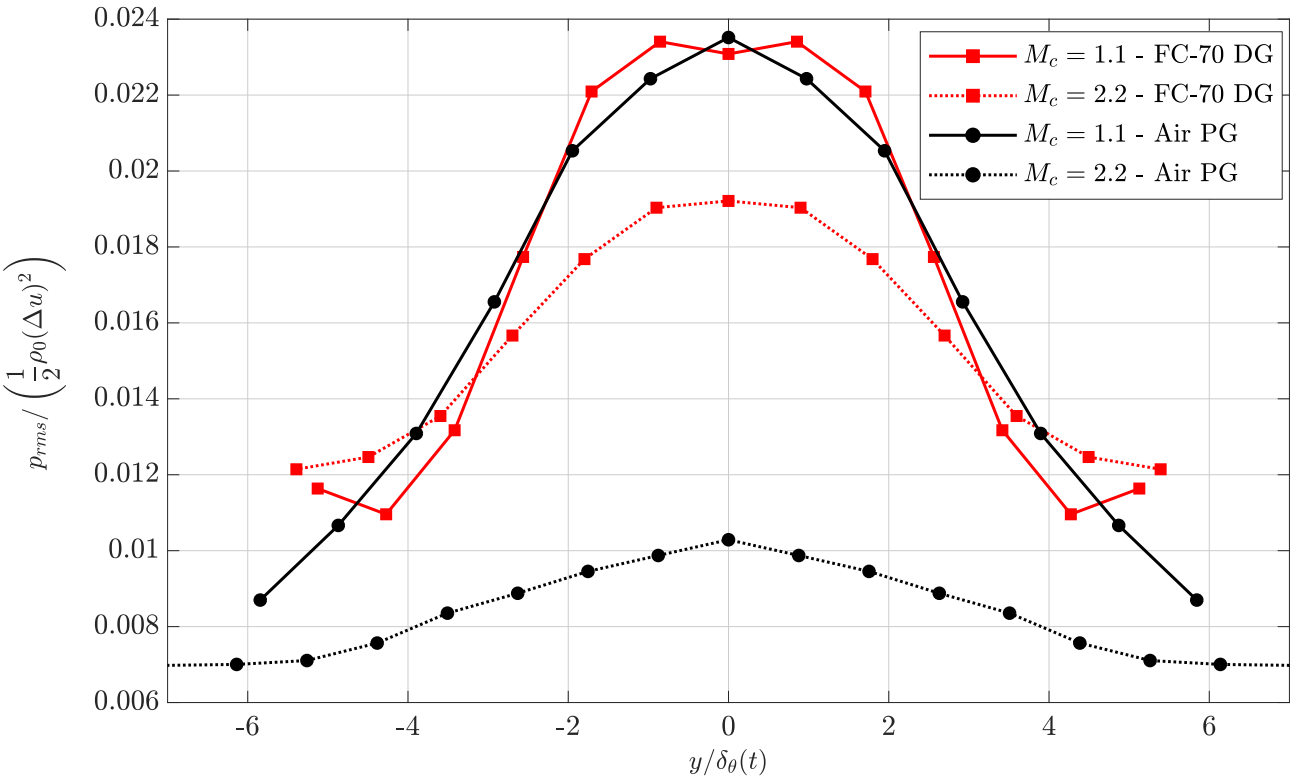

Figure 4.21: Distributions of the root mean square value of pressure averaged over the self-similar period, plotted along the y direction and compared between FC-70 and air at $M_c = 1.1$ and $M_c = 2.2$. Distributions have been averaged between the upper and the lower stream to get perfectly symmetrical distributions.

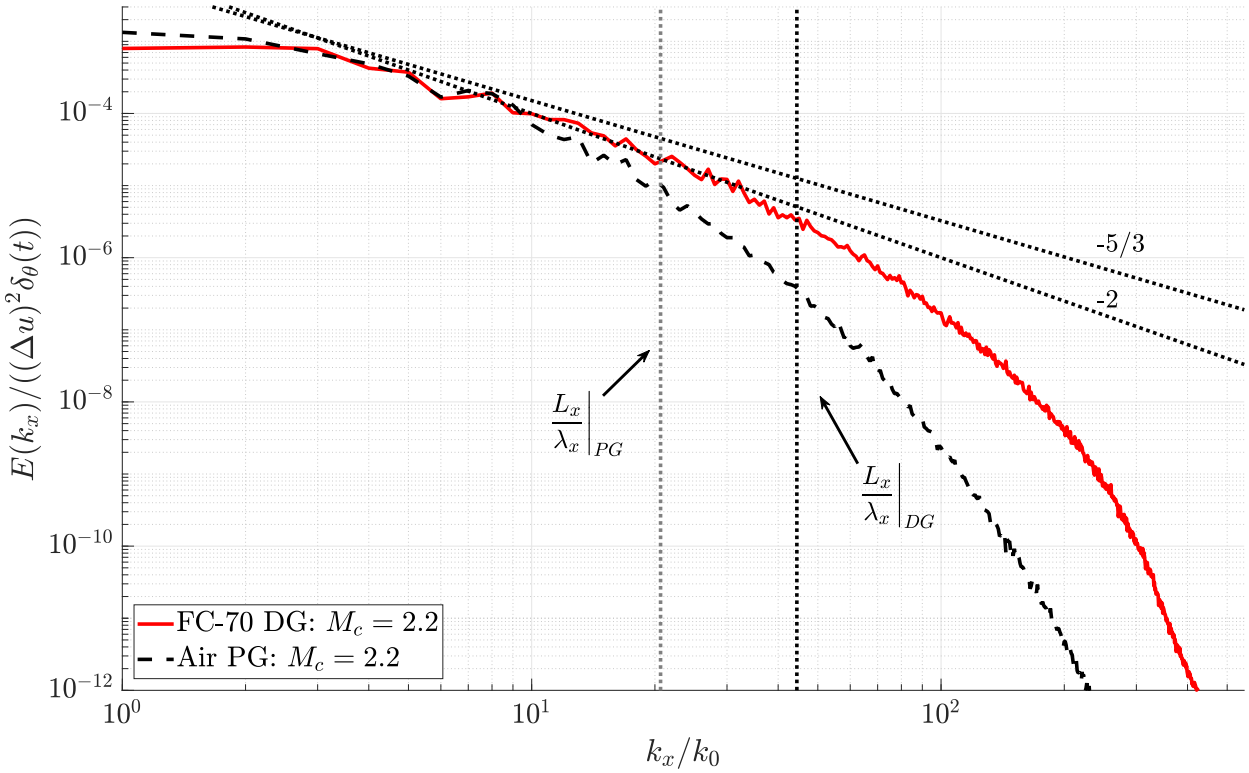

Figure 4.22: Streamwise specific TKE spectra computed along the centerline at $M_c = 2.2$.

of gas (*i.e.* the reduction of non-dimensional pressure fluctuations), its effect is significantly different between the two types of gas. For DG flows, the well-known compressibility-related reduction of the momentum thickness growth rate is almost suppressed by dense gas effects at convective Mach numbers above $M_c = 1.1$.

Figure 4.22 shows the comparison between PG and DG streamwise specific turbulent kinetic energy spectra computed over the centerline. Spectra are normalized by $(\Delta u)^2\delta_\theta(t)$ in the same way as Pirozzoli *et al.* (2015) and averaged over the self-similar period. The longitudinal Taylor microscale λ_x is also indicated for each gas in Figure 4.22. Its value is much larger for DG flow consistently with Reynolds numbers computed from Taylor microscales given in Table B.1. The inertial region is thus significantly reduced for the PG flow. Dissipation occurs at much larger scales making the comparison between the two inertial region slopes difficult. Spectra yet confirm previous results observed at $M_c = 1.1$: dense gas effects tend to increase small scales energy. The dissipation term, which is the main term at these scales, is significantly reduced.

4.4 Analysis of discrepancies between DG and PG flows

There is a significant effect of dense gas on the well-known compressibility-related reduction of the momentum thickness growth rate. Dense gas effects modify the decrease at convective Mach numbers larger than $M_c = 1.1$. Between $M_c = 1.1$ and $M_c = 2.2$, the growth rate slope does not vary much for DG when compared with PG. Several factors can be identified, which contribute to explain the observed discrepancies between DG and PG mixing layers.

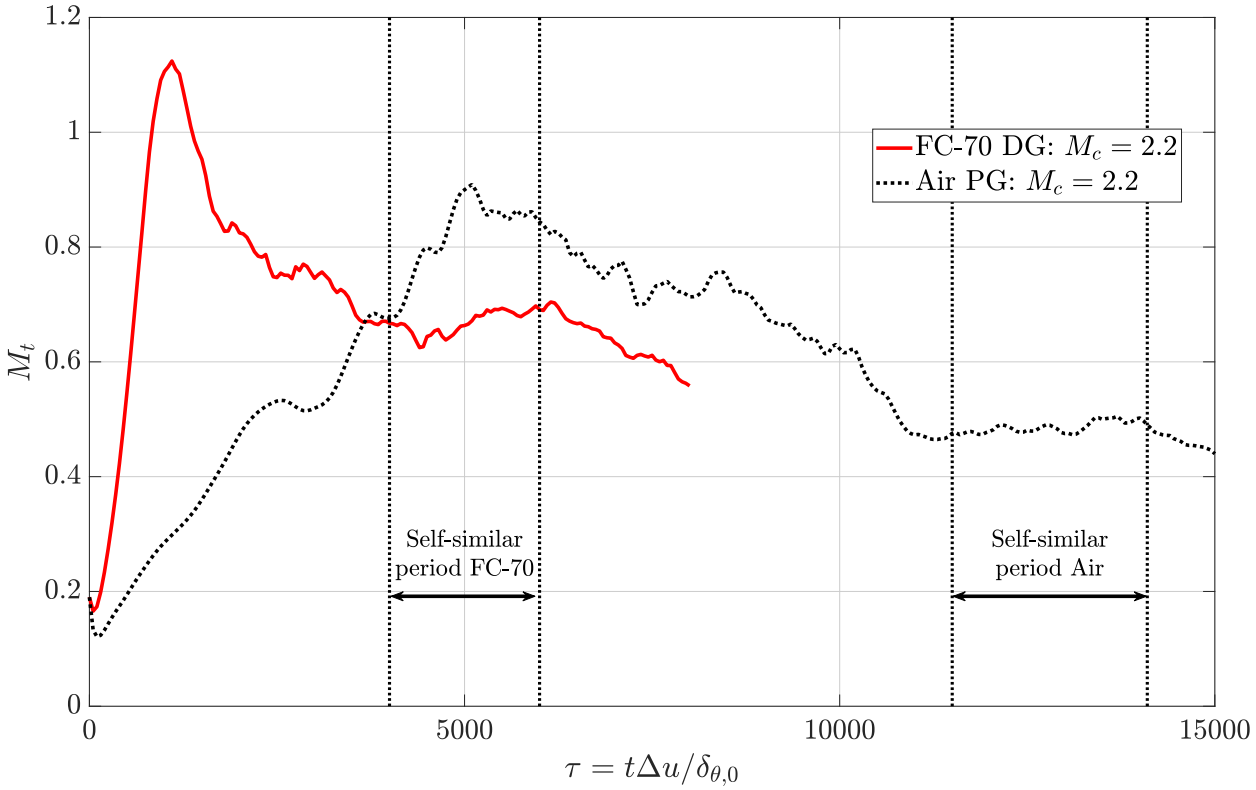

Figure 4.23: Temporal evolution of the turbulent Mach number M_t for the PG and DG mixing layers at $M_c = 2.2$.

4.4.1 Shocklets influence

The analysis conducted at $M_c = 1.1$ shows that the growth rate is not influenced by the dense gas effect during the self-similar period (see Section 4.2). However, significant differences are observed during the unstable growth phase. At $M_c = 1.1$, the evolution of the turbulent Mach number shows that shocklets might be detected during the unstable growth phase but not during the self-similar range, during which M_t decreases below the range of values for which shocklets are expected ((Samtaney *et al.*, 2001)). It is known that the generation of shocklets is different between BZT DG flow and PG flow (Giauque *et al.*, 2020), yet can shocklets alone explain discrepancies between DG and PG flows ?

In the current analysis, we increase the convective Mach number to $M_c = 2.2$ in order to reach larger turbulent Mach numbers during the self-similar period and to analyze the influence of shocklets. Figure 4.23 shows the temporal evolution of the turbulent Mach number M_t. Turbulent Mach numbers increase during the initial phase up to 1.1 and 0.9 respectively for DG and PG flows. Then M_t decreases and reaches a rather stable plateau corresponding to the self-similar period. During this phase, average values of turbulent Mach numbers are respectively equal to 0.67 and 0.49 for DG and PG flows. Shocklets can thus be observed during both DG and PG self-similar periods.

In order to analyze both PG and DG compression shocklets and possibly DG expansion shocklets, the marching cube algorithm proposed by Samtaney *et al.* (2001) is used. It consists in detecting iso-surfaces of zero density Laplacian ($\Delta\rho = 0$). In order to keep iso-surfaces corresponding only to actual shocklets, the following generalized Rankine-Hugoniot condition

is verified between left and right states on each side of the presumed shocklet.

$$h_2 - h_1 = \frac{1}{2}(p_2 - p_1)\left(\frac{1}{\rho_1} + \frac{1}{\rho_2}\right) \tag{4.5}$$

where h denotes the specific enthalpy. Jumps satisfying the relationship (4.5) within 1% of the mean enthalpy are kept because Equation (4.5) is only valid in the inviscid context. In order to ensure the detected region corresponds to an actual shocklet, it is requested the selected candidate iso-surface is associated to a local value of the velocity divergence large enough when compared to the rms value of the velocity divergence. For compressible shocklets, this threshold value is set to -5 and for expansion ones to 5.

Using the PG EoS gives:

$$h = \frac{\gamma}{\gamma - 1}\frac{p}{\rho} \tag{4.6}$$

Using Equation (4.6) allows to simplify Equation (4.5) into :

$$\frac{\rho_2}{\rho_1} = \frac{(\gamma+1)p_2 + (\gamma-1)p_1}{(\gamma-1)p_2 + (\gamma+1)p_1} \tag{4.7}$$

Note that if γ is equal to unity, the density ratio is equal to the pressure ratio. The entropy difference between left and right states on each side of the shocklet can be expressed as:

$$s_2 - s_1 = c_v\left(\ln\left(\frac{p_2}{p_1}\right) - \gamma\ln\left(\frac{\rho_2}{\rho_1}\right)\right) \tag{4.8}$$

Combining Equation (4.8) with Equation (4.7) yields:

$$s_2 - s_1 = c_v\left(\ln\left(\frac{p_2}{p_1}\right) - \gamma\ln\left(\frac{(\gamma+1)p_2 + (\gamma-1)p_1}{(\gamma-1)p_2 + (\gamma+1)p_1}\right)\right) \tag{4.9}$$

Figure 4.24 (a) shows the density and entropy jumps as a function of the pressure jump across shocklets for the PG flow at $M_c = 2.2$. Density jumps follow very well the evolution given in Equation (4.7). Since $\gamma = 1.4$, the density ratio is lower than the pressure ratio. Entropy jumps also follow the tendency given by Equation (4.8) even though they are more scattered than density jumps.

Figures 4.24 (b) and (c) show the density and entropy jumps for the compression and expansion shocklets for the DG mixing layer at $M_c = 2.2$. For compression shocklets, entropy jumps are reduced by about 60% in the DG flow when compared to the PG flow essentially because of Equation (1.2) showing that the entropy jump across a shock is linearly linked to the fundamental derivative. The number of shocklets is also strongly reduced even though the turbulent Mach number during the self-similar period is larger for the DG mixing layer.

Expansion shocklets are also detected in the present work as shown in Figure 4.24 (c). They are physically admissible because of the existence of thermodynamic states located inside the inversion region where the fundamental derivative of gas dynamics becomes negative: Figure 4.25 confirms that thermodynamic states for the DG mixing layer at $M_c = 2.2$ and $\tau = 4000$ are mainly located inside the inversion region. Figure 4.24 shows that the entropy jumps of expansion shocklets are slightly reduced compared to the jumps of compression shocklets and that the number of occurrences of expansion shocklets is larger.

Figure 4.26 displays the visualization of iso-surfaces of zero density Laplacian ($\Delta\rho = 0$) colored by the velocity divergence: (a) for the PG flow, (b) for the DG flow with negative values of the velocity divergence, and (c) for the DG flow with negative values of the velocity

(a)

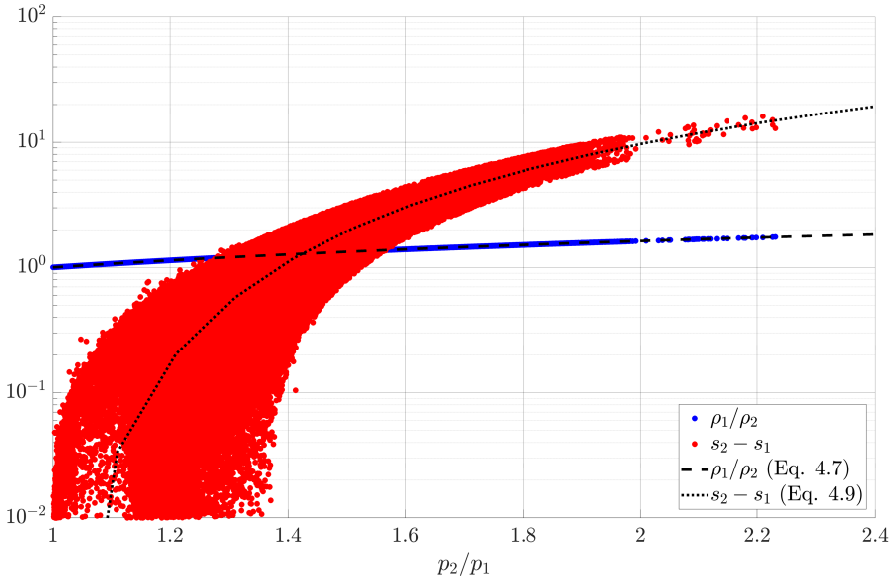

(b)

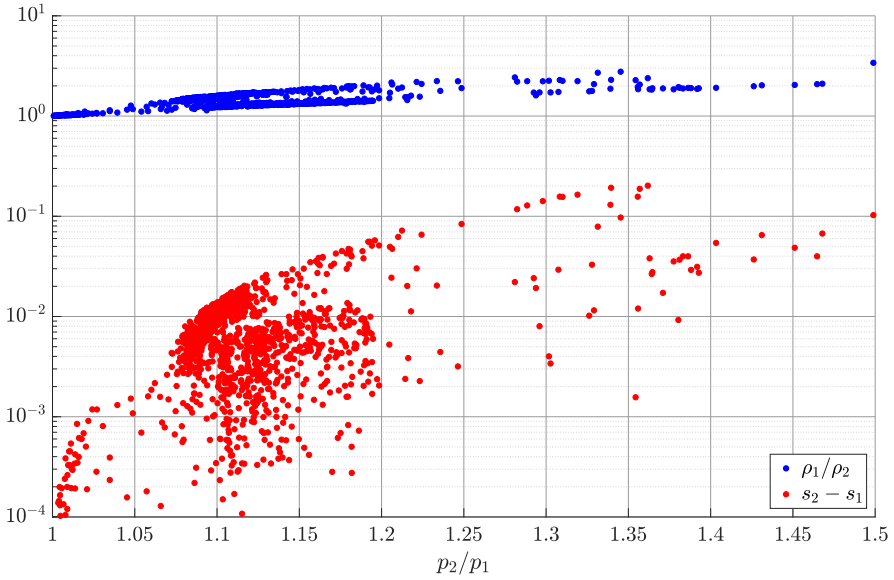

(c)

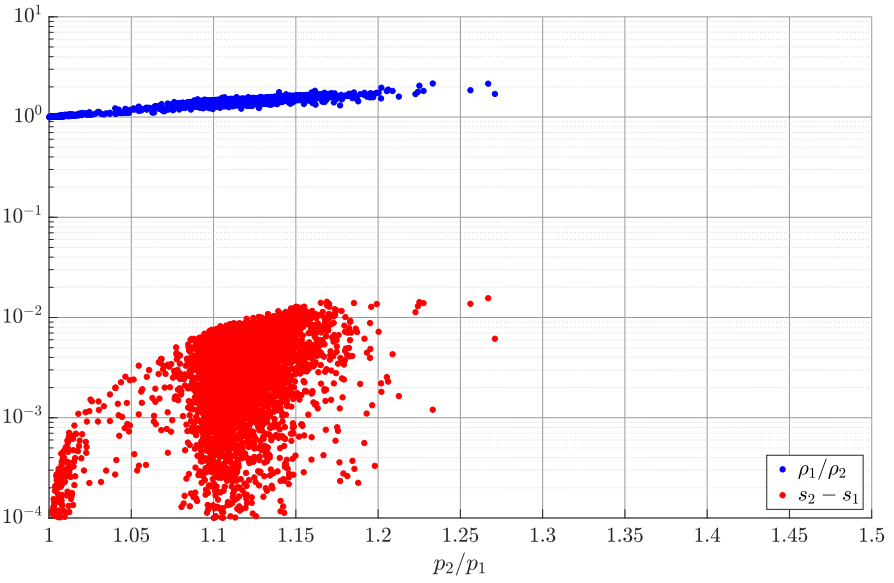

Figure 4.24: Evolution of the density jump and the entropy increase (a) in compression shocklets for the PG flow, (b) in compression and (c) in expansion shocklets for the DG flow at the beginning of the self-similar period.

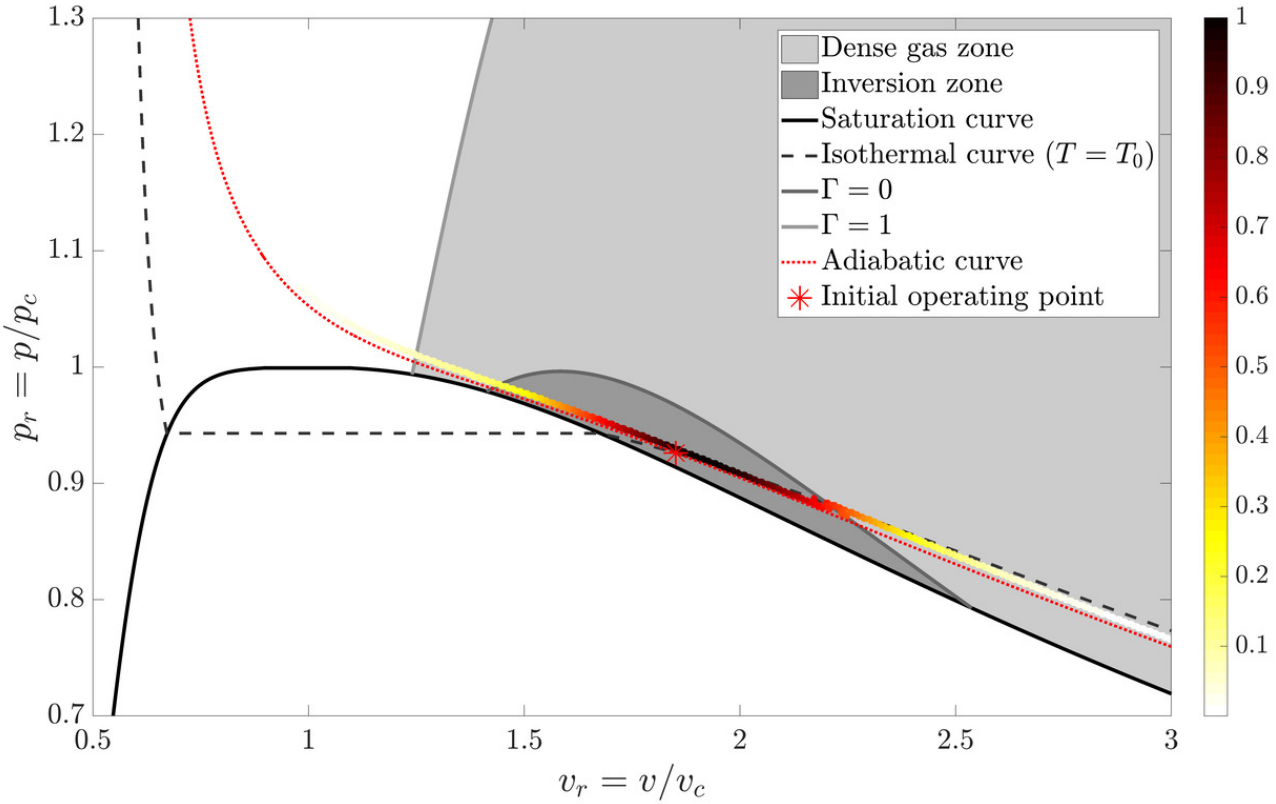

Figure 4.25: Thermodynamic states are represented in the non-dimensional $p - v$ diagram for BZT dense gas FC-70 at $M_c = 2.2$. The dense gas zone ($\Gamma < 1$) and the inversion zone ($\Gamma < 0$) are plotted for the Martin-Hou equation of state. p_c and v_c are respectively the critical pressure and the critical specific volume. The initial value of the fundamental derivative of gas dynamics is equal to $\Gamma_{initial} = -0.284$. The normalized distribution of the thermodynamic states is plotted at the beginning of the self-similar period ($\tau = 4000$) along the curve where the distribution of thermodynamic states is the largest.

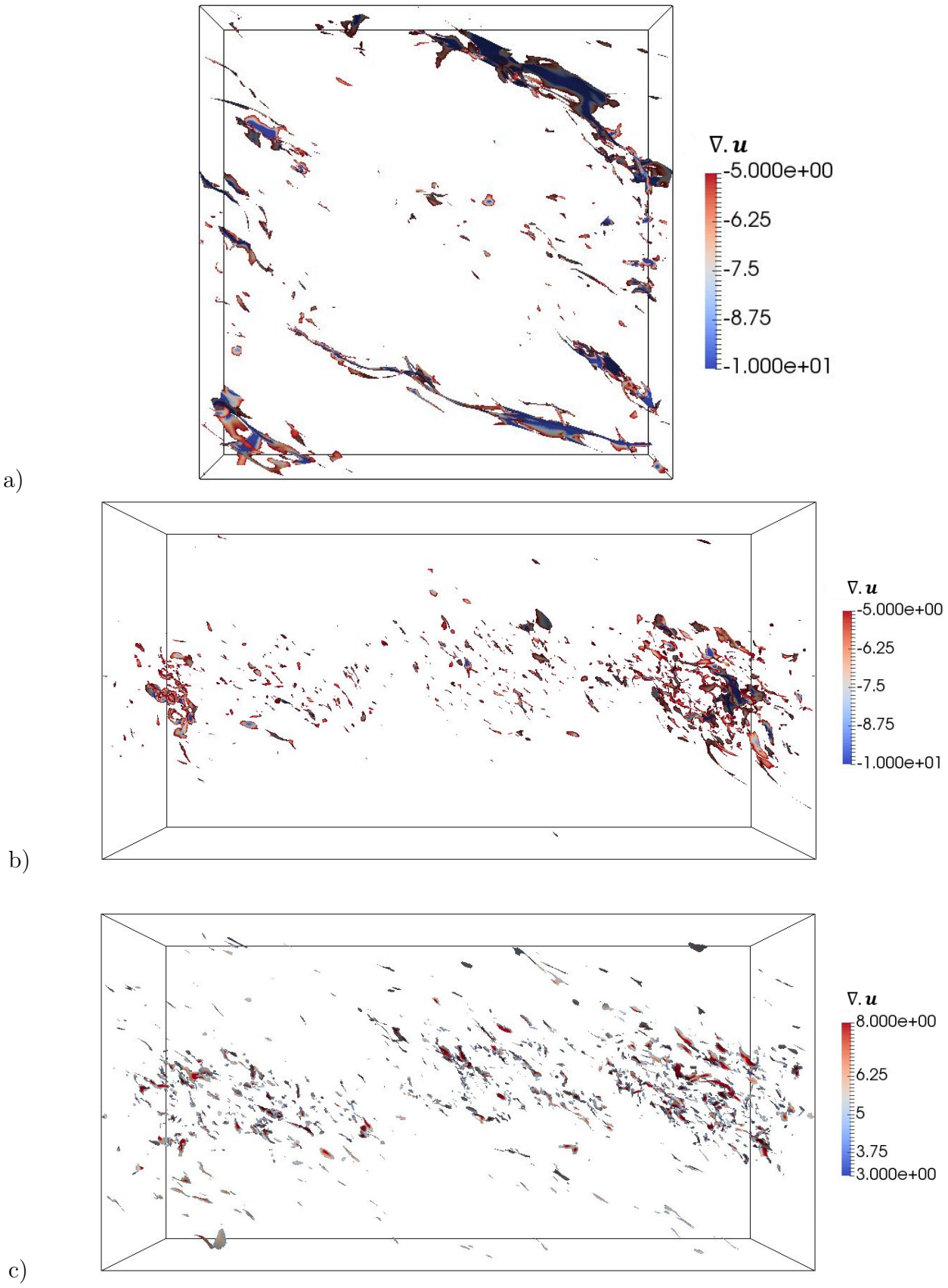

Figure 4.26: Iso-surfaces of zero density laplacian ($\Delta\rho = 0$) colored by the velocity divergence at the beginning of the self-similar period: (a) for the PG flow, (b) for the DG flow with negative values of the velocity divergence, and (c) for the DG flow with negative values of the velocity divergence.

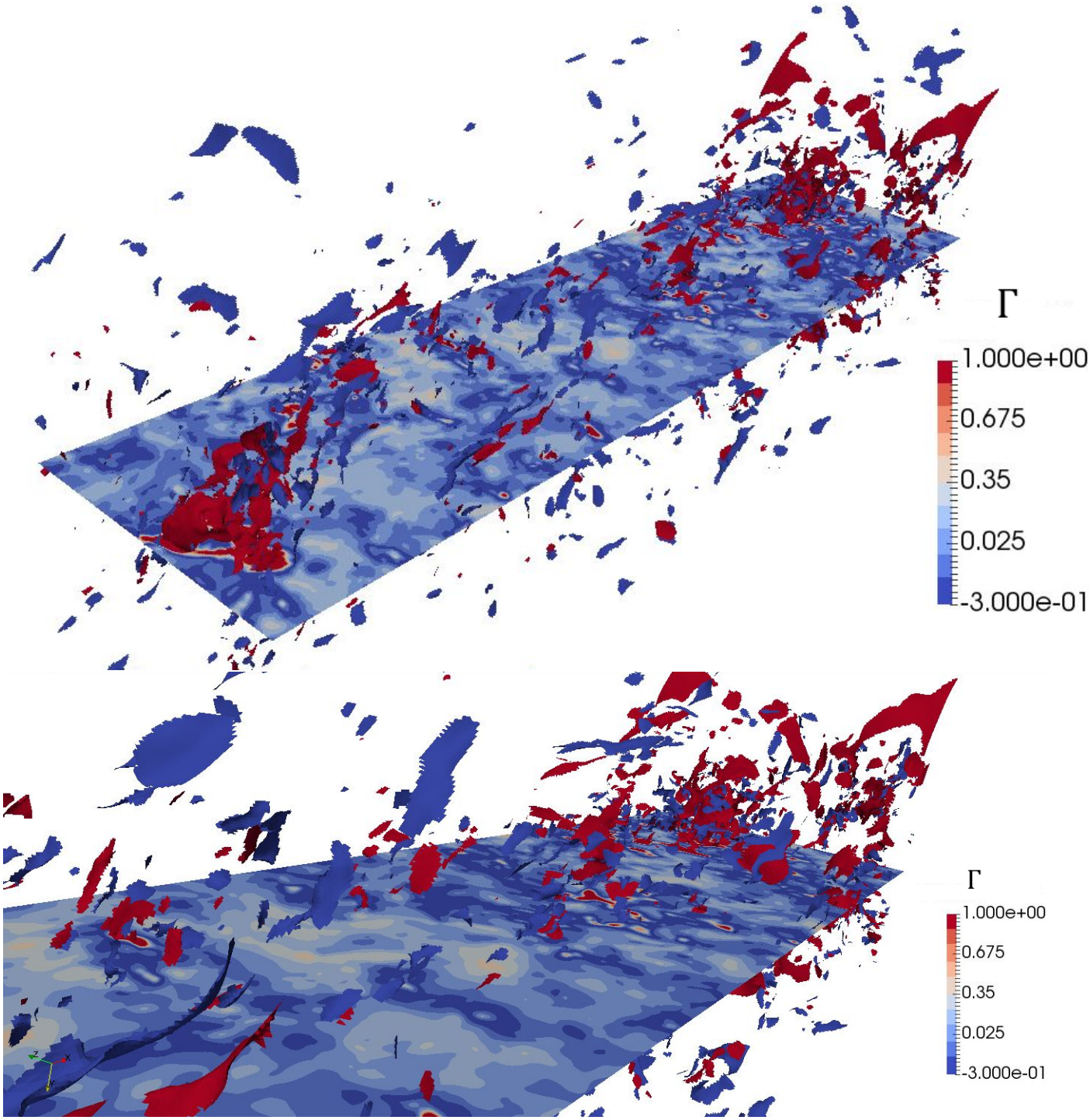

Figure 4.27: (Top) Iso-surfaces of zero density laplacian ($\Delta\rho = 0$) with positive values of the velocity divergence in blue and negative values of the velocity divergence in red together with the fundamental derivative Γ represented on the centerplane and (bottom) a closer view.

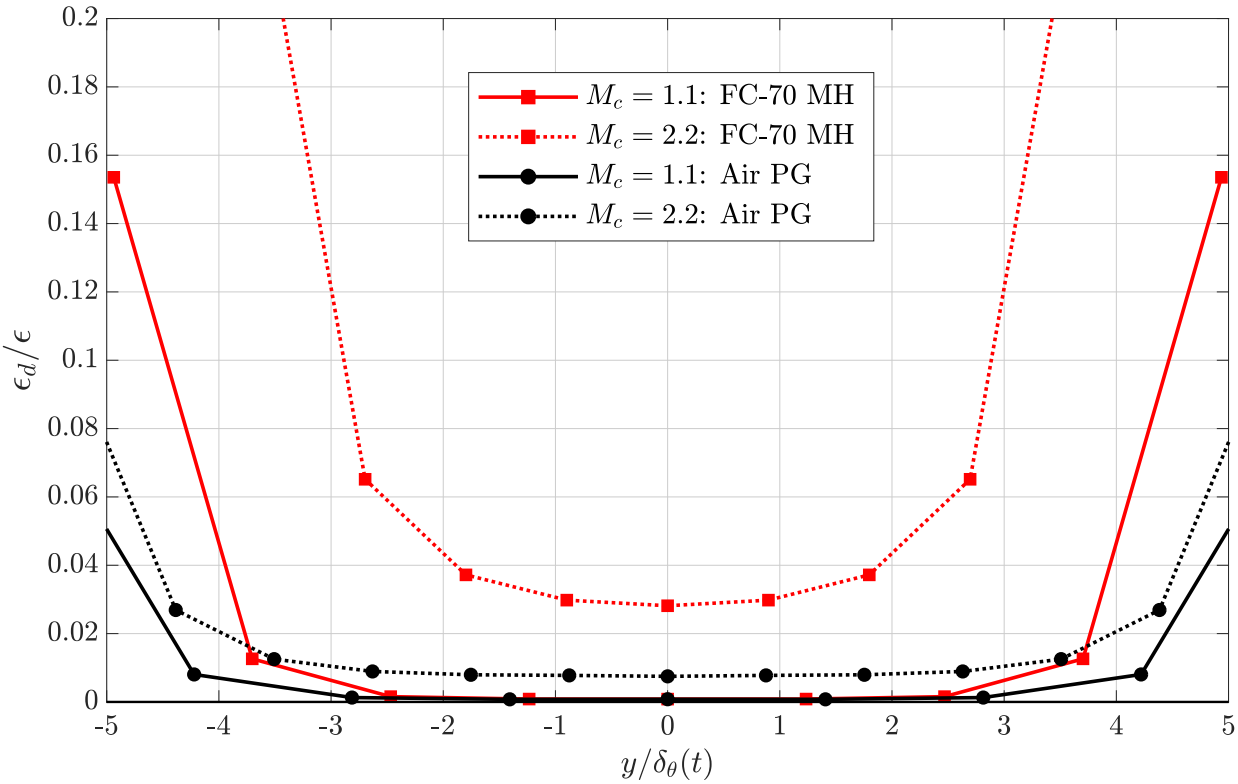

Figure 4.28: Distributions of the ratio between the compressible dissipation (ϵ_d) and the total dissipation (ϵ) (see details in Equations (3.10) and (3.11)). Results are averaged over the self-similar period. Comparison is made between FC-70 and Air at $M_c = 1.1$ and $M_c = 2.2$. Distributions have been averaged between the upper and the lower stream to get perfectly symmetrical distributions.

divergence. The location and the form of compression shocklets are very different between the DG and PG flows. For the PG flow, shocklets are mainly located outside the mixing layer and form sheet-like structures. Their shape and location are reminiscent of Mach wave radiation evidenced in Buchta & Freund (2017); Pineau & Bogey (2019). For DG flow, compression and expansion shocklets are mainly located inside the mixing layer. The range of velocity divergence is of the same order of magnitude and can reach up to ten times the rms velocity divergence.

Figure 4.27 displays the visualization of iso-surfaces of zero density Laplacian ($\Delta\rho = 0$) with positive values of the velocity divergence in blue and negative values of the velocity divergence in red. In addition, the centerplane is colored with the fundamental derivative which varies from negative to positive values as expected from Figure 4.25. Regions which exhibit negative values of velocity divergence are most of the time associated also with positive values.

In order to quantify the effect of shocklets over the TKE equation (Equation (3.10)) and therefore over the mixing layer growth rate, one can analyze the compressible component of the dissipation given in Equation (3.11). Zeman (1990) and Sarkar *et al.* (1991) show that the dilatational part of the dissipation increases with the turbulent Mach number because of the occurrence of eddy shocklets in the compressible regime. Wang *et al.* (2020) perform compressible isotropic turbulence simulations and observe that shocklets act as kinetic energy sinks which absorb large-scale kinetic energy. Shocklets are thus an additional source of dissipation. The dilatational dissipation is computed over the self-similar period. Figure 4.28 shows the ratio between the compressible and the total dissipation rate over the cross-stream direction. Around $y/\delta_\theta(t) \approx 3.5$, one can note an increase of the ratio. It corresponds to the borders of

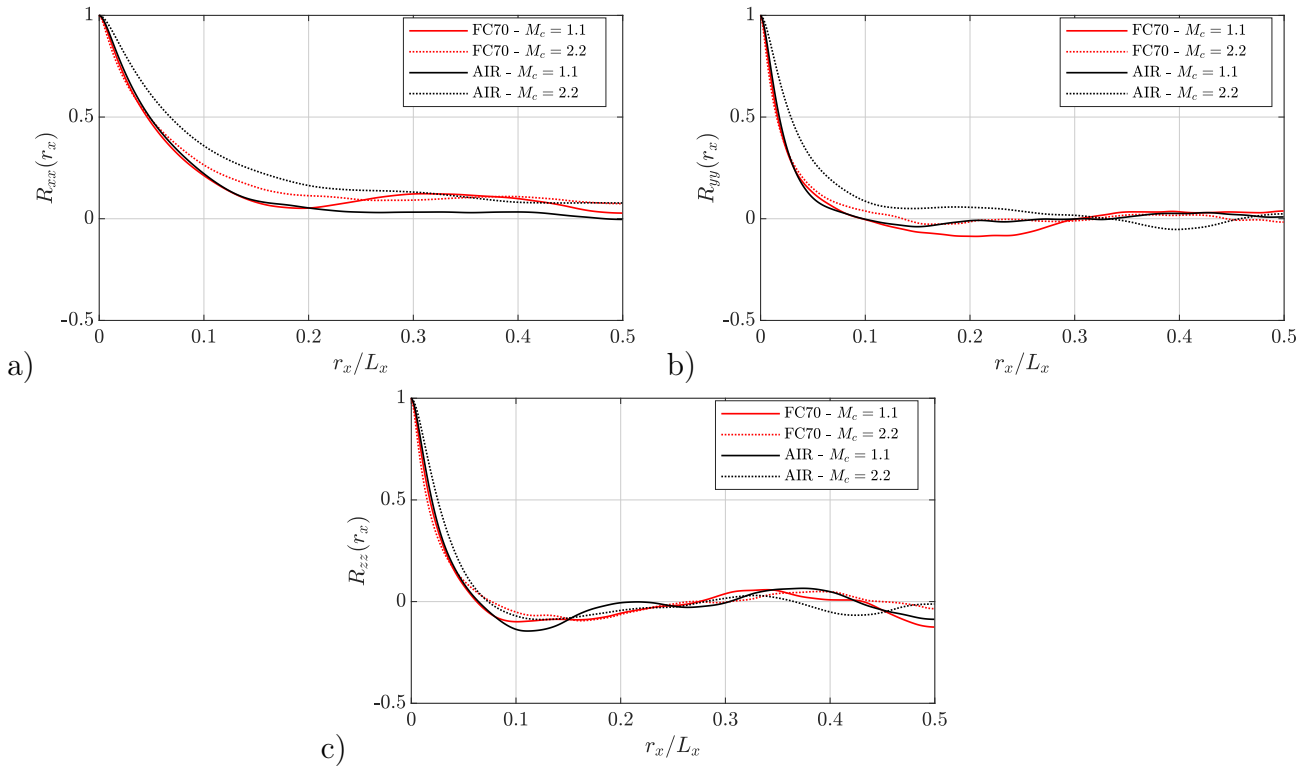

Figure 4.29: The streamwise two-point correlations of the (a) $x-$, (b) $y-$ and (c) $z-$ velocity component at the beginning of the self-similar period. Comparison is made between FC-70 and Air at $M_c = 1.1$ and $M_c = 2.2$.

the mixing layer, outside of which the dissipation ϵ drops to zero (see Figure 4.8). Except for these regions, at $M_c = 1.1$, the compressible dissipation represents less than 0.5% of the total dissipation for both DG and PG flows. At $M_c = 2.2$, the ratio increases consistently with the increase of turbulent Mach numbers. The ratio is thus larger for DG flow compared to PG flow. However, the ratio of dilatational dissipation with respect to the total dissipation remains below 4% for DG and below 1% for PG. Compressible dissipation can therefore be neglected when compared to the total dissipation. Shocklets have a limited influence on the TKE equation. Since the TKE equation governs the mixing layer dynamics, one cannot explain discrepancies observed between DG and PG flows through shocklets effects.

4.4.2 Spatial correlations

This section is devoted to the analysis of two-point spatial correlations of the velocity components. Both PG and DG flows are analyzed and compared.

In the streamwise direction, this correlation factor writes:

$$R_{ii}(r_x) = \frac{\overline{u_i{}'(\boldsymbol{x})u_i{}'(\boldsymbol{x} + r_x\boldsymbol{e_x})}}{\overline{u_i{}'(\boldsymbol{x})u_i{}'(\boldsymbol{x})}} \tag{4.10}$$

where i denotes the direction of the velocity.

Figure 4.29 shows the evolution of the two-point correlation over the streamwise direction for the three velocity components. In the PG case, the correlation increases significantly for

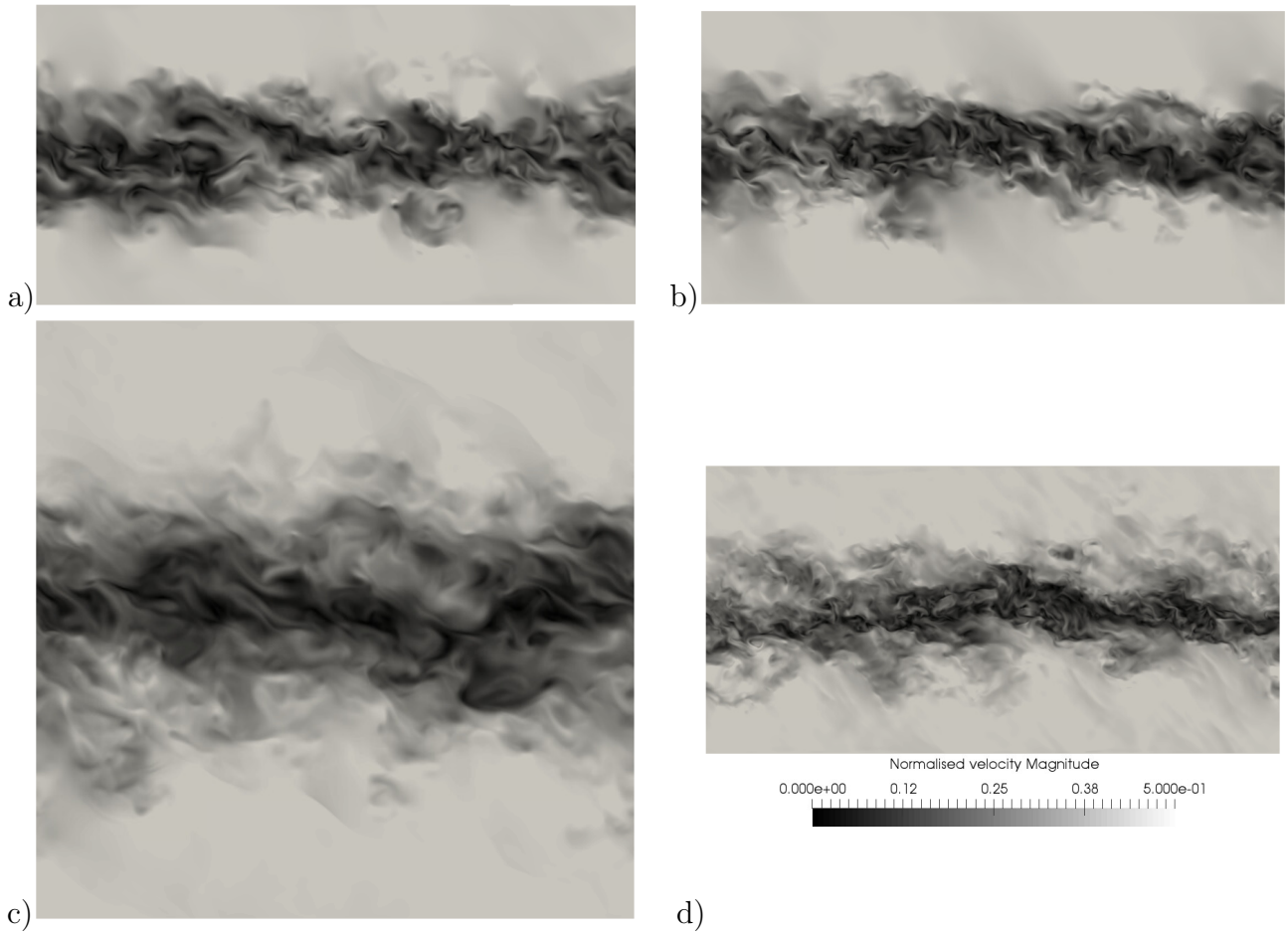

Figure 4.30: Snapshot of the velocity magnitude normalized with Δu at the beginning of the self-similar period. Comparison is made between Air at (a) $M_c = 1.1$ and (c) $M_c = 2.2$ and FC-70 at (b) $M_c = 1.1$ and (d) $M_c = 2.2$.

the $x-$ and $y-$ velocity components as M_c increases. As noticed in Freund *et al.* (2000) and Matsuno & Lele (2020), at high compressible regimes, eddies are stretched in the streamwise direction. In the DG case, the correlation stays approximately the same between $M_c = 1.1$ and $M_c = 2.2$ for the three components, except for the $x-$ component which is slightly larger for $M_c = 2.2$ when compared with $M_c = 1.1$. The structure of eddies stays therefore approximately the same in the streamwise direction unlike for PG flows. One can also notice that for all cases, the correlation drops to a low value at $r_x/L_x = 0.5$ which confirms that the streamwise domain length is sufficiently large.

Figure 4.30 shows snapshots of the velocity magnitude. As noticed in Figure 4.29, the size of turbulent structures increase from $M_c = 1.1$ to $M_c = 2.2$ in PG flow unlike in DG flow, where the size of turbulent structures remains stable between $M_c = 1.1$ to $M_c = 2.2$. At $M_c = 1.1$, there is no difference between DG and PG flow field visualization. Consistently with the evolution of the normalized momentum thickness growth rate as a function of the convective Mach number (Figure 4.18), differences between DG and PG appear at $M_c = 2.2$ in the highly compressible regime.

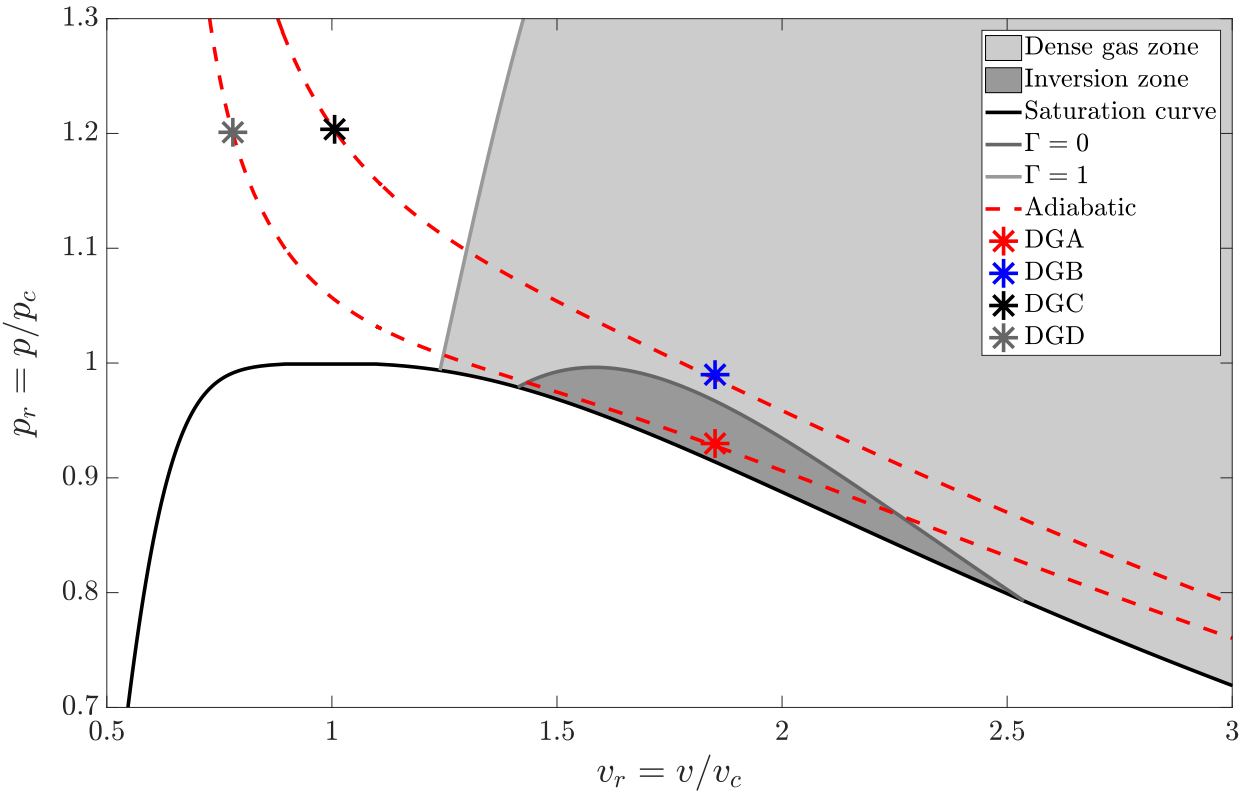

Figure 4.31: Four different initial thermodynamic states used to perform additional DNS are represented in the non-dimensional $p - v$ diagram for BZT dense gas FC-70 at $M_c = 2.2$. The dense gas zone ($\Gamma < 1$) and the inversion zone ($\Gamma < 0$) are plotted for the Martin-Hou equation of state. p_c and v_c are respectively the critical pressure and the critical specific volume.

	Γ_0	γ_0	(L_x, L_y, L_z)	(N_x, N_y, N_z)	$r = L_\eta/\Delta x$	l_x/L_x	l_z/L_z
DGA	-0.28	1.31	$(688, 344, 172)$	$(1024, 512, 256)$	$0.52 - 0.57$	$0.10 - 0.16$	$0.06 - 0.05$
DGB	0.10	1.21	$(688, 344, 172)$	$(1024, 512, 256)$	$0.51 - 0.55$	$0.11 - 0.12$	$0.06 - 0.04$
DGC	2.10	1.61	$(688, 688, 172)$	$(1024, 1024, 256)$	$0.50 - 0.55$	$0.11 - 0.166$	$0.06 - 0.04$
DGD	2.21	1.75	$(688, 688, 172)$	$(1024, 1024, 256)$	$0.50 - 0.54$	$0.09 - 0.14$	$0.07 - 0.07$

Table 4.3: Simulation parameters for additional FC-70 simulations at $M_c = 2.2$ varying the initial operating point. r, l_x/L_x and l_z/L_z are given at beginning and ending times of self-similar periods. $L_0 = L_x/8$ for all the simulations.

4.4.3 Influence of the initial thermodynamic operating point

In order to explain discrepancies observed between DG and PG flows, additional DNS are performed at $M_c = 2.2$ varying the initial thermodynamic operating point. Figure 4.31 shows the four selected operating points. DGA corresponds to the reference simulation previously analyzed and compared to PG DNS. DGA's initial operating point is located inside the inversion zone also called BZT region. The operating point of the second simulation DGB is chosen outside the inversion region and inside the dense gas zone. This enables us to investigate BZT effects on the mixing layer growth. Finally, for DGC and DGD, the initial operating points are chosen on the same adiabatic curves as respectively DGB and DGA but outside the dense gas zone. The diversity of initial thermodynamic regions thus explored aims at providing a proper understanding of the effects of dense gas on the shear layer growth rate.

One needs first to validate the DNS named DGB, DGC and DGD. Table 4.3 provides the simulations parameters including r, l_x, and l_z for the four different simulations. Values are very close to DGA and since DGA is validated in Appendix B, one can consider DGB, DGC and DGD as adequately resolved. The size of computational domains have been enlarged for DGC and DGD in the y direction in order to provide the mixing layer with more space to properly reach self-similarity (without interfering with the lower and upper boundaries).

Self-similar periods are defined for each DNS using the same methodology previously presented in Section 3.3.1. Plateaus showing constant integrated turbulent production correspond to self-similar periods. They are identified with vertical lines in Figure 4.32. In addition, beginning and ending times are given in the caption for each case. Although all the DNS are performed at the same convective Mach number $M_c = 2.2$, results are quite different. The initial evolution is similar, but after $\tau \approx 1100$, discrepancies appear especially for DGD. Maximum values and self-similar regimes are influenced by the initial thermodynamic operating point.

The comparison of mixing layer momentum thickness evolutions is shown in Figure 4.33. Slopes with standard deviations computed during self-similar regimes are indicated on the plot. From these results, one can deduce that BZT effects do not have a major influence on the mixing layer growth. DGC's growth rate is indeed very close to DGA's although the initial thermodynamic operating points are located respectively outside and inside DG and BZT regions. The relation between the mixing layer growth and the initial thermodynamic operating point is not obvious: operating points located on the same adiabatic curve (respectively DGA,

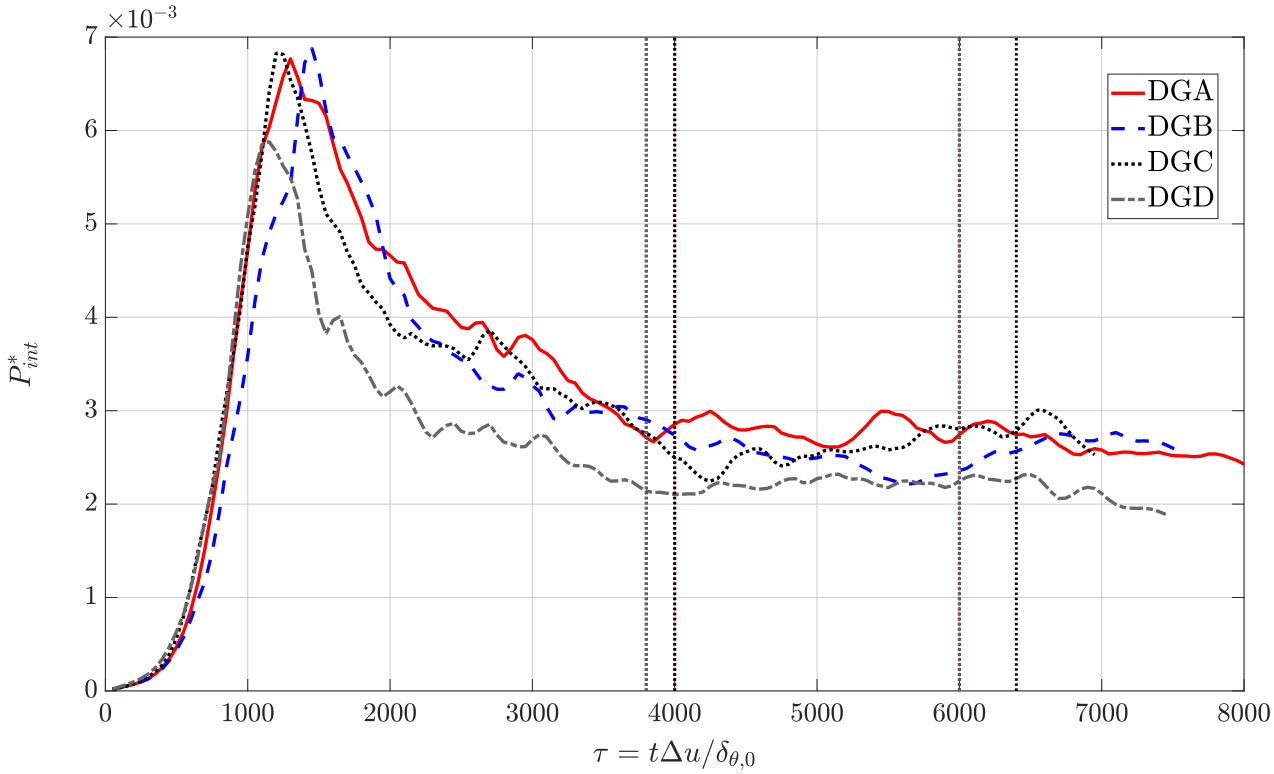

Figure 4.32: Temporal evolution of the non-dimensional streamwise turbulent production terms integrated over the whole domain $P^*_{int} = (1/(\rho_0(\Delta u)^3)) \int_{L_y} \bar{\rho} P_{xx} dV$ (with $\bar{\rho} P_{xx}(y) = -\overline{\rho u''_x u''_y} \frac{\partial \tilde{u}_x}{\partial y}$) at $M_c = 2.2$. Results are shown for the FC-70 for four different DNS: DGA, DGB, DGC and DGD. Self-similar periods are indicated on each plot: DGA ($\tau \in [4000/6000]$); DGB ($\tau \in [4000/6400]$); DGC ($\tau \in [3800/6000]$) and DGD ($\tau \in [3800/6000]$).

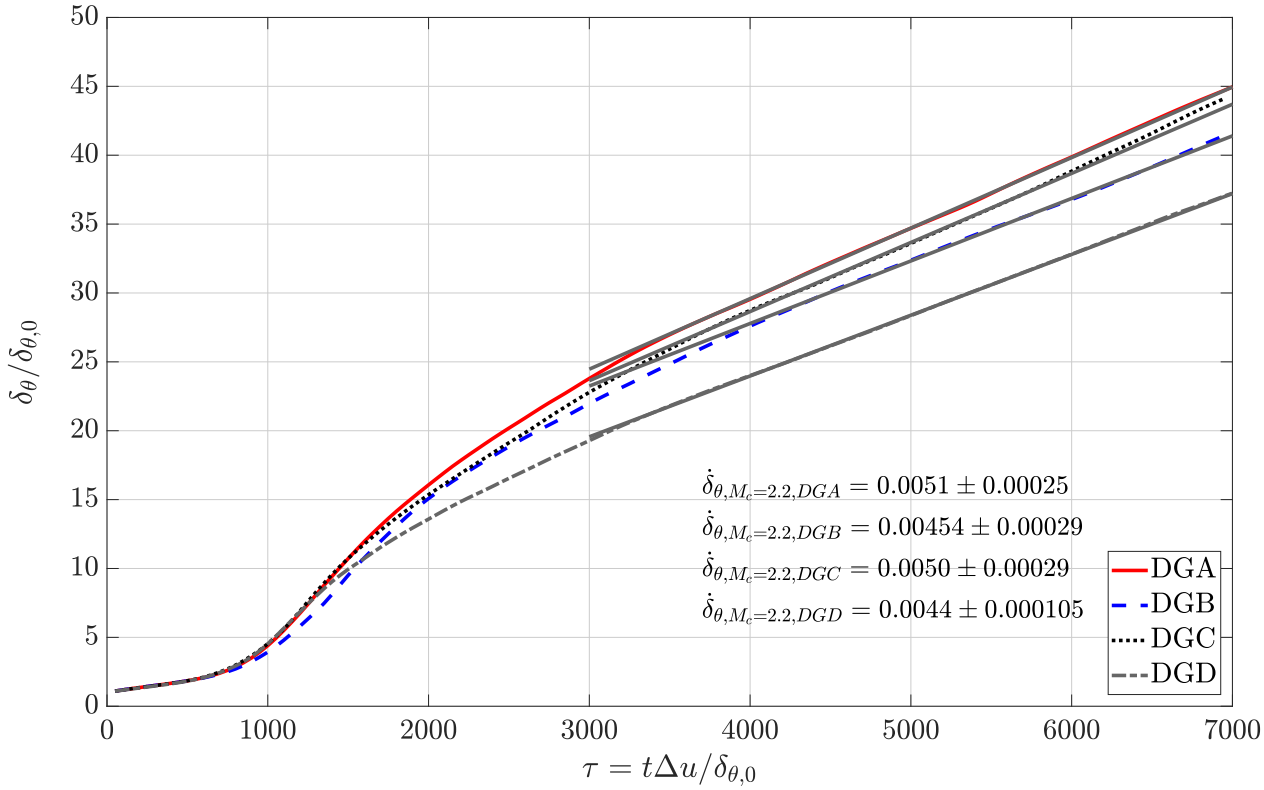

Figure 4.33: Temporal evolution of the mixing layer momentum thickness for DG at $M_c = 2.2$. Results are shown for the FC-70 for four different DNS: DGA, DGB, DGC and DGD.

DGD and DGB, DGC) are different in terms of growth rate. Looking at the growth rate, simulations can be organized by pairs: DGA and DGC display similar values while DGB and DGD also display similar values but below those of DGA and DGC. One can observe that slopes are all below that of the $M_c = 1.1$ case. Yet all DG mixing layers have a larger growth rate when compared to the PG ones meaning that the observed effect is not specific to the BZT or DG regions. This confirms the dismissed hypothesis of a shocklets influence over the mixing layer growth analyzed in Section 4.4.1. It might be more of a transcritical effect and the distance to the critical point seems to influence the mixing layer growth rate.

At the end of Section 4.3.2, the physical explanation provided by Pantano & Sarkar (2002) was verified on DGA: the reduction of the momentum thickness is due to a reduction of normalized pressure fluctuations. It remains to be checked whether this reduction of normalized pressure fluctuations is also observed for DGB, DGC and DGD. Figure 4.34 shows the normalized growth rate as a function of the normalized pressure fluctuations computed at the center of the mixing layer. For the PG flow, the reduction is significant. Between $M_c = 1.1$ and $M_c = 2.2$, growth rate and normalized pressure fluctuations are divided by a factor of two. For DG, the decrease of the normalized growth rate is also correlated with a decrease of pressure fluctuations. Among cases at $M_c = 2.2$, the ranking purely based on the level of pressure fluctuations is not entirely satisfactory but this could be explained by standard deviations caused by variations of the plateaus of integrated turbulent production. Moreover, other effects are investigated in the next sections to give further explanations.

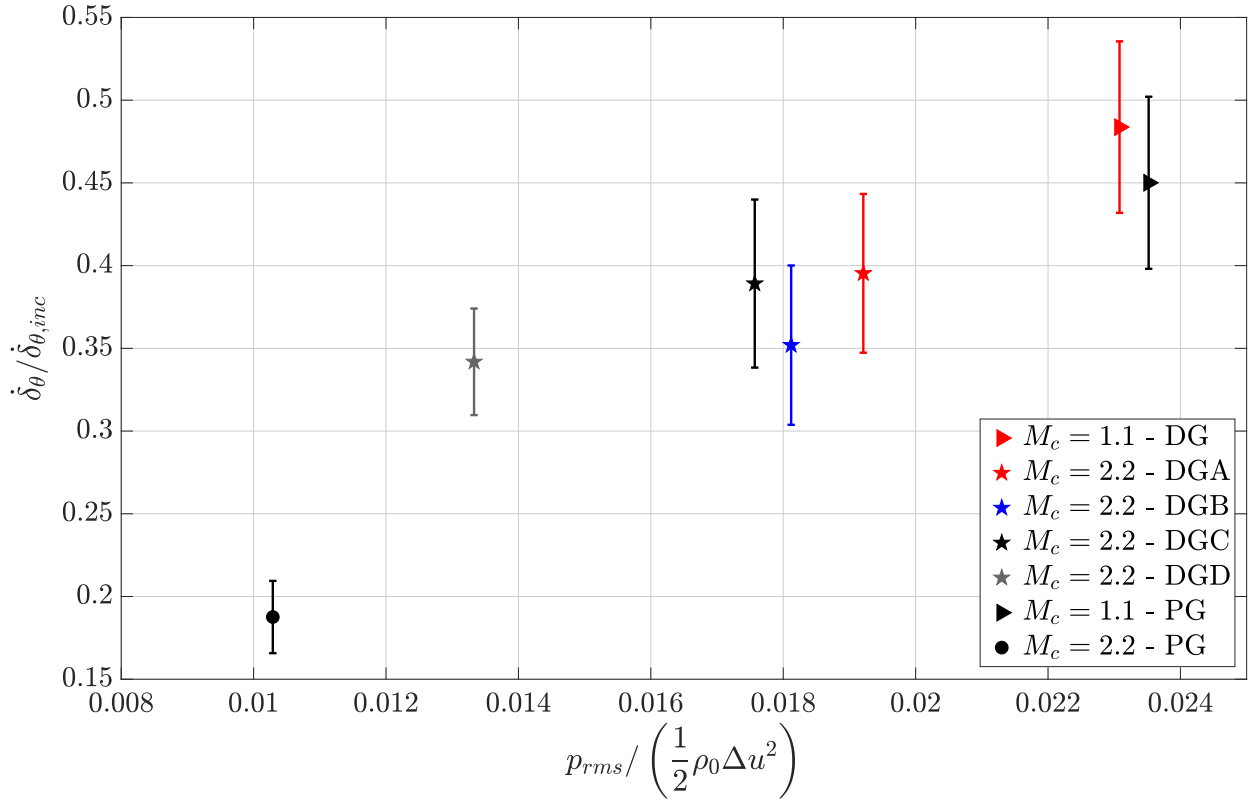

Figure 4.34: Evolution of the non-dimensional mixing layer growth rate over the center root-mean square value of pressure normalized by $\frac{1}{2}\rho_0(\Delta u)^2$. Results are given for DG and PG at $M_c = 1.1$ and $M_c = 2.2$.

4.4.4 Evolution of non-dimensional terms

To complete the evaluation of the order of magnitude for the terms appearing in the compressible Navier-Stokes equations previously made in Section 4.1.2, the non-dimensional factors given in Table 4.2 are computed for the other DG DNS corresponding to the four initial thermodynamic operating points (DGA / DGB / DGC / DGD) and the normalized mixing layer growth rate is plotted as the function of these factors.

Figure 4.35 shows the non-dimensional terms related to the momentum equations: the pressure gradient and the viscous terms. For both terms, the orders of magnitude are the same for DG and PG flows. For the pressure gradient term, no clear correlation is found. Its magnitude remains approximately the same for the three convective Mach numbers and is quite close between DG and PG mixing layers even though the growth rate strongly varies. Differences appear when the initial thermodynamic operating point is modified but this only translates into a small influence on the growth rate. The viscous term is much more correlated with the growth rate reduction. As the non-dimensional factor related to the viscous term increases, the growth rate significantly decreases. In fact, since the ratio is equal to $2M_c/Re_{\delta_\theta}$, the plot is very close to the $\dot{\delta}_\theta/\dot{\delta}_{\theta,inc} = f(M_c)$ plot. Note that the viscous term is about two orders of magnitude smaller than other terms (the pressure gradient and the temporal and convective derivatives of the momentum) because of the turbulent regime.

Figure 4.36 displays non-dimensional ratios appearing in the energy equation. Unlike the momentum equations, strong differences appear for the DG flow. As noticed in Section 4.1.2, for the DG flow, the temporal and convective derivatives of kinetic energy, the pressure gradient, the viscous work and the heat-flux can be neglected with respect to the temporal and convec-

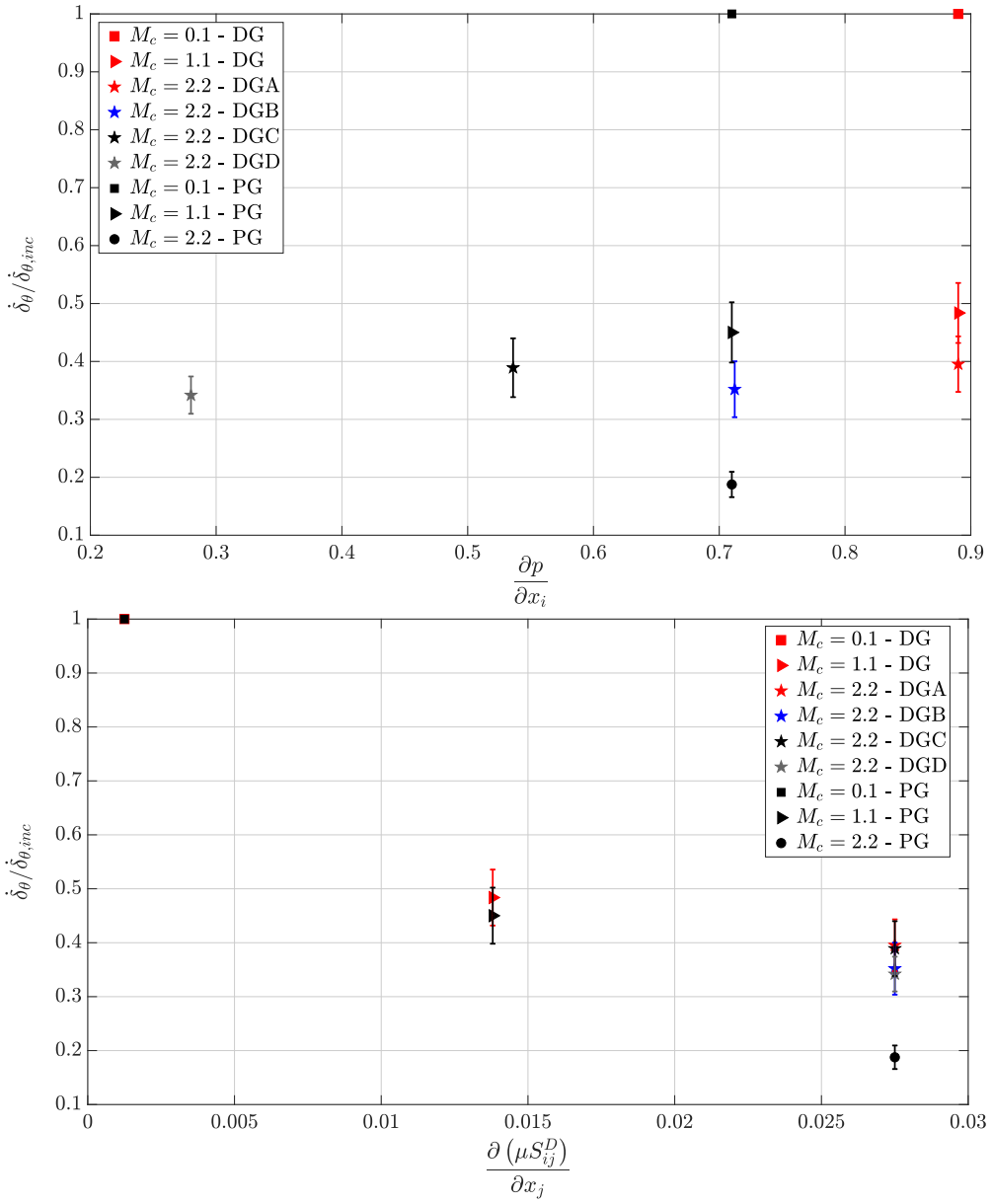

Figure 4.35: The mixing layer growth rate is plotted as a function of the non-dimensional terms appearing in the momentum equations (Equations (2.23) and (2.34)): the pressure gradient term (top) and the viscous term (bottom).

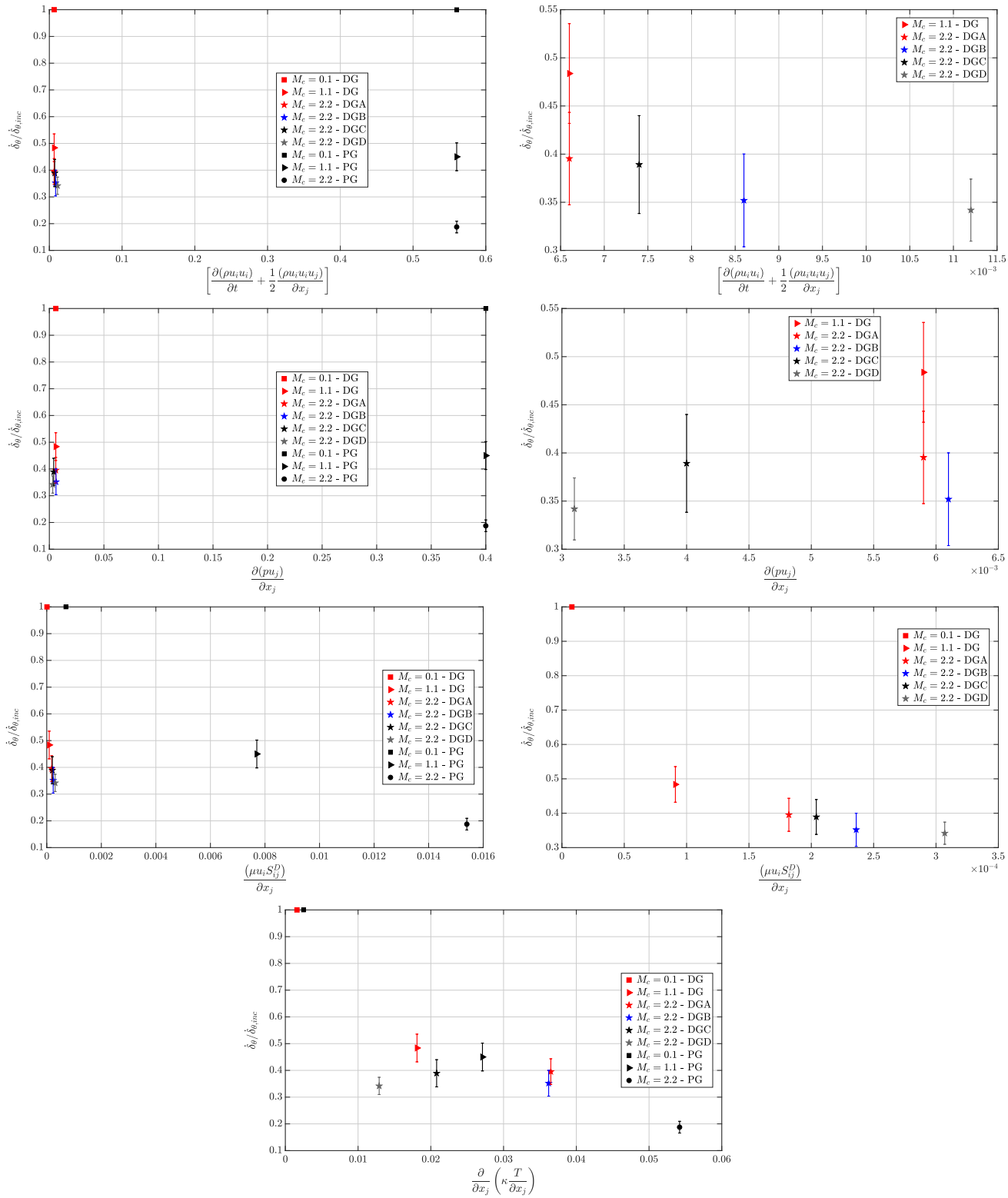

Figure 4.36: The mixing layer growth rate is plotted as a function of the non-dimensional terms appearing in the energy equation (Equations (2.23) and (2.34)): the temporal and convective derivative of the kinetic energy; the pressure work; the viscous work and the heat-flux (from top to bottom). Comparison is made between DG and PG DNS (left) and only DG DNS (right).

tive derivatives of the internal energy since they are at least two orders of magnitude smaller. Some interesting features can be noticed: as the temporal and the convective derivatives of the kinetic energy grow in the DG mixing layer, the growth rate decreases and becomes closer to the PG mixing layer growth rate; the same effect is observed for the viscous work. Even when the location of the initial thermodynamic operating point is varied for the DG flow, the order of magnitude of the energy equation terms (except for the heat-flux) remains significantly smaller when compared with the PG flow.

The main conclusion that can be drawn is that DG flows are characterized by a strong influence of the internal energy which dominates all other terms. Yet, some terms, in particular the ones associated to the kinetic energy, are correlated with the growth rate.

4.4.5 Other influencing factors

Several factors can be identified, which contribute to explain the observed discrepancies between DG and PG mixing layers. The first main difference between DG and PG flows is the ratio between the enthalpy and the kinetic energy. It is associated to the Eckert number. As evidenced in the aforementioned paragraph, the temporal and the convective derivatives of the internal energy dominate all other terms in the energy equation. Since internal energy and enthalpy are of the same order of magnitude[†], it is expected that enthalpy will dominate the kinetic energy. The Eckert number is defined for the mixing layer as:

$$Ec = \frac{(\Delta u)^2}{c_{p_0} T_0} \tag{4.11}$$

where c_{p_0} denotes the initial specific heat capacity at constant pressure and T_0, the initial temperature. Initial Eckert numbers are computed for each DNS and results are gathered in Table 4.4. For DG flows, values are about two orders of magnitude lower than PG flows. Two features of DG mixing layers are responsible for these significant differences: the large heat capacity of FC-70 and the small differential speed Δu. The differential speed is defined in order to get the same initial convective Mach number between DG and PG mixing layers. Since the sound speed is much lower in dense gases, a much lower differential speed is obtained for a given value of the convective Mach number, which mechanically reduces the Eckert number. With small Eckert numbers, kinetic energy becomes negligible when compared to the enthalpy. It is the case for all DG flows in this study even though the convective Mach number is large. As shown by the present results, kinetic energy also decouples from thermodynamics compressibility effects and the growth rate of the momentum thickness is allowed to reach larger values. It can be observed that the close values of the momentum thickness growth rates for DGA / DGC on one hand and DGB / DGD on the other hand are well correlated with the values of the initial Eckert number reported in Table 4.4. The lower Eckert numbers for DGA / DGC correspond to higher growth rates for these shear layer configurations, induced by an even stronger decoupling between internal and kinetic energy for DGA/DGC with respect to DGB/DGD. However, the Eckert number can not be the only factor explaining dense gas effect on the growth rate since DGC displays a slightly lower growth rate with respect to DGA, with a slightly lower value of the initial Eckert number.

Since the Eckert number quantifies friction heating, it is significantly reduced in DG flows as previously shown by Gloerfelt *et al.* (2020). Figure 4.38 shows the distribution of the Reynolds

[†]At the initial conditions γ is about 1.3 so that internal energy and enthalpy are of the same order of magnitude.

	M_c	Ec	$\dot{\delta}_\theta/\dot{\delta}_{\theta,inc}$
DG	1.1	0.0040	0.484
DGA	2.2	0.0162	0.395
DGB	2.2	0.0226	0.352
DGC	2.2	0.0147	0.389
DGD	2.2	0.0203	0.342
PG	1.1	1.94	0.450
PG	2.2	7.74	0.188

Table 4.4: Eckert numbers and normalized momentum thickness growth rates are given for each simulation.

averaged temperature, density and the root mean square value of density fluctuations along the cross-stream direction of the shear layer. Results are averaged over the self-similar period. It can be observed in Figure 4.38 that temperature variations are almost suppressed for DG. Sciacovelli *et al.* (2017*a*) confirm this remark in supersonic turbulent channel flows and state that dense gas flow are less subject to friction losses associated with Mach number effects. For the mixing layer, above $M_c = 1.1$, compressibility effects associated with the increase of convective Mach number have less influence on DG flows in part because of the reduction of friction heating.

The evolution of the average density confirms this reduction. The PG air density experiences a 40% decrease at the mixing layer center between $M_c = 1.1$ and $M_c = 2.2$. In the PG, friction heating is important and leads to an increase of the temperature, which induces a decrease of the density. The mechanism is significantly reduced in dense gas flows. For DG, the temperature is almost constant and average density displays very limited variations. At $M_c = 2.2$, the averaged density decrease at the center of the mixing layer represents about 8% of the initial density compared to 40% for air. Equation (3.12) shows that this effect influences the mixing layer growth rate which depends on the density. As the mixing layer develops in PG, strong friction occurs at the center, which decreases the density. The momentum thickness growth rate is thus significantly reduced for PG when compared to DG. Yet, the decrease of the Reynolds-averaged density is not the only factor. Figure 4.37 displays the growth rate of a modified momentum thickness without the influence of the average density, namely a velocity thickness:

$$\delta^*_\theta(t) = \frac{1}{(\Delta u)^2} \int_{-\infty}^{+\infty} \left(\frac{(\Delta u)^2}{4} - \widetilde{u}_x^2 \right) dy \tag{4.12}$$

The velocity thickness growth remains larger than the momentum thickness but yet still decreases with the convective Mach number. There are still differences between DG and PG mixing layers, but they are significantly reduced. They now represent about 25% against 50% previously. The decrease of the average density has a significant influence over the momentum thickness growth rate. Yet, it can only partly explain discrepancies between DG and PG flows.

Figure 4.38c displays the root mean square value of density fluctuations. Between PG and DG flows, the distribution across the mixing layer changes shape. For PG, it consists in two symmetric peaks with respect to the center of the mixing layer. Peaks are located at the borders of the mixing layer, where the cross-stream gradient of averaged density is maximal. In this region, the mixing layer flow experiences strong dynamic and thermal variations with an

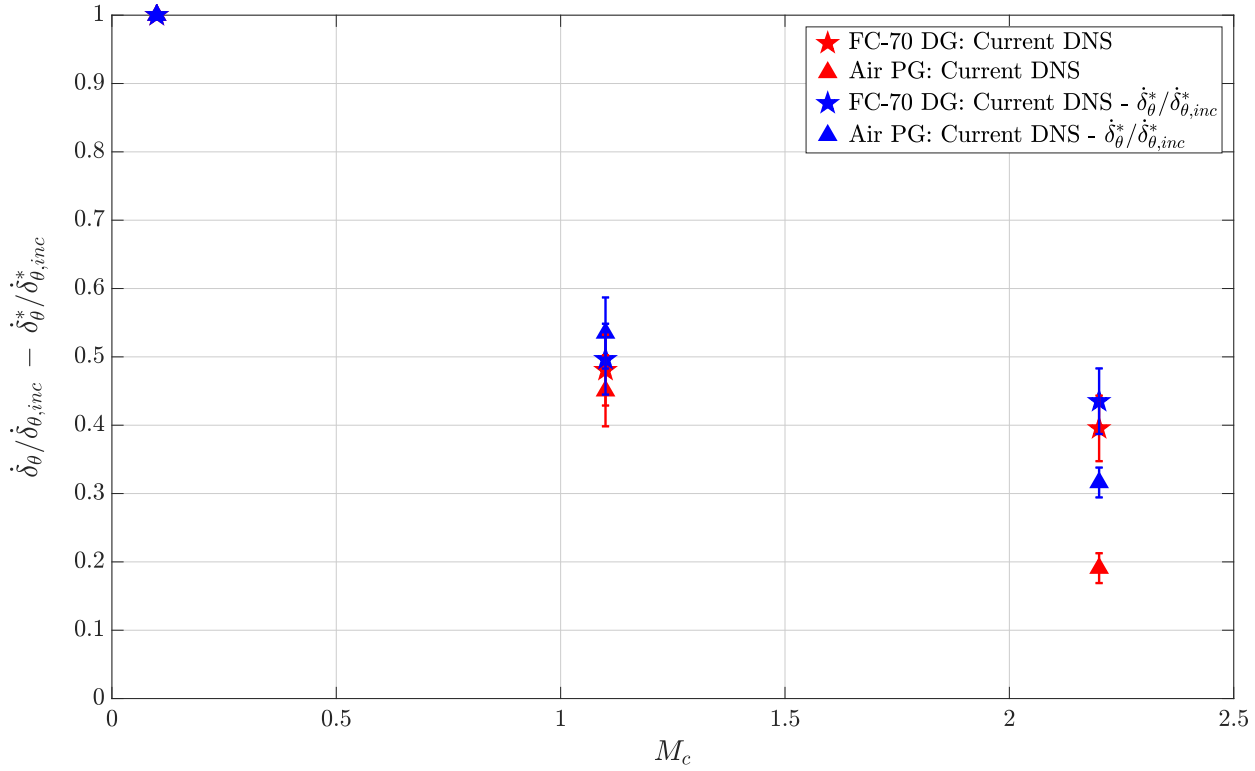

Figure 4.37: Evolution of the growth rates of the momentum thickness (δ_θ) and the velocity thickness (δ^*_θ) (see Equation (4.12)) over the convective Mach number for air and for FC-70.

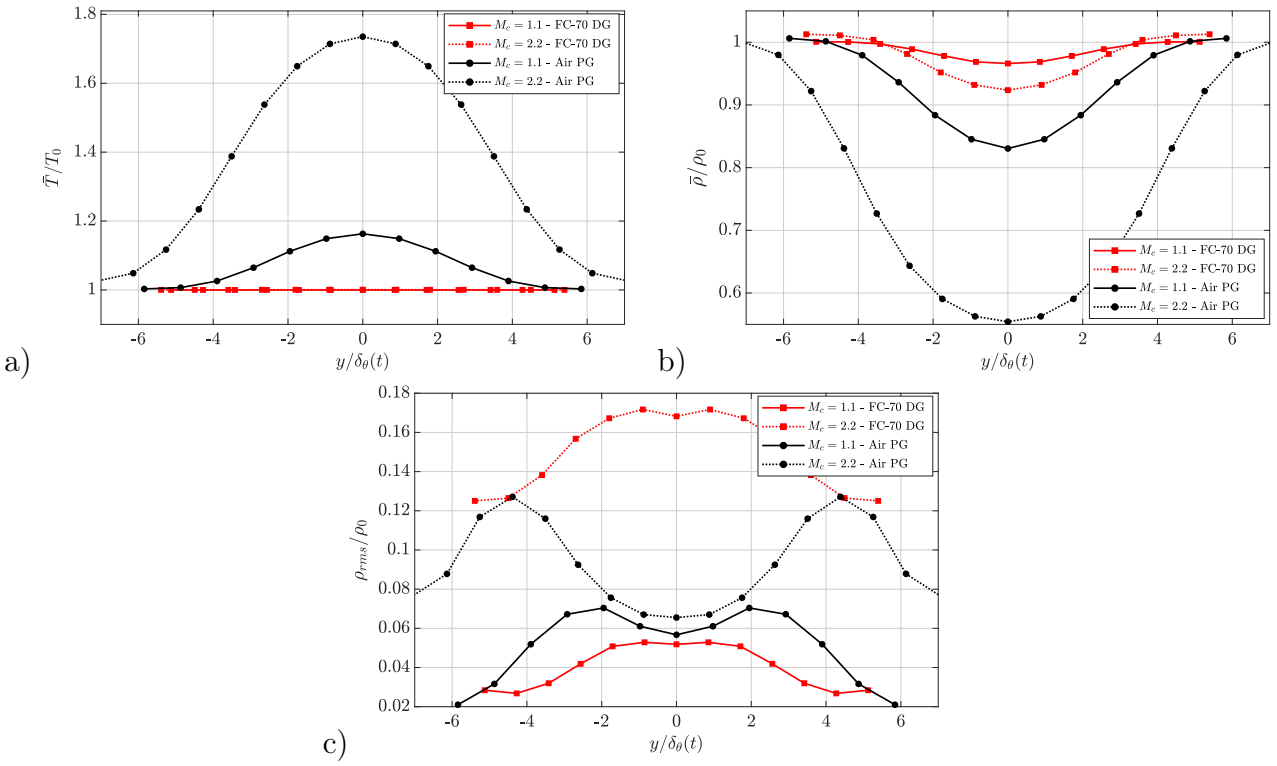

Figure 4.38: The non-dimensional Reynolds averaged temperature (a) and density (b); and root mean squared value of the density (c) are averaged over the self-similar regime and plotted along the y direction. Comparison is made between FC-70 and Air at $M_c = 1.1$ and $M_c = 2.2$.

important coupling between internal and kinetic energy. For DG, the distribution is composed of a single peak located at the center of the mixing layer. The distribution is much less affected by the variation of the averaged density. For DG, thermal quantities are less influenced by flow dynamics because of the decoupling of internal energy and kinetic energy. The root mean square value of density fluctuations therefore diffuses from the center of the mixing layer.

The amplitudes of the distributions are also quite different between DG and PG flows. For DG, the maximum root mean square value of density fluctuations is multiplied by a factor of three from $M_c = 1.1$ to $M_c = 2.2$. In the PG case, it is multiplied by a factor of about two. Compressible flows are more subject to root mean square density fluctuations which increase with the Mach number. An explanation can be found in the definition of the isentropic compressibility coefficient, which is large for DG flows:

$$\chi_s = \frac{1}{\rho}\frac{\partial \rho}{\partial p}\bigg|_s \tag{4.13}$$

For flows with large values of χ_s, small variations of pressure lead to large variations of density. The sound speed is directly linked to the isothermal compressibility since:

$$c = \frac{1}{\sqrt{\rho \chi_s}} \tag{4.14}$$

For DG flows, the large isentropic compressibility factor strongly diminishes the sound speed. As a result, the initial sound speed in the computed DG flows is about six times smaller when compared to its initial value for the PG shear layers. Figure 4.39 shows the normalized momentum growth rate at $M_c = 2.2$ as a function of the normalized sound speed. A rather clear correlation appears between the momentum thickness growth rate and the initial sound speed: the growth rate decreases with increasing sound speed.

The main conclusion that can be drawn from these observations is that the smaller Eckert number in DG flows causes a decoupling between internal and kinetic energies and induces less friction heating. Both phenomena influence the mean and fluctuating thermal physical quantities, which consequently limits the compressibility-related reduction of the momentum thickness growth rate.

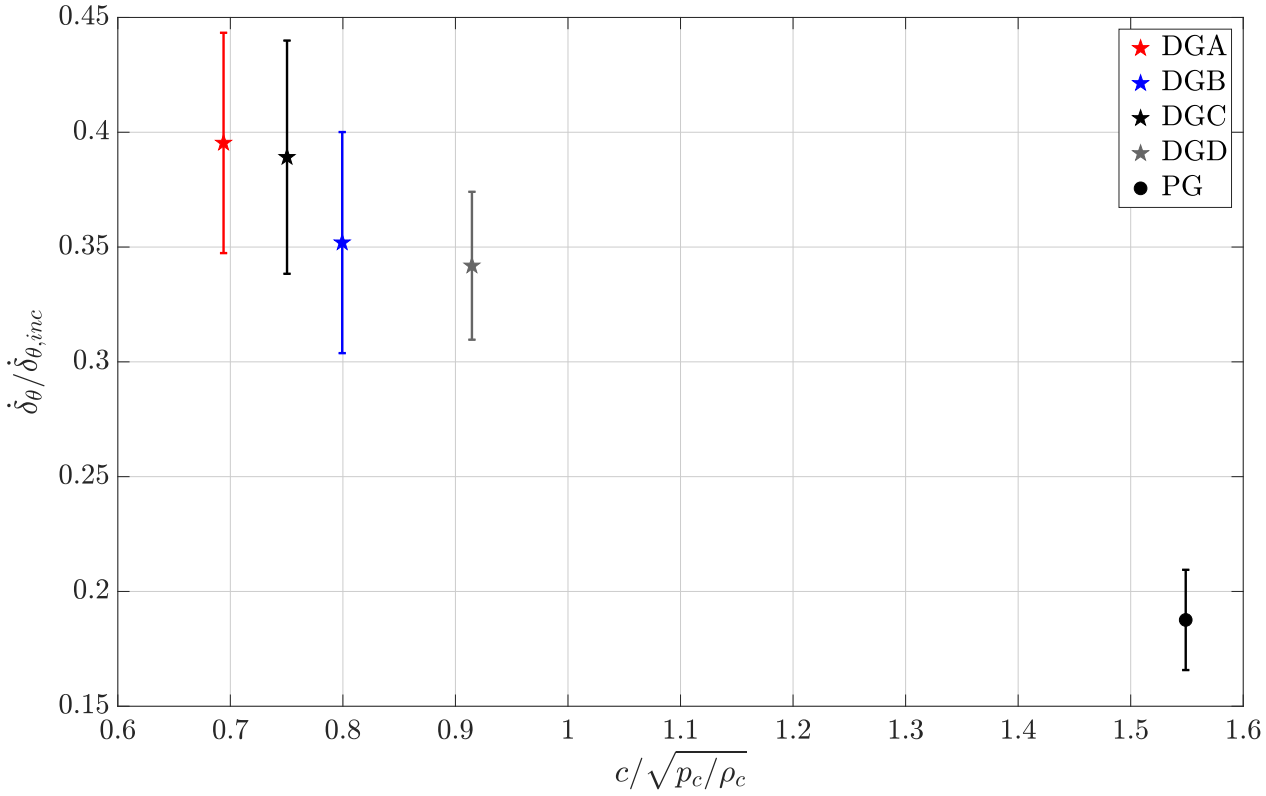

Figure 4.39: Evolution of the non-dimensional mixing layer growth rate as a function of the sound speed normalized with $\sqrt{p_c/\rho_c}$. Results are given for DG and PG at $M_c = 2.2$.

4.5 Concluding remarks

DNS of the compressible mixing layer have been achieved for air described as a perfect gas and FC-70 (BZT gas) described using Martin Hou EoS at three convective Mach numbers $M_c = 0.1 - 1.1 - 2.2$. The choice of the domain size is paramount in this study. The domain is enlarged at $M_c = 2.2$ for both DG and PG DNS when compared to DNS at $M_c = 1.1$ in order to ensure mixing layers reach self-similarity. An analysis presented in Appendix B is performed to thoroughly investigate the sensitivity of the DG mixing layer to the domain extent and to the size of the initial turbulent structures. Results establish the relevance of the choices made in the present study.

The selection of the self-similar period is a key point in the study of mixing layers: this choice is complex and the diversity of criteria used for the selection process contributes to the scattering of $\dot{\delta}_\theta/\dot{\delta}_{\theta,inc} = f(M_c)$ plots reported in the literature. In the present work, self-similar periods are selected using the integrated streamwise production over time, which is proportional to the momentum thickness growth rate under certain conditions (Vreman *et al.*, 1996*a*).

The comparison between perfect and dense gases shows major differences for the momentum thickness growth rates at $M_c = 2.2$. At $M_c = 2.2$, the growth rate is twice as large for dense gas when compared to perfect gas. Pantano & Sarkar (2002) demonstrate that for perfect gas flows the growth rate reduction is due to the reduction of pressure fluctuations leading to the reduction of pressure-strain terms. We show that growth rate is also correlated with pressure fluctuations in dense gas flows. Yet, the small scales dynamics is very different. A much larger dissipation is also observed for perfect gas mixing layer. These results call for a specific subgrid scale modeling for dense gas flows when simulated using Large Eddy Simulation. The next chapter is therefore dedicated to the *a priori* assessment of subgrid-scale terms for DG flow.

Additional dense gas DNS have been performed for three other initial thermodynamic operating points. Results show that BZT effects have only a small impact on the mixing layer growth. Discrepancies between DG and PG flows are more likely related to transcritical real gas effects than to the BZT and the DG thermodynamic regions. Shocklets indeed produce only a limited effect on the mixing layer growth. The compressible dissipation is negligible when compared with the total dissipation. For dense gas mixing layers, several physical factors tend to reduce compressibility effects: the decoupling of kinetic and internal energies reduces the effect of increasing M_c; reduced friction losses in dense gas flows modify the distribution of the averaged density, which therefore favors the momentum thickness growth rate. Finally, it is found that increasing the initial isothermal compressibility also increases the momentum thickness growth rate in dense gas flows. Initial sound speeds could therefore be an appropriate indicator when forecasting the mixing layer growth rate in real gas flows. Note that the perfect gas results are restricted to air, with heat capacity ratio equal to $\gamma = 1.4$. Further exploration could investigate the effect of γ close to unity over the perfect gas results and provide a comparison with the dense gas results in order to separate possible $\gamma-$effects from dense gas effects.

Chapter 5

A priori analysis of turbulence in dense flows: the need for (specific) modeling

Contents

3.1 Perfect gas compressible shear layer 35

3.2 Problem formulation 37

3.2.1 Initialization 37

3.2.2 Turbulent Kinetic Energy equation 39

3.3 DNS verification and validation 40

3.3.1 Temporal evolution and selection of the self-similar period 41

3.3.2 Validation over the self-similar period 45

3.3.3 Concluding remarks 50

In order to evaluate the need for specific LES modeling of DG compressible flows, this chapter is devoted to the *a priori* assessment of subgrid-scale (SGS) terms with respect to resolved terms present in the real gas LES formulation presented in Section 2.4.3. A review of compressible *a priori* results from the literature is proposed in the first section. The importance of subgrid-scale terms is assessed in the second section for the DG mixing layer thoroughly analzed in the present work and for the DG homogeneous isotropic turbulence (with results taken from the published work Giauque *et al.* (2020)). New terms which are not modeled for PG flows are shown to be significant for DG flows: the SGS pressure term in the filtered momentum equation and the SGS pressure work in the filtered total energy equation. The present chapter draws from Giauque *et al.* (2021).

5.1 State of the art

LES and SGS models Since its origin in the 1960's and the seminal articles of Smagorinsky (1963), Deardorff *et al.* (1970) and Leonard (1975), LES has brought invaluable understanding to the influence of unsteady features in numerous types of turbulent flows, from the most academic ones such as channel or mixing layer flows (Moin & Mahesh, 1998*b*; Piomelli *et al.*, 1988; Meneveau & Katz, 2000), to industrial combustion chambers or turbomachinery flows (Di Mare *et al.*, 2004; Giauque *et al.*, 2005; Wolf *et al.*, 2012). LES tends to be currently used with highly refined grids which enables the accurate description of small scales dynamics and reduces the dependence on the accuracy of the subgrid-scale turbulence modeling but also significantly increases the computational cost which limits its use in the industrial community. Since LES simulations give access to a more complete description of turbulent flows when compared to RANS simulations, the industry would strongly benefit from an increase of LES use for optimization and iterative design procedures. In order to foster its use, coarse LES must demonstrate it provides accurate statistics for the computed turbulent flows and this requires an accurate subgrid-scales description. To that end, one needs both a proper assessment of significant SGS terms and the design of accurate models for these important terms.

LES relies on the filtered Navier-Stokes equations composed of resolved and SGS terms (see Section 2.4). These SGS terms can either be modeled or neglected. Table 2.4 gathers SGS terms for the compressible LES formulation and also indicates if they are usually modeled or neglected in the PG literature. The SGS internal energy flux and the SGS turbulent stress tensor are considered to be the most important terms (Garnier *et al.*, 2009). Consequently, those two terms (and especially the SGS turbulent stress tensor) have been the focus of the subgrid-scale modeling efforts in the literature.

In order to assess the importance of SGS terms, DNS results are filtered: this procedure corresponds to an *a priori* analysis. For compressible flows, since the energy equation is involved, numerous SGS terms exist. Very few *a priori* analysis have been performed to evaluate both SGS momentum and energy terms in that context. Moreover, most of the analysis have been conducted for PG flows except for the work of Bellan's group (Selle *et al.*, 2007; Borghesi & Bellan, 2015) which will be discussed hereafter.

SGS terms for PG flows: state of the art A configuration of choice to investigate compressibility effects is the mixing layer. The pioneering compressible *a priori* analysis of Vreman *et al.* (1995) is done for a 2D mixing layer at $M_c = 0.2$ and 0.6 for $\bar{\Delta}/\Delta = 8$ [†]. They give a classification of SGS terms for momentum and energy equations using two systems of equations: system I implies the computable total energy whose evolution equation cannot be written in a conservative form; system II, which is based on the filtered total energy, is the reference system for the present work as noted in Section 2.4.3. It implies to make a distinction between the filtered temperature ($\bar{T}$) / pressure ($\bar{p}$) and the temperature ($\widehat{T}$) / pressure ($\widehat{p}$) computed from the filtered variables. This distinction is essential since at every time step, temperature and pressure are determined using the filtered conservative variables (i.e. $\bar{\rho}$, $\bar{\rho}\widetilde{u}_i$ and $\bar{\rho}\widetilde{E}$).

Vreman *et al.* (1995) show that the SGS viscous term in the momentum equation is negligible (2 orders of magnitude smaller) when compared to the resolved terms. The SGS turbulent stress is evaluated to be an order of magnitude lower than the resolved terms. The SGS pressure term present in the momentum equation is not evaluated alone so that no information about its importance is provided. For the energy equation, the SGS heat flux, the SGS viscous work

[†] Δ denotes the grid size of the DNS and $\bar{\Delta}$, the filtering size.

and the SGS pressure work are two orders of magnitude smaller than the resolved total energy flux and one order of magnitude smaller than the SGS kinetic flux and the SGS internal energy flux. An additional *a priori* analysis is performed in Martin *et al.* (2000) for an homogeneous isotropic turbulence (HIT) at $M_t = 0.52$ for $\bar{\Delta}/\Delta = 4, 8, 16$ and 32. They evaluate several SGS terms in the internal energy, the enthalpy and the total energy equations. In the latter equation, they find that the SGS internal energy flux is the dominant term. The SGS kinetic energy flux is second with an amplitude close to the SGS internal energy flux. The SGS viscous work ranks as the last term with an amplitude one order of magnitude smaller than the SGS internal energy flux. The authors do not evaluate terms coming from the difference between the filtered temperature ($\bar{T}$) / pressure ($\bar{p}$) and the computable temperature ($\widehat{T}$) / pressure ($\widehat{p}$).

Later, Okong'o & Bellan (2004) perform an *a priori* analysis of single and two phases mixing layers using the perfect gas EoS at $M_c = 0.35$. Their assessment of SGS terms in the momentum and energy equations at $\bar{\Delta}/\Delta = 4$ and 8 shows the importance of some subgrid-scale terms (the SGS pressure terms in momentum equations and the SGS pressure work in the energy equation) in two phases flows but also in single phase flows. In the momentum equations, the SGS pressure terms are always neglected in PG LES literature results even though their magnitude is shown in Okong'o & Bellan (2004)'s analysis to be of the same order as the turbulent stress, which is modeled, and larger than the resolved viscous term. As a reminder, SGS pressure terms are proportional to the isotropic part of the turbulent stress tensor in PG flows (see Section 2.4.4). In regard to this analysis conducted at a low compressibility regime, one can question the validity of the PG assumption neglecting the isotropic part of the turbulent stress tensor (Erlebacher *et al.*, 1992). Appendix D investigates this assumption by filtering the PG DNS results presented in Chapter 3.

SGS terms for real gas flows: state of the art and present contribution Since the present work investigates the need for specific SGS modeling in the case of DG flows, the *a priori* analysis is conducted using the **real gas** LES formulation (Equation (2.48)). Using higher order EoS involves more complex and non-linear correlations in the SGS pressure, SGS heat flux and SGS pressure work terms coming from the respective difference between $\widehat{T}$, $\widehat{P}$ and $\bar{T}$, $\bar{P}$. The literature devoted to real gas *a priori* analysis is scarce. Selle *et al.* (2007) achieve several transcritical binary-species DNS of transitional mixing layers at $M_c = 0.4$ using the Peng-Robinson EoS (Peng & Robinson, 1976). Their evaluation of SGS terms shows the importance of SGS pressure, SGS pressure work and SGS heat flux terms at $\bar{\Delta}/\Delta = 4$ and 8 especially for non-ideal gases which experience strong departures from perfect gases. They design a model for these terms based on a Taylor series expansion. Since their model is not effective as the filter size increases, they do not recommend it for practical use.

Borghesi & Bellan (2015) extend the previous work of Selle *et al.* (2007) confirming the importance of the SGS pressure, the SGS heat flux and the SGS pressure work. They develop dynamic models based on the Germano identity which perform well at $\bar{\Delta}/\Delta = 3$ but which are far less effective at $\bar{\Delta}/\Delta = 6$. They also show that the models only have a small effect over integrated quantities like the temporal evolution of the momentum thickness in an *a posteriori* LES at $\Delta_{\text{LES}}/\Delta = 3$. Yet, the influence of the models is significant on the distribution of the product between fluctuating velocities and temperature.

Selle *et al.* (2007) and Borghesi & Bellan (2015) both show (i) the importance of these terms which become more complex for real gases because of the use of higher order EoS and (ii) the difficulty to model these terms especially when the filter size increases. The objective of the following analysis performed in this chapter is to demonstrate and to quantify the importance

of SGS terms in the inertial zone of the TKE spectrum using the DG mixing layers results previously analyzed in Chapter 4 and HIT results taken from Giauque *et al.* (2020). The next step will be dedicated to the development of a model for the SGS pressure and will be the topic of Chapter 6.

5.2 Analysis of the subgrid-scale terms

In order to assess the importance of all SGS terms present in the filtered momentum and energy equations (Equation (2.48)), the mixing layer DNS and the forced HIT (Giauque *et al.*, 2020) are filtered using the Gaussian filter (see Section 2.4.2) with a selectivity parameter ζ set to 6. An analysis of the effect of ζ is given in Appendix C. The explicit filtering size is varied from the size of the domain down to the Kolmogorov lengthscale. When the explicit filtering size decreases to the DNS cell size, the subgrid-scale terms tend by definition to zero. For the momentum equations, all terms are normalized by the amplitude of the largest term which is the root-mean-squared (RMS) amplitude of the resolved turbulent stress $\left(\frac{\partial \bar{\rho}\widetilde{u}_i\widetilde{u}_j}{\partial x_j}\right)$ at the Kolmogorov lengthscale. For the total energy equation, all terms are normalized by the RMS amplitude of the pressure work $\left(-\frac{\partial \widetilde{p u}_i}{\partial x_i}\right)$ at the Kolmogorov scale.

5.2.1 Filtered momentum equations

The comparative analysis of the SGS terms appearing in the filtered momentum equations is performed for the two configurations under study (HIT and mixing layer). In the filtered momentum equations, six terms appear in each direction: the resolved and SGS pressure, viscous and turbulent stress terms. Let us recall that the SGS turbulent stress terms are the main focus of modeling efforts in the LES community, as other SGS terms do not even appear in the incompressible formulation. Yet, even for compressible LES, SGS terms other than the SGS turbulent stresses are usually not taken into account in the modeling process. The following analysis aims therefore at providing a well-grounded assessment of the SGS terms relative importance for DG flows, which will guide further modeling efforts.

Analysis of the Homogeneous Isotropic Turbulence configuration Results are first presented for the HIT configuration because of its isotropic nature which simplifies the analysis. Figure 5.1 displays the RMS amplitude of resolved and SGS quantities in the HIT configuration over the whole filtering sizes range. All three vector components x, y and z of the momentum equation contributions are almost superimposed thereby confirming the isotropic nature of the forced HIT flow. Note that all these terms are averaged during steady turbulence for which averaged enstrophy[†] and turbulent kinetic energy are almost constant (see Giauque *et al.* (2020)).

As expected, the resolved turbulent stress and pressure terms are the most important quantities over the whole wavenumber range and these terms increase when the filtering size tends to the DNS resolution to the right of the plot. However, the SGS turbulent stress terms, which are generally the only one modeled, are clearly not the only important terms: the three components of the SGS pressure are indeed of the same order of magnitude. In order to better assess their importance in LES, one needs to explicit the cutoff wavenumber, which is usually located in the turbulence inertial zone. The previous analysis provided in Giauque *et al.* (2020) indicates

[†]The enstrophy $\mathcal{E}$ is defined as the vorticity variance: $\mathcal{E} = \frac{1}{2}\overline{w_i w_i}$, where w_i is the fluctuating part of the vorticity.

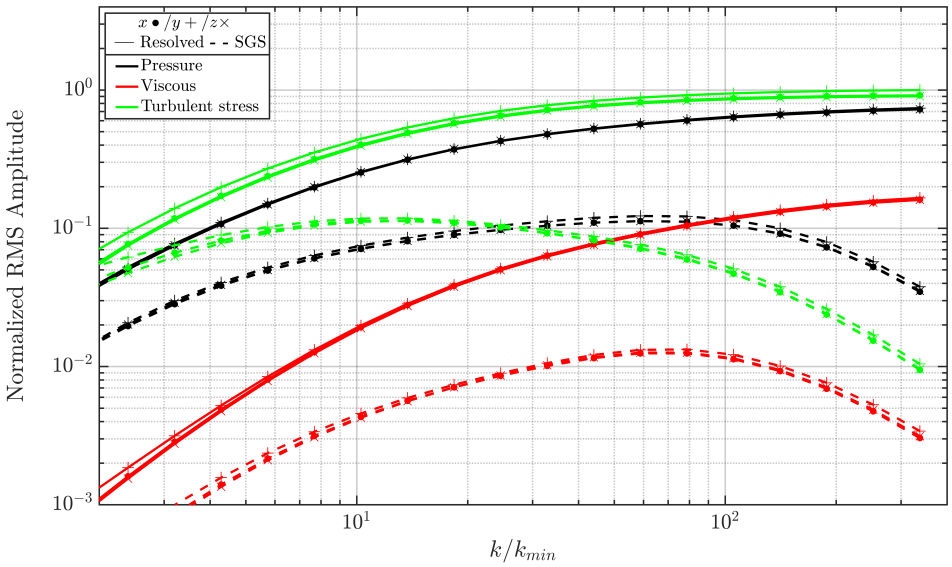

Figure 5.1: RMS amplitude of resolved and SGS terms in the filtered momentum equations (Equations 2.48) for the dense gas HIT case. The turbulent Mach number is equal to 0.8.

that the inertial zone for the HIT is located in the range $k/k_{\text{min}} \in [4; 20]$. At these scales, SGS turbulent stress and pressure terms are larger than the resolved viscous terms. Following Vreman's recommendations (Vreman *et al.*, 1995), since they are larger than a resolved term, SGS turbulent stress and pressure terms should be modeled for this configuration. The SGS viscous term is about one order of magnitude smaller than the resolved viscous one and two orders of magnitude smaller than the resolved turbulent stress and pressure terms. It can thus be neglected.

Analysis of the mixing layer configurations Figure 5.2 shows the same plot for the mixing layer at three convective Mach numbers ($M_c = 0.1 - 1.1 - 2.2$). For the three cases, consistently with the forced HIT configuration, the resolved turbulent stress and pressure terms are the most important whereas the SGS viscous terms remain negligible. Since the mixing layer is not isotropic, the three vector components are different at the largest scales but they tend to superimpose as the filter size diminishes leading to isotropic small scales dynamics. Results are averaged over each self-similar period and steadiness is well achieved.

The main difference between the three mixing layer cases is the normalized amplitude of SGS pressure terms, which increases as the convective Mach number increases. For ideal perfect gas flows, Erlebacher *et al.* (1992) suggest that SGS pressure terms, which are related in that case to the trace of the SGS turbulent stress tensor, can be neglected with respect to the resolved pressure terms for flows satisfying $M_t < 0.6$ [†]. The present dense gas results show the importance of SGS pressure terms even at $M_t \approx 0.4$ (corresponding to $M_c = 1.1$) where their amplitudes are similar to resolved viscous terms at the end of the inertial zone around $k/k_{min} \approx 20$ (see Figure 4.11). At $M_c = 2.2$, the turbulent Mach number is larger ($M_t \approx 0.67$) and the normalized amplitude of SGS pressure terms increases, reaching the same order of magnitude as SGS turbulent stress terms. Their amplitude is also closer to the one of the

[†]This assumption is discussed for perfect gas results in Appendix D

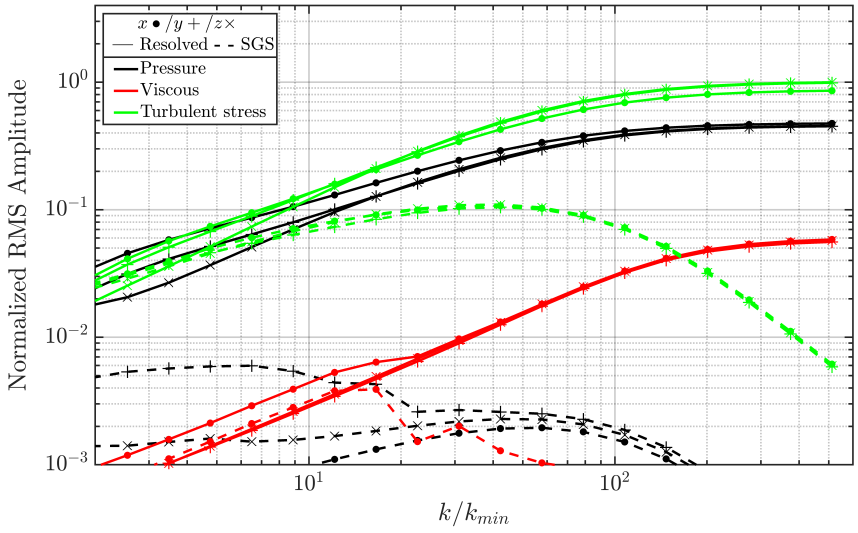

$M_c = 0.1$

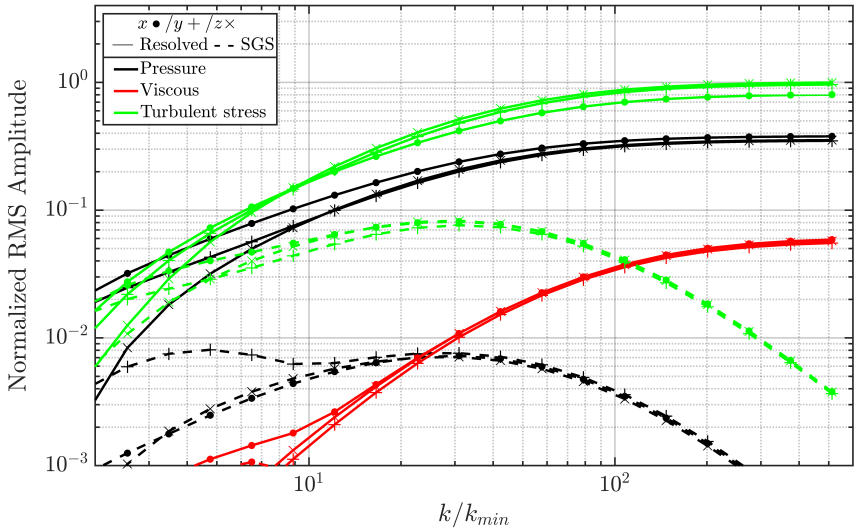

$M_c = 1.1$

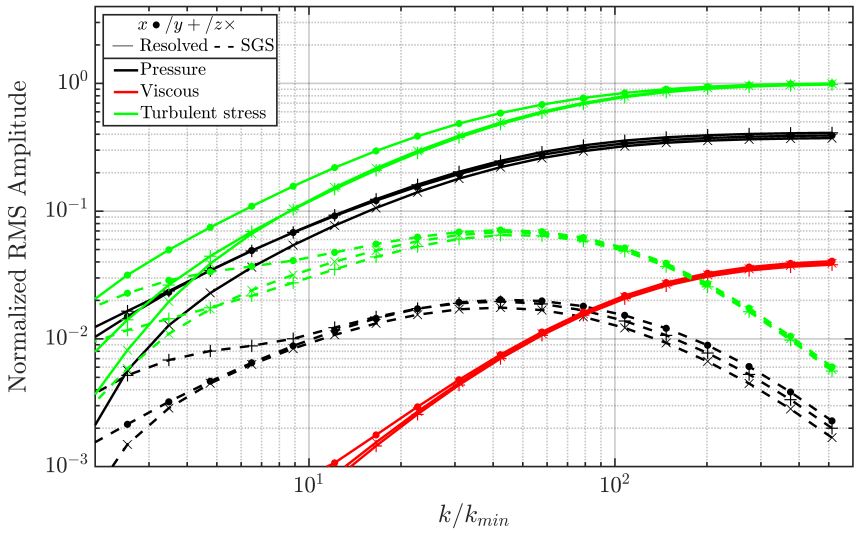

$M_c = 2.2$

Figure 5.2: RMS amplitude of terms in the filtered momentum equations (Equations (2.48)) for the dense gas mixing layer at $M_c = 0.1 - 1.1 - 2.2$ (top-middle-bottom). Results are averaged over the domain and over the self-similar period growth phase of the mixing layer. The turbulent Mach numbers averaged over the centerplane are respectively equal to $0.05 - 0.38 - 0.67$. The SGS viscous terms is very small and does not appear on the plot for $M_c = 1.1$ and $M_c = 2.2$.

HIT configuration where the turbulent Mach number is equal to $M_t = 0.8$. These consistent observations made on two different configurations strongly suggest taking into account SGS pressure terms in LES of DG flows. Since these terms are neglected in PG flows, it justifies a specific dense gas modeling effort.

5.2.2 Energy equation

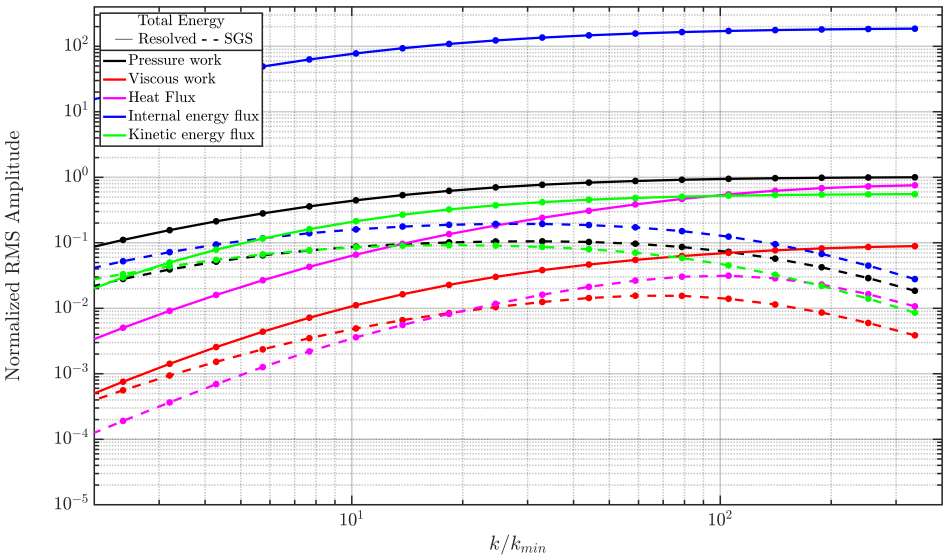

Figure 5.3: RMS amplitude of terms in the filtered total energy equation (Equation (2.48)) in the dense gas HIT configuration. The turbulent Mach is equal to 0.8.

Resolved terms Resolved source terms in the filtered total energy equation (Equation (2.48)) are the resolved net rate of work done by pressure and viscous shear stress together with the resolved heat flux, and kinetic and internal energy fluxes. Each resolved term is accompanied by its SGS counterpart. Figures 5.3 and 5.4 present the normalized RMS amplitudes for each of these terms and for both configurations (HIT and mixing layer). For all simulations, the resolved internal energy flux represents the predominant term, which is consistent with results (Non-dimensional terms and Eckert numbers) previously discussed in Sections 4.4.4 and 4.4.5. This term is followed, by order of importance, by the resolved pressure work, the resolved kinetic energy and the heat fluxes, with the resolved viscous shear stress work having the smallest contribution.

Analysis of the HIT configuration For the HIT configuration (Figure 5.3) the magnitudes of the SGS internal and kinetic energy fluxes as well as the SGS pressure work are larger than the resolved heat flux up to $k/k_{min} \approx 15$. Beyond this limit these SGS terms remain larger than the resolved viscous shear stress work up to $k/k_{min} \approx 100$, with the exception of the SGS turbulent kinetic energy, which decays below the resolved shear stress term around $k/k_{min} = 80$. These three SGS terms (SGS internal and kinetic energy fluxes and SGS pressure work) are

thus above at least one resolved term in the inertial region and thus require modeling. Note that the SGS viscous work and the SGS heat flux are smaller but close to the resolved viscous term in the inertial region. However, since they are one order of magnitude smaller than the resolved heat flux and two orders of magnitude smaller than the resolved pressure work, it is reasonable to neglect both terms, at least in these non-reactive configurations.

Analysis of the mixing layer configurations Figure 5.4 shows the RMS amplitude of resolved and SGS quantities for the mixing layer at three convective Mach numbers ($M_c = 0.1 - 1.1 - 2.2$). Observations for these cases are similar to the ones made for the HIT configuration: the previously mentioned SGS terms are greater or comparable to the resolved heat-flux for normalized wavenumbers smaller than 40, and always superior to the resolved viscous shear stress term up to very small scales beyond $k/k_{min} \approx 100$. Note that this observation is also verified at $M_c = 0.1$. One may also observe a slight increase of the SGS terms with the convective Mach number especially for the SGS heat flux. In both configurations, the SGS viscous shear stress work and SGS heat flux remain negligible in the inertial region. Yet, the SGS pressure work, which is neglected for PG flows, is of importance for DG flows justifying the need for a specific modeling.

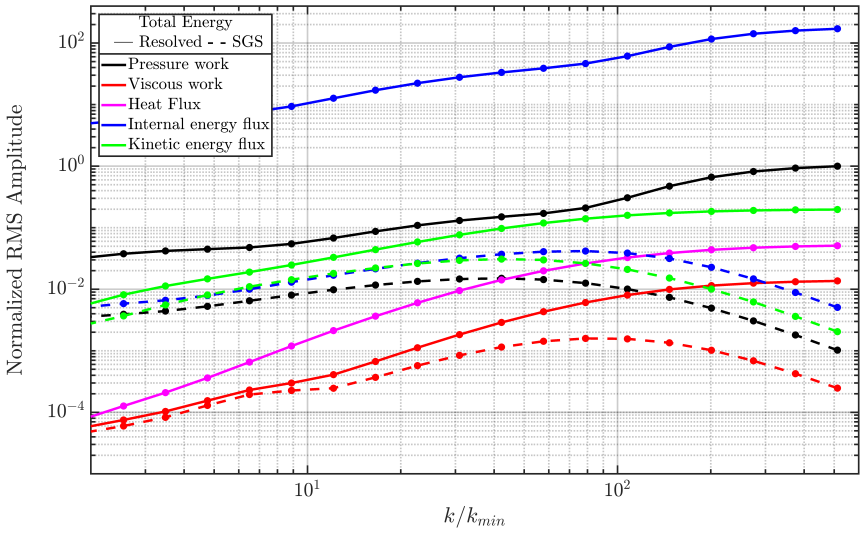

$M_c = 0.1$

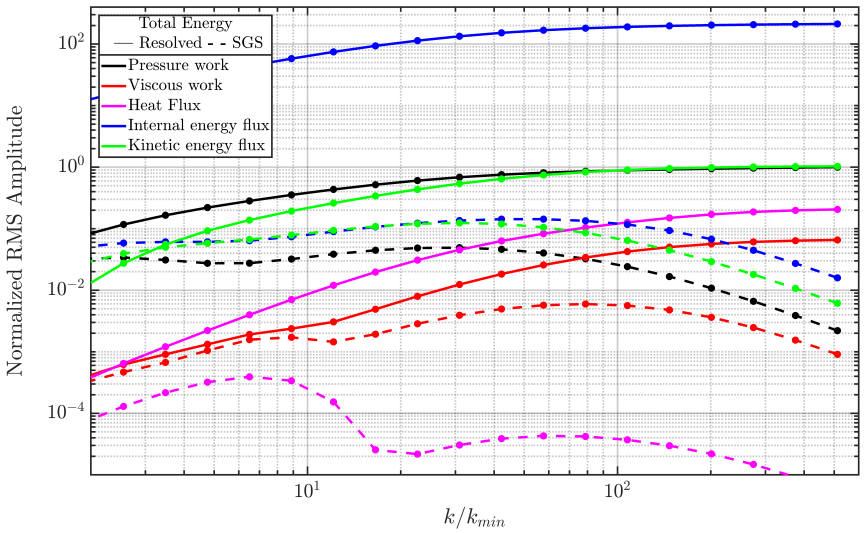

$M_c = 1.1$

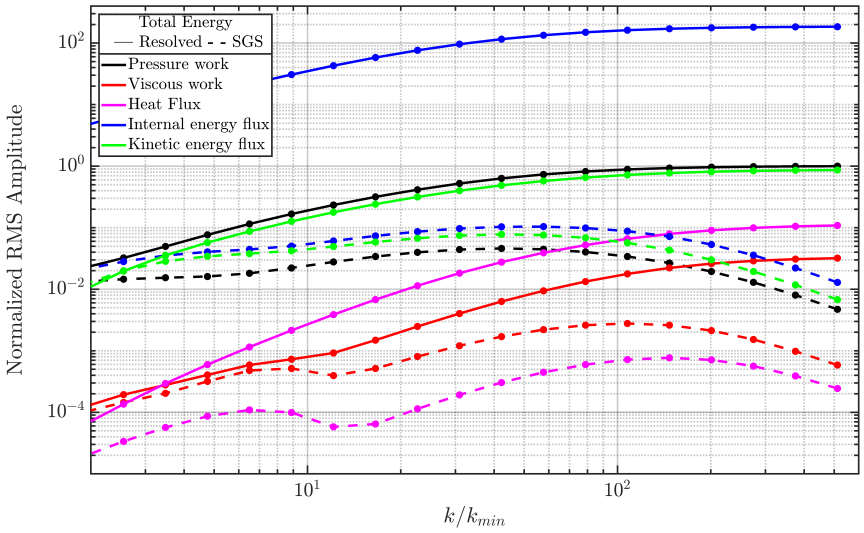

$M_c = 2.2$

Figure 5.4: RMS amplitude of terms in the filtered total energy equation (Equation (2.48)) for the dense gas mixing layer at $M_c = 0.1 - 1.1 - 2.2$ (top-middle-bottom). Results are averaged over the domain and over the self-similar period growth phase of the mixing layer. The turbulent Mach numbers averaged over the center plane are respectively equal to $0.05 - 0.38 - 0.67$.

5.3 Concluding remarks

5.3.1 LES equations to be solved

The center of the turbulence inertial range has been identified as located around the wavenumber $k/k_{min} = 15$ for the HIT and mixing layer cases (see (Giauque *et al.*, 2020) and Figures 4.11 and 4.22). Note that this wavenumber corresponds to a filtering of about $\bar{\Delta}/\Delta \approx 16 - 32$. Because it is anticipated that modeling strategies to come will take advantage of scale similarity and constant inter-scale flux of fluctuating energies (kinetic or thermodynamic) at these inertial scales, these specific wavelengths are considered hereafter.

To select the terms which require specific modeling, the two following principles first proposed by Vreman *et al.* (1995) are followed:

- The smallest term which is not a SGS term should be kept in the LES equations as it accounts for a specific physical mechanism that cannot be ignored (transport, diffusion, dissipation,...).
- All subgrid-scale terms larger than this term should be kept in the LES description of the flow.

Following these principles, the analysis of the dense gas DNS database performed in Section 5.2 consistently shows that the system of equations to be solved by LES for compressible transcritical dense gas flows should write:

$$
\begin{cases}
\dfrac{\partial \bar{\rho}}{\partial t} + \dfrac{\partial \bar{\rho}\widetilde{u}_j}{\partial x_j} = 0 \\
\dfrac{\partial \bar{\rho}\widetilde{u}_i}{\partial t} + \dfrac{\partial \bar{\rho}\widetilde{u}_i\widetilde{u}_j}{\partial x_j} = -\dfrac{\partial \widehat{p}}{\partial x_i} + \dfrac{\partial \widehat{\tau}_{ij}}{\partial x_j} \underbrace{- \dfrac{\boldsymbol{\partial}\left[\bar{\boldsymbol{p}} - \widehat{\boldsymbol{p}}\right]}{\boldsymbol{\partial x_i}}}_{\text{Pressure}} \underbrace{- \dfrac{\boldsymbol{\partial \bar{\rho}}\left[\widetilde{\boldsymbol{u_i u_j}} - \widetilde{\boldsymbol{u}}_{\boldsymbol{i}}\widetilde{\boldsymbol{u}}_{\boldsymbol{j}}\right]}{\boldsymbol{\partial x_j}}}_{\text{Turbulent stress}} \\
\dfrac{\partial \bar{\rho}\widetilde{E}}{\partial t} + \dfrac{\partial \bar{\rho}\widehat{E}_{int}\widetilde{u}_j}{\partial x_j} + \dfrac{\partial \bar{\rho}\widehat{K}\widetilde{u}_j}{\partial x_j} = -\dfrac{\partial \widehat{p}\widetilde{u}_j}{\partial x_j} + \dfrac{\partial \widehat{\tau}_{ij}\widetilde{u}_i}{\partial x_j} - \dfrac{\partial \widehat{q}_j}{\partial x_j} \underbrace{- \dfrac{\boldsymbol{\partial}\left[\overline{\boldsymbol{pu_j}} - \widehat{\boldsymbol{p}}\widetilde{\boldsymbol{u}}_{\boldsymbol{j}}\right]}{\boldsymbol{\partial x_j}}}_{\text{Pressure work}} \\
\qquad \underbrace{- \dfrac{\boldsymbol{\partial \bar{\rho}}\left[\widetilde{\boldsymbol{E_{int}u_j}} - \widehat{\boldsymbol{E}}_{\boldsymbol{int}}\widetilde{\boldsymbol{u}}_{\boldsymbol{j}}\right]}{\boldsymbol{\partial x_j}}}_{\text{Internal energy flux}} \underbrace{- \dfrac{\boldsymbol{\partial \bar{\rho}}\left[\widetilde{\boldsymbol{Ku_j}} - \widehat{\boldsymbol{K}}\widetilde{\boldsymbol{u}}_{\boldsymbol{j}}\right]}{\boldsymbol{\partial x_j}}}_{\text{Kinetic energy flux}}
\end{cases}
\tag{5.1}
$$

5.3.2 Towards SGS modeling

One can conclude that the SGS pressure term appearing in the filtered momentum energy equations and the SGS pressure work appearing in the filtered total energy equation need to be modeled in addition to the SGS terms (SGS turbulent stress, SGS internal energy and kinetic energy fluxes) usually modeled for PG flows[†]. This result confirms the earlier findings of Selle *et al.* (2007) derived from a real gas mixing layer at $M_c = 0.4$ analysis and extends them to

[†]As referenced in Table 2.4, the SGS kinetic energy flux is usually partially modeled using the SGS turbulent stress.

HIT and to mixing layers with larger convective Mach numbers. The magnitudes of other SGS terms, for which models exist for PG flows, are also found significant. Existing models for these terms would need to be assessed in the context of transcritical dense gas flows. However, such an assessment is not done in the present work.

The next chapter concentrates instead on the derivation of a novel model for the SGS pressure $(\bar{p} - \widehat{p})$. Since its analysis presented in Section 6.2.1 shows the complexity of this term comprising intricate SGS thermodynamic correlations, supervised machine learning algorithms appear as tools of choice to model $(\bar{p} - \widehat{p})$. In the next Chapter 6, Artificial Neural Networks are applied to build a model for the SGS pressure in the case of DG flows, harvesting information contained in the filtered DNS database comprising the HIT and the mixing layers. The model will then be validated in Chapter 7 thanks to *a posteriori* LES of the mixing layer configuration at several filtering sizes.

Chapter 6

SGS modeling using Artificial Neural Networks

Contents

4.1 Problem formulation 53
4.1.1 Initialization 53
4.1.2 Non-dimensional numbers in the DG context 54
4.2 Dense gas effect at $M_c = 1.1$ 57
4.2.1 Temporal evolution and selection of the self-similar period 57
4.2.2 DG effect over the unstable growth phase at $M_c = 1.1$ 58
4.2.3 DG effect over the self-similar period at $M_c = 1.1$ 61
4.3 Dense gas effect: influence of the convective Mach number 71
4.3.1 Temporal evolution and selection of the self-similar period 71
4.3.2 DG effect over the self-similar period 71
4.4 Analysis of discrepancies between DG and PG flows 77
4.4.1 Shocklets influence 78
4.4.2 Spatial correlations 85
4.4.3 Influence of the initial thermodynamic operating point 88
4.4.4 Evolution of non-dimensional terms 91
4.4.5 Other influencing factors 94
4.5 Concluding remarks 98

THE present chapter proposes a methodology using artificial neural networks (ANN) to model the SGS pressure term which must be taken into account in the LES of DG turbulent flows as shown in the *a priori* analysis presented in Chapter 5. A review of the literature, limited to ANN models designed for LES, is proposed in Section 6.1.1. The concept of ANN is introduced and the method applied to model the SGS pressure term is outlined. Next, the database used to train the ANN is analyzed using the correlations and the contours of thermodynamic variables in Section 6.2. The ANN is thereafter improved using a data parallelism method and an optimization of its hyperparameters (see Section 6.3). The ANN *a priori* performance is finally assessed in Section 6.4. The closing section focuses on the analysis of the ANN structure using small size networks in order to better understand how the ANN is functioning and possibly

to draw a link with a physical understanding of the model (instead of using it as a black box only).

6.1 ANN modeling for LES

6.1.1 State of the art

General context Among machine learning methods, artificial neural networks (ANN) are definitely one of the most popular. Their great adaptability favors their use in a wide range of application domains, from image recognition[†] to market analysis, for weather forecast or the resolution of the protein folding problem. Since ANN need a large amount of data during the initial training step, they took advantage of the tremendous growth of computational power and storing capacities during the last decades. In computational fluid dynamics and particularly for the development of LES turbulent closure models, these improved capacities make it possible to use very large DNS databases in the ANN building process. Once filtered, DNS can be used to evidence SGS terms that must be taken into account thanks to an *a priori* analysis (as done in the previous Chapter 5) but also to evaluate or to develop models required for these significant terms, as proposed in the present chapter.

ANN-based SGS modeling The first attempt to use ANN to model SGS terms was performed by Sarghini *et al.* (2003). Their ANN is trained to reproduce the turbulent viscosity coefficient of the Bardina's scale similarity model (Bardina *et al.*, 1980) using an LES of a channel flow. The purposes of this work is not to improve the modeling but to save computational time. Their ANN enables a computational time saving of about 20% achieving close results when compared to the Bardina's scale similarity model. The first LES models using ANN were truly developed almost fifteen years later for diverse modeling purposes:

- the SGS turbulent stress tensor (Gamahara & Hattori, 2017; Wang *et al.*, 2018; Zhou *et al.*, 2019; Xie *et al.*, 2019; Pawar *et al.*, 2020; Prat *et al.*, 2020),
- its derivative (Xie *et al.*, 2020),
- the total SGS flux (Beck *et al.*, 2019),
- other SGS terms (Vollant *et al.*, 2017; Maulik *et al.*, 2018; Lapeyre *et al.*, 2019; Maulik *et al.*, 2019; Xie *et al.*, 2019; Frezat *et al.*, 2021; Rosofsky & Huerta, 2020),
- or even wall models (Yang *et al.*, 2019).

***A priori* vs *a posteriori* predictions** Literature results definitely show improved *a priori* predictions when using ANN as SGS models instead of classical LES models. Yet, this approach raises several problems. The most complex one is the translation of the *a priori* performance of the developed model in the realm of *a posteriori* performance. Indeed, correct *a priori* predictions do not necessarily lead to reliable *a posteriori* predictions. Several reasons are responsible for that:

- the filtering of the DNS which does not exactly reproduce the spatial filtering induced by the LES grid;
- the *a priori* filtering size which can be small compared to that of the *a posteriori* LES often located in the inertial domain of the TKE spectrum;

[†]For image recognition, a special type of ANN named convolutional neural networks (CNN) are used.

- spatial operators such as the one used to compute derivatives which can differ between the filtered DNS and *a posteriori* LES.

Moreover, during *a posteriori* tests SGS models are applied in real flow conditions which can be very different from the configurations of the *a priori* database learned during the training phase. Another issue raised by the use of ANN when applied as a black-box tool is the strong opposition it triggers in the modeling community, whose goal is rather to understand the deep relationships that exist between filtered and SGS variables. The interested reader should refer to Duraisamy *et al.* (2019) for a thorough review of turbulence modeling using data-driven approaches.

Improvement strategies for ANN-based SGS modeling To answer some of the issues previously raised, several methods are employed by authors. Vollant *et al.* (2017) developed a model for the SGS scalar flux term trained from filtered DNS of a passive scalar forced HIT. They apply the concept of optimal estimator along with conditional expectation[†] to select the most predictive ANN inputs in order to improve the *a priori* performance. Two methods were employed: the first one consists in using directly an ANN as a surrogate model; the second one consists in conserving a functional form, the coefficients of which are computed using an ANN. The first procedure leads to an unphysical behavior of the scalar field when testing initial mixing conditions different from the ones used during the training and therefore questions the ability of the ANN to generalize outside of the training set. The second procedure is the most effective showing a significant improvement when compared to the dynamic eddy model proposed by Moin *et al.* (1991). Using a functional form for the ANN is also shown to be more robust. This idea is used by Xie *et al.* (2019) to built a model based on the dynamic Clark model (Vreman *et al.*, 1996*b*), by Pawar *et al.* (2020) to predict the eddy viscosity and by Prat *et al.* (2020) to predict the Smagorinsky constant. This method can however deteriorate the *a priori* performance (Prat *et al.*, 2020) and also requires a functional form which is not obvious to derive for some specific SGS terms.

Another method to improve the *a posteriori* performance is to train the ANN on a diverse database. This process strongly helps the ANN to generalize its prediction over flow configurations which have not been encountered during the training phase. To enrich the training database, one can use filtered DNS with several filtering sizes like Vollant *et al.* (2017) who use four different filtering sizes ($\bar{\Delta}/\Delta_{\text{DNS}} \in [4, 8, 16, 32]$). It is also possible to use several instants, several values of characteristic non-dimensional numbers or even several grid resolutions. For example, Zhou *et al.* (2019) train an ANN over two different Taylor microscale numbers Re_λ and for five different time instants and Rosofsky & Huerta (2020) train their ANN over three different grid resolutions (512^2, 1024^2, 2048^2).

The most efficient way to enrich the database remains to use different flow configurations. Most of the SGS models are developed using HIT flows (Vollant *et al.*, 2017; Wang *et al.*, 2018), some of them using channel flows (Sarghini *et al.*, 2003; Gamahara & Hattori, 2017), few of them are trained over one configuration and *a posteriori* tested over a different one[†], but to the author's knowledge, none of them is trained on several configurations at the same time. The capacity of an ANN to predict consistent results over configurations different from the ones used for the training phase is a key validation test to ensure its *a posteriori* effectiveness. The choice of hyperparameters is also very important for the ANN design. Hyperparameters

[†]Note that ANN can themselves act as optimal estimators (Moreau *et al.*, 2006).

[†]See for example Vollant *et al.* (2017) who tested their ANN over a temporal turbulent plane jet flow.

can improve both the *a priori* and the *a posteriori* performance. Their definition is given in Section 6.1.2 and a detailed comparison of choices made in the literature to select their values is presented in Section 6.3.2.

Finally, one should also take care of physically explaining ANN predictions in order to answer concerns related to their use as black-box tools. There are two main paths to better understand predictions and to relate them to a physical understanding: the analysis of data, using for instance the computation of correlations or the principal component analysis (PCA), and the analysis of the network itself. For the last option, it is recommended to use an ANN comprising a reduced number of layers and neurons (see Section 6.5). This topic is actually part of the larger explainable artificial intelligence (XAI) domain. The interested reader should refer to Adadi & Berrada (2018) for a thorough review of XAI.

The present work is devoted to the modeling of the SGS pressure term in compressible DG LES using ANN trained over two different configurations: the HIT extracted from Giauque *et al.* (2020) and the mixing layers previously presented in Chapter 4. The innovative character of this work lies in the training over two different configurations especially comprising mixing layers[†] for the same ANN, which requires the setting up of parallel computing tools hereafter introduced (Section 6.3).

6.1.2 ANN description

ANN draw from biological neural networks. Artificial neurons are elementary units, organized in successive layers which are connected to one another and with the transfer functions between the neurons input(s) and output(s) described by simple mathematical functions. Neurons are illustrated in Figure 6.1 as interconnected ellipses. Two categories of objects characterize ANN: the **parameters** and the **hyperparameters**. The parameters are corrected during the supervised training phase of the ANN thanks to an error back-propagation mechanism which relies on the computation of the difference between predicted and true output values. The hyperparameters of a network are prescribed *a priori* and play a key role on the performance of the network. The parameters of the network are composed of the **weights** (w), which can increase or decrease the strength of connections between neurons, and the **bias** (b), which are added to the activation computed as:

$$\boldsymbol{Y_1} = \phi\big(\underbrace{\boldsymbol{W_1 X} + \boldsymbol{B_1}}_{\text{Activation}}\big) \tag{6.1}$$

where $\boldsymbol{Y_1}$ denotes the output vector of the first hidden layer as referenced in Figure 6.1; $\boldsymbol{W_1} = \begin{pmatrix} w_{1,1,1} & w_{1,2,1} & w_{1,3,1} \\ w_{1,1,2} & w_{1,2,2} & w_{1,3,2} \end{pmatrix}$ represents the matrix of the weights of the first layer; $B_1 = \begin{pmatrix} b_{1,1} \\ b_{1,2} \end{pmatrix}$ is the bias vector of the first layer and $X = \begin{pmatrix} x_1 \\ x_2 \\ x_3 \end{pmatrix}$ denotes the input vector of the ANN.

The function ϕ is called the activation function. It can be different from one layer to another but in our case, it is the same in the whole network except for the output layer which is linear as commonly done for ANN designed for regression. The activation function is part of the hyperparameters characterizing the ANN. Others hyperparameters are listed below:

- the number of layers;

[†]To the author's knowledge, the mixing layer configuration has never been used to design SGS model with ANN.

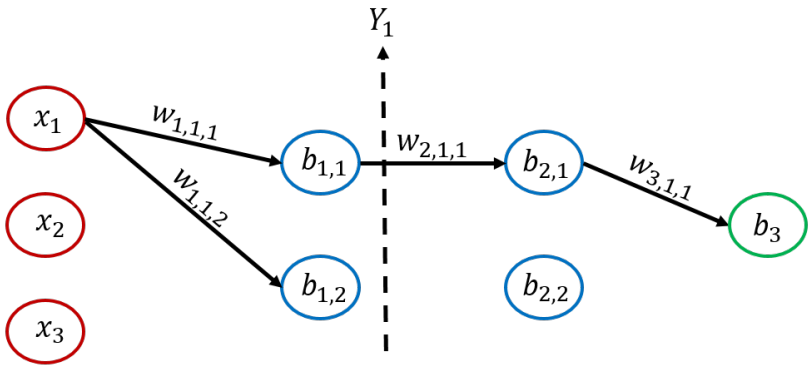

a)

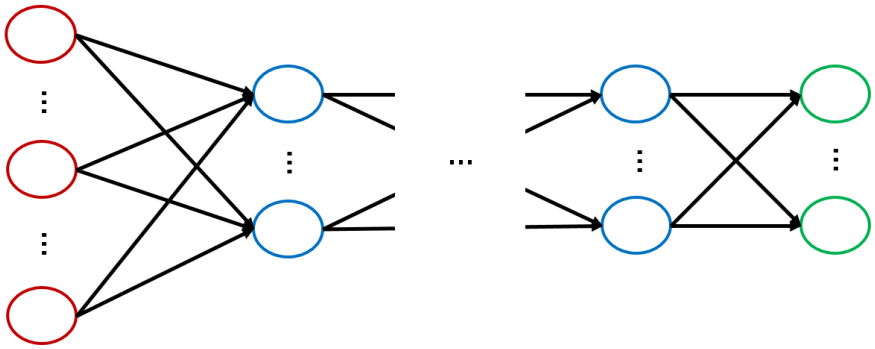

b)

Figure 6.1: Diagrams presenting the basics of ANN with (a) a simplified version and (b) a fully connected network.

- the number of neurons per layer which can be different from one layer to another;
- the activation function (ϕ) (Sigmoid, Tanh, ReLU, Leaky ReLU, ELU, ...);
- the type of data normalization (minimum / maximum or average / standard deviation);
- the type of initialization of bias and weights (Xavier, He, ...);
- the optimizer (Adam, AdaGrad, RMSProp, Stochastic Gradient Descent (SGD),...) which retro-propagates the error to correct bias and weights;
- the learning rate planning (piecewise constant, exponential, ...) if it is not automatically handled by the optimizer;
- the loss function which is a measurement of the error between predicted and true values (mean square error, root mean square error,...);
- the batch size: data are divided into batches. After each batch, weights and bias are corrected. A too small value of the batch size can lead to learning instabilities and a too large value can prevent the ANN from reaching the optimum performance;
- the regularization hyperparameters (L1, L2, elastic net, dropout,...)

These are the main hyperparameters associated with an ANN; a number of additional hyperparameters exist[†] and some of them are related to the choice of specific hyperparameters like the learning rate planning (linked with the optimizer) or even some coefficients used to tune optimizers. Hyperparameters have an influence, which can be significant, over the ANN performance. Their optimal choice is therefore a key issue in ANN design. There exists some empirical rules to select them (see for instance Géron (2017)). Yet, since the proper choice of hyperparameters strongly depends on the database used by the ANN, several methods are given in Section 6.3 to guide and justify the choices made in the present work.

6.1.3 Outline of the ANN-based modeling process

The present work aims at developing a model for the SGS pressure term which has been evidenced to be of significant importance for DG LES (see Chapter 5). The complexity of this term favors the use of ANN (see Section 6.2.1) to help identify the relationships between the SGS term and the filtered or computable quantities. ANN are trained using a database made of filtered DNS of the forced HIT and the mixing layers at $M_c = 1.1$ and $M_c = 2.2$. For the mixing layers, only self-similar temporal solutions are included in the database (Table 6.1). In order to respect the Galilean invariance of the Navier-Stokes equations (Speziale, 1985) and to improve the prediction of ANN, the filtered conservative variables are transformed into a new set of variables verifying the Galilean invariance (Figure 6.2). This imposes a weak constraint on the ANN to also verify the Galilean invariance. Further explanations about the constraints are given in the following section.

Once filtered conservative variables are transformed, the inputs are sent into the ANN, which therefore predicts the SGS pressure term. During the training phase, data extracted from filtered DNS are inserted inside the ANN. The error between predicted and true values can be computed and then back-propagated to correct the weights and bias of the ANN.

[†]For instance, the batch normalization which enables the improvement of error back-propagation on the lower layers (layers close to the inputs).

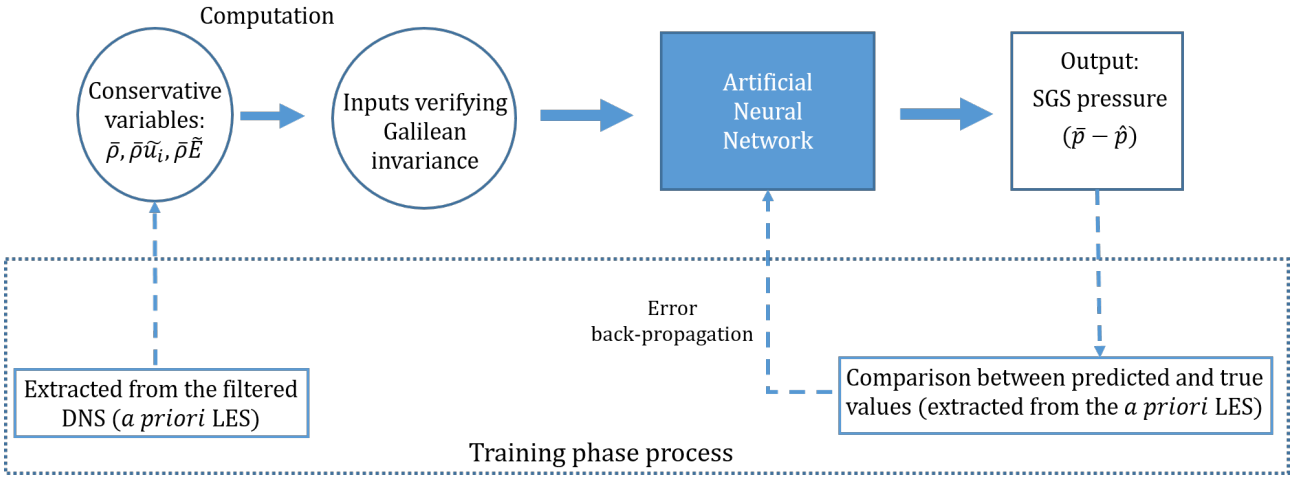

Figure 6.2: Diagrams explaining the process to model the SGS term.

Before starting the training step, data are analyzed to get a better understanding of the SGS pressure term and to select the most appropriate inputs. PCA are computed to evaluate the redundancy among inputs and to get an overview of the data.

[†]Solutions are taken each characteristic turbulent time (Giauque *et al.*, 2020).

Training database	Filtering size	Temporal solutions	Number of elements
Forced HIT	$k/k_{\min} = 18$	Solution 1	307M
Mixing layer - $M_c = 1.1$	$k/k_{\min} = 12.5$	$\tau = 1700$	134M
Mixing layer - $M_c = 2.2$ - DGA	$k/k_{\min} = 12.5$	$\tau = 4000$	134M

Additional testing database	Filtering size	Temporal solutions	Number of elements
Forced HIT	$k/k_{\min} = 18$	Solutions 2 and 8†	307M
Mixing layer - $M_c = 1.1$	$k/k_{\min} = 12.5$	$\tau = 1750 - 2100$	402M
Mixing layer - $M_c = 2.2$ - DGA	$k/k_{\min} = 12.5$	$\tau = 4050 - 5000$	402M
Mixing layer - $M_c = 2.2$ - DGB	$k/k_{\min} = 12.5$	$\tau = 4000$	134M
Mixing layer - $M_c = 2.2$ - DGC	$k/k_{\min} = 12.5$	$\tau = 3800$	268M
Mixing layer - $M_c = 2.2$ - DGD	$k/k_{\min} = 12.5$	$\tau = 3800$	268M

Table 6.1: Composition of the training and testing databases used to design the ANN modeling the SGS pressure term.

6.2 Data analysis

6.2.1 SGS pressure term

The analysis detailed in the previous chapter strongly supports the need for a specific DG modeling effort to describe SGS pressure terms in the momentum equations and SGS pressure work in the energy equation. The present work only focuses on the SGS pressure for which a model is developed in this chapter. Its complexity is directly related to the EoS describing the thermodynamic behavior of the gas. In the present analysis, since the fifth-order Martin & Hou EoS is used to describe the complexity of dense gas flows, the SGS pressure term comprises intricate SGS thermodynamic correlations and a coupling with the velocity field. The SGS pressure term depends indeed on $\widehat{T}$ (the computable temperature) and $\bar{T}$ (the filtered temperature) which are numerically obtained by reversing the caloric EoS (denoted $\mathcal{F}_c$):

$$\widehat{E}_{int} = E_{int,ref} + \int_{T_{ref}}^{\widehat{T}} c_v(T')dT' + \sum_{i=2}^{5} \frac{A_i + C_i(1 + k\widehat{T}/T_c)e^{-k\widehat{T}/T_c}}{(i-1)(1/\bar{\rho} - b)^{i-1}} \tag{6.2}$$

$$\bar{T} = \overline{\mathcal{F}_c^{-1}(E - \frac{1}{2}u_i u_i)} \tag{6.3}$$

In this expression, one can notice the influence of the kinetic energy through Equation (6.3). Because of the non-linear feature of the caloric EoS, the filtering in Equation (6.3) introduces a kinetic energy dependence. The SGS pressure can then be expressed as a function of the

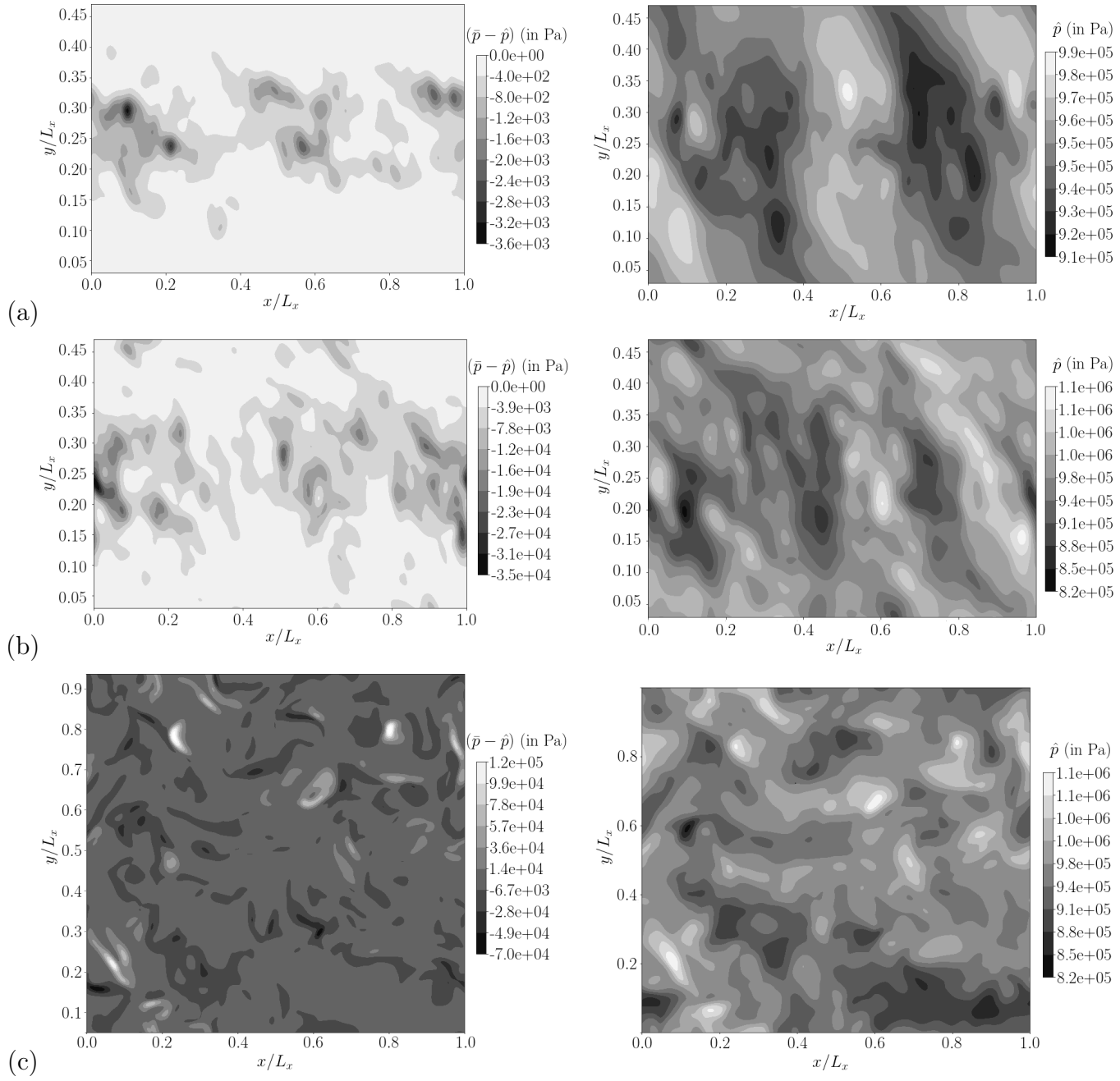

Figure 6.3: $z-$centerplane contours colored by $(\bar{p} - \widehat{p})$ (left) and $\widehat{p}$ (right) (Equation (6.4)) for the mixing layers at $M_c = 1.1 - 2.2$ ((a) and (b)) and for the forced HIT (c). The filtering length scales are respectively equal to $k/k_{min} = 18$ and $k/k_{min} = 12.5$ for the HIT and the mixing layers.

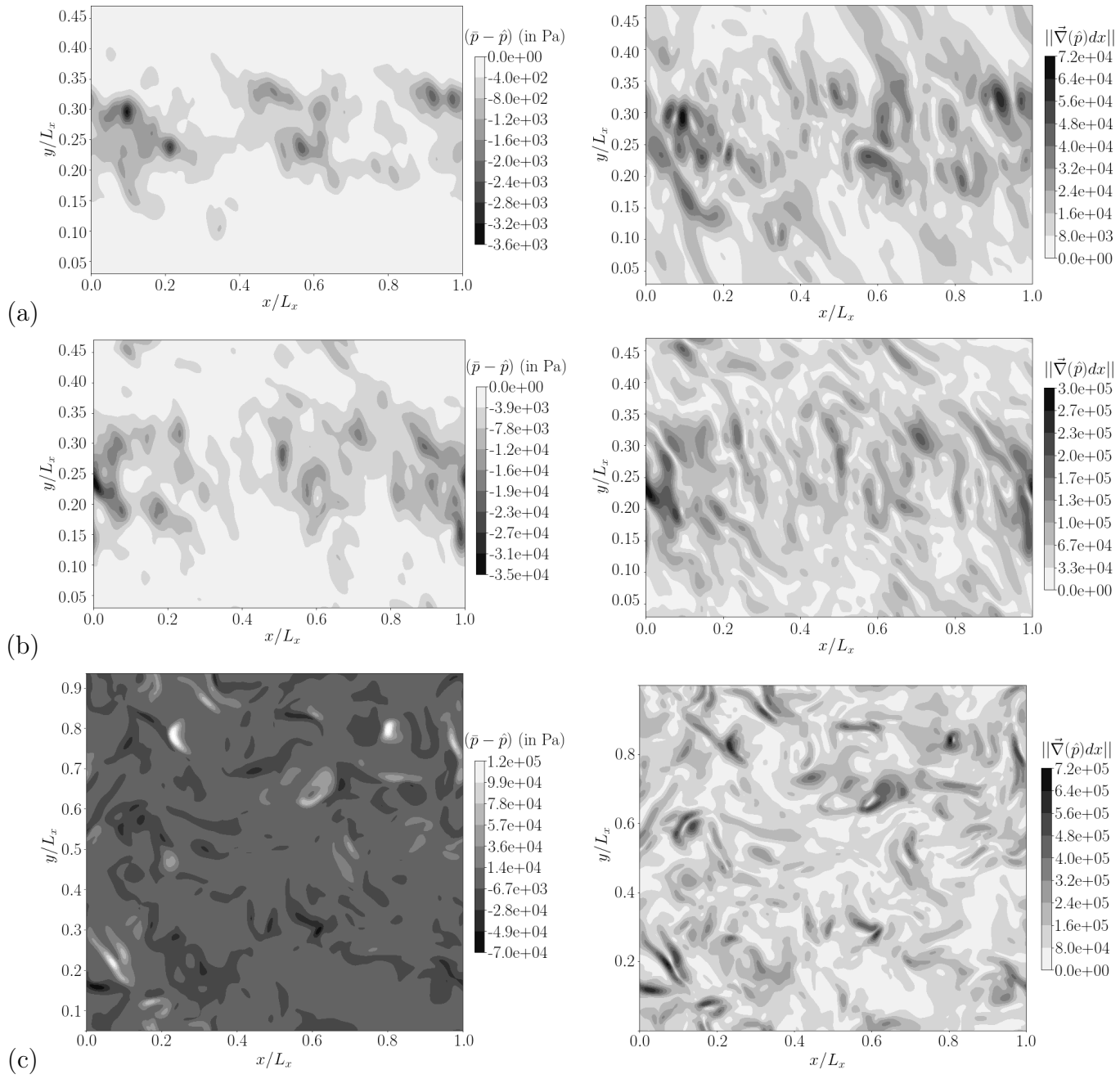

Figure 6.4: $z-$centerplane contours colored by $(\bar{p}-\widehat{p})$ (left) and $\|\nabla(\widehat{p})\|$ (right) (Equation (6.4)) for the mixing layers at $M_c = 1.1-2.2$ ((a) and (b)) and for the forced HIT (c). The filtering length scales are respectively equal to $k/k_{min} = 18$ and $k/k_{min} = 12.5$ for the HIT and the mixing layers.

computable temperature $\widehat{T}$:

$$\begin{aligned}\overline{p}-\widehat{p}=&\overline{\left(\frac{r\overline{\rho}\widetilde{T}}{1-b\rho}\right)}-\frac{r\overline{\rho}\widehat{T}}{1-b\overline{\rho}}+\overline{\left(\frac{r(\rho'\overline{T}+\overline{\rho}T')}{1-b\rho}\right)}\\&+\sum_{i=2}^{5}\left[\overline{\left(\frac{A_i\overline{\rho^i}+B_i\overline{\rho^iT}+C_i\overline{\rho^ie^{-\frac{kT}{T_c}}}}{(1-b\rho)^i}\right)}\right.\\&\qquad+\overline{\left(\frac{\overline{\rho^i}Q_i'(T)+\rho^{i'}\overline{Q_i(T)}}{(1-b\rho)^i}\right)}\\&\qquad\left.-\frac{A_i\overline{\rho}^i+B_i\overline{\rho}^i\widehat{T}+C_i\overline{\rho}^ie^{-\frac{k\widehat{T}}{T_c}}}{(1-b\overline{\rho})^i}\right]\end{aligned}\tag{6.4}$$

where $Q_i(T)=A_i+B_iT+C_ie^{-\frac{kT}{T_c}}$. Note that Equation (6.4) is not directly computable in LES because it implies SGS correlation terms. Equations (6.2) and (6.4) exhibit a strong dependence on thermodynamic averages and fluctuations and on the trace of the resolved and SGS turbulent stress tensors, which makes the modeling of the SGS pressure term especially complex.

Figure 6.3 shows contours of $(\overline{p}-\widehat{p})$ and $\widehat{p}$ for the forced HIT and the mixing layers at $M_c=1.1$ and $M_c=2.2$. For the HIT, the difference between the two pressures may exceed one bar in some flow regions and can represent up to 10% of the computable pressure $\widehat{p}$. The magnitude of $(\overline{p}-\widehat{p})$ is reduced for the mixing layers. Consistently with Figure 5.2, the larger is the value taken by M_c (and therefore M_t), the larger is the maximum level reached by the SGS pressure. Yet, in some regions, it represents about 4% of the computable pressure. A strong positive correlation appears for the forced HIT flow between $(\overline{p}-\widehat{p})$ and $\widehat{p}$. It is much less the case for the mixing layers which are in contrast more correlated with the norm of the computable pressure gradient $\|\nabla(\widehat{p})\|$ (Figure 6.4).

Note that areas of high $(\overline{p}-\widehat{p})$ intensity are sparse and that highly positive regions and highly negative regions tend to be coupled. Moreover, the sign of $(\overline{p}-\widehat{p})$ is always negative in the centerplane for the mixing layer whereas the HIT configuration exhibits positive regions. For perfect gases, the SGS pressure is related to the trace of the SGS turbulent stress tensor as:

$$(\overline{p}-\widehat{p})=-\frac{(\gamma-1)}{2}t_{ii}=-\frac{(\gamma-1)}{2}\overline{\rho}\left(\widetilde{u_iu_i}-\widetilde{u}_i\widetilde{u}_i\right)\tag{6.5}$$

Consequently only negative values of $(\overline{p}-\widehat{p})$ are allowed for PG flows since the SGS kinetic energy $k_{\mathrm{SGS}}=\frac{1}{2}\left(\widetilde{u_iu_i}-\widetilde{u}_i\widetilde{u}_i\right)$ is always positive. Because of non-linearities in the Martin & Hou EoS, Equation (6.5) is not valid for real gas let alone for DG. The possibility of having positive regions of $(\overline{p}-\widehat{p})$ is a typical real gas effect and is potentially linked to highly compressible regimes.

In order to further analyze the departure of the SGS pressure term from its perfect gas behavior, the probability density functions (PDF) of the SGS pressure term are plotted in Figure 6.5 for the HIT and for the two mixing layers at $M_c=1.1$ and $M_c=2.2$. As the turbulent Mach number increases, the distribution spreads out to large negative and positive values. Maximum absolute values are an order of magnitude larger for the mixing layer at $M_c=2.2$ when compared to the ones at $M_c=1.1$. Comparing the HIT with the mixing layer at $M_c=2.2$, the ratio between maximum absolute values is about 2 to 3. Regarding the sign

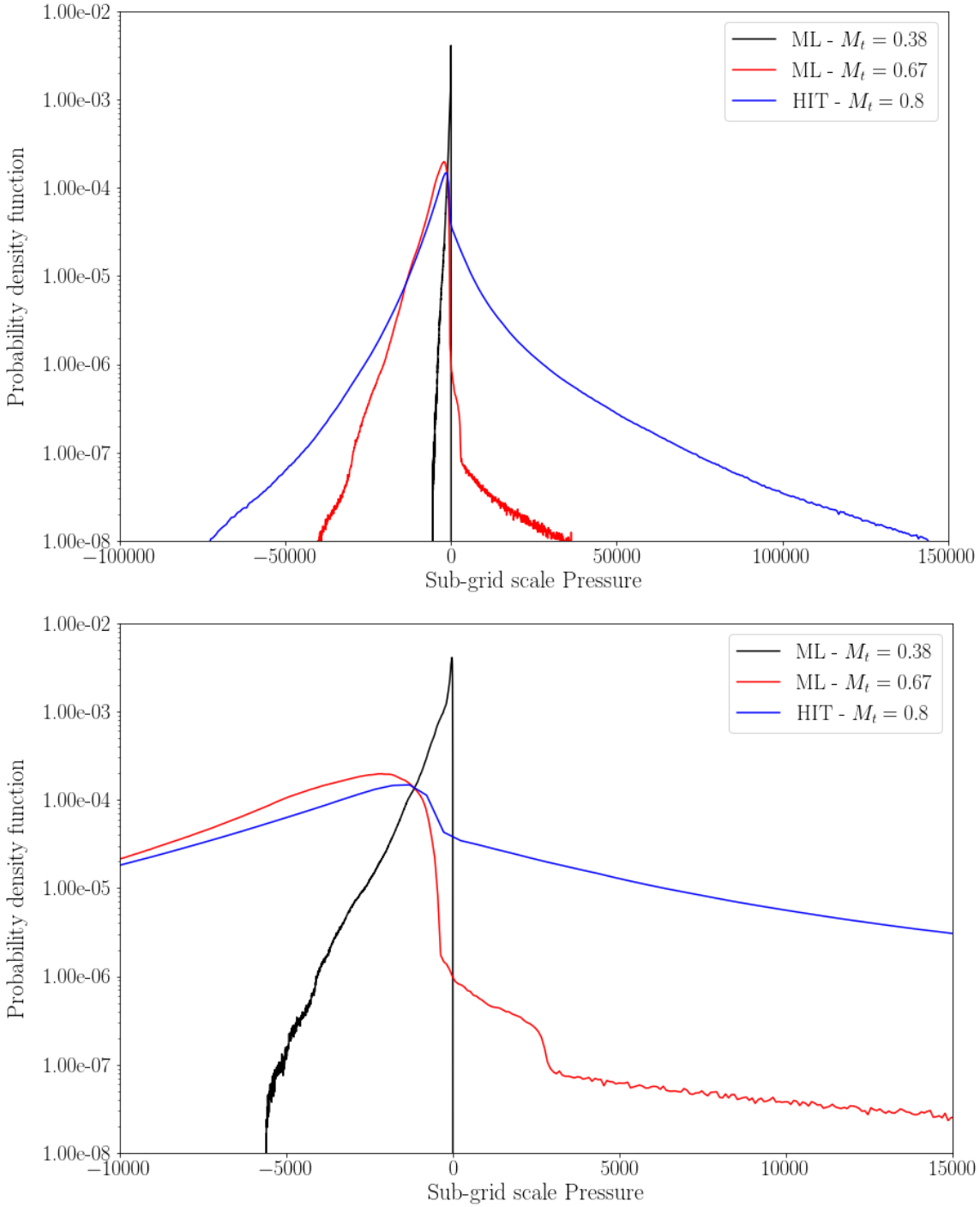

Figure 6.5: (Top) Probability density functions (PDF) of the SGS pressure term plotted for the two different configurations: the HIT at $M_t = 0.8$ and the mixing layers at $M_c = 1.1$ ($M_t = 0.38$) and $M_c = 2.2$ ($M_t = 0.67$); and (bottom) a closer view.

of $(\bar{p} - \widehat{p})$, it is always mainly negative for all configurations but only some of them contain positive values: the HIT and the mixing layer at $M_c = 2.2$. This typical real gas effect is thus related to compressibility. A strong discontinuity of the PDF is observed around zero which tends to disappear as M_t increases.

The analysis of the SGS pressure term shows its complexity. Since it comprises intricate SGS thermodynamic correlations, supervised machine learning algorithms appear as a tool of choice to be used in order to model $(\bar{p} - \widehat{p})$.

6.2.2 Choice of inputs

The inputs of the model are chosen among available variables, taking into account the nature of the SGS pressure term to assess their relevance in a preliminary screening process. Equation (6.4) shows the link of the SGS pressure term with thermodynamic quantities (the computable temperature $\widehat{T}$ and the computable density $\bar{\rho}$). Moreover, Equation (6.4) depends on the filtered temperature $\bar{T}$ which is itself computed by reversing the caloric EoS (Equation (6.3)) which introduces a kinetic energy dependence. The set of inputs should thus contain thermodynamic and kinetic energy information.

The design of the models must also respect the physical constraints of the problem. The most simple way to weakly impose physical constraints to ANN models is to apply the constraints over the inputs. For SGS models, Speziale (1985) demonstrates the necessity to respect Galilean invariance comprising spatial rotations (which implies isotropy) and translations in space and time. To this aim, the invariants of the velocity gradient are chosen to provide the necessary kinetic energy source of information (Vollant, 2015).

$$I_1 = \mathrm{tr}\left(\nabla(\vec{u})\right) \tag{6.6}$$

$$I_2 = \frac{1}{2}\left[(\mathrm{tr}(\nabla(\vec{u})))^2 - \mathrm{tr}\left(\nabla(\vec{u})\nabla(\vec{u})^T\right)\right] \tag{6.7}$$

$$I_3 = \det(\nabla(\vec{u})) \tag{6.8}$$

By taking into account the aforementioned remarks, the following set of variables emerges as natural inputs:

$$\left[\bar{\rho}; \widehat{T}; \widehat{p}; \bar{\rho}\widetilde{E};\ \ \|\nabla\left(\bar{\rho}\right)\|; \|\nabla\left(\widehat{T}\right)\|; \|\nabla\left(\widehat{p}\right)\|; \|\nabla\left(\bar{\rho}\widetilde{E}\right)\|;\ \ \Delta\left(\bar{\rho}\right); \Delta\left(\widehat{T}\right); \Delta\left(\widehat{p}\right); \Delta\left(\bar{\rho}\widetilde{E}\right);\ \ I_1; I_2; I_3\right] \tag{6.9}$$

Note that in this set, inputs which depends on differentiation (gradients, Laplacians and invariants) are normalized with the *a priori* filter size $\bar{\Delta}$ in order to not depend on the difference of resolution and filtering of each configuration (HIT and mixing layers). This set of 15 inputs satisfies the constraints of the physical problem and contains diverse variables correlated to the SGS pressure. The values of these correlations are given in Table 6.2, processing the information contained in the filtered DNS database comprising the HIT and the mixing layers. Inputs colored in red indicate the largest correlations (with absolute values above 0.40). Both mixing layers correlations are quite close. One notices a reduction of almost every value when the convective Mach number increases from 1.1 to 2.2, except for the computable temperature and pressure and the invariants.

The highest rate of correlations are obtained for the norm of the thermodynamic variables gradients for the mixing layers and for the thermodynamic variables themselves and their Laplacians in the forced HIT flow. The fundamental difference between the mixing layer and the forced HIT is the presence of a mean flow. This mean flow modifies the dynamics of the SGS

	Mixing Layer $M_c = 1.1$	Mixing Layer $M_c = 2.2$	HIT
$\bar{\rho}$	0.10	−0.08	0.53
$\widehat{T}$	−0.08	−0.30	0.49
$\widehat{p}$	0.08	−0.15	0.45
$\bar{\rho}\widetilde{E}$	0.10	−0.08	0.53
$\|\nabla(\bar{\rho})\|$	−0.82	−0.63	0.20
$\|\nabla(\widehat{T})\|$	−0.81	−0.65	0.05
$\|\nabla(\widehat{p})\|$	−0.83	−0.72	0.25
$\|\nabla(\bar{\rho}\widetilde{E})\|$	−0.82	−0.63	0.20
$\Delta(\bar{\rho})$	−0.04	−0.04	−0.46
$\Delta(\widehat{T})$	0.02	0.01	−0.41
$\Delta(\widehat{p})$	−0.03	0.09	−0.17
$\Delta(\bar{\rho}\widetilde{E})$	−0.04	−0.04	−0.46
I_1	0.03	0.11	0.04
I_2	−0.02	0.11	0.06
I_3	−0.02	−0.07	−0.10

Table 6.2: Pearson product-moment correlation coefficients ($R_{ij} = C_{ij}/\sqrt{C_{ii}C_{jj}}$), where C is the covariance matrix) between inputs and the SGS pressure term ($\bar{p} - \widehat{p}$). Correlations whose absolute value is above 0.4 are colored in red.

pressure term, which becomes more correlated in that case with the first derivative of the thermodynamic variables. Correlation rates strongly differ between cases showing the complexity of the SGS pressure term and further justifying the training of the ANN on a diverse database including both HIT and mixing layers.

In order to verify the actual effect of inputs on the ANN performance, several ANN are trained over 5.6 millions of elements randomly chosen across the database for several degrees of freedom[†] up to 10 000. The performance of ANN is measured using the coefficient of determination called r^2-score which represents the proportion of variance of a variable y that is explained by the variable $\widehat{y}$ predicted by the model. It is defined as:

$$r^2(y, \widehat{y}) = 1 - \frac{\sum_{i=1}^{n}(y_i - \widehat{y}_i)^2}{\sum_{i=1}^{n}(y_i - y_{\text{avg}})^2} \tag{6.10}$$

where $y_{\text{avg}} = \frac{1}{n}\sum_{i=1}^{n} y_i$ denotes the arithmetic average of y. Note that the best possible r^2-score is 1 and that the score can be negative in case of a bad performing model.

[†]The degree of freedom of an ANN is equal to the number of weights and bias. For an ANN with one hidden layer with n neurons, 15 inputs and one output, it is equal to $17n + 1$ ($16n$ weights and $n + 1$ biases).

$[\bar{\rho};\widehat{T};\widehat{p};\bar{\rho}\widetilde{E}]$	$[I_1;I_2;I_3]$	$\begin{bmatrix}\|\nabla(\bar{\rho})\|;\|\nabla(\widehat{T})\|;\\ \|\nabla(\widehat{p})\|;\|\nabla(\bar{\rho}\widetilde{E})\|\end{bmatrix}$	$\left[\Delta(\bar{\rho});\Delta(\widehat{T});\Delta(\widehat{p});\Delta(\bar{\rho}\widetilde{E})\right]$	r^2-score
✓	✓	✓	✓	0.93
✓		✓	✓	0.92
✓	✓	✓		0.90
✓	✓			0.76

Table 6.3: Best r^2-scores for several ANN trained over 5.6 millions of elements randomly chosen across the database (Mixing layers $M_c = 1.1$ and 2.2 and forced HIT) for several degrees of freedom up to 10 000.

If all inputs are first retained to maximize the performance, an r^2-score of 0.93 can be reached (see Table 6.3). If the invariants are discarded from the set of inputs, the best achievable r^2-score is only slightly affected since reduced from 0.93 to 0.92. Similarly when the ANN are trained without Laplacian inputs, the best r^2-score is only reduced from 0.93 to 0.90. Note however that if the norms of the thermodynamic variables gradients are also discarded from the set of inputs (along with the Laplacians) the best achievable r^2-score collapses from 0.90 to 0.76. These observations, underlining the importance of the thermodynamic variables and the norm of their gradients as input variables for the SGS pressure model are consistent with the correlation rates reported in Table 6.2 and previously discussed. If ones takes into account in the analysis, the computational cost of the model inputs, it will make sense to investigate ANN trained without Laplacian inputs, as will be done in Section 6.4. For the final model used in Chapter 7 for the *a posteriori* validation, Laplacian inputs will be removed but for another reason, namely because second order derivatives provoke discrepancies between *a priori* LES and *a posteriori* LES. In order to get additional information about the potential redundancy of inputs, a Principal Component Analysis (PCA) has also been performed; it is included in Appendix E of this manuscript, along with the key conclusions drawn from this PCA, which did not lead to a change in the choice of input variables for the SGS pressure term ANN-based modeling.

6.3 ANN tuning

The SGS pressure term and the database have been previously analyzed and a set of 15 inputs has therefore been selected to satisfy the physical constraints of the problem and to ensure a proper performance of the ANN. The present section is now devoted to the design of the ANN using the Scikit-Learn library (Pedregosa *et al.*, 2011). Since the database contains a large amount of data (see Table 6.1), a parallel computing method, detailed in Section 6.3.1, is employed to train the ANN. An optimization of the ANN hyperparameters is then performed, especially using grid search methods.

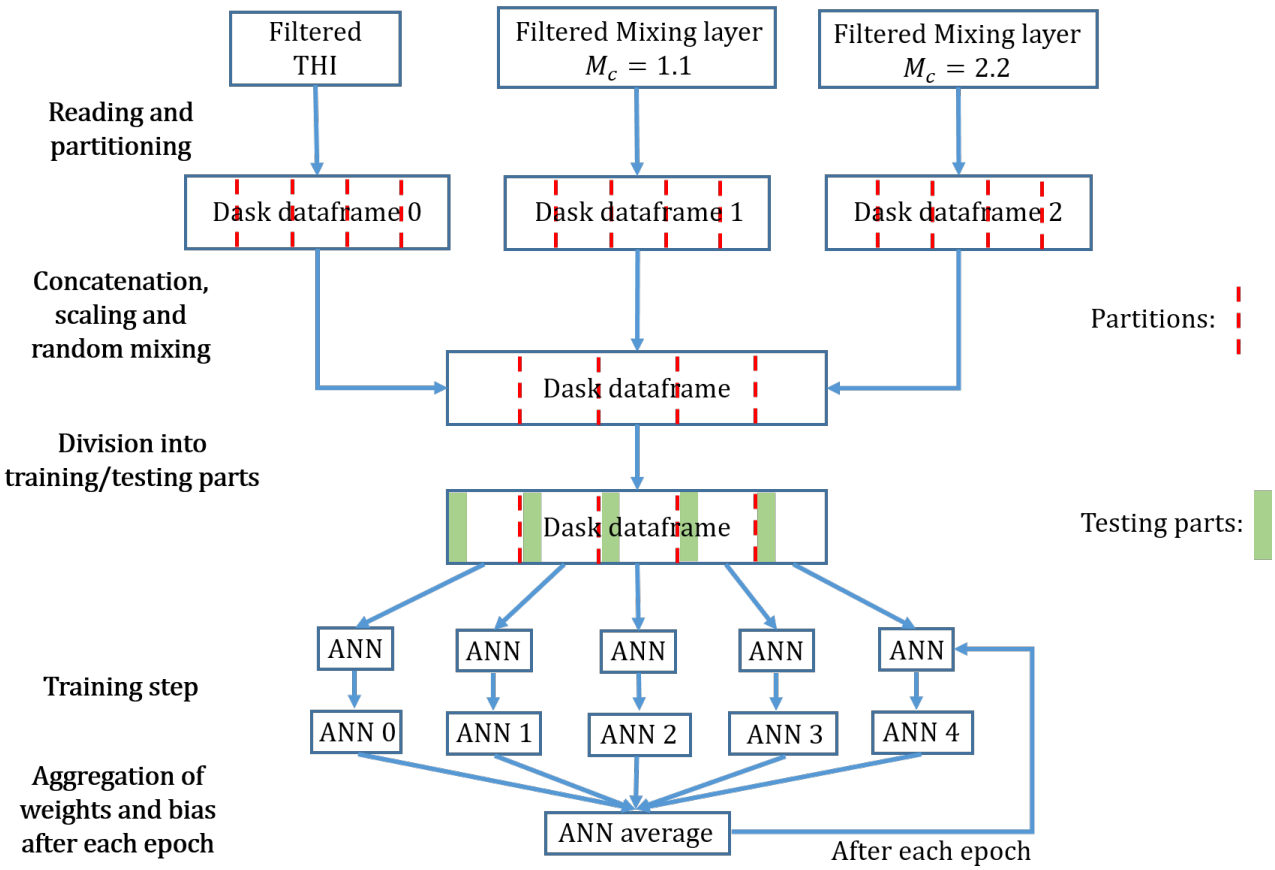

Figure 6.6: Diagrams explaining the process to parallelize the training step.

6.3.1 Data parallelism

The parallelization of the ANN answers two main issues: large size networks (in deep learning) and large databases. Thus, two different ways to proceed are possible: model parallelism and data parallelism (Géron, 2017). The first method consists in distributing the architecture of ANN over processors. This method is more suitable for deep learning with networks comprising lots of layers and neurons which is not our case. The second method distributes the data over processors. In the present work, since the training of the ANN on several configurations using all the available data raises memory issues, a process using data parallelism is implemented.

To enable the loading of a large amount of data, the Dask library (Dask Development Team, 2016) is used in complement to the Scikit-Learn library (Sklearn). Sklearn and Dask are both open-source Python libraries. The first one provides machine learning tools (ANN, random forest, classification, regression and clustering algorithms, ...) and the second one enables to manage large database by distributing the data over several processors. It is compatible with NumPy, Pandas and Sklearn. The parallelism of the ANN is described in Figure 6.6. The database comprising the three filtered DNS is first read with the Dask library. Dask creates a Python object named a dataframe which is divided into partitions. The three dataframes are then gathered into a single one. Data are scaled using the most popular average / standard deviation normalization[†] (see Section 6.1.2) computed over the entire database and randomly mixed to prevent any bias in the ANN learning. The transformed database is divided in two: the training part, which contains 80% of the database, and the testing part, which contains 20% of the database. The testing part is used to evaluate the ANN performance over elements which were not included in the training set.

At the first epoch[†], an identical ANN is replicated over each processor. Each partition is distributed over one processor and is passed into each ANN. Once all ANN have finished the first epoch, weights and bias are aggregated. The averaged ANN is replicated over each processor. The process continues until the end of the training phase. This method is simple and enables a rapid convergence to the optimal ANN when dealing with large databases (see the results given in Section 6.4).

6.3.2 Hyperparameters optimization

The choice of hyperparameters is at the heart of ANN optimization. It is mostly empirical and based on test performed over popular databases (MNIST, Cifar10, ...). Yet, since hyperparameters leading to the most effective ANN strongly depend on the data, there exists methods to quickly explore the hyperparameters space in order to make a choice well-adapted to the database used in the study. It is the point of this section to perform such an exploration, once given an overview of hyperparameters choices taken from the literature specifically dedicated to the design of ANN for SGS modeling.

Review of ANN hyperparameters selection in the SGS modeling context

[†]Note that the same scaling must be used for the training and for the testing including the *a posteriori* use of the model.

[†]An epoch is a measuring unit of the learning step. After each epoch, all data have been read once by the ANN. Note that an epoch is not an absolute measure of the learning phase. The number of error backpropagation processes indeed strongly depends on the number of elements in the database and on the batch size.

[†]Avg-std: Average-standard deviation

[†]Riedmiller & Braun (1993)

[†]MBGD: Mini-batch gradient descent

	Hidden layers composition	Activation function	Data normalization	Initialization type	Optimizer	Batch size	Regularization	Optimization method
Vollant *et al.* (2017)	(15;15) (8;5)	Sigmoid	Avg-std†	/	RPROP†	/	/	/
Gamahara & Hattori (2017)	(100)	Sigmoid	/	/	/	/	/	test of 6 mono -layer ANN
Maulik *et al.* (2018)	(10), (50), (100), (150)	ReLU	Avg-std	/	Adam	/	/	4 tests of nb of layers
Wang *et al.* (2018)	(20;10), (40;20), (90;60;30)	ReLU	/	/	/	/	L2 - 0.001	/
Zhou *et al.* (2019)	(50), (100), (200), (300), (400), (500)	Tanh	Avg-std	Weights: random Bias: zero	MBGD†	/	L2 - 0.0001	/
Xie *et al.* (2019)	(20;20), (20;20;20) (40;40)	Tanh	Min-max	/	Adam	1000	/	/
Yang *et al.* (2019)	(4;2;3), (6;4;3;3) (8;8;6;4;4)	Tanh	/	Random	SGD† LM algo†		/	/
Maulik *et al.* (2019)	(40;40;40;40;40)	ReLU Softmax	/	Random	Adam	/	/	Grid search over 1-8 layers, [10:10:100] neurons
Xie *et al.* (2020)	(1024;512), (1536;768) (1024;512;256)	Leaky ReLU	/	/	Adam	/	/	/
Rosofsky & Huerta (2020)	(64;32)	ReLU	/	/	Adam	1000	/	/
Prat *et al.* (2020)	(12;18), $H_f\times$ (2;1;2) $H_f = 4-8-12-16-20$	Tanh	/	Glorot	Adam	/	L1	/

Table 6.4: Overview of hyperparameters choices in the literature dedicated to the design of SGS models. Slash symbol indicates the lack of the information.

Initialization	He[†] (He *et al.*, 2015)
Activation function	Leaky ReLU or SELU[†]
Regularization	Drop-out
Optimizer	Nesterov accelerated gradient (Nesterov, 1983)
Learning rate	Exponential planification

Table 6.5: Recommendations to select hyperparameters (extracted from Géron (2017)).

Table 6.4 gathers the hyperparameters selected in the literature dedicated to the design of SGS models using ANN. It can be observed from this overview that the structure of ANN built by the various authors is highly variable. The number of hidden layers starts from a single one up to five. Few analysis are conducted to test the sensitivity of the ANN performance to its structure (and the choices of hyperparameters). Maulik *et al.* (2019) are actually the only authors identified who perform a grid search varying the number of layers and the number of neurons. For activation functions, the hyperbolic tangent and the ReLU are equally used. The leaky ReLU function is only used by Prat *et al.* (2020) whereas it is widely advised (see Table 6.5). The most common normalization is the one using the average and the standard deviation. Moreover, weights and bias are always (when the information is present) randomly initialized. The Adam optimizer, briefly presented in the next paragraph, is the most popular optimizer. The batch size and the information about the use of regularization are rarely given.

L1 or L2 regularization (or penalty) enables to respectively add the L1- or L2-norm of the weights weighted by a coefficient (usually equal to 0.0001) into the loss function which is used to compute the error back-propagation. When using the L1 regularization (also called Lasso regression), the ANN tries to minimize the sum of the absolute values of weights. That way, the less important weights are shrunk, keeping the most important connections. The L2 regularization (also called Ridge regression) has an opposite effect. The sum of the square values of weights is added to the loss function. This method therefore forces the ANN to balance the magnitude of weights over the whole network. It avoids the over-fitting issue improving the generalization capacity of the ANN.

Table 6.5 lists recommendations given in Géron (2017) to built an effective ANN. It is especially advised to use some drop-out to regularize the network. The drop-out is a method which consists in switching off a given percentage of neurons during the training step. The ANN is thus forced to balance the weights among the network. The effect is very close to the L2 regularization. Since the drop-out is not implemented in the Sklearn library, we use the L2

[†]SGD: Stochastic Gradient Descend.

[†]LM algo: Levenberg-Marquardt algorithm (Levenberg, 1944)

[†]The He initialization is an improved version of the Gorot initialization (Glorot & Bengio, 2010) dedicated to ReLU activation functions. It corresponds to a random initialization following a Gaussian distribution.

[†]SELU: Scaled Exponential Linear Unit. It is a normalized version of the ELU.

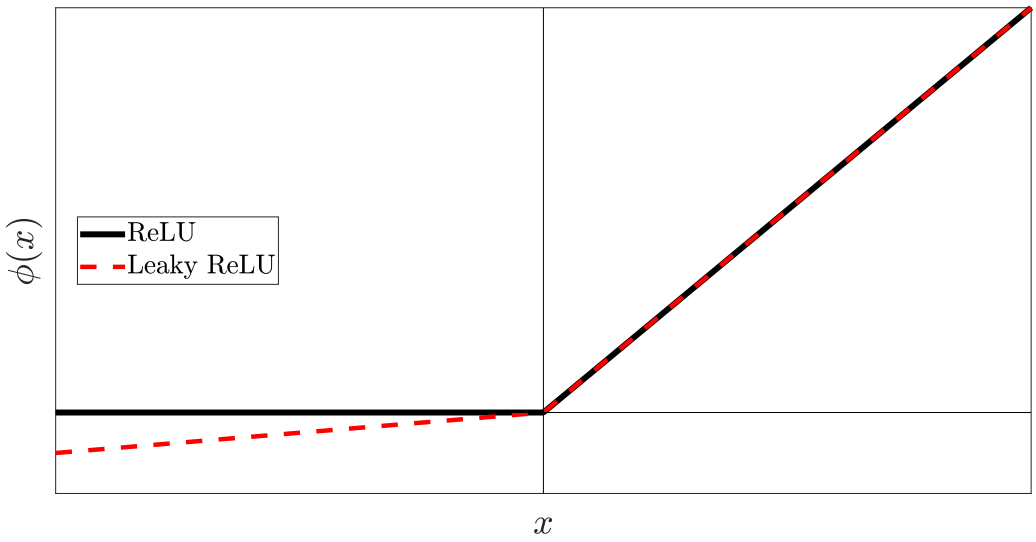

Figure 6.7: ReLU and LeakyReLU activation functions.

regularization. Moreover, the recommended Nesterov optimizer is also not available in Sklearn. We will thus preferentially use Adam.

Table 6.4 allows to identify some weaknesses regarding the choice of ANN hyperparameters in the literature focusing on SGS modeling: the number of layers and the number of neurons are the only hyperparameters subject to analysis and this analysis is rarely done using grid search methods. The choice of other hyperparameters is also never justified. The present study tries therefore to go further in the justification of the choice of hyperparameters using hyperparameters search and Hilbert-Schmidt Independence Criterion (HSIC) coefficients.

Innovative hyperparameters

Before tuning the ANN hyperparameters, let us introduce two innovative hyperparameters which are not available in Sklearn. They have thus been implemented into the Sklearn library in the course of this thesis work. The first one is the AdaBelief optimizer (Zhuang *et al.*, 2020). AdaBelief is derived from the well-known Adaptive Moment Estimation (Adam) optimizer (Kingma & Ba, 2014) which is widely used in recent ANN (see Table 6.4). AdaBelief accelerates Adam convergence in regions of small fluctuations and large values of the function loss gradient. AdaBelief is shown to improve the convergence speed and the generalization. Details about the algorithm are given in (Zhuang *et al.*, 2020).

The other hyperparameter which has been implemented during the course of this study in Sklearn is the leaky ReLU activation function. It is derived from the widely used rectified linear unit (ReLU) activation function which expresses as:

$$\phi(x) = \max(0, x) \tag{6.11}$$

The ReLU function performs better when compared to the sigmoid because it does not saturate for positive values. Yet, if weights and bias are modified such as the input value of a neuron is negative, the output of this neuron is zero. Since the gradient of the leaky ReLU function is zero in the negative part, it is very likely that the output of the neuron will remain equal to zero. These neurons are called dying ReLU. The leaky ReLU is designed to counter this phenomenon by enabling some "leak" for negative x values. They are defined as:

$$\phi(x) = \max(\alpha x, x) \tag{6.12}$$

where the hyperparameter α controls the rate of "leak" by changing the slope of the function for negative x values. Consequently, leaky ReLU neurons cannot die. These two activation functions are plotted in Figure 6.7. As mentioned above the positive part of the plot is identical unlike the negative one.

Hyperparameters Search

The most popular methods used to tune ANN are hyperparameter searches. The principle consists in browsing the largest part of the hyperparameters space, which is composed of all hyperparameters combinations, in a minimum amount of computational time. The most efficient algorithms used to solve this problem are based on the multi-armed bandit problem. The point is to find the best compromise between exploration and exploitation. That is to say between pursuing the training of an ANN or testing a new one with a different combination of hyperparameters. At first, a given number of ANN models are randomly selected among the hyperparameters space. Each of them represents a different combination of hyperparameters which is named an "arm". The algorithm establishes a competition between them. The least effective ANN are progressively eliminated in order to keep a final one which is supposed to be the most effective. The most simple hyperparameter search is called a grid search where no ANN are eliminated. All of them are equally trained. This method is yet very costly in case of large hyperparameters spaces.

Hyperparameters search methods are usually computed with parallel architectures where several ANN are tested simultaneously. In the case of a large amount of data and a large number of arms, the parallel Dask library proposes three algorithms: the successive halving search (Jamieson & Talwalkar, 2016), the hyperband search (Li *et al.*, 2017) and the inverse decay search. The three methods are based on a pyramidal competition between ANN. The only difference is the type of the elimination function.

The fundamental problem with these methods is the lack of information they provide about the sensitivity to the choice of the hyperparameters: they are often seen as black-box tools which only yield the most effective ANN. No information is provided about the most influential hyperparameters or the most relevant range for each of them. Yet, this information is stored in the results but is rarely exploited.

HSIC analysis: principles

The objective of the so-called Hilbert-Schmidt Independence Criterion (HSIC) analysis is to fully exploit grid search results by computing HSIC coefficients which measure the independence between two probability distributions. The present work is based on Novello *et al.* (2021). The authors first evaluate the probability distribution of hyperparameters among arms randomly selected by the hyperparameters search method (denoted P('hyperparameter')) and then compute the probability distribution for an ANN of being among the best decile networks (the 10% of the best ANN). This last probability is denoted P('hyperparameter'$|Z$), where Z is a random variable which is equal to one if the ANN is among the best decile. By measuring the dependency between the two probability distributions, HSIC coefficients provide a classification of the importance of hyperparameters. They also can be used to measure the independence of joint probability distributions. That way, one can emphasize interactions between hyperparameters. A simple example is given in Appendix F to illustrate how hyperparameters can

†GS: Grid Search

†ML: Mixing Layer

†[100:100:1000] denotes an interval extending from 100 to 1000 with a 100 step.

	Database	Hyperparameters	Nb of tested / Nb of total
GS† 1	ML† - $M_c = 2.2$ 4M/134M	• **Activation function:** Leaky ReLU-ReLU-Tanh • **Solver:** Adam-SGD • **Layer 1 / Layer 2:** 25-50-75-100	96 / 96
GS 2	ML - $M_c = 2.2$ 4M/134M	• **Batch size:** [100:100:1000]† • **Solver:** Adam-AdaBelief • $\boldsymbol{\epsilon}$**:** 10 log-spaced values between $10^{-12} - 10^{-6}$ • **Layer1/Layer2/Layer3:** 25-50-75-100 • **L2 regression** 10 log-spaced values between $10^{-4} - 10^{-2}$	(750 / 128 000)
GS 3	ML - $M_c = 1.1$ - $M_c = 2.2$ - HIT 4M/575M	Identical to GS2	(1000 / 128 000)

Table 6.6: List of performed grid searches with their corresponding parameters.

interact.

The computation of the HSIC coefficients is done in the post-processing step using the hyperband search results. However, the three aforementioned algorithms introduce a bias in the results because ANN are not equally trained. The best ANN are indeed trained longer and their scores tend therefore to be much improved with respect to the first eliminated ANN. To avoid this issue, classic grid searches are performed: all ANN are equally trained and HSIC coefficients are not influenced by the elimination process.

The method is first validated in Appendix F over trivial examples given in Novello *et al.* (2021) before being applied to the grid searches relevant for the design of the SGS pressure model , gathered in Table 6.6. All ANN are trained during 10 epochs which enables to reach a good compromise between the convergence and the computational time. The number of epochs can be seen as a low limit to reach convergence but this value has to be analyzed in lights of the size of data. Knowing that the grid search database contains 4 million elements, this choice of 10 epochs corresponds to 40 million ANN predictions.

HSIC analysis: results

Three different grid searches are performed. The first two ones are only performed over the mixing layer at $M_c = 2.2$. It has been indeed observed that this case is the most demanding one among the three configurations for the ANN to achieve good performance (see Section 6.4). The entire database ($134M$ of elements) is not used because, for grid search, data need to fit into a single processor in order to evaluate ANN in parallel. Four millions of elements are thus randomly selected among the whole database. The first grid search is performed over a small hyperparameters space which enables us to test all the possible combinations. The second grid search browses a large hyperparameters space. Only 750 randomly selected arms are tested over the 128 000 possibilities. The third grid search evaluates the same hyperparameters space using this time the three cases: both mixing layers and the forced HIT.

The first grid search evaluates ANN comprising two hidden layers with a number of neurons varying from 25 to 100 with a step of 25. The other hyperparameters are the activation function and the optimizer (see Table 6.6) yielding a small total number of explored ANN, equal to 96, which allows the computation of every single ANN. Figure 6.8 displays the HSIC coefficients computed for simple (a) and joint (b) PDF. Results show the greater importance of the number of neurons in the first layer and of the type of solver with respect to the number of neurons in the second layer and to the choice of the activation function. (which are about 2 to 3 times less important); In deep learning and especially in Convolutional Neural Network (CNN), the first hidden layers form the base of the network and are often therefore the most important ones whereas layers close to the output are more specialized (Géron, 2017). It seems thus consistent to find a larger HSIC for the first layer.

Once known the importance of each hyperparameter, it is also important to get an indication about the best range for each hyperparameter - we will come back to the interaction effects illustrated by Figure 6.8(b). The HSIC analysis also allows to produce Figure 6.9, which displays two PDF for each hyperparameter. The first one (P('hyperparameter')) corresponds to the initial probability in the hyperparameters space and is therefore uniform. The second one (P('hyperparameter'$|Z$)) is the probability conditioned to the best decile. For instance, looking at plot a) for the number of neurons in the first layer, it is clear choosing the largest value for this number significantly improves the quality of the ANN. Performing the same analysis for the other hyperparameters, it is advised to increase the number of neurons in both layers, to

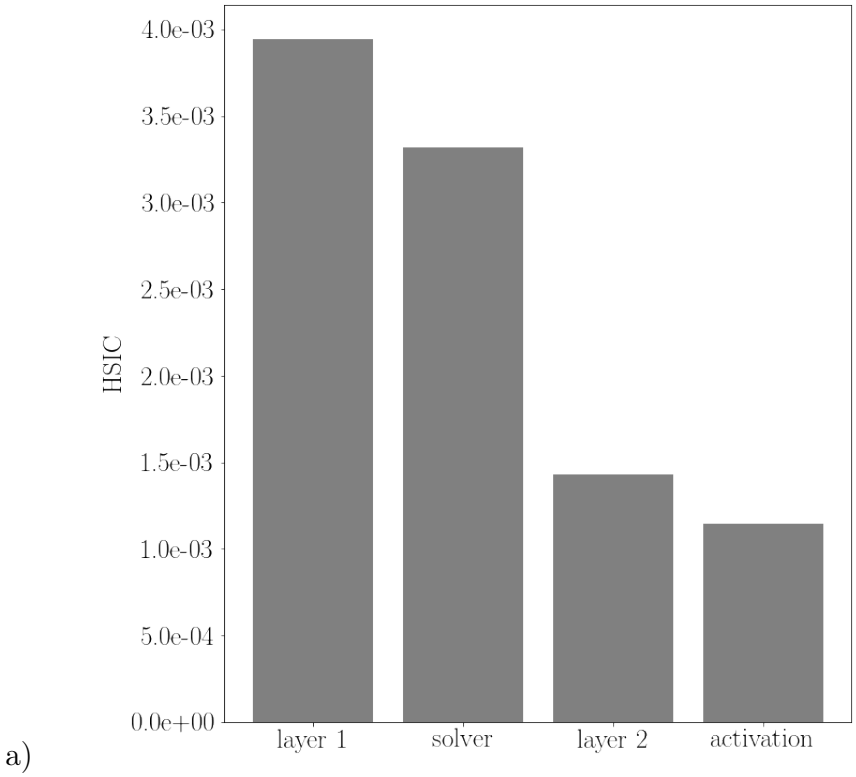

a)

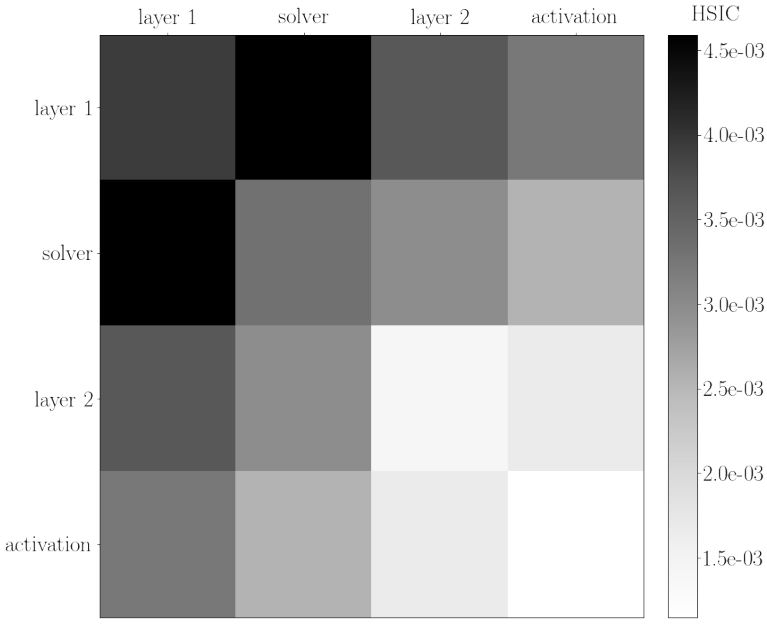

b)

Figure 6.8: (a) Classification of HSIC and (b) representation of HSIC interactions for Grid Search 1.

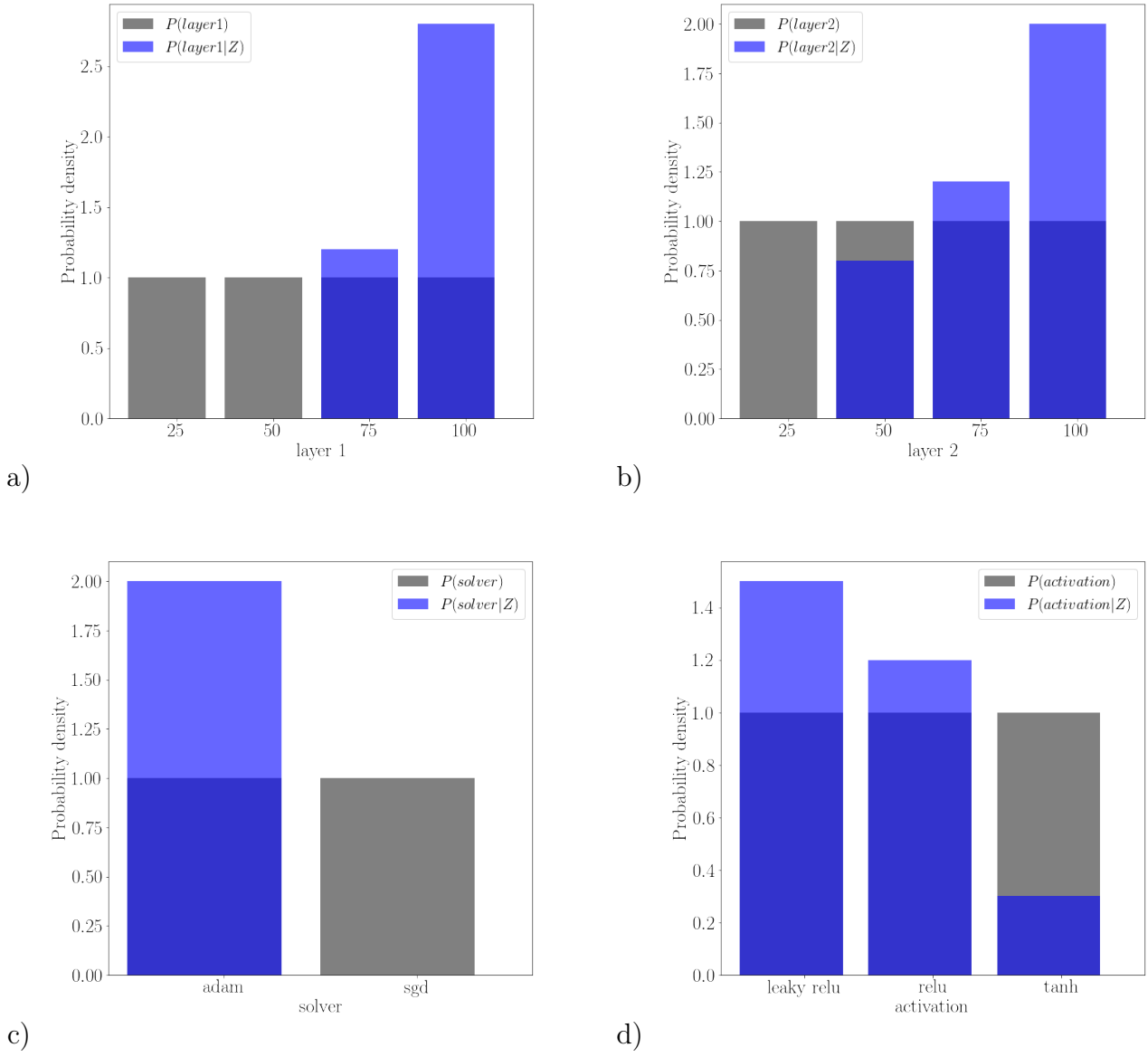

Figure 6.9: Probability density functions among hyperparameters choices for a) the number of neurons in the first layer, b) the number of neurons in the second layer, c) the type of solver and d) the activation function.

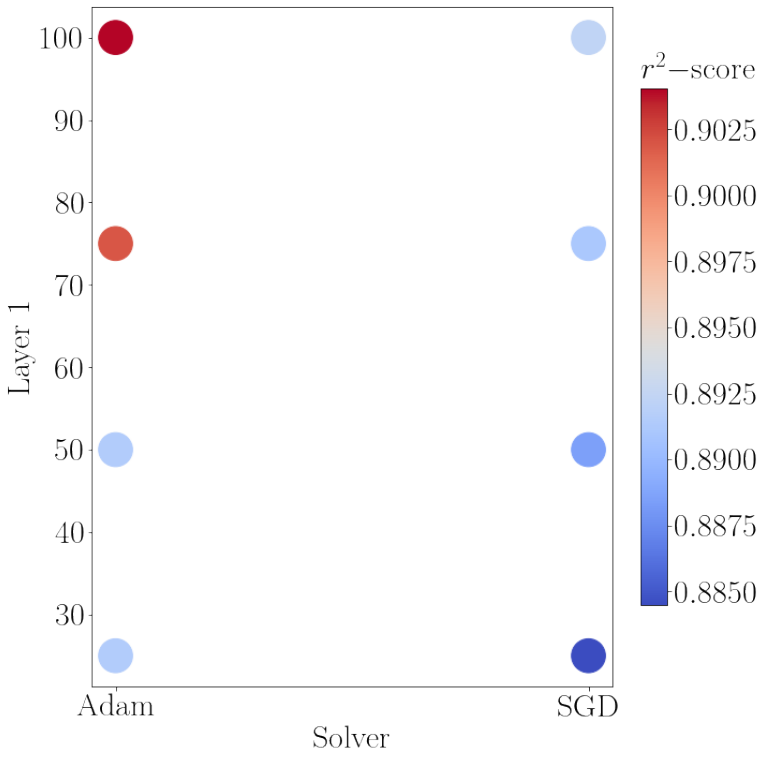

Figure 6.10: r^2-scores for the 8 Layer 1-Solver combinations averaged over each 12 possible combinations encountered during GS1 varying the two other hyperparameters (Layer 2 and the activation function).

choose the Adam solver and the leaky ReLU activation function. It can be useful to cross-check these information with Figure 6.8(a) in order to take into account the relative importance of each hyperparameter: in the present case, for a given computational cost of the ANN (which will be analyzed in a next paragraph), it is recommended to add more neurons in the first layer than in the second one.

Figure 6.8(b) represents the joint HSIC. This visualization provides information concerning interactions between two hyperparameters, with a diagonal equal to the HSIC given in Figure 6.8(a) corresponding to self-interaction. This map shows that significant interactions exist between "Layer 1", the most influential hyperparameter, and all the other hyperparameters. The interaction of "Layer 1" with the optimizer seems even slightly larger with the optimizer than with itself. In order to further investigate how these two hyperparameters interact, Figure 6.10 displays the averaged r^2-score. Two effects are observed: the performance increases with the number of neurons in the first layer and the Adam solver is always better than the SGD. The effect of both hyperparameters is monotone. The sensibility of the hyperparameters couple (Layer 1, Solver) is enhanced when compared to the influence of each hyperparameter taking separately.

Results for GS2 and GS3 are displayed respectively on the left and on the right in Figures 6.11, 6.12, 6.13 and 6.14. The only differences between the two grid searches are the change of the database and the increase of the number of tested combinations (see Table 6.6). The classification of variables (Figure 6.11(a)) is identical between the two. The second layer is this time more important than the first one. The presence of a third layer modifies the classification

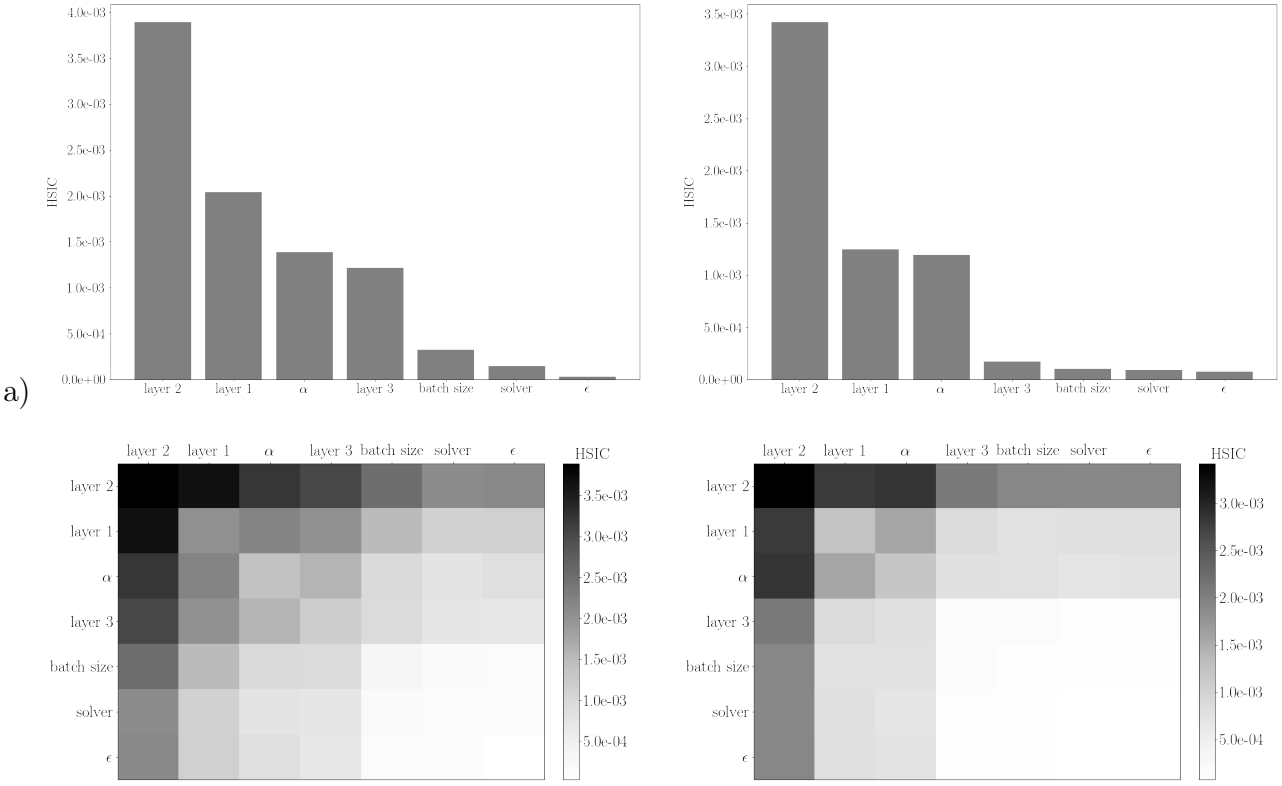

Figure 6.11: (a) Classification of HSIC and (b) representation of HSIC interactions for Grid Search 2 (left) and 3 (right).

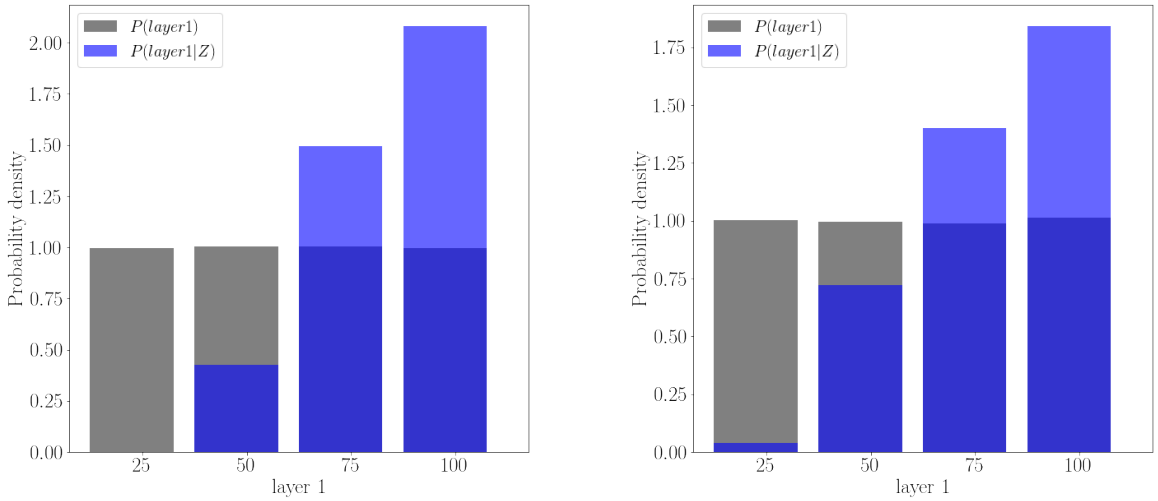

a)

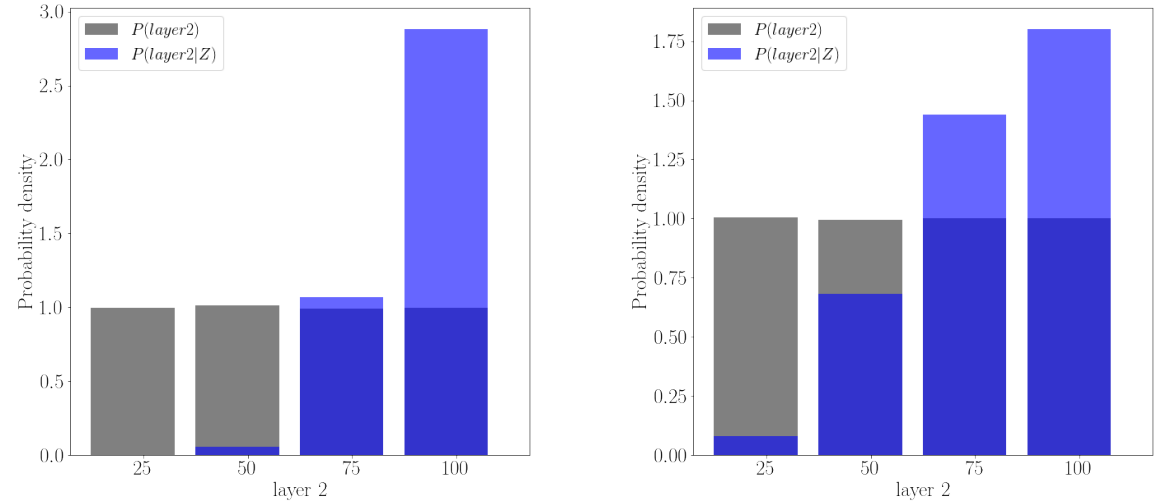

b)

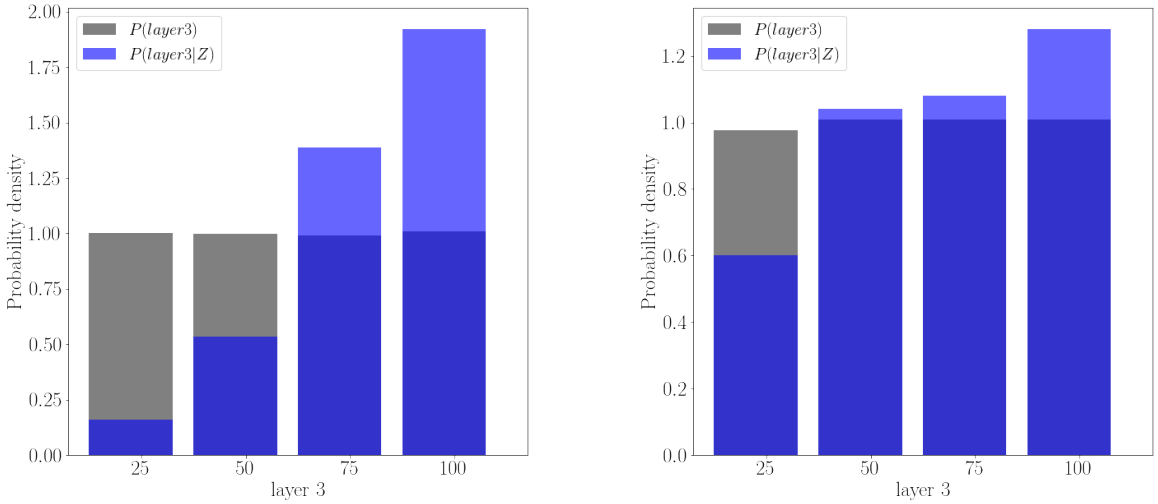

c)

Figure 6.12: Probability density functions among hyperparameters choices for a) the number of neurons in the first layer, b) the number of neurons in the second layer and c) the number of neurons in the third layer.

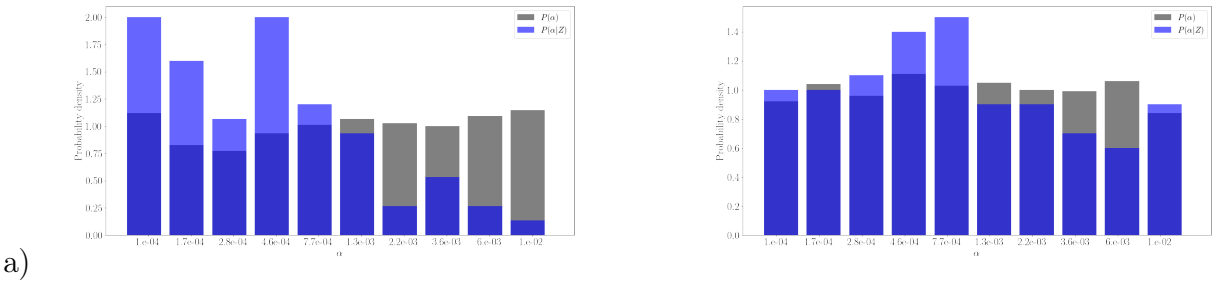

a)

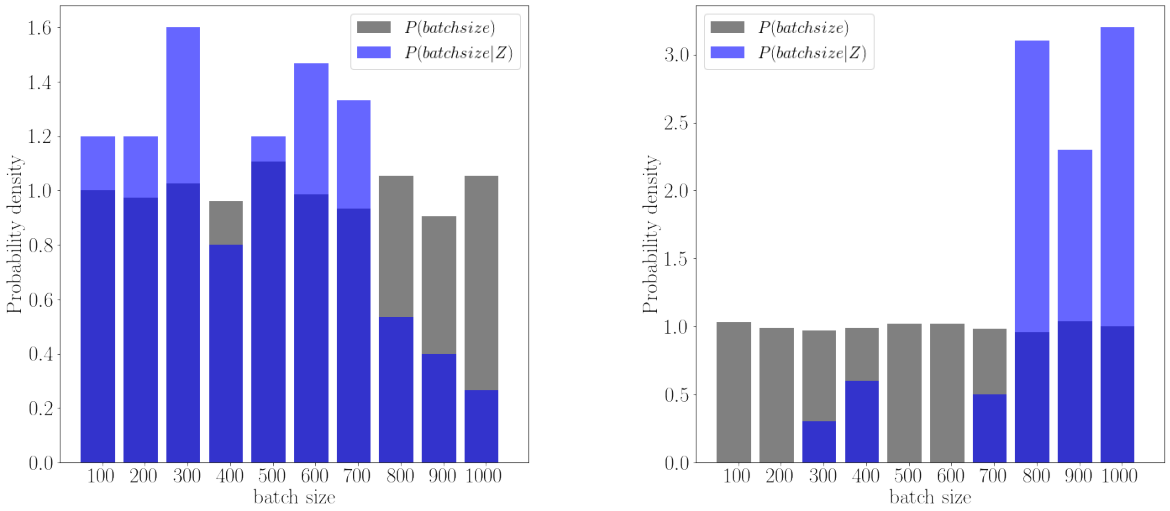

b)

Figure 6.13: Probability density functions among hyperparameters choices for a) the α parameter used for L2 regression and b) the batch size.

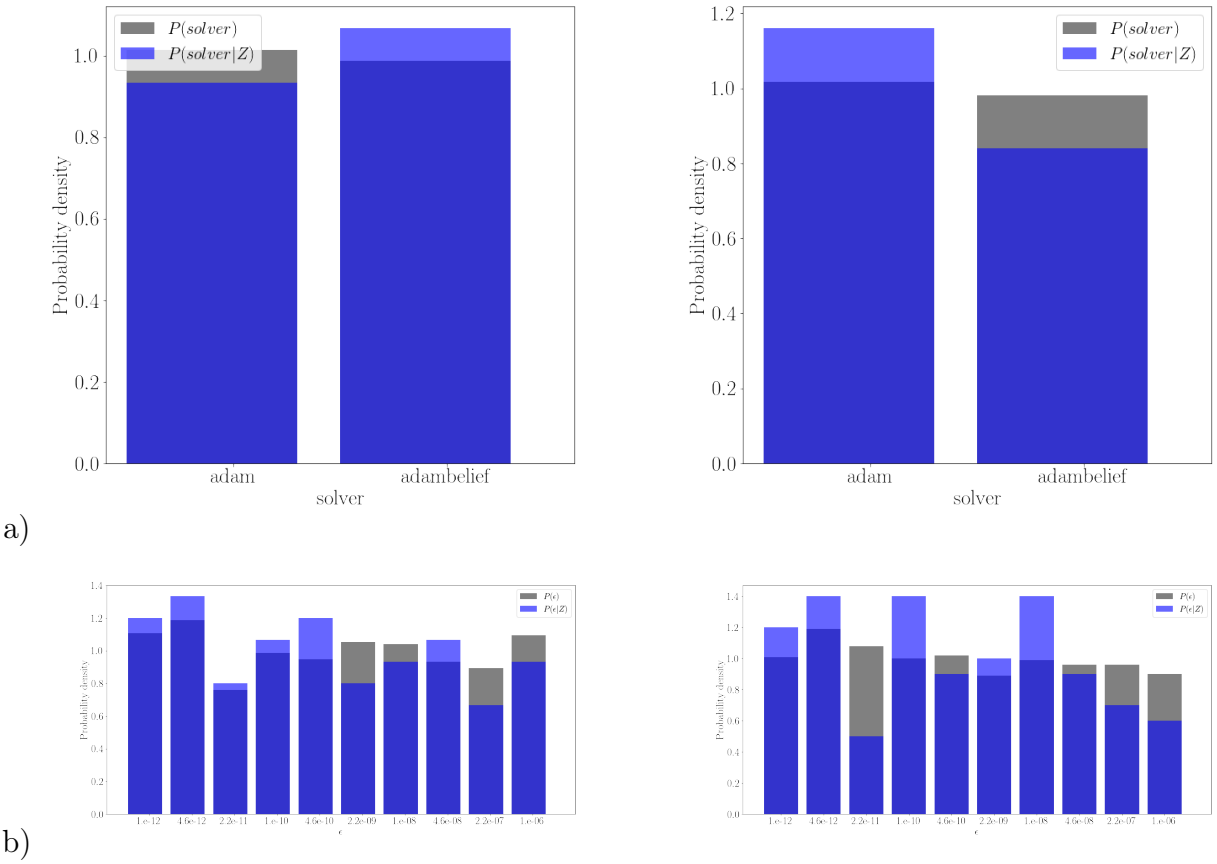

Figure 6.14: Probability density functions among hyperparameters choices for a) the type of optimizer and b) the ϵ parameter used in Adam type solvers.

previously displayed for GS1. The last layer remains however the least important one. The α parameter which controls the L2 regression has a significant effect over the performance in both grid searches. It is therefore required to carefully select this hyperparameter which is used to equalize the network. Note that this time the optimizer only has a small effect because its choice is limited to Adam and AdaBelief. HSIC strongly depends of course on the range of values allowed to the hyperparameters in the grid search.

Figure 6.11(b) does not show any significant interaction which is not related to the "Layer 2" hyperparameter. One can thus focus on Figures 6.12, 6.13 and 6.14 which display the best ranges for each hyperparameter. Consistently with GS1, increasing the number of neurons always leads to ANN improvement but it is advised to preferentially increase the first two layers (and even more the second one). For the α parameter, for the batch size and for the solver, results differ between GS2 and GS3. For α, a common range, around $\alpha = 5.10^{-4}$, can be found between the two grid searches. Yet, for the batch size, no common interval exists. Since the GS3 data set is more representative of the full database than the GS2 data set, the batch size is set to 800. For the solver, results are contradictory between the grid searches. The differences between the probability density are however very small as evidenced by the classification of HSIC (Figure 6.11(a)). In our case, the AdaBelief solver does not bring a significant improvement. Since the Adam solver is recommended in GS3 considered as more representative of the full database, it is retained for the following ANN training. The last tested hyperparameter ϵ is related to the solver. Following the results of both GS2 and GS3, its effect over the ANN score can be neglected.

All the choices made for the selected hyperparameters are gathered in Table 6.7. They include both the choices justified by the previous HSIC analysis and the other choices based on recommendations taken from reference textbooks (Géron, 2017) and options available in Sklearn. Note that the number of layers and the number of neurons per layer are not provided in this table. Since all grid searches results show that the ANN performance increases with the number of neurons in the tested range ($[25 : 100]$), the structure of the ANN is determined thanks to an analysis of the maximum realistic extra cost induced by the ANN model when performing an LES using the AVBP code.

Computational cost of the ANN

In order to foster the use of the SGS pressure model, the maximum extra cost associated with the ANN-based model should not exceed 20% to 30%. An *a posteriori* evaluation is therefore conducted to evaluate this extra cost as a function of the number of degrees of freedom of the network. This extra cost is based on a reference LES. This reference LES is computed without any model for the SGS pressure but it uses two classic LES models (the dynamic Smagorinsky and the turbulent Prandtl number models) to take into account the SGS turbulent stress tensor and the SGS internal energy (see Section 7.2). In order to make possible the use of the ANN model for the SGS pressure modeling in AVBP, an option has been implemented in the code. Results are displayed in Figure 6.15 for an ANN which does not use the inputs requiring Laplacian computation $\left(\Delta\left(\bar{\rho}\right), \Delta\left(\widehat{T}\right), \Delta\left(\widehat{p}\right) \text{ and } \Delta\left(\bar{\rho}\widetilde{E}\right)\right)$. Note that this is only a first approximation of the cost: the results could probably be improved by optimizing the implementation.

Suppressing Laplacians in the ANN design process is motivated by the following observation. The values taken by space derivatives depend on the precise implementation of the

	Results of the HSIC study
Activation function	Leaky ReLU
Regularization	L2 with $\alpha = 0.0005$
Optimizer	Adam
ϵ (Adam parameter)	10^{-11}
Batch size	800
	Other hyperparameters choices
Initialization	Glorot (Glorot & Bengio, 2010) (The He initialization is not available in Sklearn)
Loss function	Mean Square Error (MSE)
Data Normalization	Avg-std
Test ratio	0.2
(β_1,β_2) (Adam parameter)	(0.9,0.999)

Table 6.7: Appropriate hyperparameters for the present work.

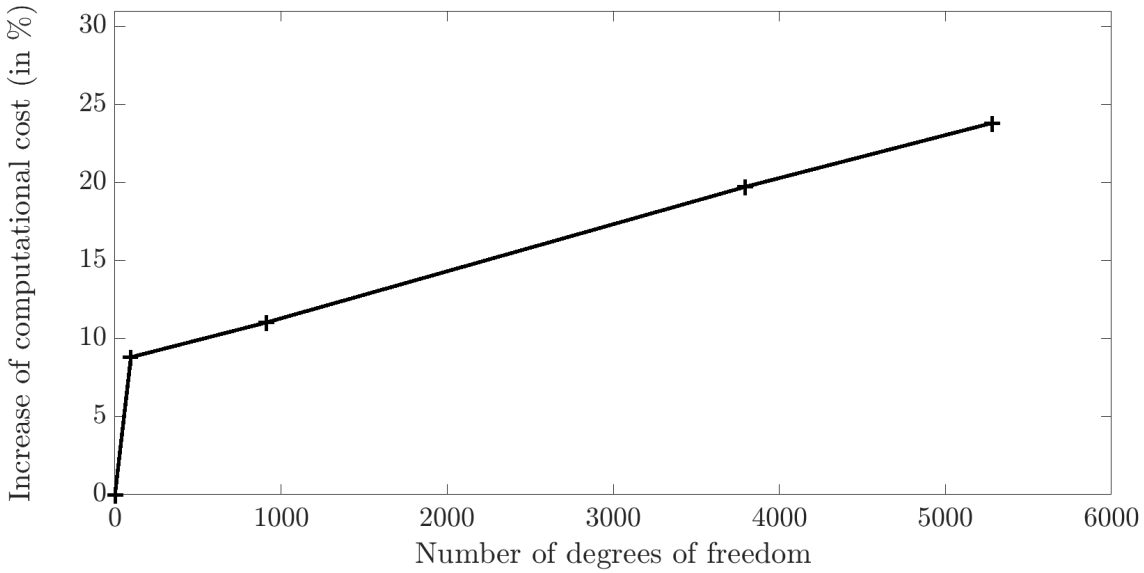

Figure 6.15: Evolution of additional computational cost related to the ANN model without using the inputs requiring Laplacian computation.

discretization formulae in the *a posteriori* step, when the model is used in its final numerical environment. In the *a priori* step, finite difference formulae are used and comparisons using the same inputs fields between *a priori* gradients and *a posteriori* gradients showed rather good agreement (see Figure 6.16(a)). However, to obtain Laplacians, this differentiation step has to be repeated which decreases the quality of the comparison. In light of this lack of representativity of the Laplacians obtained in the *a priori* step see Figure 6.16(b), it was decided to build a model which only uses primitive variables and their derivative. This choice enables computational time savings but also impacts the ANN performance. The evaluation of this type of model is provided in Section 6.4.1.

Figure 6.15 shows that the use of the ANN model induces two types of extra cost: a fixed cost (independent of the ANN size) and a variable cost depending (linearly) on the number of degrees of freedom. The fixed extra cost arises from the management of ANN model parameters and from the necessary computation of ANN inputs. It is therefore present even for very small networks. Its value is about 8% in our case. The variable extra cost evolves linearly with the number of degrees of freedom, which is directly related to the size of networks. To not exceed 20% to 30%, which could be considered as a "reasonable" extra cost for the SGS pressure model, the number of degrees of freedom must be limited to approximately 5500. This corresponds to a network comprising two hidden layers of 66 neurons each (11;66;66;1).

Since we know that the ANN performance increases with the number of degrees of freedom and since the maximum size limit of the network has been evaluated, it remains to quantify the influence of the network size over the r^2-score. Figure 6.17 displays grid search results obtained when varying the number of neurons for single and double hidden layers networks evaluated using the full database (see Figure 6.6). For single hidden layers, each bar symbolizes the r^2-score of one ANN trained over 10 epochs. For double hidden layers networks, since several combinations of neurons can correspond to the same number of degrees of freedom, each bar symbolizes the r^2-score of the most effective ANN trained over 10 epochs.

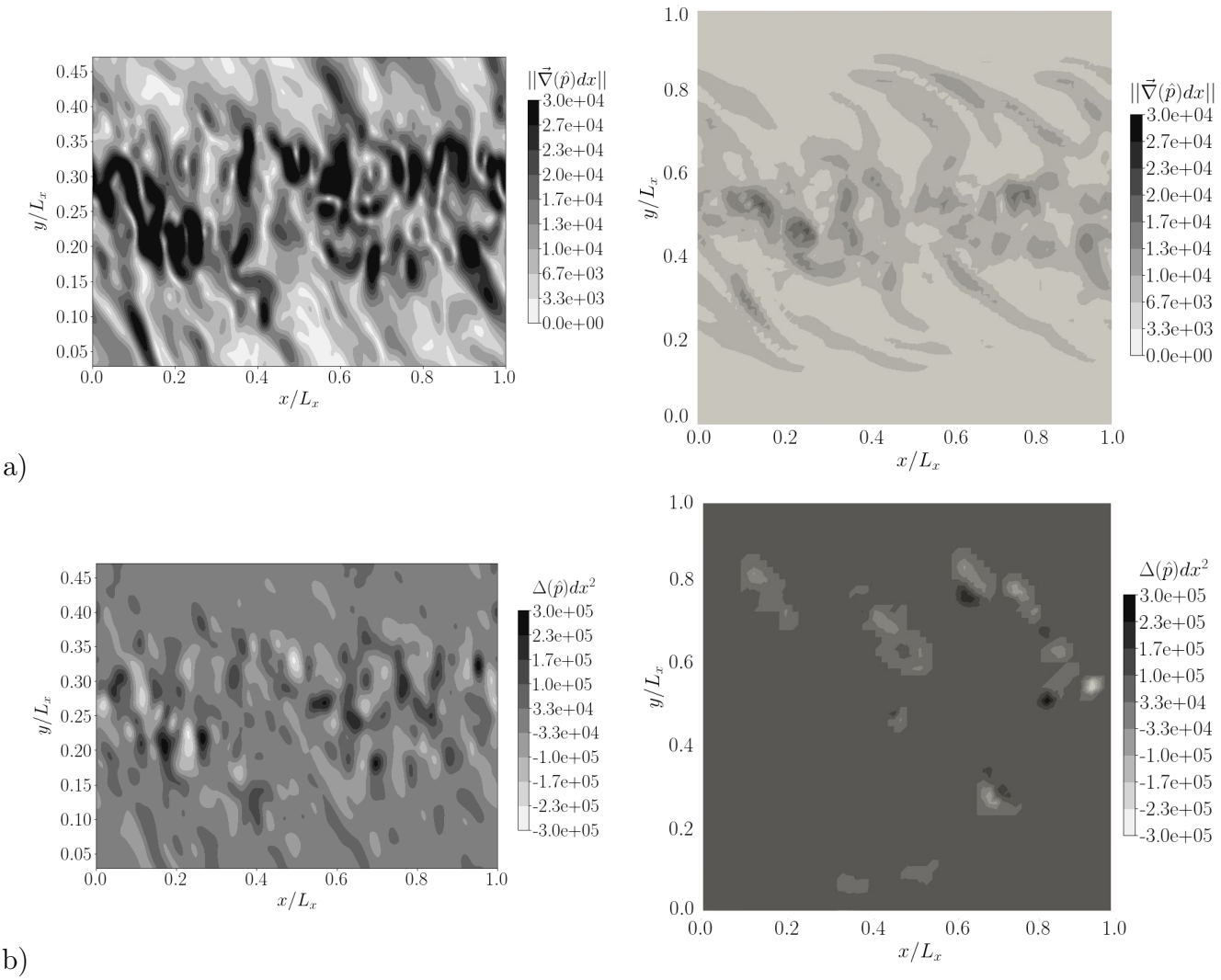

Figure 6.16: $z-$centerplane contours colored by (a) $\|\nabla(\widehat{p})\|$ and (b) $\Delta\widehat{p}$ for the mixing layer at $M_c = 1.1$ for (left) the *a priori* LES (filtered DNS) and for (right) the *a posteriori* LES at $\bar{\Delta}/\Delta_{\mathrm{DNS}} = 64$. Results are plotted at $\tau = 1750$. Note that the domain length in the $y-$direction is twice larger for the *a posteriori* LES than the filtered DNS because it has been enlarged in order to obtain long enough LES simulations without reaching domain boundaries (see Chapter 7).

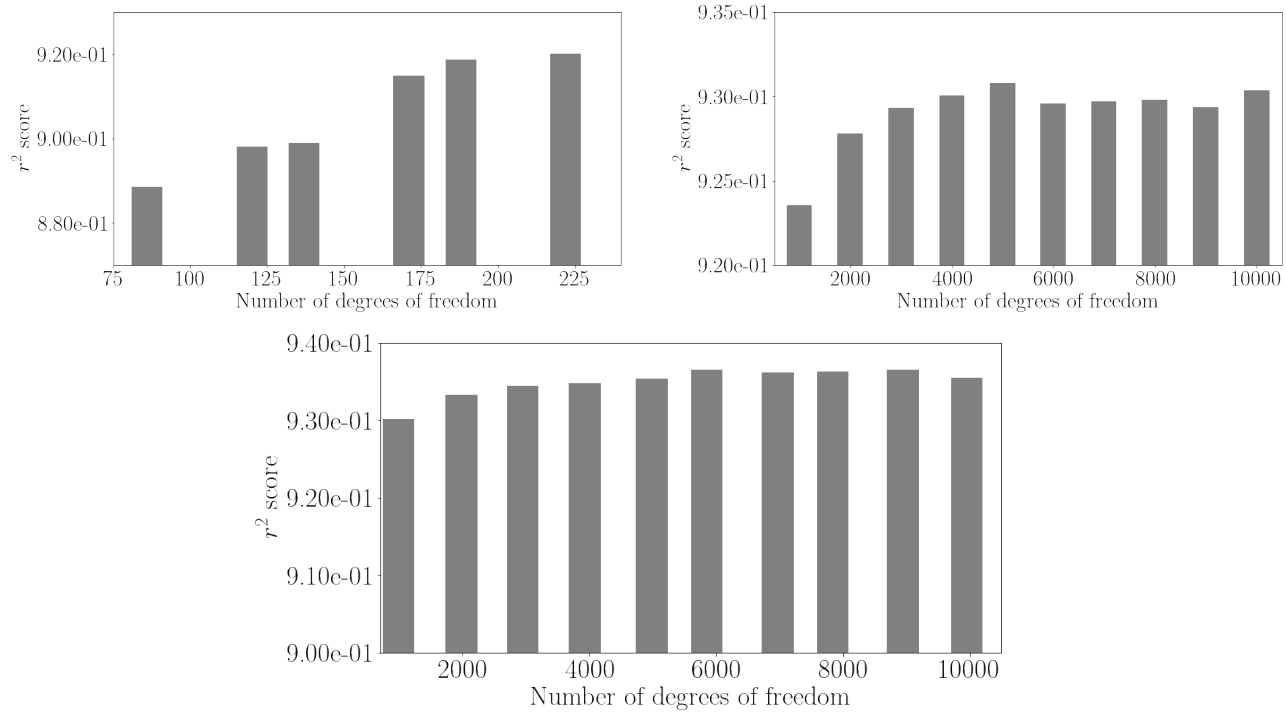

Figure 6.17: Distribution of the r^2-score as a function of the number of degrees of freedom for (top) single hidden layers ANN and (bottom) double hidden layers ANN. Networks are trained over 10 epochs. Each bar corresponds to the r^2-score of the most effective ANN for a given DoF.

For single hidden layer networks, the r^2-score is almost constant and equal to 0.93 from 3000 to 10000 degrees of freedom. Surprisingly, when decreasing the number of degrees, the performance remains very reasonable for very small networks. A network comprising one hidden layer of 6 neurons achieves a r^2-score of approximately 0.90. Note that the score for 5000 degrees of freedom (DoF) is slightly larger than for a larger number of DoF. Two reasons could explain this counter-intuitive result: ANN are trained only over 10 epochs so that the r^2-score analyzed here is not necessarily a converged value; the grid search should be repeated several times to get rid of stochastic effects and obtain a statistically averaged value.

For double hidden layers networks, given the same number of degrees of freedom, the performance is slightly better than for single hidden layer networks (0.935 against 0.93). Moreover, the decrease of the performance at small numbers of DoF is even more reduced. Using two hidden layers instead of a single one leads to more effective ANN. All results show a very limited effect of the size of network and even for very small networks, the performance remains reasonable.

Note that the score computed for these experiments is evaluated over the three flow configurations (HIT and mixing layer at $M_c = 1.1$ and $M_c = 2.2$). In the following section, other tests are performed to better assess the influence of the number of degrees of freedom on the performance of the ANN defined with the choice of hyperparameters properly justified in this section.

6.4 ANN training and testing

The present section is devoted to the training and the testing of the ANN characterized by the choices of hyperparameters reported in Table 6.7. Several tests are performed:

- to evaluate the ANN performance for each flow configuration (HIT and both mixing layers),
- to quantify the effect of the removal of Laplacian inputs,
- and to complement the previous grid search results by evaluating the evolution of the ANN performance for each flow configuration when the number of degrees of freedom is varied.

Some generalization tests are computed next to evaluate the capacity of the model to provide reliable results for cases (flow configurations) which have not been encountered during the learning process. The retained model will be eventually *a posteriori* evaluated in the final Chapter 7.

6.4.1 Final tests for the tuned ANN

Performance evaluation

In addition to the issue of managing a very large amount of data, the ANN training using a database which combines several configurations causes learning disparities, which have been carefully investigated for a two hidden layers network, with 55 neurons in each hidden layer, yielding a total of 4016 degrees of freedom (weights and bias). Let us remind the reader that the ANN is trained using a training database (or sub-database or partition) corresponding to 80% of the full database which combines the three flow configurations: HIT, mixing layer at $M_c = 1.1$ and $M_c = 2.2$. The remaining 20% define the testing database (or sub-database or partition) on which the ANN designed in the training stage can be assessed using information not included in the training partition. Figure 6.18 displays the learning curves (r^2-score and mean square error (MSE)) for the $(15; 55; 55; 1)$ network (with hyperparameters defined in Table 6.7). Note these accuracy indicators are computed after each epoch by applying the current ANN (with its weights and bias computed from the optimization step) to the testing database only. The "Full database" plots correspond to r^2-score and MSE computed for the totality of the testing database or partition (which includes 20% of the three flow configurations data). The "HIT" (respectively "$M_c = 1.1$", "$M_c = 2.2$") plots correspond to r^2-score and MSE computed only for the subset of the testing database corresponding to the HIT flow configuration (respectively the mixing layer at $M_c = 1.1$ and $M_c = 2.2$). Consequently, Figure 6.18 reports the training behavior of a single ANN but with an enriched information on the predictive efficiency on the network since given not only for the whole testing partition but also for the subsets associated with each flow configuration.

The network accuracy indicators converge very quickly, in approximately 10 epochs, to their asymptotic value. This is due to the very large amount of data: after each epoch, about 575 million elements have passed through the network. Although the overall performance of the network is about 0.97 at the end of the learning step (see Table 6.8), it is much smaller when computed for both mixing layers only: 0.92 at $M_c = 1.1$ and 0.88 at $M_c = 2.2$. Its performance when computed for the forced HIT only remains however satisfactory with a r^2-score of 0.97.

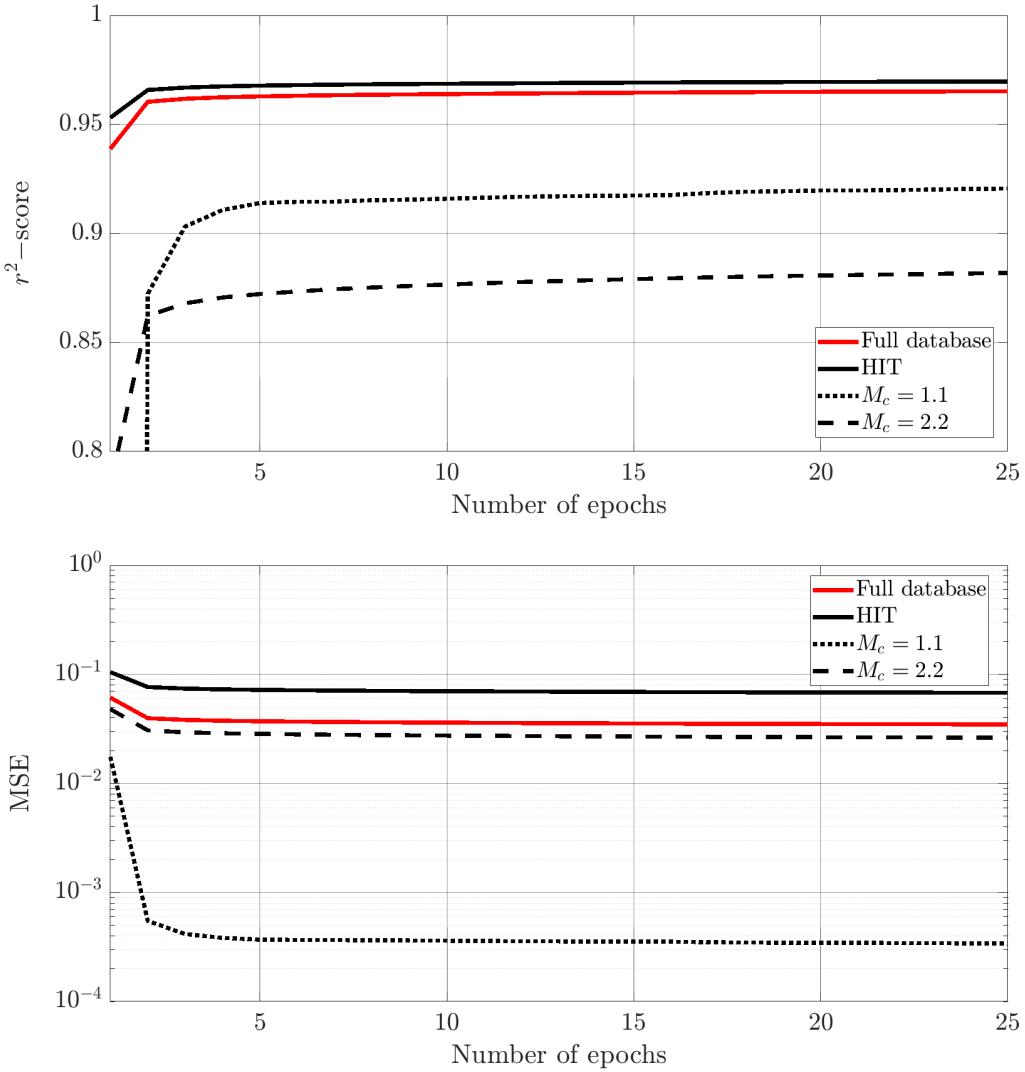

Figure 6.18: Evolution of (a) the r^2-score and (b) the mean square error (MSE) as a function of the number of epochs. r^2-scores and MSE are evaluated on the testing partition (full partition or subset corresponding to a given flow configuration). The (15;55;55;1) ANN contains 4016 degrees of freedom and the training is performed using the Laplacians inputs as indicated by the 15 input data.

Two main reasons can explain this behavior of the ANN.

The first reason that comes to mind is the difference in the size of the data among the cases (see Table 6.1). However, the ANN analyzed here has been trained over a database where data sizes have been balanced between each configuration. It has been checked (the results are not reported here) that the difference between a non-balanced and a balanced database is not significant anyway. The second reason, more convincing, for this learning inhomogeneity is related to the distribution of the SGS pressure term $(\bar{p} - \widehat{p})$. The PDF, given in Figure 6.5, shows indeed a much wider distribution for the forced HIT. The larger magnitude of the SGS pressure term for this configuration significantly influences the computation of the r^2-score. Note that the correlation coefficients are much less influenced by this effect (see Table 6.8). The learning inhomogeneity is also visible for the MSE learning curve (Figure 6.18) where the forced HIT displays the largest amplitude. Since the MSE is used in the loss function to correct weights and biases, it is likely that a larger amplitude of the MSE over a given configuration

Testing configuration	r^2-score	Correlation coefficient
Full testing partition	0.97	0.98
Testing partition subset: forced HIT	0.97	0.98
Testing partition subset: $M_c = 1.1$	0.92	0.96
Testing partition subset: $M_c = 2.2$	0.88	0.94

Table 6.8: Performance of the (15;55;55;1) ANN model (4016 degrees of freedom) trained using Laplacian inputs and with the full database training partition (80% of the data corresponding to the 3 flow configurations). r^2-scores and MSE are computed using the testing partition (remaining 20%) or subsets of the testing partition.

is related to a stronger correction and thereby a possibly better learning for this configuration. Yet, this can only be partially true since the r^2-score for the mixing layer at $M_c = 2.2$ is smaller than that for the mixing layer at $M_c = 1.1$ whereas the MSE is larger for $M_c = 2.2$ than for $M_c = 1.1$. This contradiction is likely to be due to the strong decrease of correlations between the 15 inputs and the output when going from $M_c = 1.1$ to $M_c = 2.2$, which significantly hinders the ANN performance.

Figure 6.19 compares predicted versus true (or observed) output values plotted for the three configurations and for the overall database. Let us emphasize again the predicted values are those given by the unique ANN defined at the end of the training stage depicted in Figure 6.18. The various plots of Figure 6.19 actually detail the final values of the global accuracy indicators (r^2-score and MSE) by successively providing an overview of "ANN predictions vs observations" for the subsets of the testing partition (plots (a) to (c)) and the full testing partition (plot (d)). These plots confirm the comments made on the curves of Figure 6.19 and the asymptotic values of Table 6.8. The magnitude of the predicted and true values is significantly larger for the forced HIT. When the r^2-score is evaluated over the entire testing partition, residuals for both mixing layers are flattened by the forced HIT. When evaluated separately for each flow configuration, the ANN prediction shows much larger discrepancies. As a result, no visible difference can be detected between the forced HIT (Figure 6.19(c)) and the overall (testing) database (Figure 6.19(d)).

Finally, although the performance is inhomogeneous over the different configurations, when looking at the correlation coefficients, the trained ANN remains very effective in comparison to the literature (Gamahara & Hattori, 2017; Wang *et al.*, 2018; Prat *et al.*, 2020). Note that very few authors use the r^2-score (Pawar *et al.*, 2020) whereas this measure is a much more discriminant metric when compared to the correlation coefficient. An ANN with an acceptable (generally a value over 0.7) correlation coefficient between predicted and true values would not necessarily lead to a good r^2-score.

Removal of the Laplacian inputs

As previously mentioned when discussing the evaluation of the ANN computational cost (see Section 6.3.2), the removal of inputs requiring Laplacian computation offers two main benefits: i) the reduction of discrepancies in ANN inputs between *a priori* and *a posteriori* LES, ii) com-

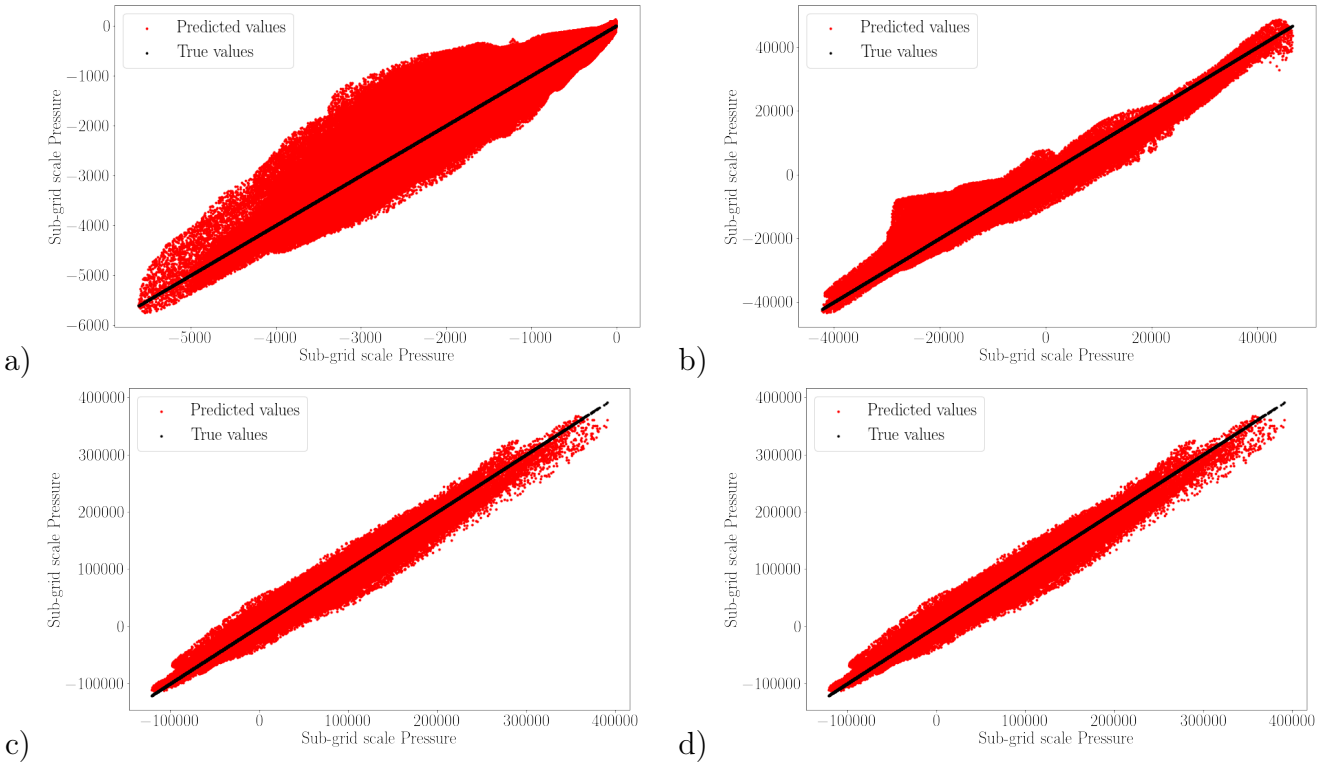

Figure 6.19: In red, representation of the values predicted by a (15;55;55;1) ANN model (4016 degrees of freedom) versus the true values and in black, representation of true values versus true values. Flow configuration(s) (a) mixing layer only at $M_c = 1.1$, (b) mixing layer only at $M_c = 2.2$, (c) forced HIT only, (d) full testing partition.

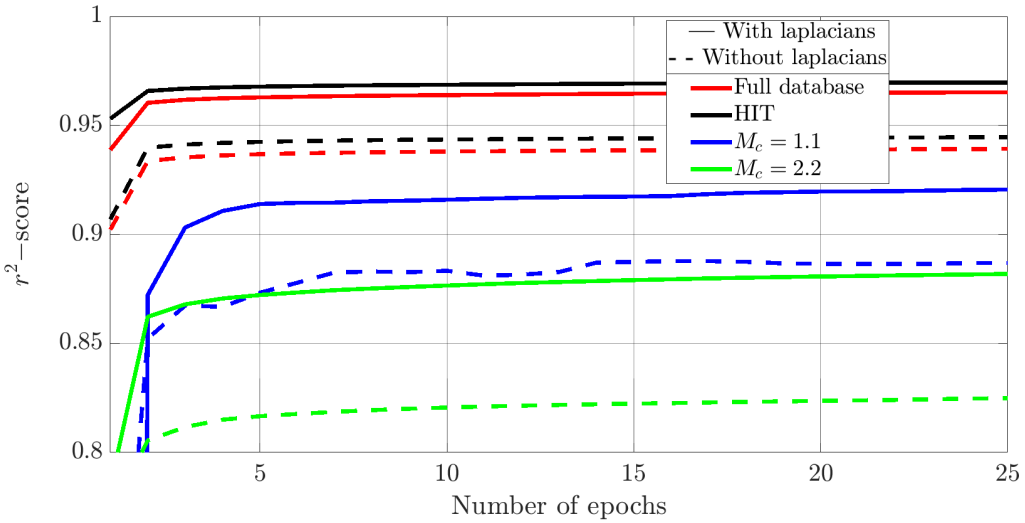

Figure 6.20: Comparison of the r^2-score evolutions between ANN with and without Laplacian inputs as a function of the number of epochs. Results are evaluated over the testing partition.

putational cost savings. The objective here is to evaluate the impact on the ANN performance (accuracy of the ANN prediction) of the Laplacian inputs removal.

In addition to the preliminary tests summarized in Table 6.3, which indicated a r^2-score reduction from 0.93 to 0.90 when removing the Laplacian inputs, Figure 6.20 compares the scores during the learning process for two ANN sharing the same two hidden layers structure with 55 neurons for each layer but one being trained with Laplacian inputs, hence of the form (15;55;55;1), while the other is trained without these 4 Laplacian inputs, hence of the form (11;55;55;1). When removing the Laplacian inputs, the overall r^2-score is reduced by about 0.03, consistently with Table 6.3. Note the values (after 10 epochs) of the r^2-score and the correlation coefficient for the ANN without Laplacian inputs are reported in Table 6.9 for the (11;55;55;1) ANN (corresponding to 3796 degrees of freedom). Figure 6.20 allows to detail the effect of the Laplacian inputs removal on the prediction specific to a given flow configuration (HIT or mixing layer). This effect is found particularly significant for the mixing layer at $M_c = 2.2$ since the difference between the two r^2- scores (ANN with and without Laplacian inputs) is about 0.06. Note this was not really expected as Laplacian inputs were shown to poorly correlate with the SGS pressure (see Table 6.2). Note that even though the r^2-score without Laplacian inputs goes down to 0.82 for this $M_c = 2.2$ mixing layer configuration, the correlation coefficient between predicted and true output values remains satisfactory with a value of 0.91.

These experiments justify to retain from now on a simplified model without Laplacian inputs, which is known to be slightly less effective than the one including Laplacian inputs but which strongly facilitates the *a posteriori* validation (see Chapter 7).

Variation of the number of degrees of freedom

In Section 6.3.2, it has been shown that the increase of the network size goes along with the performance improvement, though this improvement remains very small in terms of r^2-score amplitude. This observation would tend to favor the use of a small size ANN, since its computational cost is smaller and its predictive efficiency appears to remain acceptable. However, the first tests reported in Section 6.3.2 have been evaluated using the global r^2-score computed for the full testing partition (see Table 6.1), which tends to hide the potentially significant discrepancies that might exist when applying the ANN model to one flow configuration or another. In order to properly quantify the influence of the network size on the ANN performance, scores need to be evaluated separately over each case or flow configuration.

Table 6.9 compares four double hidden layers ANN (without Laplacian inputs) with a number of degrees of freedom increasing from 96 to 3796. For each ANN, the r^2-score and correlation coefficient are computed not only for the full testing database but also separately for the 3 subsets of this testing database, corresponding to the 3 flow configurations. For a very small size ANN (11;5;5;1) (corresponding to 96 degrees of freedom), the overall performance (r^2-score about 0.90) appears very reasonable but it actually hides the far less satisfactory scores computed for the mixing layers only, which are respectively equal to 0.47 and 0.67 for $M_c = 1.1$ and $M_c = 2.2$. One can note that the correlation coefficients remain high (superior to 0.84) in any case, despite the drop in the r^2-score: as previously mentioned, this underlines the importance of selecting a relevant metric for the network efficiency and the choice of the r^2-score should be favored over the usual correlation coefficient.

Number of degrees of freedom	Testing configuration	r^2-score	Correlation coefficient
96	Full database	0.90	0.95
	Forced HIT	0.92	0.95
	$M_c = 1.1$	0.47	0.88
	$M_c = 2.2$	0.67	0.84
436	Full database	0.93	0.97
	Forced HIT	0.94	0.97
	$M_c = 1.1$	0.81	0.92
	$M_c = 2.2$	0.79	0.89
913	Full database	0.93	0.97
	Forced HIT	0.94	0.97
	$M_c = 1.1$	0.86	0.94
	$M_c = 2.2$	0.79	0.89
3796	Full database	0.94	0.97
	Forced HIT	0.94	0.97
	$M_c = 1.1$	0.89	0.94
	$M_c = 2.2$	0.82	0.91

Table 6.9: Accuracy assessment for several ANN with a different number of degrees of freedom (96-436-913-3796). r^2-scores and correlation coefficients are computed after 10 epochs using the testing partition (full or its subsets corresponding to the 3 flow configurations). All ANN are trained without Laplacian inputs.

Training configuration	Testing configuration	r^2-score	Correlation coefficient
HIT	Full database	0.91	0.96
	Forced HIT	0.96	0.98
	$M_c = 1.1$	0.40	0.64
	$M_c = 2.2$	0.13	0.84
$M_c = 1.1$	Full database	-1.42	0.10
	Forced HIT	-1.66	0.16
	$M_c = 1.1$	0.93	0.97
	$M_c = 2.2$	-0.09	0.53
$M_c = 2.2$	Full database	-0.39	0.66
	Forced HIT	-0.49	0.70
	$M_c = 1.1$	-45.5	0.68
	$M_c = 2.2$	0.86	0.93
Full database	Full database	0.96	0.98
	Forced HIT	0.97	0.98
	$M_c = 1.1$	0.91	0.96
	$M_c = 2.2$	0.88	0.94

Table 6.10: Results of generalization tests for the (15;55;55;1) ANN (4016 degrees of freedom) trained with Laplacian inputs. Metrics (r^2-score and correlation coefficient) are evaluated over the full solutions after 10 epochs.

The increase of the network size quickly leads to an improvement of the network performance, even when selectively applied to the mixing layer cases. For a (11;15;15;1) network comprising 436 degrees of freedom, all r^2-scores are larger than 0.79. Further increasing the number of degrees of freedom yields a very slight improvement of the global performance (metrics computed for the full testing database) but enables a significant improvement of the r^2-score for both mixing layers. The network with 3796 degrees of freedom appears eventually as a good trade-off between the computational cost (about 20% increase with respect to the baseline LES calculation without SGS pressure model) and the prediction performance for mixing layers.

6.4.2 Generalization tests

The generalization test focus on the ability of the ANN to generalize its good prediction to other cases / flow configurations which were not present in the training database. The first test consists in:

- training an ANN over one of the configurations among the database (Table 6.1)
- and testing it over the other configurations (which were not included in the training database).

Tested configuration	Temporal solutions	r^2-score	Correlation coefficient
Forced HIT	Solutions 2-8	0.94-0.93	0.97-0.97
ML - $M_c = 1.1$	$\tau = 1750 - 2100$	0.86-0.69	0.93-0.91
ML - $M_c = 2.2$ - DGA	$\tau = 4050 - 5000$	0.81-0.70	0.90-0.89
ML - $M_c = 2.2$ - DGB	$\tau = 4000$	0.53	0.79
ML - $M_c = 2.2$ - DGC	$\tau = 3800$	0.36	0.71
ML - $M_c = 2.2$ - DGD	$\tau = 3800$	0.35	0.66

Table 6.11: Performance of the (11;55;55;1) ANN model (3796 degrees of freedom) trained (without Laplacian inputs) over the full training database. r^2-scores and correlation coefficients are evaluated over the full solutions which were not included in the ANN training database (see the additional testing database in Table 6.1)

Table 6.10 gathers the results obtained for this series of tests. Consistently with the spreading of the PDF (see Section 6.2), the configuration of choice to train an ANN capable to generalize its performance is the forced HIT. Yet, the scores are not satisfying. Even though the correlation coefficients are rather good, the r^2-score remains low, especially for the mixing layer at $M_c = 2.2$. Results are even worse when the ANN is trained over the mixing layer only. Note that the r^2-scores for the mixing layer at $M_c = 2.2$ are smaller when compared to the mixing layer at $M_c = 1.1$, likely because of the increase of the compressibility which causes a reduction of correlation coefficients between the output and the inputs (see Table 6.2). These tests demonstrate the necessity to train the ANN over a diverse database in order to strengthen its generalization capabilities, as illustrated by the scores and correlation coefficients obtained when training on the full database as done previously. Note the very slight differences between the values reported for the full database training in Table 6.10 and the values previously reported in Table 6.8 come from the fact values in the later table were computed after 25 epochs (at the end of the training process) while values in the former table are computed after 10 epochs only.

The second series of generalization test consists in:

- training the ANN over the entire database (Table 6.1)
- and testing it over additional temporal solutions and over additional DNS not included in the training database. These additional solutions have also been provided in Table 6.1 and are recalled in Table 6.11 along with the corresponding efficiency metrics.

Let us briefly review the content of the additional testing database and comment on the level of generalization it provides:

- for the forced THI, let us remember the solution index corresponds to the multiple of the characteristic time at which the solution is saved. Consequently, solution 2 is still close to solution 1 included in the training database while solution 8 is clearly more distinct since computed at a very different instant.
- for the mixing layer at $M_c = 1.1$, the solution included in the training database is taken at time $\tau = 1700$ (beginning of the self-similar period). Therefore, the solution at time

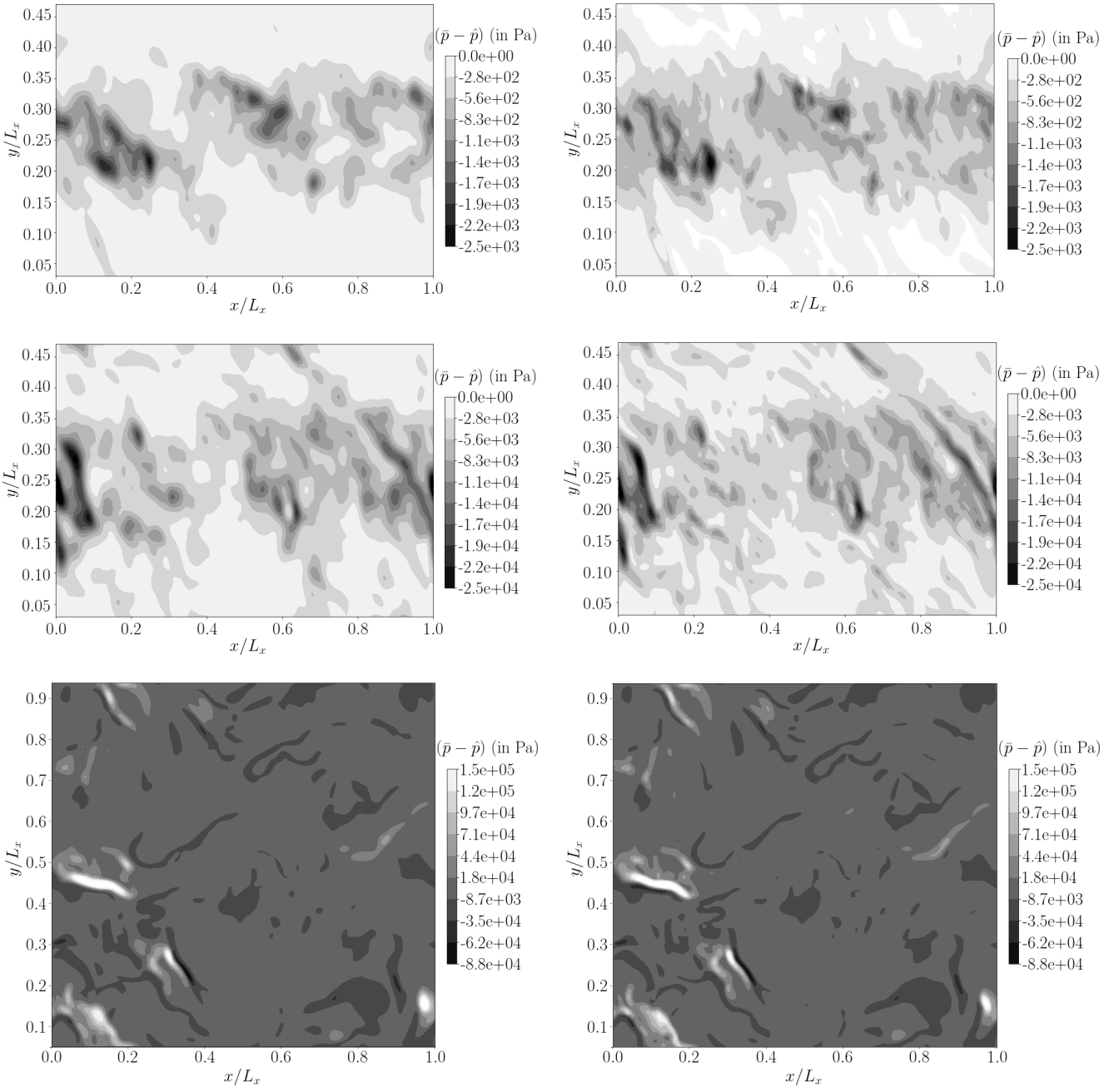

Figure 6.21: $z-$centerplane contours colored by $\bar{p}-\widehat{p}$ for true (left) and ANN predicted (right) values. Results are plotted for the second stored temporal solution (see Table 6.1) for each configuration: (top) the mixing layer at $M_c = 1.1$ ($\tau = 1750$), (middle) the mixing layer at $M_c = 2.2$ ($\tau = 4050$) and (bottom) the forced HIT (Solution 2). The (11;55;55;1) ANN model comprises 3796 degrees of freedom and is trained without Laplacian inputs. None of the flow solutions have been included into the ANN training.

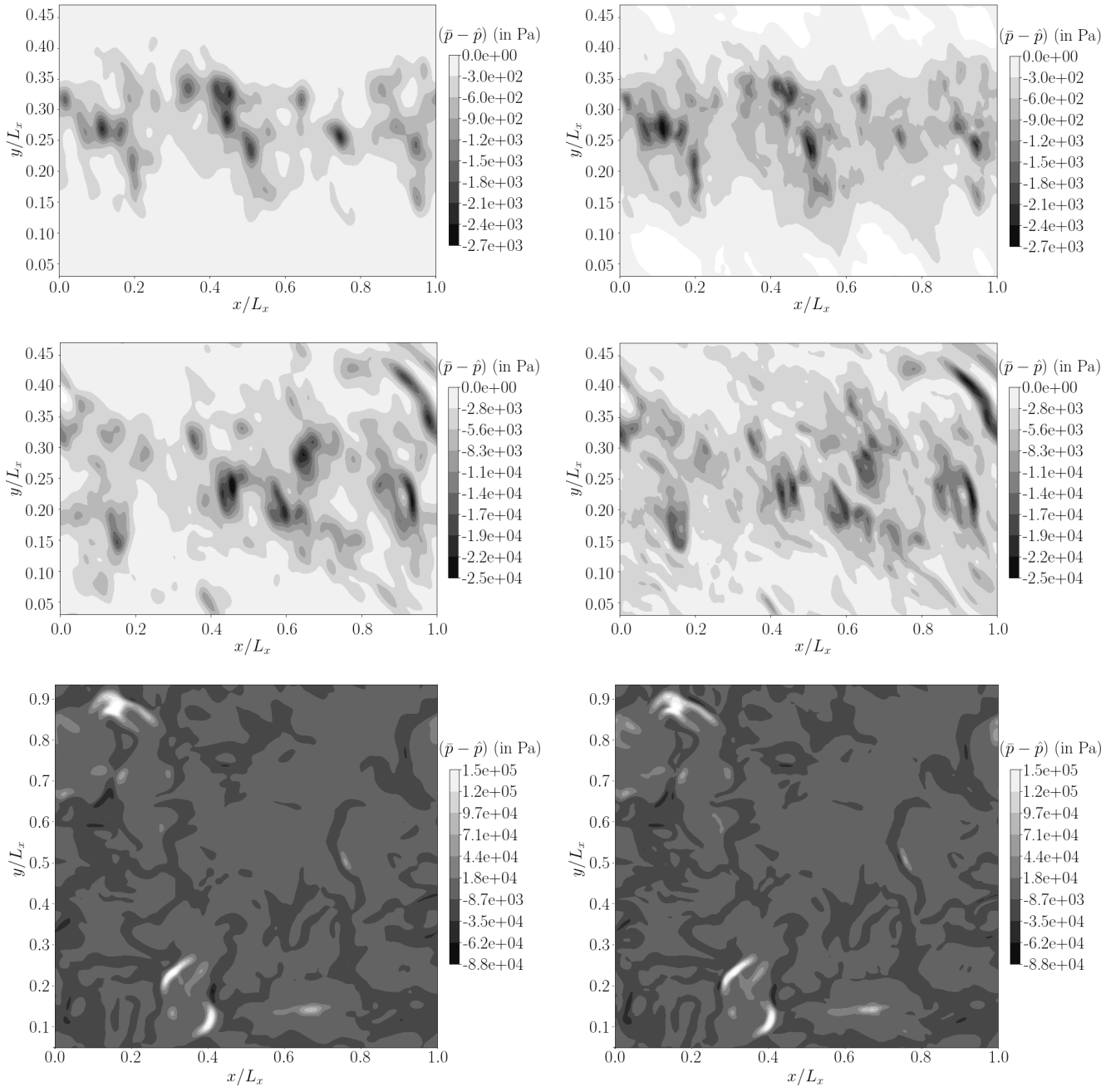

Figure 6.22: $z-$centerplane contours colored by $\bar{p}-\widehat{p}$ for true (left) and ANN predicted (right) values. Results are plotted for the third stored temporal solution (see Table 6.1) for each configuration: (top) the mixing layer at $M_c = 1.1$ ($\tau = 2100$), (middle) the mixing layer at $M_c = 2.2$ ($\tau = 5000$) and (bottom) the forced HIT (Solution 8). The (11;55;55;1) ANN model comprises 3796 degrees of freedom and is trained without Laplacian inputs. None of the flow solutions have been included into the ANN training.

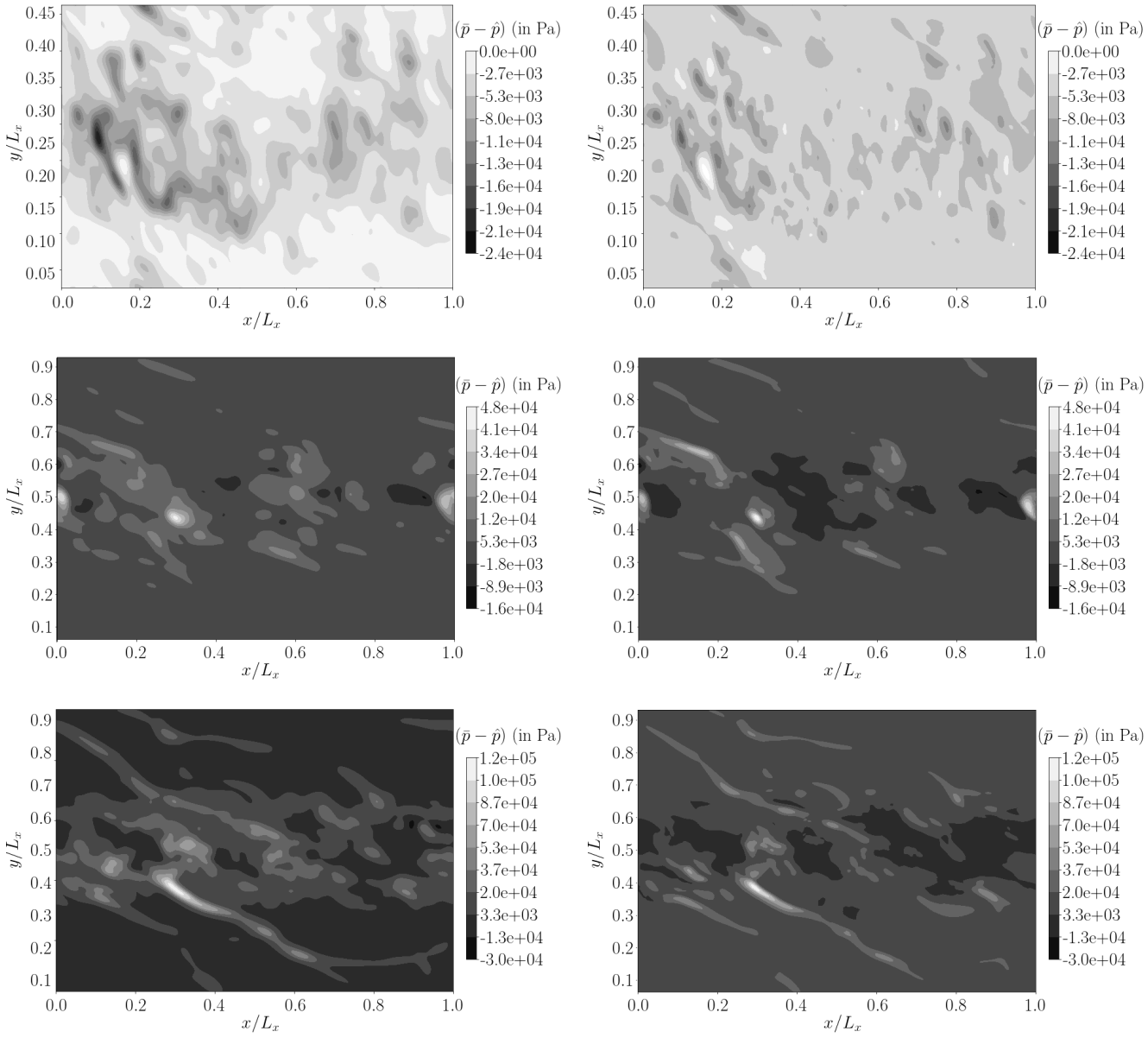

Figure 6.23: $z-$centerplane contours colored by $\bar{p}-\widehat{p}$ for true (left) and ANN predicted (right) values. Results are plotted for the mixing layers at $M_c = 2.2$: (top) DGB, (middle) DGC and (bottom) DGD. The (11;55;55;1) ANN model comprises 3796 degrees of freedom and is trained without Laplacian inputs. None of the flow solutions have been included into the ANN training.

$\tau = 1750$ included in the additional testing database is still very close to the training solution while the solution at time $\tau = 2100$ also included is quite different from the training solution.

- similarly, for the mixing layer at $M_c = 2.2$, the solution at time $\tau = 4050$ in the additional testing database is still very close to the training solution extracted at time $\tau = 4000$ (beginning of the self-similar period) while the solution at time $\tau = 5000$ also included is quite different from this training solution.

- finally, recalling that the $M_c = 2.2$ training solution corresponds to the DGA initial thermodynamic state and the start of the corresponding self-similar period, it can be observed that the DGB, DGC and DGD solutions in the additional testing database are also extracted at the start of their respective self-similar period (see Section 4.4.3). Judging the "distance" between these 3 solutions and the DGA training solution is delicate. From the flow analysis proposed in Section 4.4.3 one could however assume that DGD could be considered as closer to DGA than DGB and DGC based for instance on the slope of momentum thickness time evolution.

The network applied to predict these 9 additional flow configurations is the (11;55;55;1) ANN (corresponding to 3796 DOF) trained on the full database including the 3 originally selected flow configurations (with a performance summarized at the bottom of Table 6.9). Table 6.11 gathers the r^2-scores and the correlation coefficients for this reference ANN applied to the additional flow configurations.

It can be observed from the three first lines of Table 6.11 that very good predictions are provided by the ANN for all the new temporal solutions that are considered. Even for the mixing layer at $M_c = 2.2$, the r^2-score and the correlation coefficient remain respectively equal to 0.70 and 0.89 after 1000 non-dimensional times (corresponding to half the self-similar period for this flow) elapsed since the instant of capture for the training solution. Figures 6.21 and 6.22 display SGS pressure contours for true (left) and ANN-predicted (right) values respectively for the temporal testing solutions close to the training solutions and for the temporal testing solutions with a large time separation with respect to the training solutions. It can be clearly observed on these plots that the contours of SGS pressure are very well predicted by the ANN both in the positive and negative regions.

For other thermodynamic operating points, results deteriorate as can be observed from the three last lines of Table 6.11. This is especially noticeable for DGC and DGD with r^2-score coefficients decreasing respectively to 0.36 and 0.35 (from 0.88 for the training DGA solution). The DGB r^2-score is slightly better likely because its initial thermodynamic operating point is located closer to the DGA one (but even though the flow development for DGB is not especially closer to DGA than DGC and DGD). Despite these average scores, the structure of the SGS pressure field is still quite correctly captured by the ANN as can be observed in Figure 6.23. Note that this represents an interesting feature of the model which is entirely local and has not been designed to reproduce the structure of turbulent features spanning on numerous grid cells.

The values obtained for the correlation coefficients when performing this second series of generalization tests appear obviously as weak when compared to the one previously obtained for the testing partition of the initial full database. However, it should be emphasized that the performance provided by the ANN designed in the present work remains actually in the

upper limit when compared to usual SGS turbulent tensor models derived in the literature (see for instance the evaluations reported in Gamahara & Hattori (2017) and Wang *et al.* (2018)). The above tested model based on the (11;55;55;1) ANN deserves therefore to be selected for the next and final step of our study which is the *a posteriori* evaluation presented in the next chapter.

6.5 Analysis of small size ANN

Motivation

In this last section, we wish to address a point raised in the introduction of the chapter, namely the need to go beyond a black-box ANN-based model that is the need to try and explain the relationships identified by the network between the filtered and SGS variables. In order to simplify the network analysis and help the identification of significant connections between neurons, only small size ANN are investigated. Note this choice remains quite sensible as it has been previously established that ANN with a low number of DOF were still able to provide a reliable prediction of the SGS pressure terms (see Figure 6.17).

Methodology

The small size networks analyzed in this study are made of two hidden layers comprising two neurons each, with inputs which do not include the Laplacians, hence 11 inputs. These (11;2;2;1) ANN count therefore 28 weights and 5 bias yielding a total of 33 DOF. Some tests (not reported here) have been conducted with these small size ANN trained over the entire database; it was then found the r^2-scores computed over each case separately were not high enough to justify a thorough analysis of the networks structure. Consequently, these (11;2;2;1) ANN (with hyperparameters selected according to Table 6.7) are trained over each database configuration separately and their structure is analyzed for each flow case (HIT and mixing layers with $M_c = 1.1$, $M_c = 2.2$).

In order to evaluate the reproducibility of the results, four different ANN are initialized with the same Glorot method (Glorot & Bengio, 2010) using different seeds. The performance of each network is given in Table 6.12 for all ANN. r^2-scores are overall correct when ANN are tested over the same configuration as the training one (using the same $80\% - 20\%$ partitioning between training database and testing database as previously retained). The results obtained confirm the difficulty for these ANN to generalize to other configurations than the one they were trained with. Only a partial generalization is achieved for the ANN trained with one of the mixing layers and tested on the other one. Note also that the generalization results are not well reproducible. For instance, the r^2-score of the ANN trained with the mixing layer at $M_c = 1.1$ varies from 0.06 to 0.43 when tested over the mixing layer at $M_c = 2.2$. Note however that such simple ANN remain quite effective for the configuration they were trained with since the r^2-scores can reach 0.90 (for the mixing layer at $M_c = 1.1$).

Analysis of the networks

In order to study the very structure of the networks, Figures 6.24, 6.25 and 6.26 display this structure for the four ANN built for each flow configuration, using the following choices of visualization:

Training configuration	$M_c = 1.1$			
Testing configuration	ANN 0	ANN 1	ANN 2	ANN 3
ML - $M_c = 1.1$	0.90	0.90	0.90	0.88
ML - $M_c = 2.2$	0.06	0.21	0.38	0.43
Forced HIT	-0.03	-0.34	-2.11	-0.97
Training configuration	$M_c = 2.2$			
Testing configuration	ANN 0	ANN 1	ANN 2	ANN 3
ML - $M_c = 1.1$	0.14	-7.71	-1.69	-3.52
ML - $M_c = 2.2$	0.76	0.73	0.76	0.72
Forced HIT	-0.12	-0.66	0.004	-0.77
Training configuration	Forced HIT			
Testing configuration	ANN 0	ANN 1	ANN 2	ANN 3
ML - $M_c = 1.1$	-9.17	-0.98	-8.39	-5.67
ML - $M_c = 2.2$	-0.19	-0.59	-0.30	-0.29
Forced HIT	0.89	0.85	0.86	0.88

Table 6.12: r^2-scores of small size ANN (of the form (11;2;2;1) yielding 33 degrees of freedom) trained over each flow configuration. Scores are evaluated over the testing partition after 10 epochs.

- each network is plotted with, from bottom to top, the input layer with 11 variables, the 2 hidden layers of 2 neurons each and the single output
- the magnitude of each weight is directly proportional to the width of the lines connecting neurons from one layer to the next layer: a very thick line indicates a very large weight (in absolute value) while a very thin line (almost not visible on the plot) corresponds to an almost zero weight
- the positive weights are colored in orange and the negative ones in blue. When the absolute value of a weight exceeds unity, its value is reported on the plot.

The analysis of networks makes also use of Tables 6.13, 6.14 and 6.15 where correlation coefficients between the intermediate inputs at the entrance of the first hidden layer and other variables are given.

Mixing layer at $\mathbf{M_c = 1.1}$ Although r^2-scores are almost identical for the 4 ANN (except maybe for ANN 3 which is slightly less effective with a score of 0.88 instead of 0.90 for the three other networks), their structure is very different, especially for ANN 3. The results do not appear as well reproducible and because of the strong difference between weights magnitudes and signs from one network to another, averaging the weights does not seem judicious. Yet, it is possible to identify some common features for these four ANN. First, the weights associated to the branches connected to the first four thermodynamic variables $\left(\bar{\rho}; \widehat{T}; \widehat{p}; \bar{\rho}\widetilde{E}\right)$ are always significant even though the SGS pressure is not strongly correlated with these variables for both mixing layers (see Table 6.2). Note that these significant weights do not necessarily lead to high correlations between intermediate variables and the SGS pressure. For instance, the first intermediate input of ANN 0 is more connected to inputs when compared to the second one but its correlation with the SGS pressure is about 0.37 only, compared to 0.88 for the second intermediate output. Note also that ANN 3 displays much larger weights with respect to the other networks. Its score computed over the same configuration is smaller than the scores of the other networks but its ability to generalize for the mixing layer at $M_c = 2.2$ is significantly better than the other ANN.

Mixing layer at $\mathbf{M_c = 2.2}$ and forced HIT Looking at the other ANN trained over the mixing layer at $M_c = 2.2$ and the forced HIT confirms the lower rate of reproducibility of the results obtained for the structure of the network. Very different structures can lead to almost identical performance. The weights connected to the physical variables $\left(\bar{\rho}; \widehat{T}; \widehat{p}; \bar{\rho}\widetilde{E}\right)$ are always larger than other weights, even for mixing layers where these variables are poorly correlated with the SGS pressure.

Analysis of correlations Tables 6.13, 6.14 and 6.15 seem to evidence two main situations encountered during the training:

- In the first situation, two intermediate inputs significantly correlated with the SGS pressure are obtained (see for instance M_c = 1.1-ANN 1, M_c = 1.1-ANN 3, HIT-ANN 0, HIT-ANN 1 and HIT-ANN 3). In that case, their correlation coefficients are very close to each other but with an opposite sign.

Intermediate inputs	ANN 0		ANN 1		ANN 2		ANN 3	
	1st	2nd	1st	2nd	1st	2nd	1st	2nd
1st input	1	0.59	1	-0.81	1	-0.99	1	-0.99
$\bar{p} - \widehat{p}$	0.37	0.88	-0.81	0.88	-0.89	0.90	0.89	-0.90
$\bar{\rho}$	-0.03	0.14	0.01	0.14	-0.13	0.18	0.17	-0.09
$\widehat{T}$	-0.22	-0.08	0.17	-0.08	0.08	-0.03	-0.05	0.12
$\widehat{p}$	-0.07	0.12	-0.01	0.12	-0.11	0.17	0.14	-0.08
$\bar{\rho}\widetilde{E}$	-0.03	0.14	-0.01	0.15	-0.13	0.18	0.17	-0.09
$\|\nabla(\bar{\rho})\|$	-0.22	-0.82	0.78	-0.85	0.85	-0.86	-0.83	0.88
$\|\nabla(\widehat{T})\|$	-0.09	-0.80	0.81	-0.82	0.83	-0.86	-0.83	0.85
$\|\nabla(\widehat{p})\|$	-0.16	-0.84	0.82	-0.86	0.87	-0.89	-0.87	0.89
$\|\nabla(\bar{\rho}\widetilde{E})\|$	-0.22	-0.82	0.78	-0.85	0.85	-0.86	-0.83	0.88
I_1	0.13	0.03	0.04	0.02	-0.02	0.003	0.01	-0.02
I_2	0.03	-0.02	0.09	-0.01	0.03	-0.04	-0.03	0.02
I_3	0.002	-0.01	0.01	-0.02	0.01	-0.01	-0.004	0.02

Table 6.13: **Mixing layer at $\mathbf{M_c = 1.1}$** - Correlation coefficients are computed between the two intermediate ANN inputs (1st and 2nd inputs) at the entrance of the first hidden layer and the ANN inputs and the true value of the SGS pressure term ($\bar{p} - \widehat{p}$). Correlations with absolute values above 0.4 are colored in red. Small size ANN are trained during 10 epochs.

- In the second situation, only one variable is significantly correlated with the exit, the other one being weakly correlated. As a consequence, the weights of branches connected between the poorly correlated neuron and the second hidden layer are very low. This side of the network is therefore almost not used by the ANN (see for instance $M_c = 1.1$-ANN 0, $M_c = 2.2$-ANN 0, $M_c = 2.2$-ANN 1 and $M_c = 2.2$-ANN 3). This kind of ANN could be used to further simplify the network by progressively removing unnecessarily branches in order to possibly write an analytical relation between the inputs and the output.

Note that consistently with correlations between inputs and the output (see Table 6.2), intermediate variables tend to be more correlated with gradients for the mixing layer at $M_c = 1.1$ and with the thermodynamic variables for the forced HIT. The mixing layer at $M_c = 2.2$ seems to be an intermediate case between the two other flow configurations which could explain the lower performance of ANN when trained other this configuration.

Conclusion This attempt to thoroughly investigate small scale networks shows in particular a low rate of reproducibility of the learning process. Several combinations of weights and bias can actually lead to approximately the same performance. Note that it is not possible to train such a simple ANN over the entire database with a good ability to yield consistent scores over each configuration separately. The modeling problem at stake seems therefore too difficult to be analytically solved and more complex networks are needed (such as the (11;55;55;1) ANN previously designed), which escape a simple description.

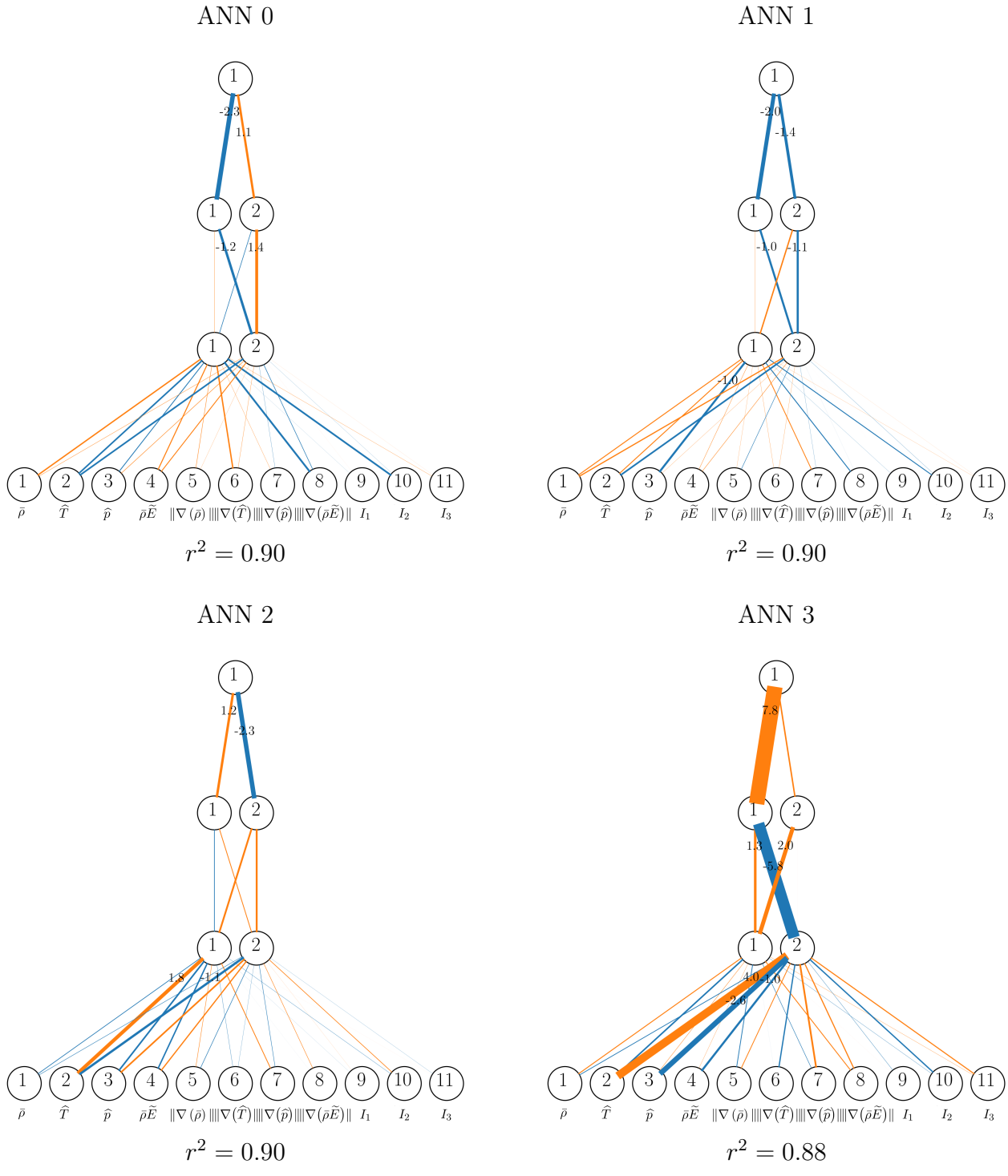

Figure 6.24: **Mixing layer at $\mathbf{M_c = 1.1}$** - Four small size ANN are identically with four different Glorot initializations (Glorot & Bengio, 2010). Positive weights are colored in orange and negative ones in blue. Values of weights are only given when the absolute value is larger than 1.

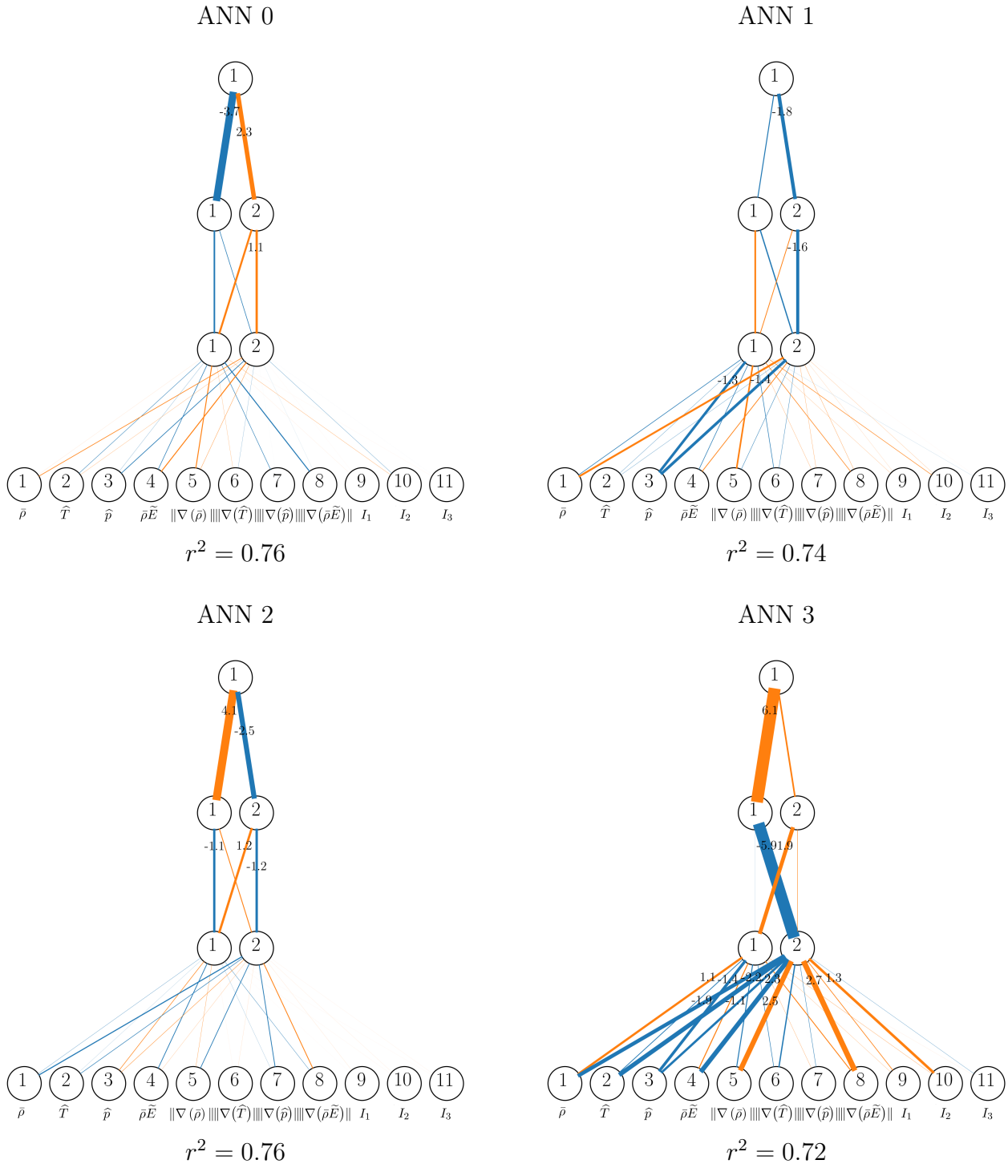

Figure 6.25: **Mixing layer at $\mathbf{M_c = 2.2}$** - Four small size ANN are identically trained with four different Glorot initializations (Glorot & Bengio, 2010). Values of weights are only given when the absolute value is larger than 1.

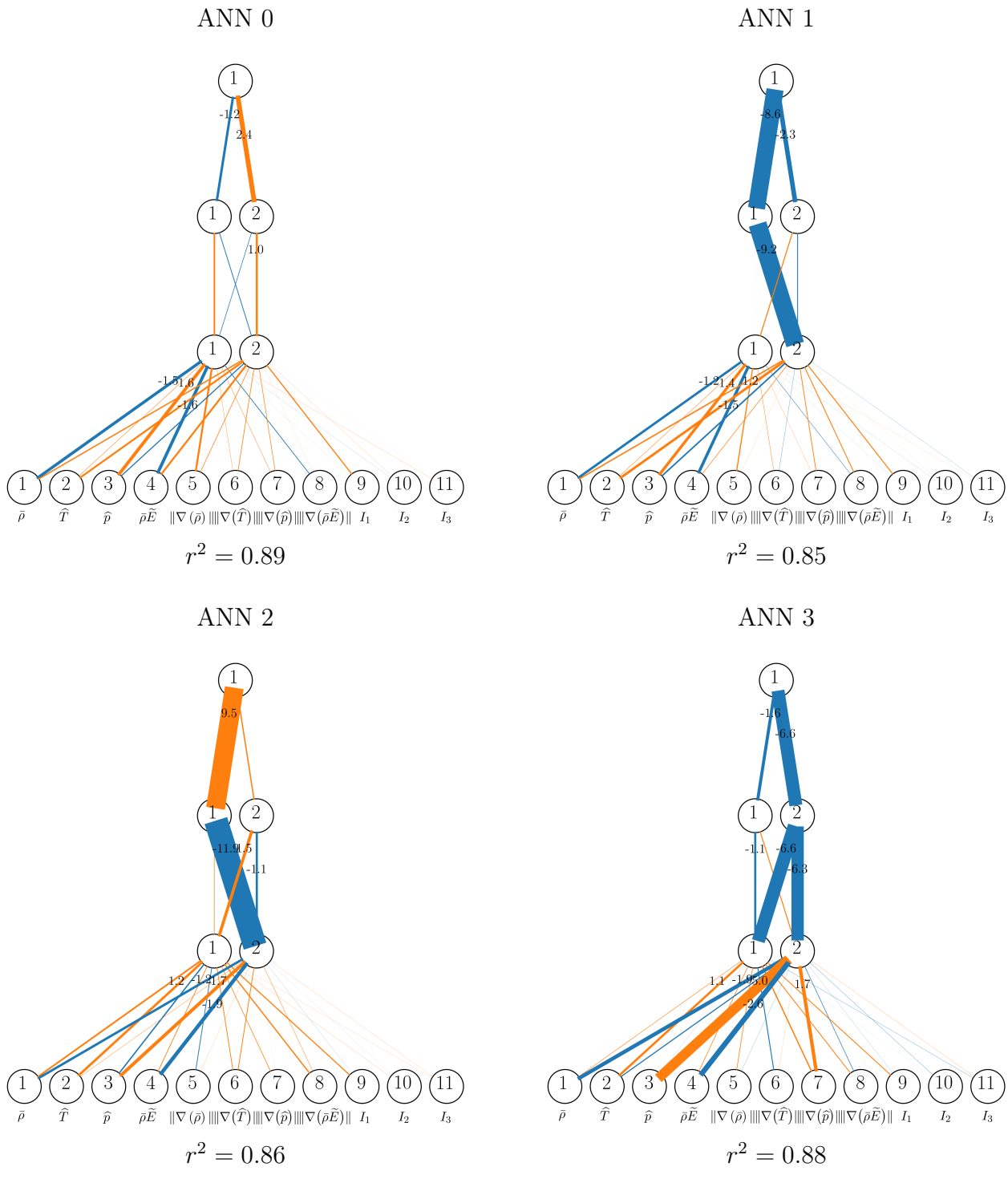

Figure 6.26: **Forced HIT** - Four small size ANN are identically trained with four different Glorot initializations (Glorot & Bengio, 2010). Values of weights are only given when the absolute value is larger than 1.

Intermediate inputs	ANN 0		ANN 1		ANN 2		ANN 3	
	1^{st}	2^{nd}	1^{st}	2^{nd}	1^{st}	2^{nd}	1^{st}	2^{nd}
1^{st} input	1	-0.93	1	0.53	1	0.93	1	0.25
$\bar{p} - \widehat{p}$	0.40	-0.11	-0.17	0.49	0.24	0.49	0.63	-0.26
$\bar{\rho}$	-0.91	0.99	-0.88	-0.60	-0.94	-0.82	-0.50	-0.80
$\widehat{T}$	-0.93	0.91	-0.76	-0.69	-0.88	-0.87	-0.70	-0.72
$\widehat{p}$	-0.91	0.94	-0.89	-0.74	-0.88	-0.80	-0.64	-0.80
$\bar{\rho}\widetilde{E}$	-0.91	0.99	-0.88	-0.60	-0.94	-0.82	-0.50	-0.80
$\|\nabla(\bar{\rho})\|$	-0.77	0.56	-0.07	-0.55	-0.72	-0.86	-0.64	-0.09
$\|\nabla(\widehat{T})\|$	-0.70	0.48	0.00	-0.53	-0.65	-0.81	-0.63	0.16
$\|\nabla(\widehat{p})\|$	-0.43	0.13	0.36	-0.33	-0.33	-0.59	-0.48	0.49
$\|\nabla(\bar{\rho}\widetilde{E})\|$	-0.77	0.58	-0.07	-0.55	-0.72	-0.86	-0.64	0.09
I_1	0.01	0.02	-0.05	-0.002	-0.01	0.01	0.00	-0.06
I_2	0.30	-0.26	0.25	0.35	0.25	0.27	0.32	0.20
I_3	-0.16	0.14	-0.10	-0.16	-0.14	-0.16	-0.17	-0.08

Table 6.14: **Mixing layer at $\mathbf{M_c = 2.2}$** - Correlation coefficients are computed between the two intermediate ANN inputs (1^{st} and 2^{nd} inputs) at the entrance of the first hidden layer and the ANN inputs and the true value of the SGS pressure term ($\bar{p} - \widehat{p}$). Correlations with absolute values above 0.4 are colored in red. Small scale ANN are trained during 10 epochs.

Intermediate inputs	ANN 0		ANN 1		ANN 2		ANN 3	
	1^{st}	2^{nd}	1^{st}	2^{nd}	1^{st}	2^{nd}	1^{st}	2^{nd}
1^{st} input	1	-0.38	1	-0.47	1	-0.06	1	-0.51
$\bar{p} - \widehat{p}$	-0.47	0.48	-0.51	0.51	-0.15	0.58	0.47	-0.55
$\bar{\rho}$	-0.69	0.89	-0.75	0.89	-0.28	0.92	0.87	-0.80
$\widehat{T}$	-0.64	0.90	-0.69	0.89	-0.24	0.91	0.88	-0.74
$\widehat{p}$	-0.56	0.86	-0.61	0.84	-0.18	0.84	0.84	-0.66
$\bar{\rho}\widetilde{E}$	-0.69	0.89	-0.75	0.89	-0.28	0.92	0.87	-0.80
$\|\nabla(\bar{\rho})\|$	0.23	0.75	0.14	0.74	0.55	0.62	0.77	0.05
$\|\nabla(\widehat{T})\|$	0.40	0.63	0.32	0.62	0.70	0.47	0.66	0.23
$\|\nabla(\widehat{p})\|$	0.31	0.54	0.22	0.55	0.78	0.48	0.56	0.13
$\|\nabla(\bar{\rho}\widetilde{E})\|$	0.23	0.75	0.14	0.74	0.55	0.62	0.77	0.05
I_1	0.21	0.32	0.18	0.34	0.34	0.26	0.36	0.14
I_2	-0.17	-0.20	-0.14	-0.19	-0.32	-0.13	-0.22	0.11
I_3	0.23	0.19	0.19	0.16	0.33	0.11	0.21	0.17

Table 6.15: **Forced HIT** - Correlation coefficients are computed between the two intermediate ANN inputs (1^{st} and 2^{nd} inputs) at the entrance of the first hidden layer and the ANN inputs and the true value of the SGS pressure term ($\bar{p} - \widehat{p}$). Correlations with absolute values above 0.4 are colored in red. Small scale ANN are trained during 10 epochs.

Chapter 7

Preliminary *a posteriori* test of the ANN-based SGS pressure model

Contents

5.1 State of the art 101

5.2 Analysis of the subgrid-scale terms 103

5.2.1 Filtered momentum equations 103

5.2.2 Energy equation 106

5.3 Concluding remarks 109

5.3.1 LES equations to be solved 109

5.3.2 Towards SGS modeling 109

THIS chapter is devoted to the *a posteriori* testing of the ANN model designed in the previous chapter for the SGS pressure term, which has been shown to be significant for dense gas flows thanks to the *a priori* analysis presented in Chapter 5. The methodology adopted to perform this preliminary *a posteriori* test of the model is described in Section 7.1. The effects of the model for DG mixing layers are analyzed through both structural and functional criteria using SGS pressure contours in Section 7.2 and momentum thickness temporal evolutions in Section 7.3. Some explanations for the results of the LES computed with the SGS pressure term are provided in Section 7.4, using a comparison between the SGS pressure and the SGS turbulent stress tensor as well as an analysis of the averaged thermodynamic distributions.

7.1 Methodology

Several *a posteriori* LES are performed for both compressible mixing layers at $M_c = 1.1$ and $M_c = 2.2$. The present work does not seek to represent DG effects on all SGS terms but only focuses on the SGS pressure term. Other SGS terms must nonetheless be modeled. The straightforward choice made at this stage, in the context of the present thesis, is to use existing models designed for PG flows. Simulations are thus computed using (see Equation (5.1) for the details of the LES equations to be solved):

- the dynamic Smagorinsky model for the SGS turbulent stress tensor
- the ANN model designed in Chapter 6 to take into account the SGS pressure in the filtered momentum equation
- a turbulent Prandtl number modeling (with $Pr_{\text{SGS}} = 0.6$ (Lesieur, 2012)) to model the SGS internal energy in the filtered energy equation (see Section 2.4.6)
- the works of the SGS turbulent stress tensor model and of the SGS pressure model are added in the filtered energy equation to respectively partially model the SGS kinetic energy flux and the SGS pressure work.

Consistently with Section 5.2, the SGS viscous term is neglected in the filtered momentum equation; also, the SGS viscous work and the heat flux are neglected in the filtered energy equation. Note that the use of the (11;55;55;1) ANN model in LES simulations required an implementation step inside the AVBP code which is not detailed here. The computational extra cost has been previously evaluated (see Figure 6.15). It is approximately equal to 20% for the (11;55;55;1) ANN model which corresponds to 3796 degrees of freedom. The 11 input of the model are the variables $\bar{\rho}$, $\hat{T}$, $\hat{p}$, $\bar{\rho}\tilde{E}$, the norm of their respective gradient and the three invariants I_1, I_2 and I_3.

Since the ANN model has been trained using temporal solutions extracted during the self-similar period, the initial LES solution is built from an interpolation[†] of the first self-similar DNS solutions occurring respectively at $\tau = 1700$ and $\tau = 4000$ for the mixing layers at $M_c = 1.1$ and $M_c = 2.2$. DNS solutions are interpolated with four different filtering sizes ($\bar{\Delta}/\Delta_{\text{DNS}} \in [4, 8, 16, 32]$). The largest filtering size $\bar{\Delta}/\Delta_{\text{DNS}} = 32$ is located in the inertial zone close to the one of the filtered DNS training database (see Table 6.1). Moreover, the domain size of these interpolated solutions is doubled in the $y-$direction in order to obtain long enough LES simulations without reaching the lower and upper domain boundaries.

7.2 SGS pressure contours

The first results are presented in Figures 7.1 and 7.2 where centerplane contours of the SGS pressure are plotted for both mixing layers respectively at $M_c = 1.1$ and $\tau = 1750$, and at $M_c = 2.2$ and $\tau = 4050$. Each figure displays (a) (and (a') for $M_c = 2.2$) *a priori* values and (b,c,d,e) *a posteriori* ANN predictions of the contours for the four filter sizes. Because of the differences already mentioned (see Figure 2.2) between *a priori* and *a posteriori* methodologies, it is not expected to find exactly the same structure between the contours of the *a priori* values

[†]The interpolation is performed using the inverse distance weighting method proposed in the Antares Python library (antares Development Team, 2020) compatible with AVBP solutions.

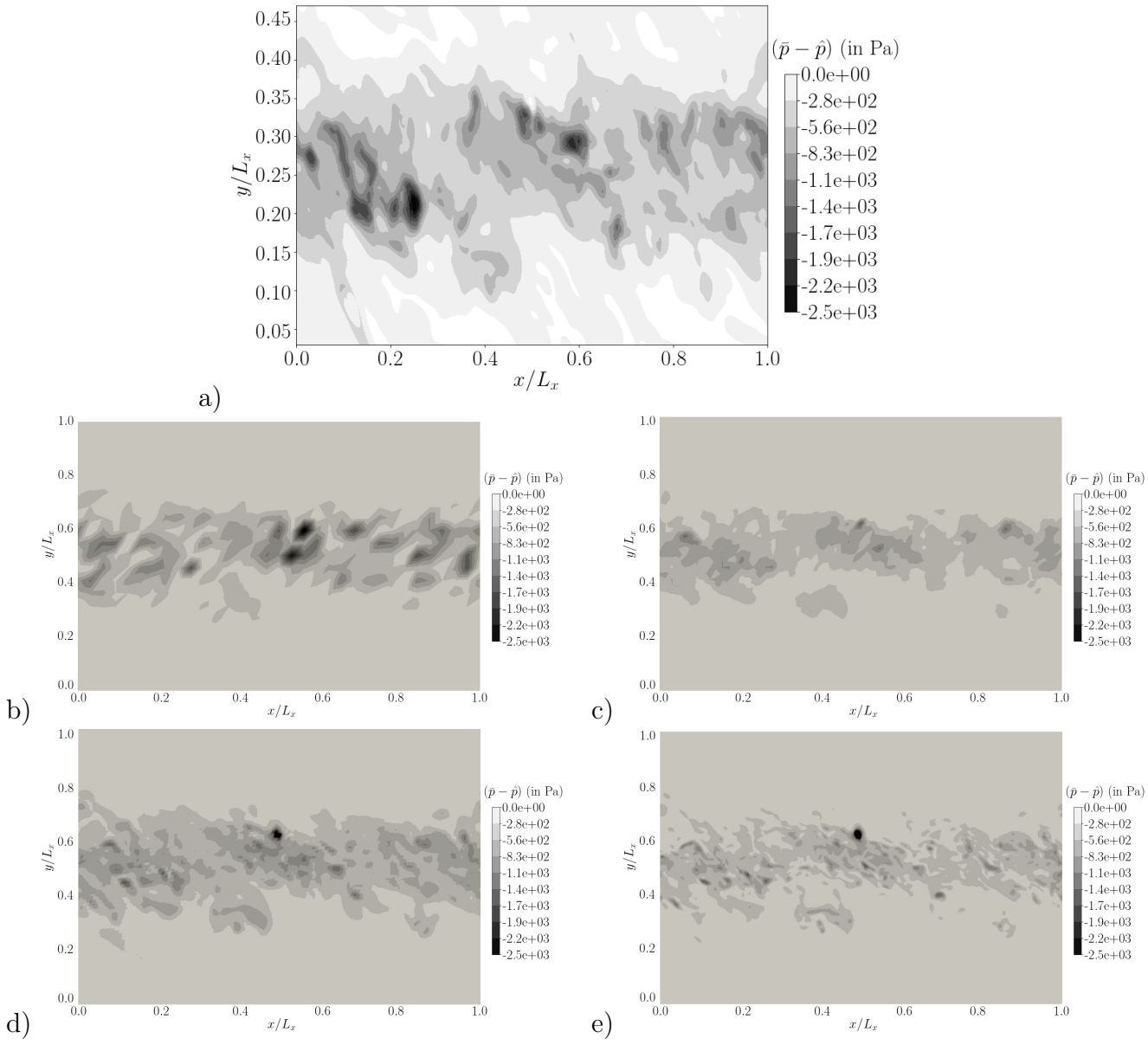

Figure 7.1: Mixing layer at $M_c = 1.1$. $z-$centerplane contours colored by $\bar{p} - \widehat{p}$ for (a) predicted *a priori* values and computed *a posteriori* values with (b) $\bar{\Delta}/\Delta_{\text{DNS}} = 32$, (c) $\bar{\Delta}/\Delta_{\text{DNS}} = 16$, (d) $\bar{\Delta}/\Delta_{\text{DNS}} = 8$ and (d) $\bar{\Delta}/\Delta_{\text{DNS}} = 4$. Results are plotted at $\tau = 1750$. Note that the domain length in the $y-$direction is identical for the four LES but is twice larger than the one used for the filtered DNS.

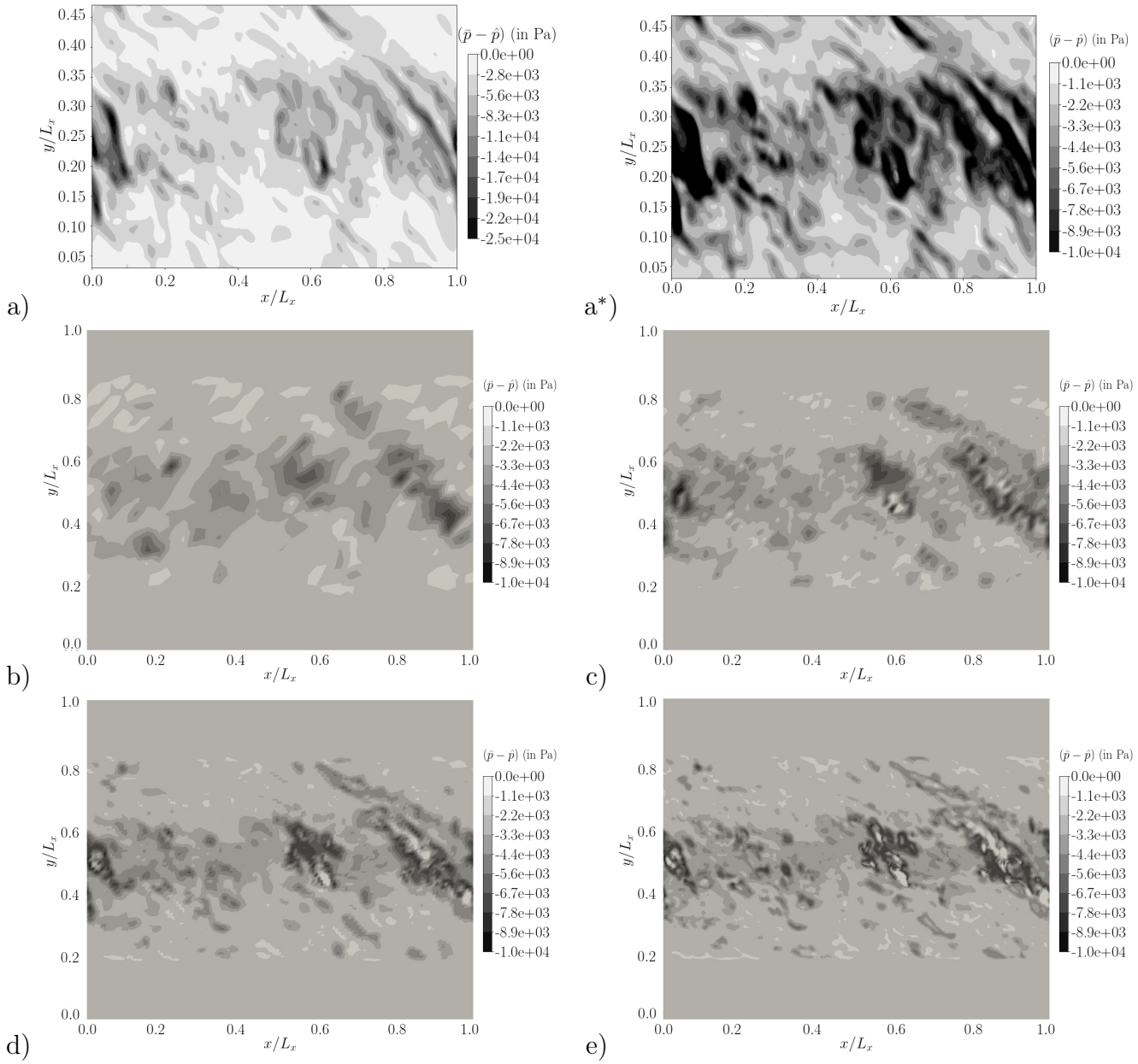

Figure 7.2: Mixing layer at $M_c = 2.2$. $z-$centerplane contours colored by $\bar{p} - \widehat{p}$ for the (a) and (a*) predicted *a priori* values and computed *a posteriori* values with (b) $\bar{\Delta}/\Delta_{\text{DNS}} = 32$, (c) $\bar{\Delta}/\Delta_{\text{DNS}} = 16$, (d) $\bar{\Delta}/\Delta_{\text{DNS}} = 8$ and (d) $\bar{\Delta}/\Delta_{\text{DNS}} = 4$. Results are plotted at $\tau = 4050$. *A priori* results are plotted twice: (a) with the scale found in the *a priori* analysis and (a') with the scale computed in the *a posteriori* LES. Note that the domain length in the $y-$direction is identical for the four LES but is twice larger than the one used for the filtered DNS.

of $\bar{p} - \hat{p}$ and the *a posteriori* values of the LES on increasingly refined grids but similarities are expected as well as matching order of magnitude.

At $M_c = 1.1$ (Figure 7.1), the order of magnitude is the same in the two cases (*a priori* and *a posteriori* analyses) but high magnitude regions in *a priori* LES are only partially reproduced in *a posteriori* LES. Yet, the ANN model prediction is consistent between the four filtering sizes.

At $M_c = 2.2$ (Figure 7.2), SGS pressure structures are very close between *a priori* and *a posteriori* LES but the order of magnitude is smaller for the *a posteriori* LES. The maximum amplitude of predicted values is approximately twice larger in the *a priori* LES when compared to *a posteriori* ones, as clarified by the choice of scale used for the *a priori* plots: (a) full range and (a') range of the *a posteriori* LES.

In both mixing layers, visualizations show a proper implementation of the ANN in the AVBP code and the ability of the the ANN-based model to predict consistent values over the four different filtering sizes in *a posteriori* LES. Yet, because of the stochastic nature of turbulent flows, the comparison between *a priori* and *a posteriori* predictions should be done with averaged quantities which is the purpose of the next section.

7.3 Temporal evolution of the momentum thickness

The next step in the validation process consists in testing the ability of the LES using the SGS pressure model to reproduce the temporal evolution of the momentum thickness (integrated over the whole domain).

Figure 7.3 displays this temporal evolution at $M_c = 1.1$ and $M_c = 2.2$ for two types of LES: one with the SGS pressure model and one without. This comparison is available for each tested filtering size (from $\bar{\Delta}/\Delta_{DNS} = 32$ to $\bar{\Delta}/\Delta_{DNS} = 4$). The DNS result is also provided for reference.

The effect of the SGS pressure model on the prediction of the momentum thickness time evolution is not visible since curves overlap for LES with and without the model. The SGS pressure seems actually to have no effect on the mixing layer growth. Possible reasons for this lack of influence of the SGS pressure on the growth of the mixing layer are proposed in the next section.

With and without the SGS pressure model, the evolution is well captured by the LES at $\bar{\Delta}/\Delta_{DNS} = 4$ for both $M_c = 1.1$ and $M_c = 2.2$ mixing layers. As the filter size increases, results depart from the DNS reference. At $\bar{\Delta}/\Delta_{DNS} = 8$, the value of $\delta_\theta/\delta_\theta(t)$ is about 10% larger when compared to the DNS evolution, but the growth rate slope tends to stabilize and becomes close to the DNS slope as the non-dimensional time increases. At $\bar{\Delta}/\Delta_{DNS} = 16$, the growth is successively under-predicted and over-predicted by SGS models for both convective Mach numbers. Note that results at this filter size are slightly better at $M_c = 1.1$. At $\bar{\Delta}/\Delta_{DNS} = 32$, the momentum thickness is significantly under-predicted with a growth rate decrease of about 50% for both convective Mach numbers when compared to DNS.

SGS models fail to reproduce the overall behavior of DG compressible mixing layers at medium to large filtering sizes. The well-known compressibility-related decrease of the momentum thickness growth rate (related to the increase of the Mach number) is thus not reproduced

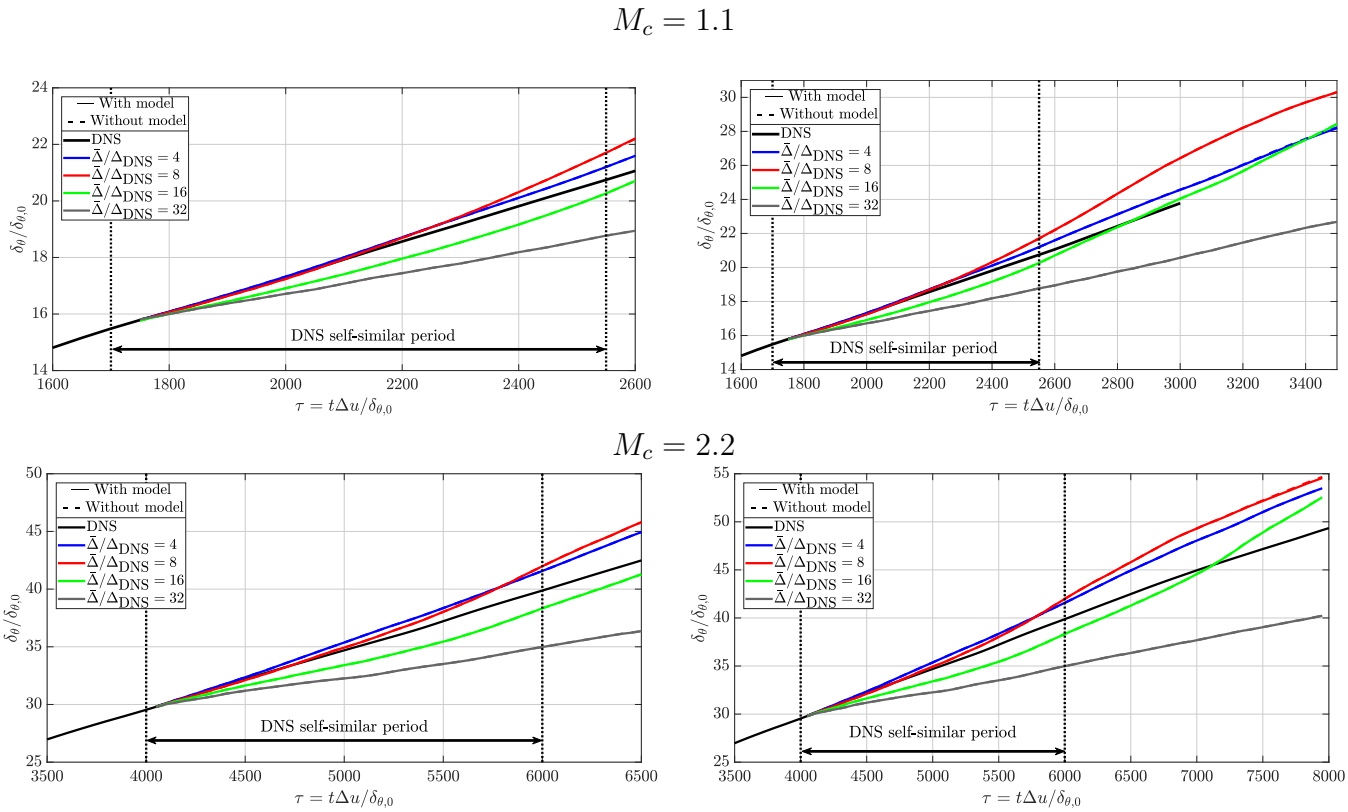

Figure 7.3: Temporal evolution of the momentum thickness. Comparison is made between DNS and *a posteriori* LES at four filtering sizes ($\bar{\Delta}/\Delta_{\mathrm{DNS}} \in [4, 8, 16, 32]$) with and without the SGS pressure model. No difference is visible since curves overlap. Two different non-dimensional time ranges are represented for each convective Mach number: for $M_c = 1.1$, $\tau \in [1600; 2600]$ (left) and $\tau \in [1600; 3500]$ (right); for $M_c = 2.2$, $\tau \in [3500; 6500]$ (left) and $\tau \in [3500; 8000]$ (right).

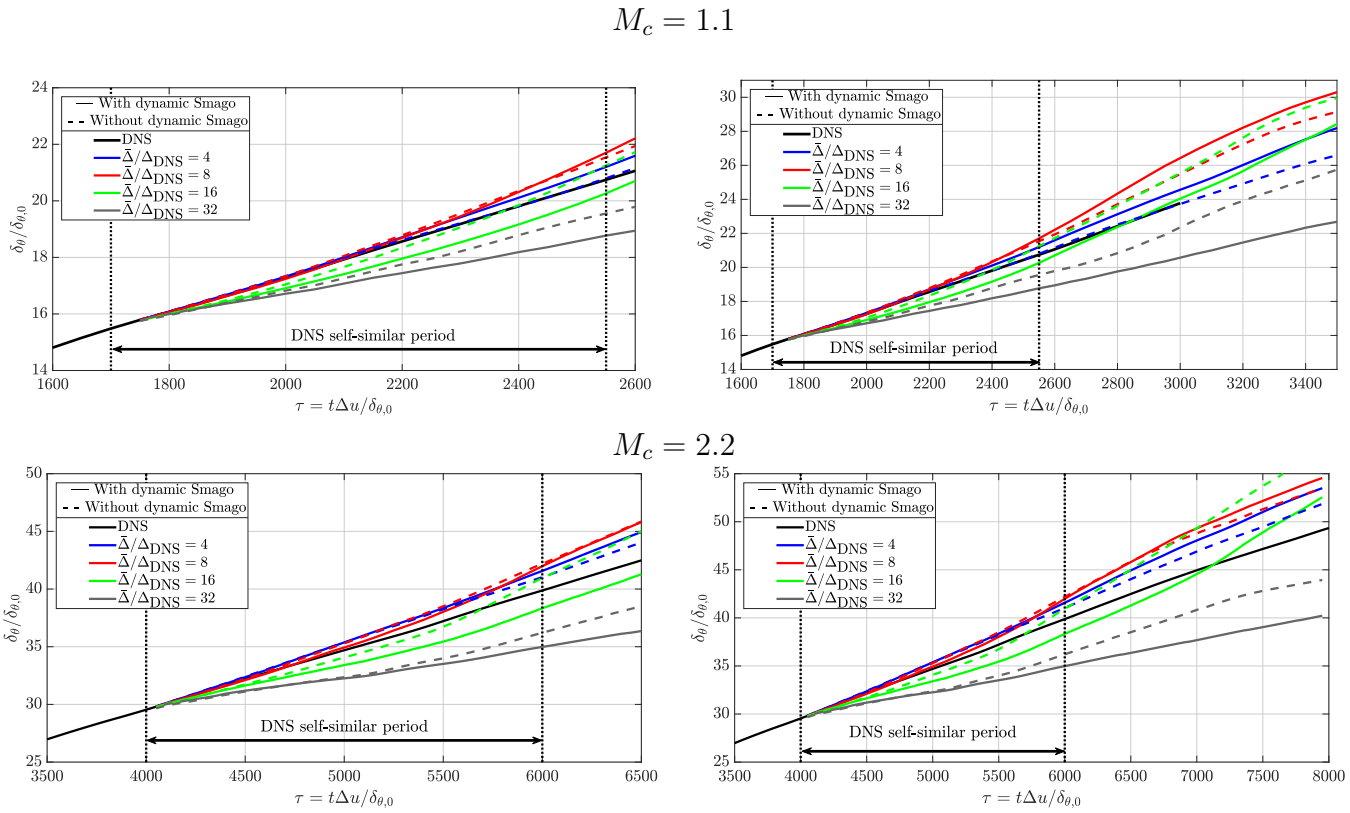

Figure 7.4: Temporal evolution of the momentum thickness for the mixing layers at (top) $M_c = 1.1$ and (bottom) $M_c = 2.2$. Comparison is made between DNS and *a posteriori* LES at four filtering sizes ($\bar{\Delta}/\Delta_{\mathrm{DNS}} \in [4, 8, 16, 32]$) with and without the dynamic Smagorinsky model. Two different non-dimensional time ranges are represented for each convective Mach number: for $M_c = 1.1$, $\tau \in [1600; 2600]$ (left) and $\tau \in [1600; 3500]$ (right); for $M_c = 2.2$, $\tau \in [3500; 6500]$ (left) and $\tau \in [3500; 8000]$ (right).

by LES using the aforementioned SGS models in DG flows. Accounting for the SGS pressure does not allow to capture this effect either. The effect of other SGS terms should thus be investigated, in particular the effect of the SGS turbulent stress tensor.

In order to evaluate the effect of the dynamic Smagorinsky model on the momentum thickness growth, Figure 7.4 displays LES at $M_c = 1.1$ and $M_c = 2.2$ performed with and without the dynamic Smagorinsky model. The removal of the model for the SGS turbulent stress tensor consistently leads to a larger growth rate of the mixing layer with respect to the case where the model is active. This could be expected since the model dissipates part of the TKE energy at the filter scale, which damps the growth of the mixing layer. This effect of the SGS turbulent stress tensor removal leads therefore to an over-prediction of the growth rate when the LES using the SGS model yields an already acceptable prediction, which is the case for $\bar{\Delta}/\Delta_{\text{DNS}} = 16$. For other filtering sizes, removing the dynamic model tends actually to improve the prediction because of the under-prediction trend of the LES with the SGS turbulent stress model.

Further investigations are needed to determine whether this observed behavior is specific to the DG LES modeling or is also encountered for the PG LES modeling. If not the case, this would probably call for a specific modeling task for the SGS turbulent stress tensor in the case of DG flows.

7.4 Further analysis of the SGS pressure

7.4.1 Comparison between SGS pressure and SGS turbulent stress tensor

Since no effect of the SGS pressure is observed in the previous section when analyzing the temporal evolution of the momentum thickness, one could question the assessment made in Chapter 5 of the SGS pressure magnitude, the flux of which was evaluated to be of a magnitude comparable to that of the SGS turbulent stress. To reinforce these conclusions drawn in Chapter 5, both fluxes are extracted from the *a posteriori* LES in the three space directions. Figure 7.5 displays the $z-$centerplane contours colored by both fluxes (SGS pressure on the left and SGS turbulent stress tensor on the right) for the mixing layer at $M_c = 2.2$, $\bar{\Delta}/\Delta_{\text{DNS}} = 8$ and $\tau = 6000$ (which corresponds to the end of the DNS self-similar period): similar orders of magnitude are observed.

Since Figure 7.4 shows that removing the model for the SGS turbulent stress tensor has a strong effect on the mixing layer growth rate, one can wonder how and why the SGS pressure term which has a similar magnitude can have zero effect on the growth of the mixing layer. A tentative explanation is that the SGS pressure force might not significantly induce or damp turbulence roll-up which is the mechanism at the heart of the mixing layer growth. To substantiate this assumption, the vorticity equation (Bailly & Comte-Bellot, 2003) can be used:

$$\frac{\partial \boldsymbol{\omega}}{\partial t} + \nabla \times (\boldsymbol{\omega} \times \boldsymbol{u}) = \frac{1}{\rho^2} \nabla \rho \times \nabla p + \nu \nabla \times (\nabla^2 \boldsymbol{u}) \tag{7.1}$$

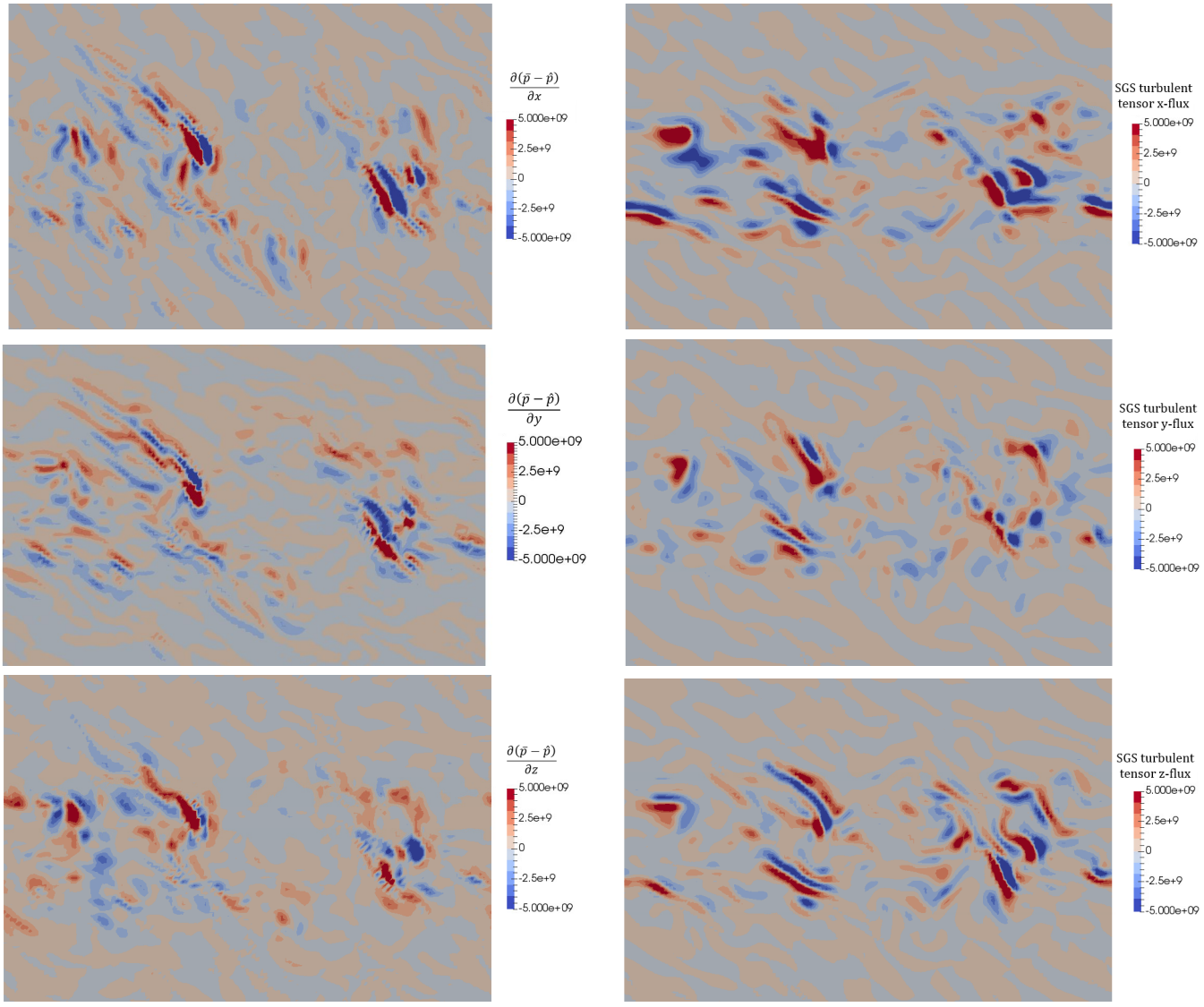

Figure 7.5: $z-$centerplane contours colored by (left) SGS pressure $\left(\frac{\partial[\bar{p}-\hat{p}]}{\partial x_i}\right)$ and SGS turbulent stress tensor $\left(\frac{\partial\bar{\rho}[\widetilde{u_i u_j}-\widetilde{u}_i\widetilde{u}_j]}{\partial x_j}\right)$ fluxes for the mixing layer at $M_c = 2.2$ and $\bar{\Delta}/\Delta_{\text{DNS}} = 8$ in (top) $x-$, (middle) $y-$ and (bottom) $z-$ directions. Results are plotted at $\tau = 6000$. The ANN model comprises 3796 degrees of freedom (11;55;55;1) and is trained without Laplacian inputs.

where $\boldsymbol{\omega} = \Delta \times \boldsymbol{u}^{\dagger}$. The LES filtering operator is applied to Equation (7.1) to yield:

$$\begin{aligned}\frac{\partial \bar{\boldsymbol{\omega}}}{\partial t} + \nabla \times (\bar{\boldsymbol{\omega}} \times \bar{\boldsymbol{u}}) &= \frac{1}{\bar{\rho}^2}\nabla\bar{\rho} \times \nabla\widehat{p} + \widehat{\nu}\nabla \times (\nabla^2 \bar{\boldsymbol{u}}) \\ &\quad - \left[\frac{1}{\bar{\rho}^2}\nabla\bar{\rho} \times \nabla(\widehat{p} - \bar{p})\right] - \left[\frac{1}{\bar{\rho}^2}\nabla\bar{\rho} \times \nabla\bar{p} - \overline{\left(\frac{\nabla\rho \times \nabla p}{\rho^2}\right)}\right] \\ &\quad - \left[\widehat{\nu}\nabla \times (\nabla^2\bar{\boldsymbol{u}}) - \overline{\nu\nabla \times (\nabla^2 \boldsymbol{u})}\right] - \left[\nabla \times (\bar{\boldsymbol{\omega}} \times \bar{\boldsymbol{u}}) - \nabla \times \overline{(\boldsymbol{\omega} \times \boldsymbol{u})}\right]\end{aligned} \tag{7.2}$$

where $\bar{\boldsymbol{\omega}} = \nabla \times \bar{\boldsymbol{u}}^{\dagger}$.

The SGS pressure term contribution to Equation (7.1) depends therefore on the alignment of its gradient vector with that of the filtered density. Figure 7.6 compares the contours of both terms in the three space directions. These contours are found to be very close between the two quantities, especially in the $x-$ and $y-$ directions taking part in the $z-$vorticity equation. This observation shows therefore that it is indeed possible to have a significant SGS pressure term, of amplitude comparable to that of the SGS turbulent stress tensor, but which has no effect on the mixing layer growth. An attempt could be made at explaining the observed alignment between the gradient of the SGS pressure term and the gradient of the filtered density. It is known that, for dense gases, the large heat capacity leads to almost isothermal flows regardless of the Mach number. Note that the RMS temperature profiles shown next in Figures 7.7 and 7.8 confirm that it is also the case here. In that context, it is expected that pressure and density fluctuations are strongly related. However, it remains to explain how quantities at different scales (resolved density on one hand and SGS pressure on the other hand) can display such a similar behavior.

7.4.2 Influence on the thermodynamic profiles

Figures 7.7 and 7.8 display the averaged and rms thermodynamic profiles for pressure, temperature and density in the mixing layers at $M_c = 1.1$ and $M_c = 2.2$, computed using the LES with the dynamic Smagorinski model for the SGS turbulent stress tensor but with or without the ANN model for the SGS pressure.

At both convective Mach numbers, the SGS pressure model is found to have a negligible effect on the LES results, except for a slight modification of the averaged temperature - the evolution of which remains quasi-isothermal anyway. *A posteriori* LES performed with the SGS pressure model predict a slightly reduced averaged temperature which leads to under-estimated distributions at $M_c = 2.2$ and to a slightly improved predictions at $M_c = 1.1$. The lack of significant modification of the averaged thermodynamic variables could be induced by the large amount of internal energy present in dense gas flows, which mitigates the influence of the SGS pressure model.

[†]The expression $\boldsymbol{a} \times \boldsymbol{b}$ denotes the vector product of $\boldsymbol{a}$ with $\boldsymbol{b}$

[†]It is assumed that the filtering operator commutes with temporal and spatial differentiations. This assumption is satisfied if the domain is not bounded and if the filtering size Δ is constant and homogeneous.

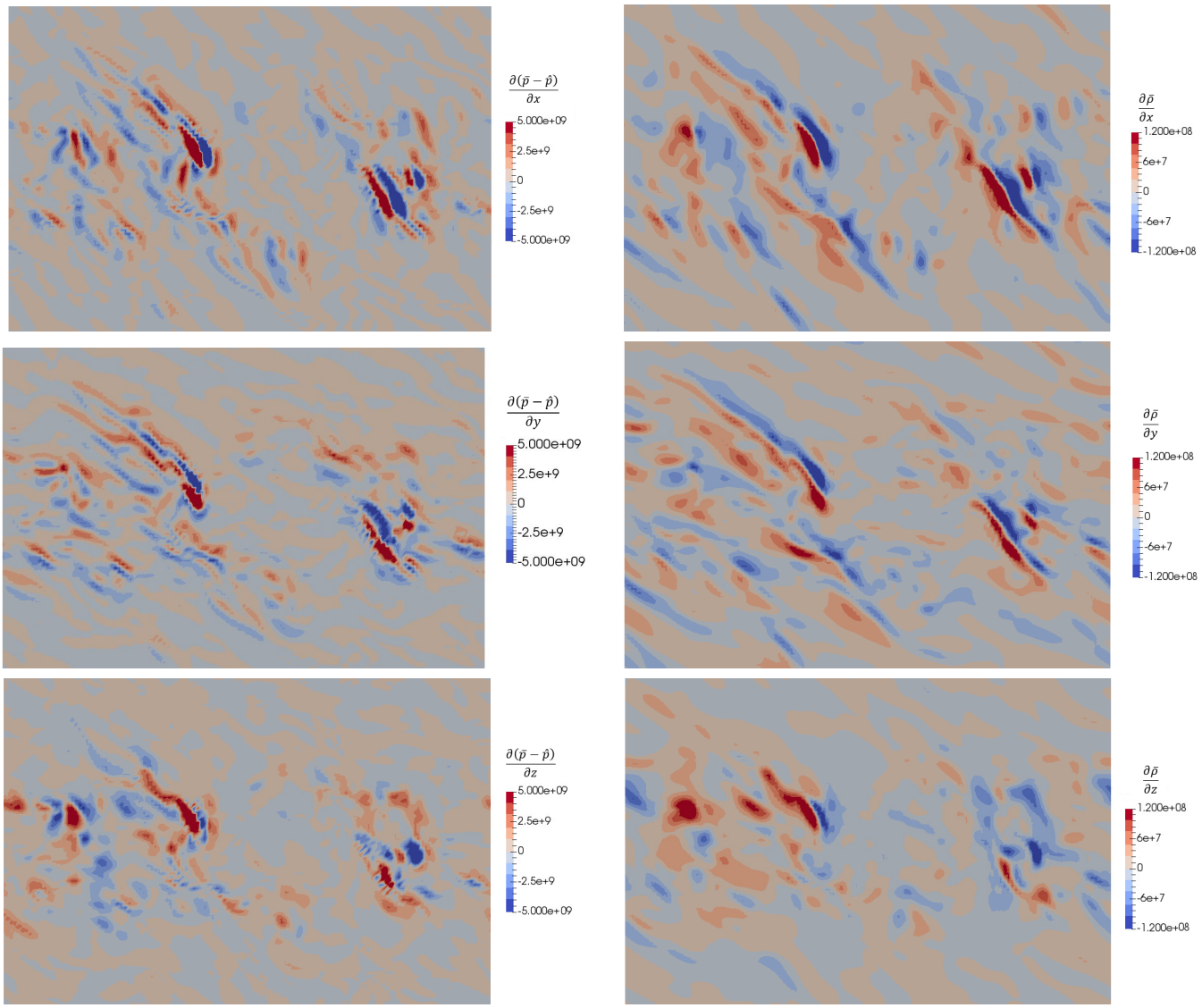

Figure 7.6: $z-$centerplane contours colored by (left) the SGS pressure $\left(\frac{\partial[\bar{p}-\hat{p}]}{\partial x_i}\right)$ gradients and (right) the density gradients for the mixing layer at $M_c = 2.2$ and $\bar{\Delta}/\Delta = 8$ in (top) $x-$, (middle) $y-$ and (bottom) $z-$ directions. Results are plotted at $\tau = 6000$. The ANN model comprises 3796 degrees of freedom (11;55;55;1) and is trained without Laplacian inputs.

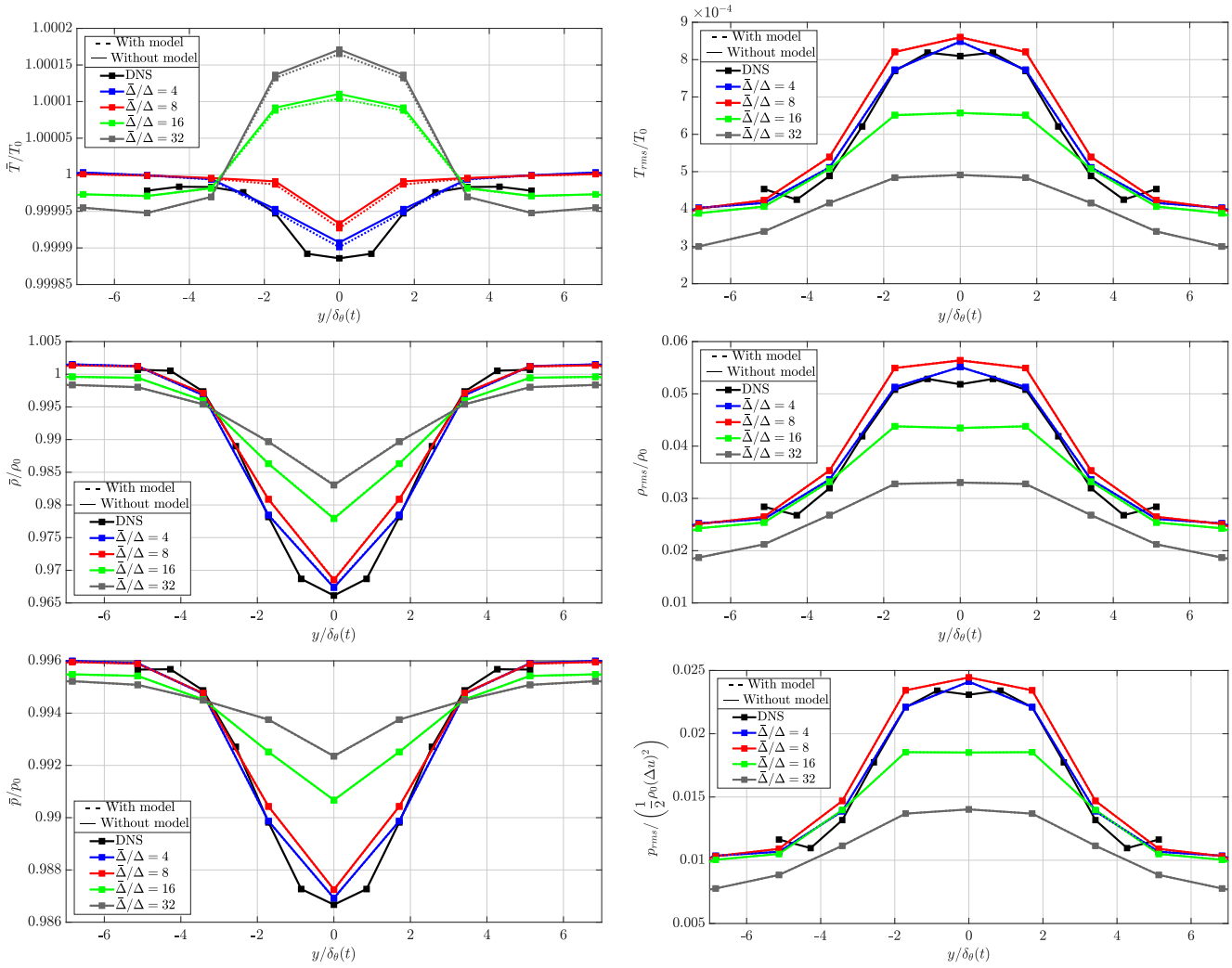

Figure 7.7: Mixing layer at $M_c = 1.1$. The non-dimensional Reynolds averaged (left) and root mean square (right) values of temperature (top), density (middle) and pressure (bottom) are averaged over the self-similar period ($\tau \in [1700; 2550]$), plotted along the y-direction and compared between DNS and *a posteriori* LES with and without the SGS pressure model at four different filtering sizes. Note that the bar symbol refers here to the Reynolds averaged of LES quantities and not to the LES filtering symbol.

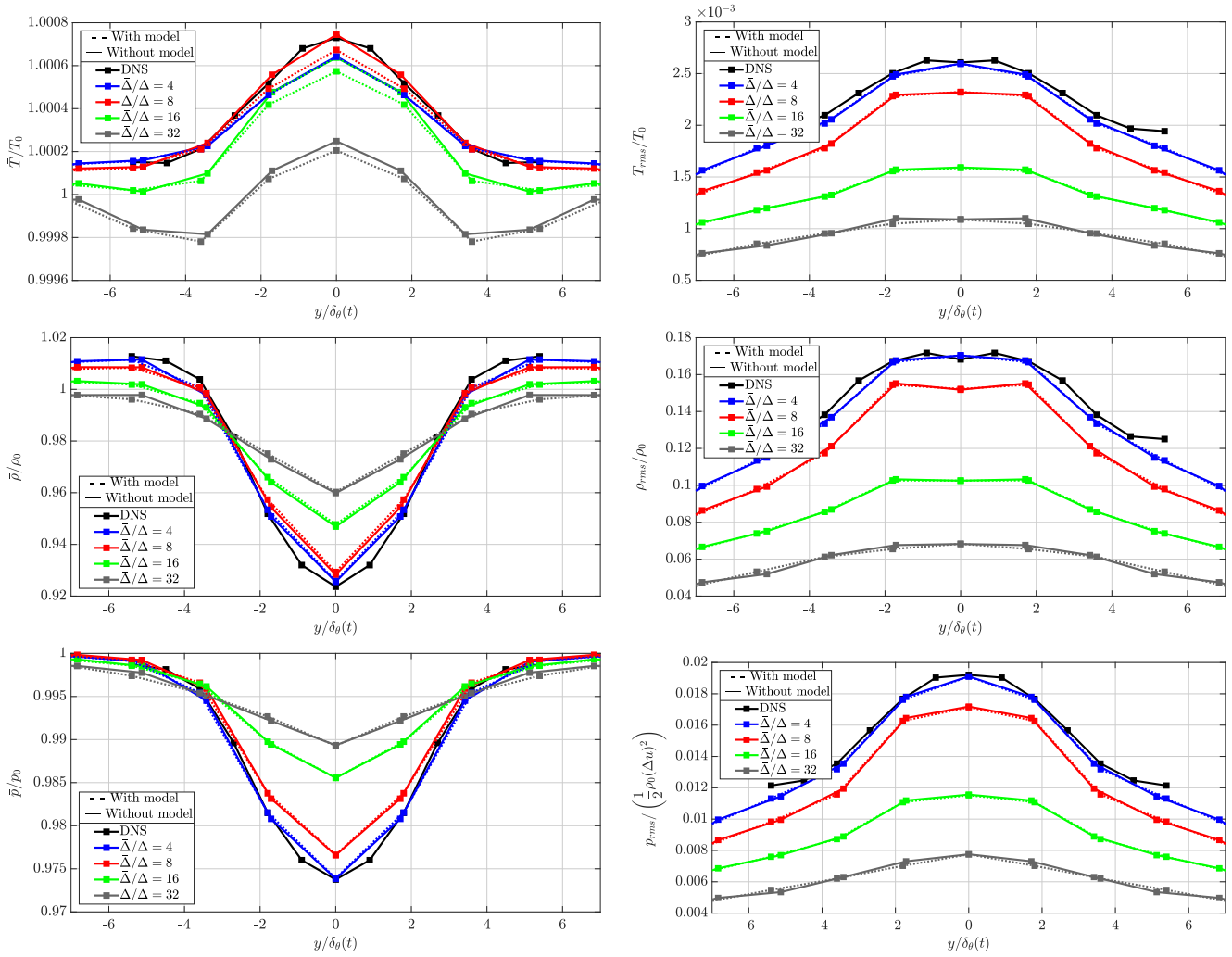

Figure 7.8: Mixing layer at $M_c = 2.2$. The non-dimensional Reynolds averaged (left) and root mean square (right) values of temperature (top), density (middle) and pressure (bottom) are averaged over the self-similar period ($\tau \in [4000; 6000]$), plotted along the y-direction and compared between DNS and *a posteriori* LES with and without the SGS pressure model at four different filtering sizes. Note that the bar symbol refers here to the Reynolds averaged of LES quantities and not to the LES filtering symbol.

7.4.3 Summary

The results obtained in this preliminary *a posteriori* test of the proposed ANN-based SGS pressure model raise interesting question on the relevance of this model. Its effect over the mixing layer growth is found indeed negligible likely because of the alignment of its gradient with the filtered density gradient which consequently drops its contribution in the vorticity equation which controls the turbulent structure roll-up. This hypothesis needs however further investigation to explain in particular how quantities defined at different scales (the gradient of the filtered density and the gradient of the SGS pressure) can display such a strong correlation. Also, no clear improvement is observed from the comparison of the thermodynamic variables computed with and without the SGS pressure model and this behavior remains yet unexplained. Results have also been obtained regarding the influence of the SGS turbulent stress tensor: by switching on or off the dynamic Smagorinsky model (with the SGS pressure model switched on) it was possible to establish the significant influence of the SGS turbulent stress tensor on the momentum thickness evolution and the poor performance of this same model at medium to large filtering sizes. Further research effort could therefore focus on the assessment of usual SGS turbulent stress tensor models for DG flows and in case of poor performance to the development of a dedicated DG model for the SGS turbulent stress tensor. This model development will benefit from the ANN design framework detailed in the previous chapter.

Chapter 8

Conclusion and Perspectives

Conclusion

THE present thesis has been devoted to the analysis and the modeling of turbulence in flows of dense gases (DG). This type of gas presents many benefits when compared to water, arousing a growing interest from the ORC turbine industry. In particular, the DG capacity to exchange large amount of energy at low to moderate temperatures for the heat sources enables a great adaptability of ORCs. In the vicinity of the critical point, DG exhibit an unusual behavior when compared with classical perfect gases (PG). In this study, specific DG called BZT gases, also widely used in the industry, have been considered. In addition to DG, Bethe-Zel'dovich-Thompson (BZT) gases display a thermodynamic inversion region where the fundamental derivative of gas dynamics Γ becomes negative, allowing the existence of expansion shock-waves.

The use of DG in ORCs raises modeling issues when numerically designing ORC turbines since the turbulent flows at stake include both significant compressibility effects and differences with respect to PG flows. Up to now, although DG thermodynamic features strongly differ from those of PG, turbulence closure models developed for PG have been applied for RANS simulations and LES of DG flows, for the lack of a better option. The peculiar thermodynamic behavior of DG, in particular BZT gases, questions the relevance of this choice, which implicitly assumes that turbulent structures are not affected by neither DG nor BZT effects.

This thesis tackles the DG LES modeling issue by considering 3 main steps: 1) the detailed analysis of DG mixing layers using DNS; 2) an *a priori* assessment of LES SGS terms using filtered DNS; 3) the construction and the *a posteriori* analysis of a new LES SGS model using supervised machine learning algorithms.

The physical features of DG, their fields of application and the related numerical modeling issues were introduced in Chapter 1. Chapter 2 detailed the governing equations and constitutive laws used to perform both real gas DNS and LES: instantaneous Navier-Stokes equations, thermodynamic models and LES filtered equations. DG peculiarities and their influence on the mathematical framework were also emphasized through the investigation of non-dimensional numbers involved in the governing equations.

The first DNS were performed and analyzed in Chapter 3 at three different convective Mach numbers $M_c = 0.1 - 1.1 - 2.2$ and for air described as a perfect gas. The simulations computed using the AVBP code were compared with available results from the literature (in particular

(Pantano & Sarkar, 2002)) in order to demonstrate the accuracy of the present DNS solver. The well-known compressibility-related reduction of the momentum thickness growth rate was well captured up to large convective Mach numbers. A great attention was paid in the present study (i) to precisely select the self-similar period, based on the analysis of the integrated streamwise production overtime, which is proportional to the momentum thickness growth rate under certain conditions (Vreman *et al.*, 1996*a*) and (ii) to properly select the domain size of simulations which has an important effect for the achievement of self-similarity.

After this PG validation process, DNS were performed with DG described using the Martin-Hou EoS at three convective Mach numbers $M_c = 0.1 - 1.1 - 2.2$. In addition, an analysis of the influence of the domain size, the size of initial turbulent structures and the resolution was also performed and reported in Appendix B. The comparison between perfect and dense gases showed major differences for the momentum thickness growth rates when the convective Mach numbers is equal to $M_c = 2.2$: the growth rate is twice as large for DG when compared to PG. The compressibility-related reduction of the momentum thickness growth rate is thus dampened in DG flows beyond $M_c = 1.1$. As shown by (Pantano & Sarkar, 2002) for PG flows, the growth rate reduction is also related for DG flows to the reduction of normalized pressure fluctuations. In addition, small scale dynamics of the specific kinetic energy spectra are also observed to be significantly more intense in DG flows when compared to PG flows.

Additional DNS were performed for three others initial thermodynamic operating points. Results show that BZT effects have only a small impact on the mixing layer growth. Discrepancies between DG and PG flows are more likely related to transcritical real gas effects than to the BZT and the DG thermodynamic peculiar properties. Shocklets indeed only have a limited effect on the mixing layer growth. The compressible dissipation is negligible when compared with the total dissipation. For dense gas mixing layers, several physical factors tend to reduce compressibility effects: the decoupling of kinetic and internal energies reduces the effect of increasing M_c; reduced friction losses in dense gas flows modify the distribution of the averaged density, which therefore favors the momentum thickness growth rate. Finally, it was found that larger initial isothermal compressibility also leads to an increased momentum thickness growth rate in dense gas flows.

After having analyzed the DG mixing layers DNS, simulations were filtered in Chapter 5 in order to *a priori* assess SGS terms with respect to resolved terms present in the real gas LES formulation. An additional DNS of a forced HIT flow extracted from Giauque *et al.* (2020) completes the filtered DNS database. The system of LES equations to be solved for compressible transcritical dense gas flows is rewritten taking into account SGS terms which are of significant amplitude (at least larger than a resolved term) inside the turbulence inertial zone. The following additional SGS terms neglected in PG flows should be taken into: the SGS pressure term appearing in the filtered momentum equations and the SGS pressure work appearing in the filtered total energy equation.

A new modeling was then developed in Chapter 6 for the SGS pressure term ($\bar{p} - \widehat{p}$). Because of the complexity of this term comprising intricate SGS thermodynamic correlations, the modeling methodology makes use of supervised machine learning algorithms. Several artificial neural networks (ANN) were trained, harvesting information contained in the filtered DNS database comprising the forced HIT (Giauque *et al.*, 2020) and the mixing layers at $M_c = 1.1$ and $M_c = 2.2$. The analysis of the database confirms the complexity of this term whose correlations are significantly different between cases. For the forced HIT, the SGS pressure is strongly

correlated with the thermodynamic variables whereas for both mixing layers, the correlations are the strongest with the gradient of those same thermodynamic quantities likely because of the presence of the mean flow.

The optimization and the training of an ANN using a diverse database enabled to obtain effective SGS models capable to provide reliable results for cases which were not encountered during the training phase (different temporal solutions and initial thermodynamic operating points). Yet, training an ANN on a diverse database also causes learning inhomogeneity issues. It was noticed that the forced HIT is favored by the ANN likely because of its wider SGS pressure distribution. The additional analysis of small size networks showed the lack of reproducibility in the ANN architecture. Very different structures of ANN with identical performance were indeed obtained. Results also showed the ability of such simple networks to reach very reasonable performance with a very low number of degrees of freedom but only when trained on separate configurations.

The preliminary *a posteriori* study of the SGS pressure model using ANN performed in Chapter 7 was less conclusive. The use of the SGS pressure model did not interfere with the convergence of the computations and results could be analyzed for a range of filtering sizes. However, even though the magnitude of the SGS pressure flux was shown to be significant in *a priori* and *a posteriori* LES, its effect on the growth of the mixing layer was found negligible. The alignment of SGS pressure and density gradients leads to a negligible contribution of the model to the generation of vorticity, so that it could explain its minor effect on the turbulent structures roll-up and therefore on the mixing layer growth. The SGS pressure model was found to have a slight effect on the averaged temperature but which remains negligible anyhow considering the isothermal nature of the flow. No visible effect was observed on other averaged and rms thermodynamics distributions.

Future work and perspectives

The final *a posteriori* results obviously question both the use of the ANN model and the importance of the effect of the SGS pressure term in LES of DG turbulent flows. It was also shown however that the dynamic Smagorinsky model, used to take into account the SGS turbulent stress tensor, had a significant effect on the momentum thickness temporal evolution but failed to reproduce DG mixing layers growth at moderate to large filtering sizes. Once usual PG SGS models are evaluated over DG flows, the methodology using ANN developed in the present thesis could be applied to other SGS terms and especially to the SGS turbulent stress tensor in order to improve *a posteriori* LES performance at large filtering sizes in the inertial region. The design of such models could indeed foster the computation of coarse and yet accurate LES in industry for iterative design and optimization applications.

Such models could also be developed using an additional channel flow DNS, which has already been performed (see Giauque *et al.* (2021)), in order to take into account wall effects on SGS models. Finally, the *a posteriori* validation of these models could be achieved through a comparison with the experimental study of Dura Galiana *et al.* (2017) involving a flat plate inserted in a transonic nozzle.

Moreover, to improve the physical understanding of turbulence in real gas close to the supercritical point, future work could perform mixing layers DNS using another fluid than FC-70. One can for example think of supercritical CO_2, which has recently seen its use in thermodynamic cycles increases significantly. If the results regarding the momentum thickness growth

rate appear to be impacted by this change of fluid, a physical parameter characterizing the fluid might be emphasized to describe the diminution of the compressibility-related reduction of the momentum thickness growth rate in DG flows. According to the present results, the initial isothermal compressibility could be a good candidate to characterize this reduction rate.

References

Adadi, Amina & Berrada, Mohammed 2018 Peeking inside the black-box: a survey on explainable artificial intelligence (XAI). *IEEE access* **6**, 52138–52160.

Almagro, Antonio, García-Villalba, Manuel & Flores, Oscar 2017 A numerical study of a variable-density low-speed turbulent mixing layer. *Journal of Fluid Mechanics* **830**, 569–601.

Anders, J. B., Anderson, W. K. & Murthy, A. V. 1999 Transonic similarity theory applied to a supercritical airfoil in heavy gas. *Journal of aircraft* **36** (6), 957–964.

antares Development Team 2020 Antares Documentation Release 1.17.0.

Argrow, B. M. 1996 Computational analysis of dense gas shock tube flow. *Shock Waves* **6** (4), 241–248.

Bailly, C. & Comte-Bellot, G. 2003 Turbulence (CNRS éditions). *Sciences et techniques de l'ingénieur* .

Bardina, Jorge, Ferziger, J & Reynolds, W 1980 Improved subgrid-scale models for large-eddy simulation. In *13th fluid and plasmadynamics conference*, p. 1357.

Barre, S. & Bonnet, J. P. 2015 Detailed experimental study of a highly compressible supersonic turbulent plane mixing layer and comparison with most recent DNS results:"towards an accurate description of compressibility effects in supersonic free shear flows". *International Journal of Heat and Fluid Flow* **51**, 324–334.

Batchelor, G. K. 1953 *The theory of homogeneous turbulence*. Cambridge University Press.

Beck, Andrea, Flad, David & Munz, Claus-Dieter 2019 Deep neural networks for data-driven les closure models. *Journal of Computational Physics* **398**, 108910.

Bell, Ian H, Wronski, Jorrit, Quoilin, Sylvain & Lemort, Vincent 2014 Pure and pseudo-pure fluid thermophysical property evaluation and the open-source thermophysical property library coolprop. *Industrial & engineering chemistry research* **53** (6), 2498–2508.

Bethe, H. A. 1942 The theory of shock waves for an arbitrary equation of state. technical paper 545, office sci. *Res. & Dev* .

Bogdanoff, D. W. 1983 Compressibility effects in turbulent shear layers. *AIAA Journal* **21** (6), 926–927.

Borghesi, Giulio & Bellan, Josette 2015 A priori and a posteriori investigations for developing large eddy simulations of multi-species turbulent mixing under high-pressure conditions. *Physics of Fluids* **27** (3), 035117.

Borisov, A. A., Borisov, Al. A., Kutateladze, S. S. & Nakoryakov, V. E. 1983 Rarefaction shock wave near the critical liquid-vapour point. *Journal of Fluid Mechanics* **126**, 59–73.

Boussinesq, Joseph 1897 *Théorie de l'écoulement tourbillonnant et tumultueux des liquides dans les lits rectilignes a grande section*, , vol. 1. Gauthier-Villars.

Bradshaw, P. 1966 The effect of initial conditions on the development of a free shear layer. *Journal of Fluid Mechanics* **26** (2), 225–236.

Bradshaw, P. 1977 Compressible turbulent shear layers. *Annual Review of Fluid Mechanics* **9** (1), 33–52.

Breidenthal, R. E. 1992 Sonic eddy-a model for compressible turbulence. *AIAA Journal* **30** (1), 101–104.

Brown, B. P. & Argrow, B. M. 1998 Nonclassical dense gas flows for simple geometries. *AIAA Journal* **36** (10), 1842–1847.

Brown, G. L. & Roshko, A. 1974 On density effects and large structure in turbulent mixing layers. *Journal of Fluid Mechanics* **64** (4), 775–816.

de Bruin, I. 2001 Direct and Large-Eddy Simulation of the Spatial Turbulent Mixing Layer. PhD thesis, Eindhoven University of Technology.

Buchta, David A & Freund, Jonathan B 2017 The near-field pressure radiated by planar high-speed free-shear-flow turbulence. *Journal of Fluid Mechanics* **832**, 383.

Cadieux, F., Domaradzki, J. A., Sayadi, T., Bose, T. & Duchaine, F. 2012 DNS and LES of separated flows at moderate reynolds numbers. *Proceedings of the 2012 Summer Program, Center for Turbulence Research, NASA Ames/Stanford University, Stanford, CA, June* pp. 77–86.

Chung, T. H., Ajlan, M., Lee, L. L. & Starling, K. E. 1988 Generalized multiparameter correlation for nonpolar and polar fluid transport properties. *Industrial & engineering chemistry research* **27** (4), 671–679.

Cinnella, P. & Congedo, P. M. 2005 Aerodynamic performance of transonic Bethe-Zel'dovich-Thompson flows past an airfoil. *AIAA Journal* **43** (2), 370–378.

Cinnella, P. & Congedo, P. M. 2007 Inviscid and viscous aerodynamics of dense gases. *Journal of Fluid Mechanics* **580**, 179–217.

Clark, Robert A, Ferziger, Joel H & Reynolds, William Craig 1979 Evaluation of subgrid-scale models using an accurately simulated turbulent flow. *Journal of fluid mechanics* **91** (1), 1–16.

Colin, O. & Rudgyard, M. 2000 Development of high-order taylor–galerkin schemes for LES. *Journal of Computational Physics* **162** (2), 338–371.

Colonna, P., Casati, E., Trapp, C., Mathijssen, T., Larjola, J., Turunen-Saaresti, T. & Uusitalo, A. 2015 Organic Rankine Cycle Power Systems: From the Concept to Current Technology, Applications, and an Outlook to the Future. *Journal of Engineering for Gas Turbines and Power* **137** (10), 100801.

Colonna, P. & Guardone, A. 2006 Molecular interpretation of nonclassical gas dynamics of dense vapors under the van der Waals model. *Physics of Fluids* **18** (5).

Colonna, P., Guardone, A., Nannan, N. R. & Zamfirescu, C. 2008 Design of the dense gas flexible asymmetric shock tube. *Journal of Fluids Engineering* **130** (3), 034501.

Colonna, P. & Rebay, S. 2004 Numerical simulation of dense gas flows on unstructured grids with an implicit high resolution upwind Euler solver. *International Journal for Numerical Methods in Fluids* **46** (7), 735–765.

Congedo, P. M., Corre, C. & Cinnella, P. 2007 Airfoil shape optimization for transonic flows Bethe-Zel'dovich-Thompson fluids. *AIAA Journal* **45** (6), 1303–1316.

Congedo, P. M., Corre, C. & Cinnella, P. 2011 Numerical investigation of dense-gas effects in turbomachinery. *Computers & Fluids* **49** (1), 290–301.

Cook, Andrew W & Cabot, William H 2004 A high-wavenumber viscosity for high-resolution numerical methods. *Journal of Computational Physics* **195** (2), 594–601.

Costello, M. G., Flynn, R. M. & Owens, J. G. 2000 Fluoroethers and fluoroamines. *Kirk-Othmer Encyclopedia of Chemical Technology* .

Cramer, M. S. 1989 Negative nonlinearity in selected fluorocarbons. *Physics of Fluids A: Fluid Dynamics* **1** (11), 1894–1897.

Cramer, M. S. 1991 Nonclassical dynamics of classical gases. In *Nonlinear waves in real fluids*, pp. 91–145. Springer.

Cramer, M. S. & Crickenberger, A. B. 1991 The dissipative structure of shock waves in dense gases. *Journal of Fluid Mechanics* **223**, 325–355.

Cramer, M. S. & Kluwick, A. 1984 On the propagation of waves exhibiting both positive and negative nonlinearity. *Journal of Fluid Mechanics* **142**, 9–37.

Cramer, M. S. & Park, S. 1999 On the suppression of shock-induced separation in Bethe-Zel'dovich-Thompson fluids. *Journal of Fluid Mechanics* **393**, 1–21.

Cramer, M. S. & Sen, R. 1986 Shock formation in fluids having embedded regions of negative nonlinearity. *The Physics of Fluids* **29** (7), 2181–2191.

Dai, Q., Jin, T., Luo, K. & Fan, J. 2018 Direct numerical simulation of particle dispersion in a three-dimensional spatially developing compressible mixing layer. *Physics of Fluids* **30** (11), 113301.

Dask Development Team 2016 *Dask: Library for dynamic task scheduling*.

Deardorff, James W & others 1970 A numerical study of three-dimensional turbulent channel flow at large reynolds numbers. *J. Fluid Mech* **41** (2), 453–480.

Desoutter, G., Habchi, C., Cuenot, B. & Poinsot, T. 2009 DNS and modeling of the turbulent boundary layer over an evaporating liquid film. *International Journal of Heat and Mass Transfer* **52** (25-26), 6028–6041.

Di Mare, F, Jones, WP & Menzies, KR 2004 Large eddy simulation of a model gas turbine combustor. *Combustion and Flame* **137** (3), 278–294.

Dura Galiana, F. J., Wheeler, APS, Ong, J & de M Ventura, CA 2017 The effect of dense gas dynamics on loss in ORC transonic turbines. In *Journal of Physics: Conference Series*, , vol. 821, p. 012021. IOP Publishing.

Dura Galiana, F. J., Wheeler, A. P. S. & Ong, J. 2016 A study of trailing-edge losses in organic rankine cycle turbines. *Journal of Turbomachinery* **138** (12), 121003.

Duraisamy, Karthik, Iaccarino, Gianluca & Xiao, Heng 2019 Turbulence modeling in the age of data. *Annual Review of Fluid Mechanics* **51**, 357–377.

Eidson, Thomas M 1985 Numerical simulation of the turbulent rayleigh–bénard problem using subgrid modelling. *Journal of Fluid Mechanics* **158**, 245–268.

Erlebacher, Gordon, Hussaini, M Yousuff, Speziale, Charles G & Zang, Thomas A 1992 Toward the large-eddy simulation of compressible turbulent flows. *Journal of fluid mechanics* **238**, 155–185.

Favre, A & others 1971 Equations statistiques aux fluctuations turbulentes dans les ecoulements compressibles: cas des vitesses et des temperatures. *CR Acad Sci Paris* **273**.

Fergason, S. H. & Argrow, B. M. 2001 Simulations of nonclassical dense gas dynamics. In *35th AIAA Thermophysics Conference*.

Fergason, S. H., Ho, T. L., Argrow, B. M. & Emanuel, G. 2001 Theory for producing a single-phase rarefaction shock wave in a shock tube. *Journal of Fluid Mechanics* **445**, 37–54.

Freund, J. B., Lele, S. K. & Moin, P. 2000 Compressibility effects in a turbulent annular mixing layer. Part 1. Turbulence and growth rate. *Journal of Fluid Mechanics* **421**, 229–267.

Frezat, Hugo, Balarac, Guillaume, Le Sommer, Julien, Fablet, Ronan & Lguensat, Redouane 2021 Physical invariance in neural networks for subgrid-scale scalar flux modeling. *Physical Review Fluids* **6** (2), 024607.

From, C. S., Sauret, E., Armfield, S. W., Saha, S. C. & Gu, Y. T. 2017 Turbulent dense gas flow characteristics in swirling conical diffuser. *Computers and Fluids* **149**, 100–118.

Fu, S. & Li, Q 2006 Numerical simulation of compressible mixing layers. *International journal of heat and fluid flow* **27** (5), 895–901.

Fujiwara, Hitoshi, Matsuo, Yuichi & Arakawa, Chuichi 2000 A turbulence model for the pressure–strain correlation term accounting for compressibility effects. *International Journal of Heat and Fluid Flow* **21** (3), 354–358.

Gaia, Mario 2011 30 years of organic rankine cycle development. In *First International Seminar on ORC Power Systems, Delft, The Netherlands, Sept*, pp. 11–23.

Gamahara, Masataka & Hattori, Yuji 2017 Searching for turbulence models by artificial neural network. *Physical Review Fluids* **2** (5), 054604.

Garnier, E., Adams, N. & Sagaut, P. 2009 *Large eddy simulation for compressible flows*. Springer Science & Business Media.

Germano, Massimo, Piomelli, Ugo, Moin, Parviz & Cabot, William H 1991 A dynamic subgrid-scale eddy viscosity model. *Physics of Fluids A: Fluid Dynamics* **3** (7), 1760–1765.

Géron, Aurélien 2017 *Deep Learning avec TensorFlow*. Dunod.

Giauque, A., A., Vadrot, P., Errante & C., Corre 2021 A-priori analysis of subgrid-scale terms in compressible transcritical real gas flows. *Physics of Fluids* .

Giauque, A., Corre, C. & Menghetti, M. 2017 Direct numerical simulations of homogeneous isotropic turbulence in a dense gas. *Journal of Physics: Conference Series* **821** (1), 012017.

Giauque, A, Corre, C & Vadrot, A 2020 Direct numerical simulations of forced homogeneous isotropic turbulence in a dense gas. *Journal of Turbulence* **21** (3), 186–208.

Giauque, A, Selle, L, Gicquel, L, Poinsot, T, Buechner, H, Kaufmann, P & Krebs, W 2005 System identification of a large-scale swirled partially premixed combustor using LES and measurements. *Journal of Turbulence* (6), N21.

Gloerfelt, Xavier, Robinet, Jean Christophe, Sciacovelli, Luca, Cinnella, Paola & Grasso, Francesco 2020 Dense-gas effects on compressible boundary-layer stability. *Journal of Fluid Mechanics* **893**.

Glorot, Xavier & Bengio, Yoshua 2010 Understanding the difficulty of training deep feedforward neural networks. In *Proceedings of the thirteenth international conference on artificial intelligence and statistics*, pp. 249–256. JMLR Workshop and Conference Proceedings.

Gori, Giulio, Zocca, Marta, Cammi, Giorgia, Spinelli, Andrea, Congedo, Pietro Marco & Guardone, Alberto 2020 Accuracy assessment of the non-ideal computational fluid dynamics model for siloxane mdm from the open-source SU2 suite. *European Journal of Mechanics-B/Fluids* **79**, 109–120.

Grieser, D. R. & Goldthwaite, W. H. 1963 Experimental determination of the viscosity of air in the gaseous state at low temperatures and pressures. *Tech. Rep.*. BATTELLE MEMORIAL INST COLUMBUS OH.

Grooms, Ian, Lee, Yoonsang & Majda, Andrew J 2015 Numerical schemes for stochastic backscatter in the inverse cascade of quasigeostrophic turbulence. *Multiscale Modeling & Simulation* **13** (3), 1001–1021.

Guardone, Alberto & Argrow, BM 2005 Nonclassical gasdynamic region of selected fluorocarbons. *Physics of Fluids* **17** (11), 116102.

Guardone, ALBERTO, Vigevano, Luigi & Argrow, BM 2004 Assessment of thermodynamic models for dense gas dynamics. *Physics of Fluids* **16** (11), 3878–3887.

Hamba, Fujihiro 1999 Effects of pressure fluctuations on turbulence growth in compressible homogeneous shear flow. *Physics of Fluids* **11** (6), 1623–1635.

Harinck, J., Colonna, P., Guardone, A. & Rebay, S. 2010*a* Influence of thermodynamic models in two-dimensional flow simulations of turboexpanders. *Journal of turbomachinery* **132** (1), 011001.

Harinck, J., Turunen-Saaresti, T., Colonna, P., Rebay, S. & van Buijtenen, J. 2010*b* Computational Study of a High-Expansion Ratio Radial Organic Rankine Cycle Turbine Stator. *Journal of Engineering for Gas Turbines and Power* **132** (5), 054501.

Hayes, W. D. 1958 The basic theory of gasdynamic discontinuities, fundamentals of gas dynamics (ed. HW Emmons), High Speed Aerodynamics and Jet Propulsion 3, 416-481.

He, Kaiming, Zhang, Xiangyu, Ren, Shaoqing & Sun, Jian 2015 Delving deep into rectifiers: Surpassing human-level performance on imagenet classification. In *Proceedings of the IEEE international conference on computer vision*, pp. 1026–1034.

Hoarau, Jean-Christophe, Cinnella, Paola & Gloerfelt, Xavier 2021 Large Eddy Simulations of Strongly Non-Ideal Compressible Flows through a Transonic Cascade. *Energies* **14** (3), 772.

Huang, Siyuan & Fu, Song 2008 Modelling of pressure–strain correlation in compressible turbulent flow. *Acta Mechanica Sinica* **24** (1), 37–43.

Invernizzi, C. M. 2010 Stirling engines using working fluids with strong real gas effects. *Applied Thermal Engineering* **30** (13), 1703–1710.

Invernizzi, Costante Mario 2013 Closed power cycles. *Lecture Notes in Energy* **11**.

Jamieson, Kevin & Talwalkar, Ameet 2016 Non-stochastic best arm identification and hyperparameter optimization. In *Artificial Intelligence and Statistics*, pp. 240–248. PMLR.

Jolliffe, Ian 2005 Principal component analysis. *Encyclopedia of statistics in behavioral science* .

Kingma, Diederik P & Ba, Jimmy 2014 Adam: A method for stochastic optimization. *arXiv preprint arXiv:1412.6980* .

Kirillov, N. G. 2004 Analysis of modern natural gas liquefaction technologies. *Chemical and Petroleum Engineering* **40** (7-8), 401–406.

Kluwick, A. 2004 Internal flows of dense gases. *Acta mechanica* **169** (1-4), 123–143.

Kolmogorov, A. N. 1941 The local structure of turbulence in incompressible viscous fluid for very large Reynolds numbers. *Dokl. Akad. Nauk SSSR* **30** (4), 299–303.

Kourta, Azeddine & Sauvage, R 2002 Computation of supersonic mixing layers. *Physics of Fluids* **14** (11), 3790–3797.

Kritsuk, A. G., Norman, M. L., Paolo Padoan, A. N. D. & Wagner, R. 2007 The statistics of supersonic isothermal turbulence. *Astrophysical Journal* **665** (1), 416–431.

Kutateladze, S. S., Nakoryakov, V. E. & Borisov, A. A. 1987 Rarefaction waves in liquid and gas-liquid media. *Annual review of fluid mechanics* **19** (1), 577–600.

Lamarque, Nicolas 2007 Schémas numériques et conditions limites pour la simulation aux grandes échelles de la combustion diphasique dans les foyers d'hélicoptère. PhD thesis, Institut National Polytechnique de Toulouse-INPT.

Lapeyre, Corentin J, Misdariis, Antony, Cazard, Nicolas, Veynante, Denis & Poinsot, Thierry 2019 Training convolutional neural networks to estimate turbulent subgrid scale reaction rates. *Combustion and Flame* **203**, 255–264.

Lee, Sangsan, Lele, Sanjiva K & Moin, Parviz 1991 Eddy shocklets in decaying compressible turbulence. *Physics of Fluids A: Fluid Dynamics* **3** (4), 657–664.

Lemmon, Eric W, Huber, Marcia L & Mclinden, Mark O 2007 Nist standard reference database 23: reference fluid thermodynamic and transport properties-refprop, version 8.0 .

Leonard, Anthony 1975 Energy cascade in large-eddy simulations of turbulent fluid flows. In *Advances in geophysics*, , vol. 18, pp. 237–248. Elsevier.

Lesieur, Marcel 2012 *Turbulence in fluids*, , vol. 40. Springer Science & Business Media.

Levenberg, Kenneth 1944 A method for the solution of certain non-linear problems in least squares. *Quarterly of applied mathematics* **2** (2), 164–168.

Li, Lisha, Jamieson, Kevin, DeSalvo, Giulia, Rostamizadeh, Afshin & Talwalkar, Ameet 2017 Hyperband: A novel bandit-based approach to hyperparameter optimization. *The Journal of Machine Learning Research* **18** (1), 6765–6816.

Liepmann, H. W. & Laufer, J. 1947 Investigations of free turbulent mixing. *NACA Technical Note No. 1257* .

Lilly, Douglas K 1992 A proposed modification of the germano subgrid-scale closure method. *Physics of Fluids A: Fluid Dynamics* **4** (3), 633–635.

Luo, K. H. & Sandham, N. D. 1994 On the formation of small scales in a compressible mixing layer. In *Direct and Large-Eddy Simulation I*, pp. 335–346. Springer.

Martin, J. J. & Hou, Y. 1955 Development of an Equation of State for Gases. *AIChE journal* **2** (4), 142–151.

Martin, J. J., Kapoor, R. M. & De Nevers, N. 1959 An improved equation of state for gases. *AIChE Journal* **5** (2), 159–160.

Martin, M Pino, Piomelli, Ugo & Candler, Graham V 2000 Subgrid-scale models for compressible large-eddy simulations. *Theoretical and Computational Fluid Dynamics* **13** (5), 361–376.

Martínez Ferrer, P. J., Lehnasch, G. & Mura, A. 2017 Compressibility and heat release effects in high-speed reactive mixing layers I.: Growth rates and turbulence characteristics. *Combustion and Flame* **180** (M), 284–303.

Mathijssen, T., Gallo, M., Casati, E., Nannan, N. R., Zamfirescu, C., Guardone, A. & Colonna, P. 2015 The flexible asymmetric shock tube (FAST): a Ludwieg tube facility for wave propagation measurements in high-temperature vapours of organic fluids. *Experiments in Fluids* **56** (10), 195.

Matsuno, Kristen & Lele, Sanjiva K 2020 Compressibility effects in high speed turbulent shear layers–revisited. In *AIAA Scitech 2020 Forum*, p. 0573.

Maulik, Romit, San, Omer, Rasheed, Adil & Vedula, Prakash 2018 Data-driven deconvolution for large eddy simulations of kraichnan turbulence. *Physics of Fluids* **30** (12), 125109.

Maulik, Romit, San, Omer, Rasheed, Adil & Vedula, Prakash 2019 Subgrid modelling for two-dimensional turbulence using neural networks. *Journal of Fluid Mechanics* **858**, 122–144.

Meneveau, Charles & Katz, Joseph 2000 Scale-invariance and turbulence models for large-eddy simulation. *Annual Review of Fluid Mechanics* **32** (1), 1–32.

Menikoff, R. & Plohr, B. J. 1989 The Riemann problem for fluid flow of real materials. *Reviews of modern physics* **61** (1), 75.

Merle, X. & Cinnella, P. 2014 Bayesian quantification of thermodynamic uncertainties in dense gas flows. *Reliability Engineering & System Safety* pp. 1–19.

Moin, P. & Mahesh, K. 1998*a* Direct numerical simulation: a tool in turbulence research. *Annual review of fluid mechanics* **30** (1), 539–578.

Moin, Parviz & Mahesh, Krishnan 1998*b* Direct numerical simulation: A tool in turbulence research. *Annual Review of Fluid Mechanics* **30** (1), 539–578.

Moin, Parviz, Squires, Kyle, Cabot, W & Lee, Sangsan 1991 A dynamic subgrid-scale model for compressible turbulence and scalar transport. *Physics of Fluids A: Fluid Dynamics* **3** (11), 2746–2757.

Monaco, J. F., Cramer, M. S. & Watson, L. T. 1997 Supersonic flows of dense gases in cascade configurations. *Journal of Fluid Mechanics* **330**, 31–59.

Moreau, Antoine, Teytaud, Olivier & Bertoglio, Jean-Pierre 2006 Optimal estimation for large-eddy simulation of turbulence and application to the analysis of subgrid models. *Physics of fluids* **18** (10), 105101.

Nematollahi, Omid & Kim, Kyung Chun 2020 Real-gas effects: the State of the art of organic Rankine cycles. *Journal of Cleaner Production* p. 124102.

Nesterov, Yurii E 1983 A method for solving the convex programming problem with convergence rate o (1/kˆ 2). In *Dokl. akad. nauk Sssr*, , vol. 269, pp. 543–547.

Ni, Ron-Ho 1982 A multiple-grid scheme for solving the euler equations. *AIAA journal* **20** (11), 1565–1571.

Novello, Paul, Poëtte, Gaël, Lugato, David & Congedo, Pietro 2021 Explainable hyperparameters optimization using hilbert-schmidt independence criterion .

Okong'o, N. A. & Bellan, J. 2002 Direct numerical simulation of a transitional supercritical binary mixing layer: heptane and nitrogen. *Journal of Fluid Mechanics* **464**, 1–34.

Okong'o, Nora A & Bellan, Josette 2004 Consistent large-eddy simulation of a temporal mixing layer laden with evaporating drops. part 1. direct numerical simulation, formulation and a priori analysis. *Journal of Fluid Mechanics* **499**, 1–47.

Pantano, C. & Sarkar, S. 2002 A study of compressibility effects in the high-speed turbulent shear layer using direct simulation. *Journal of Fluid Mechanics* **451**, 329–371.

Papamoschou, D. & Roshko, A. 1988 The compressible turbulent shear layer: an experimental study. *Journal of Fluid Mechanics* **197**, 453–477.

Park, CH & Park, Seung O 2005 A compressible turbulence model for the pressure–strain correlation. *Journal of Turbulence* (6), N2.

Pawar, Suraj, San, Omer, Rasheed, Adil & Vedula, Prakash 2020 A priori analysis on deep learning of subgrid-scale parameterizations for kraichnan turbulence. *Theoretical and Computational Fluid Dynamics* **34** (4), 429–455.

Pedregosa, F., Varoquaux, G., Gramfort, A., Michel, V., Thirion, B., Grisel, O., Blondel, M., Prettenhofer, P., Weiss, R., Dubourg, V., Vanderplas, J., Passos, A., Cournapeau, D., Brucher, M., Perrot, M. & Duchesnay, E. 2011 Scikit-learn: Machine learning in Python. *Journal of Machine Learning Research* **12**, 2825–2830.

Peng, Ding-Yu & Robinson, Donald B 1976 A new two-constant equation of state. *Industrial & Engineering Chemistry Fundamentals* **15** (1), 59–64.

Pineau, Pierre & Bogey, Christophe 2019 Steepened mach waves near supersonic jets: study of azimuthal structure and generation process using conditional averages. *Journal of Fluid Mechanics* **880**, 594–619.

Piomelli, Ugo, Moin, Parviz & Ferziger, Joel H 1988 Model consistency in large eddy simulation of turbulent channel flows. *The Physics of fluids* **31** (7), 1884–1891.

Pirozzoli, S., Bernardini, M., Marié, S. & Grasso, F. 2015 Early evolution of the compressible mixing layer issued from two turbulent streams. *Journal of Fluid Mechanics* **777**, 196–218.

Poinsot, T. J. & Lele, S. K. 1992 Boundary conditions for direct simulations of compressible viscous flows. *Journal of computational physics* **101** (1), 104–129.

Prandtl, Ludwig 1904 Über flussigkeitsbewegung bei sehr kleiner reibung. *Verhandl. III, Internat. Math.-Kong., Heidelberg, Teubner, Leipzig, 1904* pp. 484–491.

Prat, Alvaro, Sautory, Theophile & Navarro-Martinez, S 2020 A priori sub-grid modelling using artificial neural networks. *International Journal of Computational Fluid Dynamics* **34** (6), 397–417.

Rankine, William John Macquorn 1873 *A manual of the steam engine and other prime movers*. Charles Griffin.

Razaaly, Nassim, Persico, Giacomo & Congedo, Pietro Marco 2019 Impact of geometric, operational, and model uncertainties on the non-ideal flow through a supersonic ORC turbine cascade. *Energy* **169**, 213–227.

Redlich, Otto & Kwong, Joseph NS 1949 On the thermodynamics of solutions. v. an equation of state. fugacities of gaseous solutions. *Chemical reviews* **44** (1), 233–244.

Richardson, LF 1922 Weather prediction by numerical processes, cambridge univ. *P., London* .

Riedmiller, Martin & Braun, Heinrich 1993 A direct adaptive method for faster backpropagation learning: The rprop algorithm. In *IEEE international conference on neural networks*, pp. 586–591. IEEE.

Rogers, M. M. & Moser, R. D. 1994 Direct simulation of a self-similar turbulent mixing layer. *Physics of Fluids* **6** (2), 903–923.

Romei, Alessandro, Vimercati, Davide, Persico, Giacomo & Guardone, Alberto 2020 Non-ideal compressible flows in supersonic turbine cascades. *Journal of Fluid Mechanics* **882**.

Rosofsky, Shawn G & Huerta, EA 2020 Artificial neural network subgrid models of 2d compressible magnetohydrodynamic turbulence. *Physical Review D* **101** (8), 084024.

Rossmann, Tobias, Mungal, M Godfrey & Hanson, Ronald K 2001 Evolution and growth of large scale structures in high compressibility mixing layers. In *TSFP Digital Library Online*. Begel House Inc.

Rusak, Z. & Wang, C.-W. 1997 Transonic flow of dense gases around an airfoil with a parabolic nose. *Journal of Fluid Mechanics* **346**, 1–21.

Samtaney, Ravi, Pullin, Dale I & Kosović, Branko 2001 Direct numerical simulation of decaying compressible turbulence and shocklet statistics. *Physics of Fluids* **13** (5), 1415–1430.

Sandham, N. D. & Reynolds, W. C. 1990 Compressible mixing layer - Linear theory and direct simulation. *AIAA Journal* **28** (4), 618–624.

Sarghini, Fabrizio, De Felice, G & Santini, Stefania 2003 Neural networks based subgrid scale modeling in large eddy simulations. *Computers & fluids* **32** (1), 97–108.

Sarkar, S. 1995 The stabilizing effect of compressibility in turbulent shear flow. *Journal of Fluid Mechanics* **282**, 163–186.

Sarkar, S., Erlebacher, G., Hussaini, M. Y. & Kreiss, H. O. 1991 The analysis and modelling of dilatational terms in compressible turbulence. *Journal of Fluid Mechanics* **227**, 473–493.

Sarkar, Sutanu & Lakshmanan, B 1991 Application of a reynolds stress turbulence model to the compressible shear layer. *AIAA journal* **29** (5), 743–749.

Sciacovelli, L., Cinnella, P., Content, C. & Grasso, F. 2016 Dense gas effects in inviscid homogeneous isotropic turbulence. *Journal of Fluid Mechanics* **800**, 140–179.

Sciacovelli, L., Cinnella, P. & Gloerfelt, X. 2017*a* Direct numerical simulations of supersonic turbulent channel flows of dense gases. *Journal of Fluid Mechanics* **821**, 153–199.

Sciacovelli, L., Cinnella, P. & Grasso, F. 2017*b* Small-scale dynamics of dense gas compressible homogeneous isotropic turbulence. *Journal of Fluid Mechanics* **825**, 515–549.

Selle, Laurant C, Okong'o, Nora A, Bellan, Josette & Harstad, Kenneth G 2007 Modelling of subgrid-scale phenomena in supercritical transitional mixing layers: an a priori study. *Journal of Fluid Mechanics* **593**, 57–91.

Smagorinsky, Joseph 1963 General circulation experiments with the primitive equations: I. the basic experiment. *Monthly weather review* **91** (3), 99–164.

Soave, Giorgio 1972 Equilibrium constants from a modified redlich-kwong equation of state. *Chemical engineering science* **27** (6), 1197–1203.

Speziale, Charles G 1985 Galilean invariance of subgrid-scale stress models in the large-eddy simulation of turbulence. *Journal of fluid mechanics* **156**, 55–62.

Speziale, Charles G, Erlebacher, Gordon, Zang, TA & Hussaini, MY 1988 The subgrid-scale modeling of compressible turbulence. *The Physics of fluids* **31** (4), 940–942.

Spinelli, A., Dossena, V., Gaetani, P., Osnaghi, C. & Colombo, D. 2010 Design of a Test Rig for Organic Vapours. In *ASME Turbo Expo 2010: Power for Land, Sea, and Air*, pp. 109–120. American Society of Mechanical Engineers.

Spinelli, A., Pini, M., Dossena, V., Gaetani, P. & Casella, F. 2013 Design, Simulation, and Construction of a Test Rig for Organic Vapors. *Journal of Engineering for Gas Turbines and Power* **135** (4), 042304.

Stephan, Karl & Laesecke, A 1985 The thermal conductivity of fluid air. *Journal of physical and chemical reference data* **14** (1), 227–234.

Stull, D. R. & Prophet, H. 1971 Janaf thermochemical tables. *Tech. Rep.*. National Standard Reference Data System.

Sutherland, W. 1893 LII. The viscosity of gases and molecular force. *The London, Edinburgh, and Dublin Philosophical Magazine and Journal of Science* **36** (223), 507–531.

Tanahashi, M., Iwase, S. & Miyauchi, T. 2001 Appearance and alignment with strain rate of coherent fine scale eddies in turbulent mixing layer. *Journal of Turbulence* **2** (6), 1–17.

Tartière, Thomas & Astolfi, Marco 2017 A world overview of the organic rankine cycle market. *Energy Procedia* **129**, 2–9.

Thompson, P. A. 1971 A fundamental derivative in gasdynamics. *Physics of Fluids* **14** (9), 1843–1849.

Thompson, P. A. & Lambrakis, K. C. 1973 Negative shock waves. *Journal of Fluid Mechanics* **60** (1), 187–208.

Vadrot, Aurélien, Giauque, Alexis & Corre, Christophe 2020 Analysis of turbulence characteristics in a temporal dense gas compressible mixing layer using direct numerical simulation. *Journal of Fluid Mechanics* **893**.

Vadrot, Aurélien, Giauque, Alexis & Corre, Christophe 2021 Direct Numerical Simulations of temporal compressible mixing layers in a BZT Dense Gas: influence of the convective Mach number. *Journal of Fluid Mechanics* .

Vollant, Antoine 2015 Evaluation et développement de modèles sous-maille pour la simulation des grandes échelles du mélange turbulent basés sur l'estimation optimale et l'apprentissage supervisé. PhD thesis, Université Grenoble Alpes.

Vollant, Antoine, Balarac, Guillaume & Corre, C 2017 Subgrid-scale scalar flux modelling based on optimal estimation theory and machine-learning procedures. *Journal of Turbulence* **18** (9), 854–878.

Vreman, A. W., Sandham, N. D. & Luo, K. H. 1996*a* Compressible mixing layer growth rate and turbulence characteristics. *Journal of Fluid Mechanics* **320**, 235–258.

Vreman, Bert, Geurts, Bernard & Kuerten, Hans 1995 A priori tests of large eddy simulation of the compressible plane mixing layer. *Journal of engineering mathematics* **29** (4), 299–327.

Vreman, Bert, Geurts, Bernard & Kuerten, Hans 1996*b* Large-eddy simulation of the temporal mixing layer using the clark model. *Theoretical and Computational Fluid Dynamics* **8** (4), 309–324.

Wagner, B. & Schmidt, W. 1978 Theoretical investigations of real gas effects in cryogenic wind tunnels. *AIAA Journal* **16** (6), 580–586.

Wang, C.-W. & Rusak, Z. 1999 Numerical studies of transonic BZT gas flows around thin airfoils. *Journal of Fluid Mechanics* **396**, 109–141.

Wang, Jianchun, Wan, Minping, Chen, Song, Xie, Chenyue, Zheng, Qinmin, Wang, Lian-Ping & Chen, Shiyi 2020 Effect of flow topology on the kinetic energy flux in compressible isotropic turbulence. *Journal of Fluid Mechanics* **883**.

Wang, Jianchun, Yang, Yantao, Shi, Yipeng, Xiao, Zuoli, He, XT & Chen, Shiyi 2013 Cascade of kinetic energy in three-dimensional compressible turbulence. *Physical review letters* **110** (21), 214505.

Wang, Zhuo, Luo, Kun, Li, Dong, Tan, Junhua & Fan, Jianren 2018 Investigations of data-driven closure for subgrid-scale stress in large-eddy simulation. *Physics of Fluids* **30** (12), 125101.

Wheeler, A. P. S. & Ong, J. 2013 The Role of Dense Gas Dynamics on Organic Rankine Cycle Turbine Performance. *Journal of Engineering for Gas Turbines and Power* **135** (10), 102603.

White, F. M. 1998 Fluid Mechanics, McGraw-Hill Series in Mechanical Engineering.

Wolf, Pierre, Staffelbach, Gabriel, Gicquel, Laurent YM, Müller, Jens-Dominik & Poinsot, Thierry 2012 Acoustic and large eddy simulation studies of azimuthal modes in annular combustion chambers. *Combustion and Flame* **159** (11), 3398–3413.

Xie, Chenyue, Wang, Jianchun, Li, Hui, Wan, Minping & Chen, Shiyi 2018 A modified optimal les model for highly compressible isotropic turbulence. *Physics of Fluids* **30** (6), 065108.

Xie, Chenyue, Wang, Jianchun, Li, Hui, Wan, Minping & Chen, Shiyi 2019 Artificial neural network mixed model for large eddy simulation of compressible isotropic turbulence. *Physics of Fluids* **31** (8), 085112.

Xie, Chenyue, Wang, Jianchun & Weinan, E 2020 Modeling subgrid-scale forces by spatial artificial neural networks in large eddy simulation of turbulence. *Physical Review Fluids* **5** (5), 054606.

Yang, XIA, Zafar, Suhaib, Wang, J-X & Xiao, Heng 2019 Predictive large-eddy-simulation wall modeling via physics-informed neural networks. *Physical Review Fluids* **4** (3), 034602.

Yoshizawa, Akira 1986 Statistical theory for compressible turbulent shear flows, with the application to subgrid modeling. *The Physics of fluids* **29** (7), 2152–2164.

Zel'dovich, J. 1946 On the possibility of rarefaction shock waves. *Zhurnal Eksperimentalnoi i Teoreticheskoi Fiziki* **16** (4), 363–364.

Zeman, O. 1990 Dilatation dissipation: the concept and application in modeling compressible mixing layers. *Physics of Fluids A: Fluid Dynamics* **2** (2), 178–188.

Zhou, Q., He, F. & Shen, M. Y. 2012 Direct numerical simulation of a spatially developing compressible plane mixing layer: flow structures and mean flow properties. *Journal of Fluid Mechanics* **711**, 1–32.

Zhou, Zhideng, He, Guowei, Wang, Shizhao & Jin, Guodong 2019 Subgrid-scale model for large-eddy simulation of isotropic turbulent flows using an artificial neural network. *Computers & Fluids* **195**, 104319.

Zhuang, Juntang, Tang, Tommy, Ding, Yifan, Tatikonda, Sekhar, Dvornek, Nicha, Papademetris, Xenophon & Duncan, James S 2020 Adabelief optimizer: Adapting stepsizes by the belief in observed gradients. *arXiv preprint arXiv:2010.07468* .

Appendix A

Averaging methodology for plots using $\delta_\theta(t)$

When studying the temporal mixing layer, it is usual to average TKE budget (or thermodynamic) distributions over time (during the self-similar period) and space (over the periodic x and z directions) and to plot the averaged quantities in the y direction normalized using $\delta_\theta(t)$. This process can actually induce a significant variability in the plots produced.

For instance, Figures 3.5, 4.8 and 4.9 display the various terms of the TKE budget. One can notice that these distributions show fairly abrupt changes (especially Figure 4.9 for production and pressure-strain terms) when compared with Pantano & Sarkar (2002) but show rather fairly smooth changes when compared to Zhou *et al.* (2012) (see Figure A.1) or Martínez Ferrer *et al.* (2017) (see Figure A.2).

This difference from one publication to another deserves some explanation. We believe it results from the choice of vertical (along y) space step used to obtain the curves. As illustrated in the explanatory Figure A.3, distributions plotted over $y/\delta_\theta(t)$ (see for instance Figures 3.5, 4.8 and 4.9) all require to average several solutions over the self-similar period which do not share the same step along the abscissa $y/\delta_\theta(t)$ since $\delta_\theta(t)$ increases during the self-similar period. For instance, at $M_c = 1.1$, each solution used in the averaging process contains $N_y = 512$ points along y, distributed between $-L_y/\delta_\theta(t)$ and $L_y/\delta_\theta(t)$.

A constant non-dimensional step dy^* is defined to discretize the interval corresponding to the initial time of the self-similar period ($\tau = 1700$ for the mixing layer at $M_c = 1.1$). Its value, which is given in the caption of the figures, depends on the number of points we want to represent these plots with and not on the resolution of the simulation itself. In the current work, for the TKE budget plots we choose this number of points two times larger than the one used by Pantano & Sarkar (2002). Figure A.4 shows the evolution of the TKE budget plots as the number of points (or dy^*) is varied for the PG mixing layer at $M_c = 1.1$: the choice made in this thesis (Chapters 3 and 4) seeks to optimize the impact of the post-processing on the quality of the plots (with changes neither too smooth nor too abrupt).

In the vicinity of $y/\delta_\theta(t) = 0$, DG distributions show non-monotonic behavior, that are likely to be explained by the difference of density fluctuations distributions (see Figure 4.13). For DG, the RMS value is large even at the center of the mixing layer unlike PG, where two peaks values are located at the boundaries of the mixing layer. This higher density fluctuations rate at the center is likely to disturb the distributions of production since it is calculated using Favre-averaging. In the vertical direction, production terms are even more non-monotonic both for DG and PG (Figure 4.9(b)) because they involve the vertical gradient of the mean vertical velocity. Since this gradient is calculated in the vertical direction, which corresponds to the direction of the mixing layer growth, it induces noisier distributions.

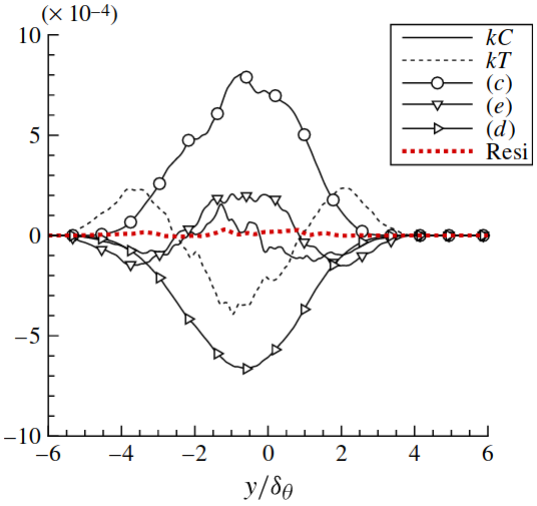

Figure A.1: TKE budget in the self-similar turbulent region, where kC, kT, (c), (e), (d) denote respectively the convective, transport, production, pressure dilatation and dissipation terms respectively at $M_c = 0.7$. Resi denotes the residual error of TKE transport equation. Taken from Zhou *et al.* (2012).

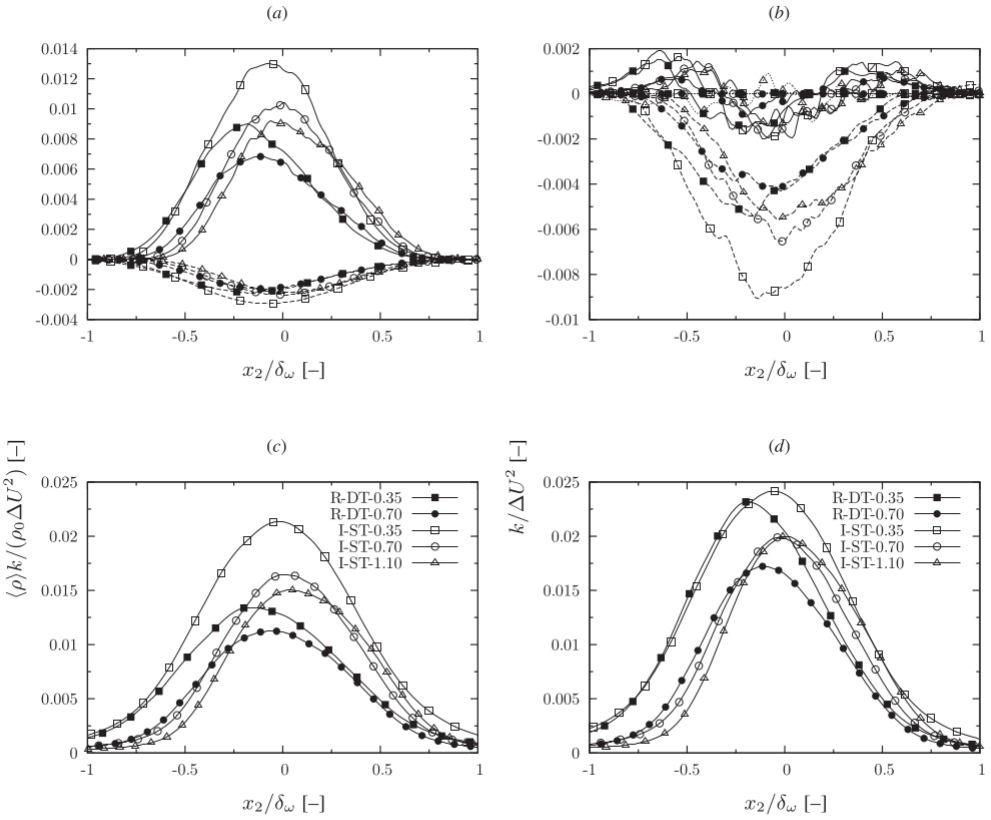

Fig. 14. Budget of the (a) and (b) streamwise Reynolds stress normalised by $\rho_0\Delta U^3/\delta_\omega$ and (c) and (d) two normalised forms of the turbulent kinetic energy. Fig. (a): (—) production and (- -) dissipation; Fig. (b): (—) turbulent transport, (- -) pressure-dilatation and (· · ·) mass flux; symbols as in Fig. 12.

Figure A.2: Figure taken from Martínez Ferrer *et al.* (2017). (a) and (b) correspond to the TKE budget terms.

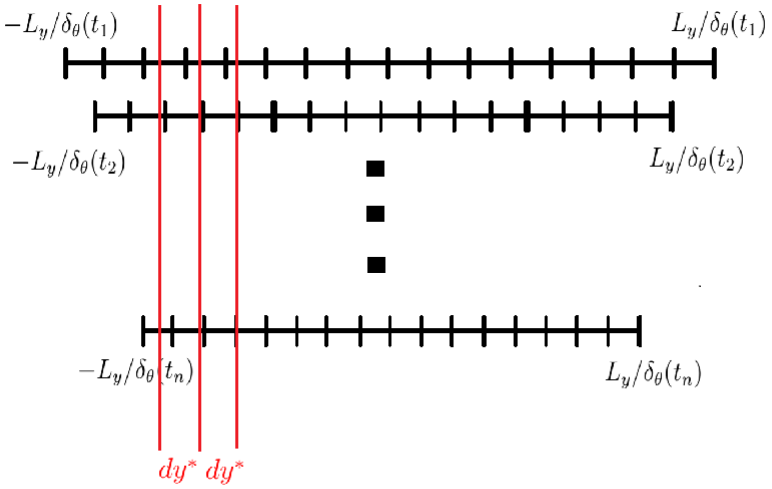

Figure A.3: Schematic view of the averaging process applied to generate the TKE budget and thermodynamic distributions (see for instance Figures 3.5, 4.8 and 4.9). Each line corresponds to a discrete time t_i in the selected self-similar period, for which a solution is available. Each solution at $t = t_i$ contains a distribution of $N_y = 512$ points (only 17 are reported on this schematic view) distributed on the non-dimensional interval $[-L_y/\delta_\theta(t_i), L_y/\delta_\theta(t_i)]$.

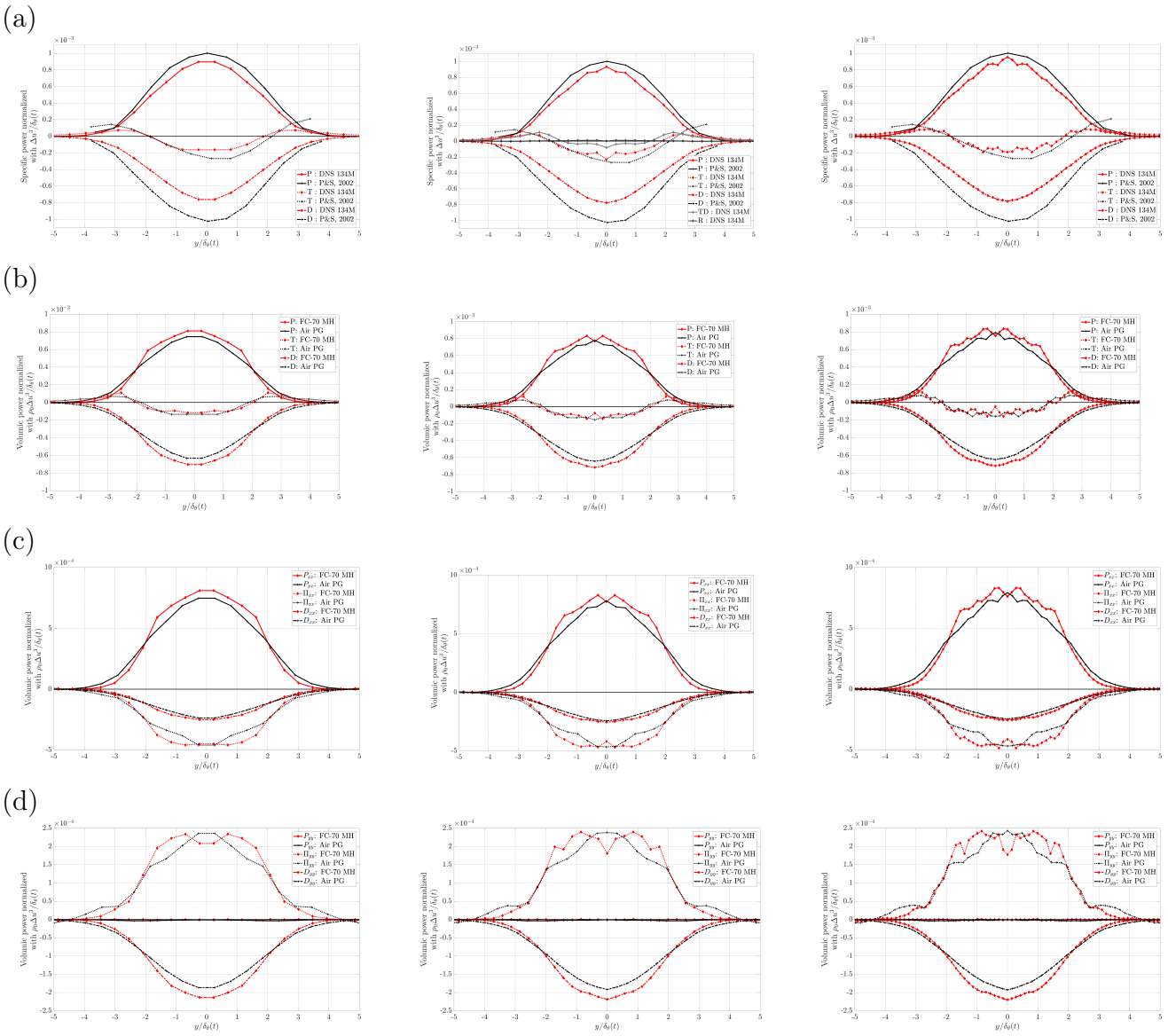

Figure A.4: TKE budget plots at $M_c = 1.1$ with different numbers of points: first column: 24 points; second column: 39 points (used in the thesis); third column: 79 points. (a): Distributions of the PG normalized specific power quantities (see Figure 3.5); (b): Distribution of the volumetric normalized powers (see Figure 4.8); (c) $x-$turbulent stress tensor (R_{xx}) equation (see Figure 4.9(a)); (d): $y-$turbulent stress tensor (R_{yy}) equation (see Figure 4.9(b)).

Appendix B

DG mixing layer: influence of domain size, resolution and initial turbulent structures size

This appendix provides verification data confirming the proper computation of mixing layers DNS. Table B.1 gathers DG and PG simulation parameters at the starting and ending times of self-similar periods. Integral length scales show that the domain is chosen sufficiently large. The largest value 0.20 is obtained at the end of the self-similar period for DG flow at $M_c = 1.1$. Otherwise, values do not exceed 0.16 in the streamwise direction and 0.13 in the z direction. As a comparison, Pantano & Sarkar (2002)'s integral length scale reaches 0.178 in the streamwise direction for a configuration with $M_c = 0.7$ and a density ratio of 4. The following paragraphs also confirm that domain lengths have been properly chosen for DG mixing layer at $M_c = 2.2$.

The ratio $r = L_\eta/\Delta x$ characterizes the resolution of the simulations: the larger the ratio, the better the resolution. The minimum value is about 0.52 computed for the DG DNS at $M_c = 2.2$. For other simulations, values are larger than 0.6 and the maximum value is 1.64 for PG at $M_c = 2.2$ because of the smaller dissipation found in high compressible regimes. As a comparison, Matsuno & Lele (2020) recently perform a DNS at $M_c = 2.0$ with a L_η/dx ratio equal to 0.41. One can thus consider that turbulent scales are adequately resolved for all simulations presented in this paper since in addition the turbulent kinetic energy is very low close to the Kolmogorov scale (Moin & Mahesh, 1998*a*).

Additional simulations have been performed for the DG mixing layer with $Re_{\delta_{\theta,0}} = 160$ and $M_c = 2.2$ in order to confirm the appropriate choice of domain size and to quantify the influence of initial turbulent structures size. The computational parameters corresponding to these simulations are summarized in Table B.2 along with the parameters used in the previous study at $M_c = 1.1$.

Figure B.1 shows the temporal evolutions of the momentum thickness for the simulations listed in Table B.2. DG1 is performed with the same domain lengths and size of initial turbulent structures (relatively to the initial momentum thickness) as in the previous $M_c = 1.1$ study DG0. At $\tau = 4000$, self-similarity is not yet achieved but flow field visualizations indicate that the y boundaries of the domain are reached. DG2 is then conducted with a domain size doubled in the y direction and with smaller initial turbulent structures corresponding to $L_x/4 = 86\delta_{\theta,0}$, in order to speed up the mixing layer development. Simulations show that the modification of the initial structures size only modifies the time necessary to reach the unstable growth phase but not the growth rate itself.

	M_c	Re_{δ_θ}	Re_{λ_x}	$r = L_\eta/\Delta x$	l_x/L_x	l_z/L_z
Air ($\tau = 700$)	0.1	1879	209	0.63	0.10	0.04
Air ($\tau = 1450$)	0.1	3444	194	0.81	0.11	0.13
FC-70 ($\tau = 550$)	0.1	1448	135	0.58	0.04	0.05
FC-70 ($\tau = 900$)	0.1	2176	201	0.7	0.07	0.06
Air ($\tau = 1700$)	1.1	1874	143	0.97	0.07	0.06
Air ($\tau = 2550$)	1.1	2413	156	1.09	0.12	0.08
FC-70 ($\tau = 1700$)	1.1	2469	176	0.80	0.09	0.05
FC-70 ($\tau = 2550$)	1.1	3304	241	0.87	0.20	0.05
Air ($\tau = 11500$)	2.2	3487	146	1.44	0.12	0.07
Air ($\tau = 14100$)	2.2	3700	191	1.64	0.11	0.10
FC-70 ($\tau = 4000$)	2.2	4663	263	0.52	0.10	0.06
FC-70 ($\tau = 6000$)	2.2	6259	390	0.57	0.16	0.05

Table B.1: Non-dimensional parameters computed at the beginning and at the end of the self-similar period. Re_{λ_x} denotes the Reynolds number based on the longitudinal Taylor microscale $\lambda_x = \sqrt{2\overline{u'^2_x}/\overline{(\partial u'_x/\partial x)^2}}$ computed at the centerline. L_η denotes the Kolmogorov length scale computed at the centerline.

	M_c	$L_x \times L_y \times L_z$	$N_x \times N_y \times N_z$	L_0
DG0	1.1	$344 \times 172 \times 86$	$1024 \times 512 \times 256$	$L_x/48$
DG1	2.2	$344 \times 172 \times 86$	$1024 \times 512 \times 256$	$L_x/48$
DG2	2.2	$344 \times 344 \times 86$	$1024 \times 1024 \times 256$	$L_x/4 = 86$
DG3	2.2	$648 \times 344 \times 172$	$1024 \times 512 \times 256$	$L_x/8 = 86$

Table B.2: Simulation parameters for temporal mixing layer DNS ($Re_{\delta_{\theta,0}} = 160$) with varying domain extent, resolution and size of initial structures. L_x, L_y and L_z denote computational domain lengths measured in terms of initial momentum thickness. N_x, N_y and N_z denote the corresponding numbers of grid points. L_0 denotes the size of initial turbulent structures ($k_0 = 2\pi/L_0$) measured in terms of initial momentum thickness. All grids are uniform.

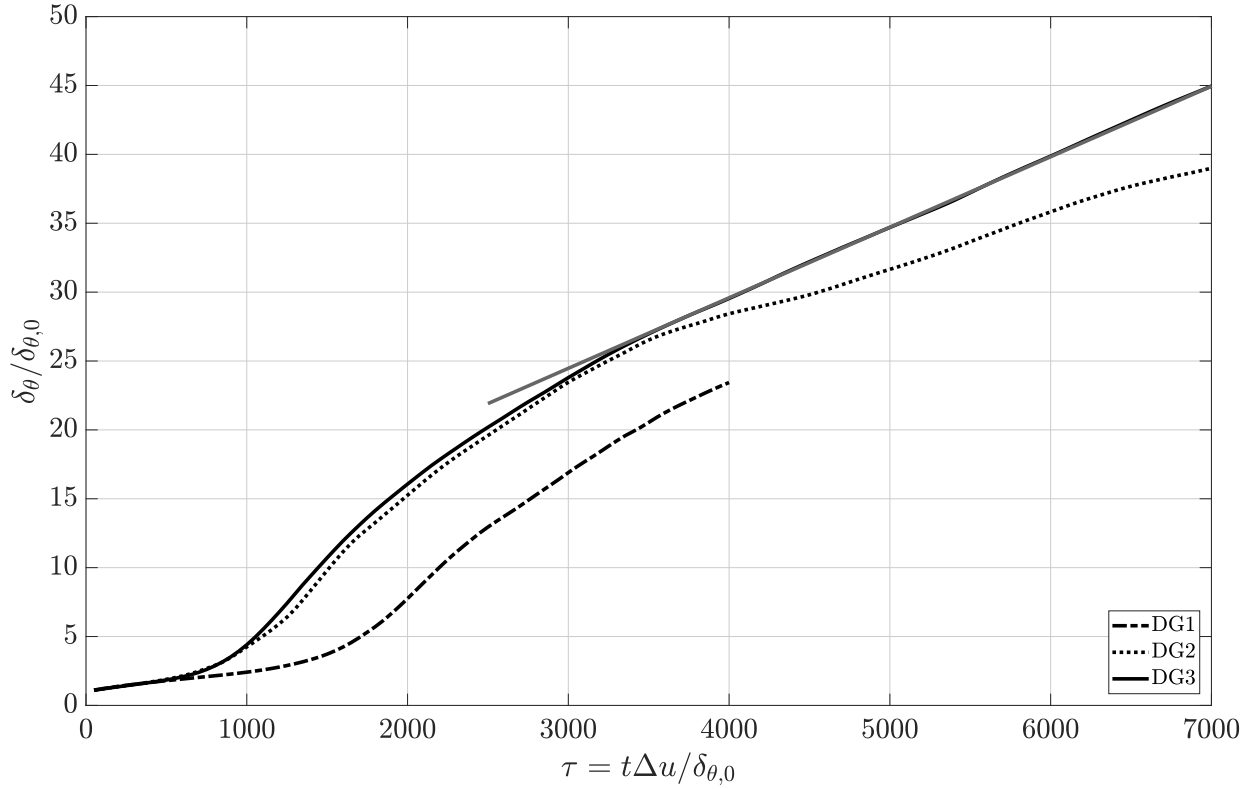

Figure B.1: Temporal evolution of the mixing layer momentum thickness.

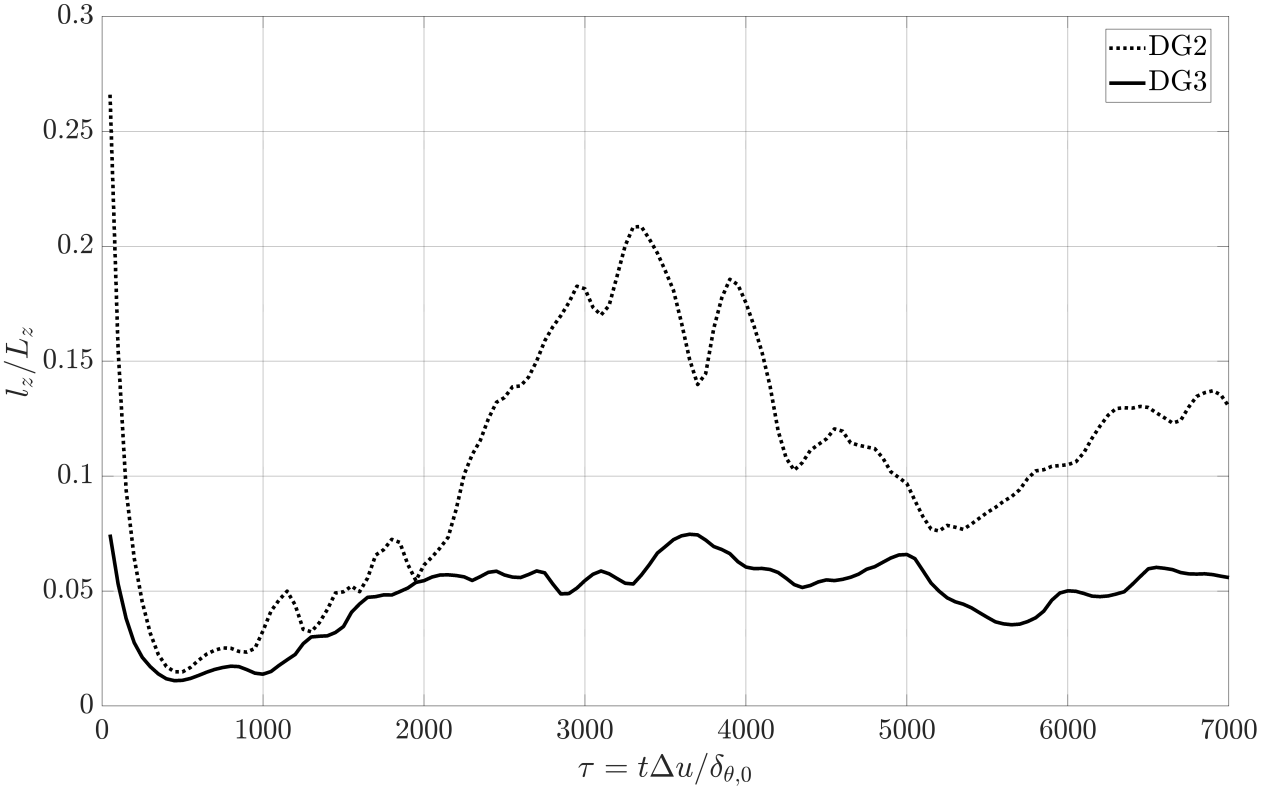

Figure B.2: Temporal evolution of the integral length scale l_z.

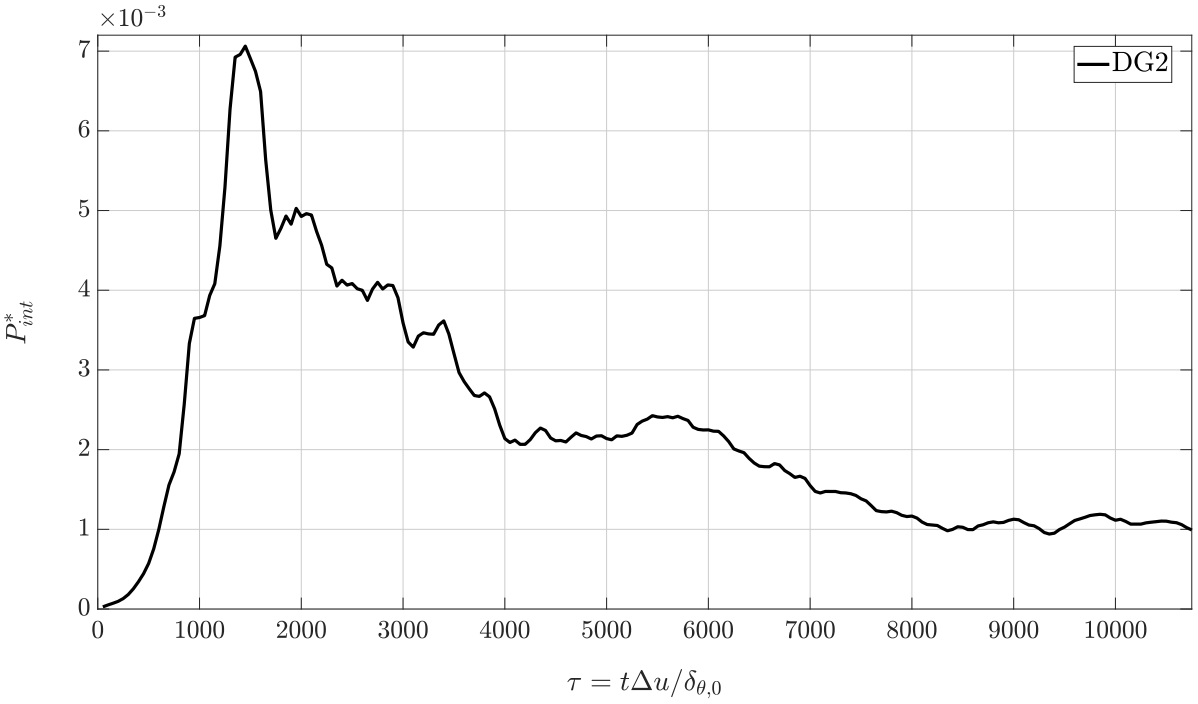

Figure B.3: Temporal evolution of the non-dimensional streamwise turbulent production term integrated over the whole domain $P^*_{int} = (1/(\rho_0(\Delta u)^3)) \int_{L_y} \bar{\rho} P_{xx} dV$ (with $\bar{\rho} P_{xx}(y) = -\overline{\rho u''_x u''_y} \frac{\partial \tilde{u}_x}{\partial y}$) for the DG2 simulation.

Yet, a large decrease of the growth rate is observed for DG2 around $\tau = 4000$: self-similarity cannot be reached. Figure B.2 displays the time evolution of the integral length scale in the z direction l_z for DG2 and DG3 simulations. Around $\tau = 4000$, the integral length scales l_z/L_z suddenly decreases for DG2 after having reached a value of 0.2. The domain is thus not large enough to account for spanwise turbulent structures, which causes a growth rate decrease and prevents the transition to self-similarity.

Figure B.3 displays the temporal evolution of the turbulent production for the DG2 simulation. The evolution follows a piecewise decrease, reaching two distinct plateaus. It is observed that the transition from the first plateau to the second one is related to integral lengths scales. When some turbulent structures grow and become too large for the computational domain, the integrated turbulent production decreases and reaches another plateau lower than the previous one. The mixing layer therefore adapts its growth to domain lengths when the computational box is not large enough. Since the integrated turbulent production is related to the mixing layer growth rate, a lower plateau leads to a smaller mixing layer growth rate.

Because of the aforementioned observations, domain sizes have been doubled in the x and z directions with respect to DG1. This choice corresponds to the DG3 simulation, which is the reference DNS used in Chapter 4 to compare results between DG and PG. For DG3, the momentum thickness evolution reaches a perfectly linear stage and self-similarity is well achieved as confirmed in Figures B.1 and 4.17.

Appendix C

Filter influence

The *a priori* analysis conducted in Chapter 5 requires to filter mixing layers and HIT DNS. The present appendix is dedicated to the study of the filtering effect on the mixing layer DNS at $M_c = 1.1$. Results are first compared between three types of filters given in Table 2.3. Then the influence of the filtering selectivity for the Gaussian filter is analyzed.

Comparison between the Gaussian, top-hat (or box) and sharp (or spectral cut-off) filters

This section proposes to compare the results obtained using the top-hat and the sharp filters with the ones gathered with the Gaussian filter preferred in Chapter 5. Figure C.1 displays a comparison of resolved and SGS terms in the filtered momentum equation for the three types of filters in the case of the mixing layer at $M_c = 1.1$. For the first two plots, the filter type only significantly influences the activity of resolved and SGS terms for large scales below $k/k_{min} = 8$. However, most of the inertial zone ($k/k_{min} \in [6; 20]$) is only marginally affected by the filter. Since in the present work the analysis about the relative importance of the terms in the filtered equations has been conducted over the inertial zone (see Section 5.2), its conclusions can be considered as independent from the filter type.

Results for the sharp filter are very different. Since this filter is not local in space, it produces inconsistent results generating strong anisotropy and over-prediction of SGS terms at small scales. This filter type is therefore almost never used in the literature unlike the two others.

Conclusions are the same for resolved and SGS terms in the filtered energy equation (Figure C.2). Results are identical in the inertial zone for Gaussian and top-hat filters unlike the sharp filter which yields inconsistencies. The analysis performed in Section 5.2 is thus independent from the filter type for both filtered momentum and energy equations.

Effect of filtering selectivity

According to the expression given in Table 2.3, the parameter ζ controls the selectivity of the Gaussian filter. Decreasing ζ diminishes the selectivity in the physical space and increases it in the spectral space. The smaller the value of ζ, the slower the SGS terms drop to zero. A low value of ζ will indeed strongly filter the energy at small scales and will thus induce a significant difference between resolved and SGS terms.

As an illustration, Figure C.3 displays a comparison of resolved and SGS terms in the

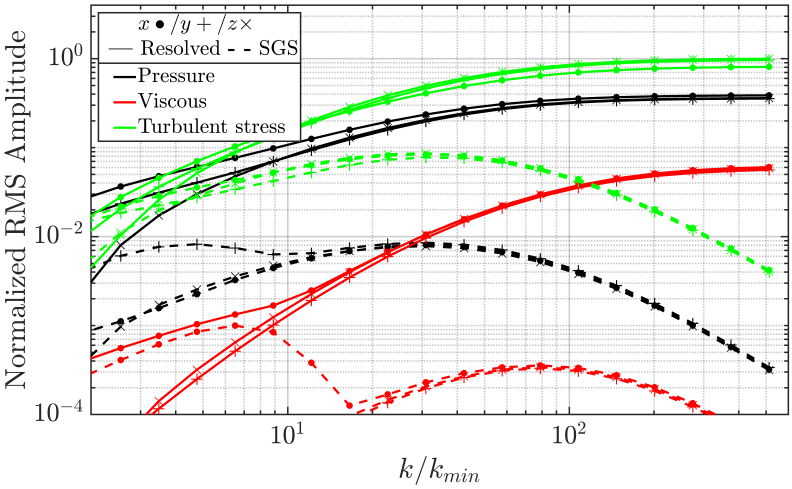

Gaussian filter ($\zeta = 6$)

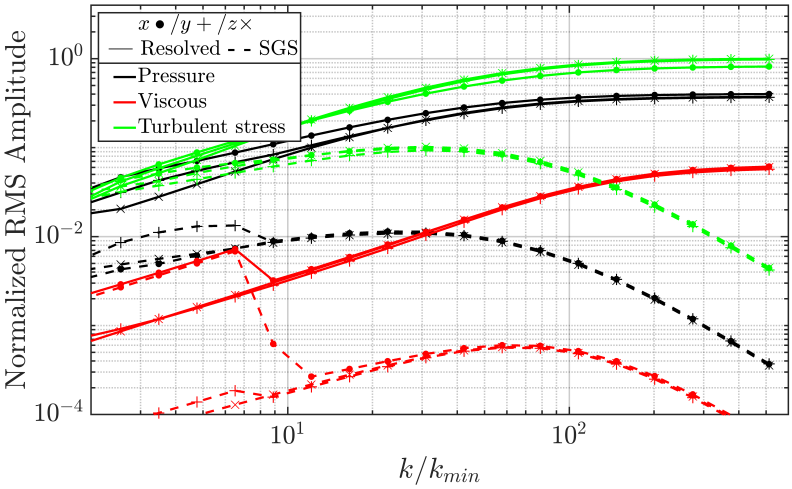

Top-hat filter

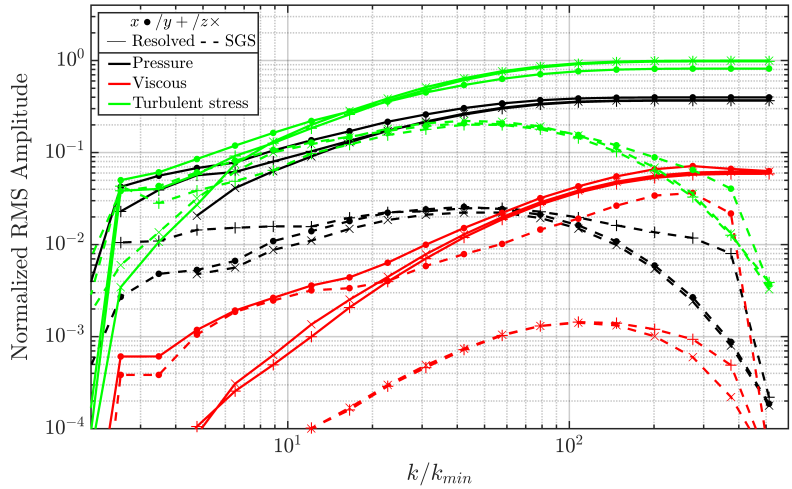

Sharp filter

Figure C.1: RMS amplitude of terms in the real gas filtered momentum equation (Equation (2.48)) for the DG mixing layer at $M_c = 1.1$. Results are given at the initial time of each self-similar period for the three filter types (Gaussian, top-hat and sharp filters).

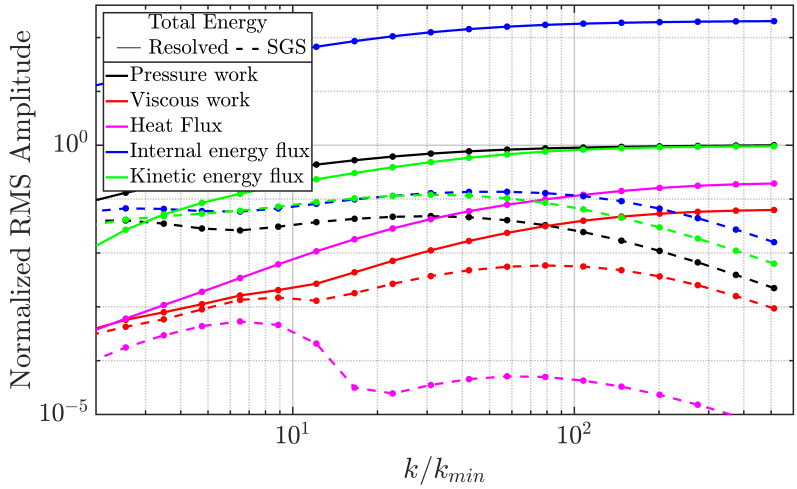

Gaussian filter ($\zeta = 6$)

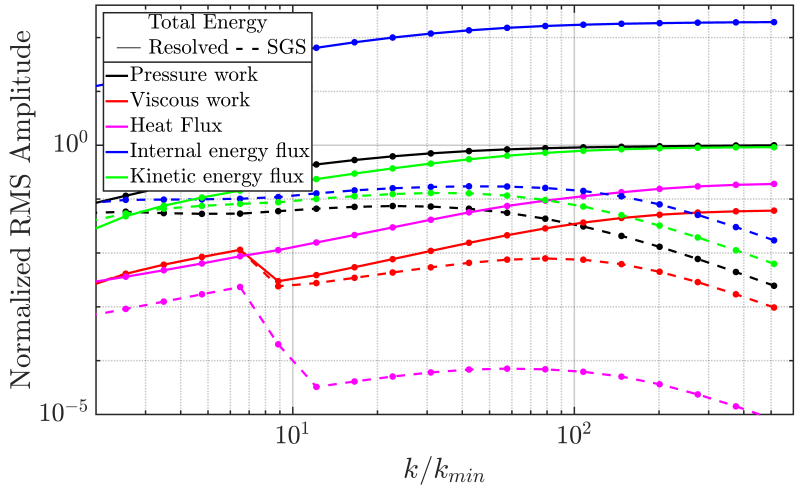

Top-hat filter

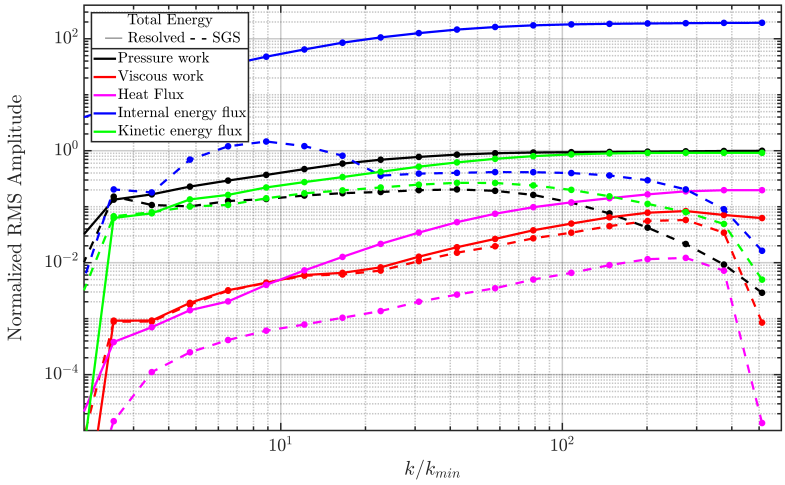

Sharp filter

Figure C.2: RMS amplitude of terms in the filtered energy equation (Equation (2.48)) for the DG mixing layer at $M_c = 1.1$. Results are given at the initial time of each self-similar period for the three filter types (Gaussian, top-hat and sharp filters).

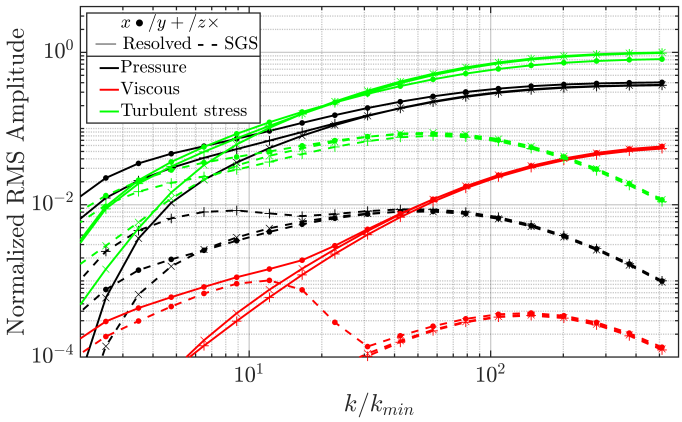

$\zeta = 2$

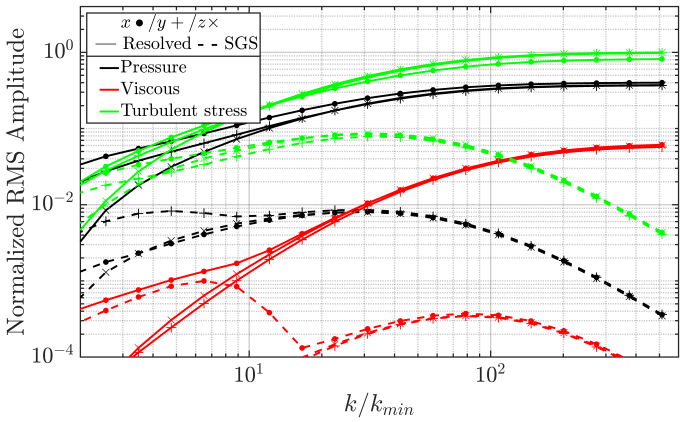

$\zeta = 6$

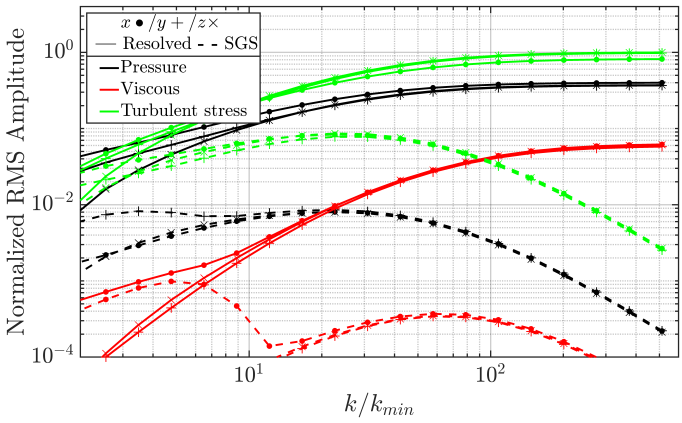

$\zeta = 10$

Figure C.3: RMS amplitude of terms in the real gas filtered momentum equation (Equation (2.48)) for the DG mixing layer at $M_c = 1.1$. Results are given at the initial time of each self-similar period for three different filter parameters $\zeta = 2 - 6 - 10$ (top-middle-bottom).

filtered momentum equation for three different values of $\zeta = 2 - 6 - 10$ when filtering the DNS results of the mixing layer at $M_c = 1.1$. As expected, SGS terms drop to zero much faster when the parameter ζ increases. Results are very similar for the three values of the filter selectivity, with differences appearing only at small scales. The inertial zone ($k/k_{min} \in [6; 20]$) is only marginally affected by the filter. Since the analysis about the relative importance of the terms in the filtered equations has been conducted over the inertial zone (see Section 5.2), it can therefore be considered as independent from the filtering selectivity. As recommended in Garnier *et al.* (2009), the parameter ζ is set to 6 in the analysis conducted in Chapter 5.

Appendix **D**

A priori analysis of PG mixing layers

In compressible flows, since the energy conservation equation is involved, numerous SGS terms exist. SGS models are often associated to the SGS turbulent stress tensor only. However, in the formulation of the filtered compressible Navier-Stokes equations, several SGS terms are present both in the filtered momentum equation and in the filtered energy equation, even for the PG formulation. As noticed in Section 5.1, very few *a priori* analyses have been performed to evaluate both SGS momentum and energy terms in that context. This appendix is therefore devoted to the assessment of the importance of SGS terms corresponding to the PG filtered LES formulation given in Equation (2.54).

Filtered momentum equation

The filtered momentum equation comprises three SGS terms related to pressure, viscous and convective terms. Yet, the SGS turbulent stress tensor has been the center of attention in the LES community whereas the two other terms are neglected. The SGS turbulent stress tensor can be decomposed into an isotropic part t_{ij}^I and a deviatoric part t_{ij}^D (see Equation (2.55)). Both parts are modeled together in gradient type models (Clark *et al.*, 1979) whereas the isotropic part is neglected in all eddy-viscosity models based on the Boussinesq hypothesis even though Yoshizawa (1986) proposes a model specific for this term[†]. This assumption is based on Erlebacher *et al.* (1992)'s recommendations. They express the isotropic part as:

$$t_{ij}^I = \frac{2}{3} k_{\mathrm{SGS}} \delta_{ij} = \frac{2}{3} \gamma M_{\mathrm{SGS}}^2 \bar{p} \delta_{ij} \tag{D.1}$$

where $M_{\mathrm{SGS}} = \sqrt{k_{\mathrm{SGS}}/(\gamma R \widetilde{T})}$ is the SGS Mach number. Note that this Mach number strongly depends on the filtering size. If $M_{\mathrm{SGS}} < 0.4$, Erlebacher *et al.* (1992) consider the isotropic part as being negligible[‡]. They perform several HIT DNS up to $M_t = 0.4$ and show that:

$$\frac{\left(\nabla . t_{ij}^I\right)_{\mathrm{RMS}}}{\left(\nabla p\right)_{\mathrm{RMS}}} < 3.10^{-3} \tag{D.2}$$

They compare here a SGS term (the isotropic part of the SGS turbulent stress tensor) with a resolved term (the pressure gradient). Yet, Vreman *et al.* (1995) consider that all SGS terms

[†]Speziale *et al.* (1988) show that Yoshizawa (1986)'s model poorly correlates (about 15%) with the exact isotropic part of the SGS turbulent stress tensor.

[‡]If $M_{\mathrm{SGS}} < 0.4$, for air with $\gamma = 1.4$, the isotropic part of the SGS turbulent stress tensor represents less than 15% of the pressure for air.

that are larger than the smallest resolved term should be kept in the LES description of the flow. In that case, since the smallest resolved term is more likely to be the viscous term and not the pressure gradient, Erlebacher *et al.* (1992)'s comparison does not allow to conclude about the inclusion of the isotropic part into the PG LES modeling.

The modeling issue of the isotropic part of SGS turbulent stress tensor is in fact very close to the one of the SGS pressure since both are linked as:

$$(\bar{p} - \widehat{p}) = -\frac{(\gamma - 1)}{2} t_{ii} \tag{D.3}$$

The filtered Navier-Stokes equations (Equation (2.54)) for PG flows can be transformed as:

$$\frac{\partial \bar{\rho}\widetilde{u}_i}{\partial t} + \frac{\partial \bar{\rho}\widetilde{u}_i\widetilde{u}_j}{\partial x_j} = -\frac{\partial \widehat{p}}{\partial x_i} + \frac{\partial \widehat{\tau}_{ij}}{\partial x_j} + \left(\frac{(\gamma - 1)}{2} - \frac{1}{3}\right)\frac{\partial t_{ii}}{\partial x_i} + \frac{\partial \left[\bar{\tau}_{ij} - \widehat{\tau}_{ij}\right]}{\partial x_j} - \frac{\partial t_{ij}^D}{\partial x_j} \tag{D.4}$$

$$\tag{D.5}$$

The effects of the SGS pressure and of the isotropic part of the SGS turbulent stress tensor compensate. In case of a PG flow, the ratio $\left(\frac{(\gamma-1)}{2} - \frac{1}{3}\right)$ is about -0.13. This rearranged term loses one order of magnitude when compared to the deviatoric part of the SGS turbulent stress tensor.

The assessment of the importance of SGS terms appearing in Equation (2.48) is displayed in Figure D.1 for mixing layers DNS at $M_c = 0.1$, $M_c = 1.1$ and $M_c = 2.2$. Amplitudes are normalized with the resolved turbulent stress. For the three cases, the SGS pressure term is of the same order of magnitude as the SGS turbulent stress term and its magnitude is superior to the SGS viscous term in the inertial zone ($k/k_{\min} \in [6; 20]$) (see Figure 4.22). Results are consistent with Okong'o & Bellan (2004)'s results which exhibit a ratio of approximately three in each direction between SGS pressure and SGS turbulent stress tensor terms for their PG single phase flow mixing layer DNS at $M_c = 0.35$.

Moreover, Xie *et al.* (2018) show that for a given filtering size, the ratio between the SGS kinetic energy and the total kinetic energy is weakly dependent on the turbulent Mach number. It is therefore consistent to observe that the normalized amplitude of the SGS pressure, which is related to the SGS kinetic energy, is almost independent from the convective Mach number. Following Vreman *et al.* (1995)'s principles, the SGS pressure term should be taken into account even in PG flows. Note that for an incompressible formulation, this term does not appear in the filtered LES equations.

Filtered energy equation

Five SGS terms appear in the filtered energy equation related respectively to the pressure work, the viscous work, the heat flux, the internal energy flux and the kinetic energy flux (see Table 2.4). The last two SGS terms are usually the only ones modeled in the PG LES formulation. Note that the SGS heat flux and the SGS internal energy are distinguished. The SGS heat flux term refers here to the Fourier heat flux. The SGS internal energy is often named SGS heat flux because of its link with the temperature, which is valid in the PG case only.

Figure D.1 displays the results for the three mixing layers ($M_c = 0.1 - 1.1 - 2.2$). Amplitudes are normalized with the pressure work. For the three convective Mach numbers, the pressure work, which is usually neglected, is of the same order of magnitude as SGS kinetic energy and SGS internal energy fluxes and superior to the resolved viscous work in the inertial zone

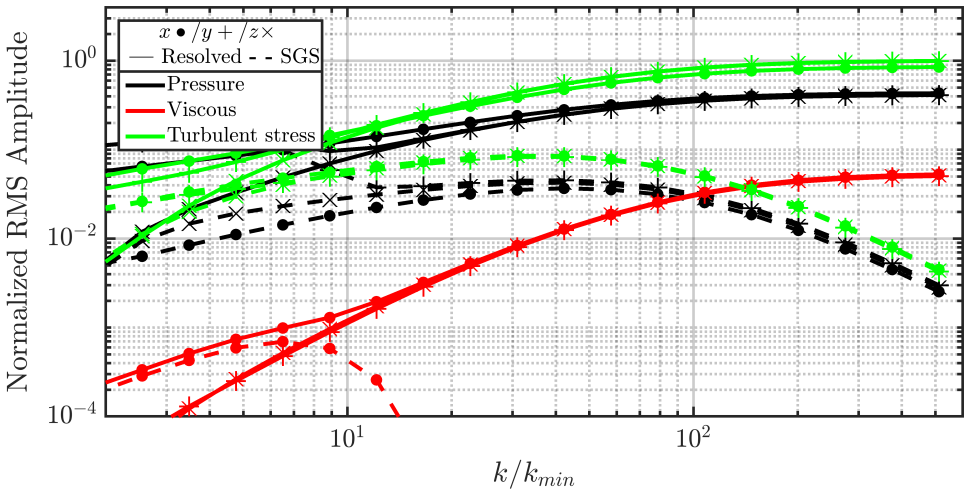

$M_c = 0.1$

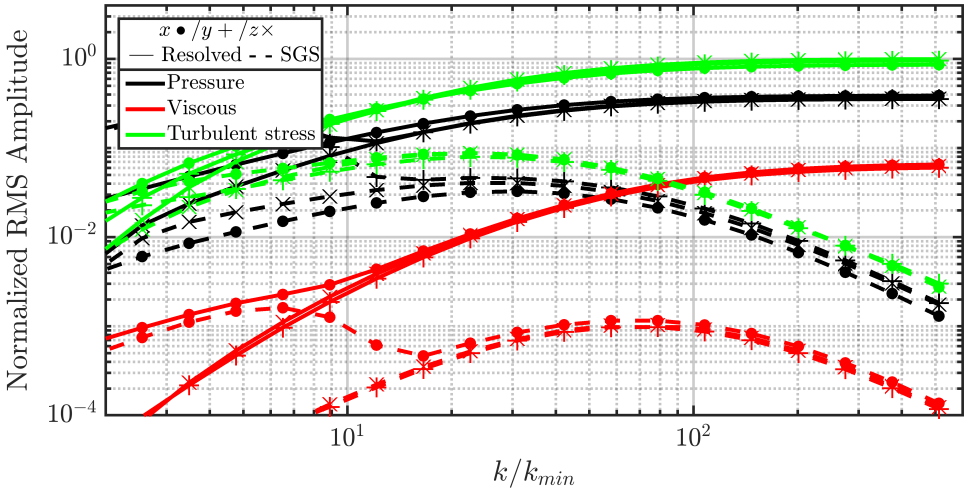

$M_c = 1.1$

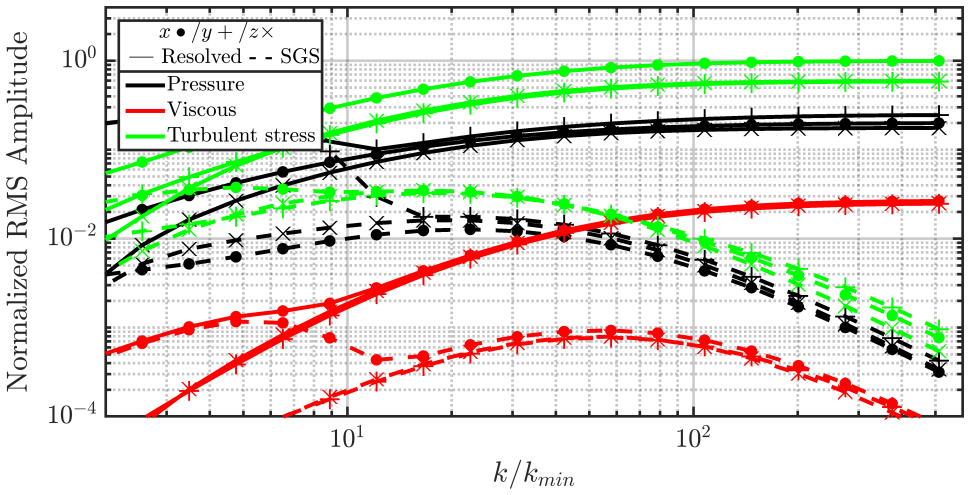

$M_c = 2.2$

Figure D.1: RMS amplitude of terms in the filtered momentum equations (Equations (2.48)) for the perfect gas mixing layer at $M_c = 0.1 - 1.1 - 2.2$ (top-middle-bottom). Results are averaged over the domain and over the self-similar period growth phase of the mixing layer. The turbulent Mach numbers averaged over the centerplane are respectively equal to $0.05 - 0.4 - 0.5$. The SGS viscous terms is very small and does not appear on the plot for $M_c = 1.1$ and $M_c = 2.2$.

($k/k_{\min} \in [6; 20]$). Following Vreman *et al.* (1995)'s principles, the SGS pressure work should be taken into account even in PG flows. The amplitudes of other SGS heat work and viscous work terms are smaller than the smallest resolved term and can therefore be neglected.

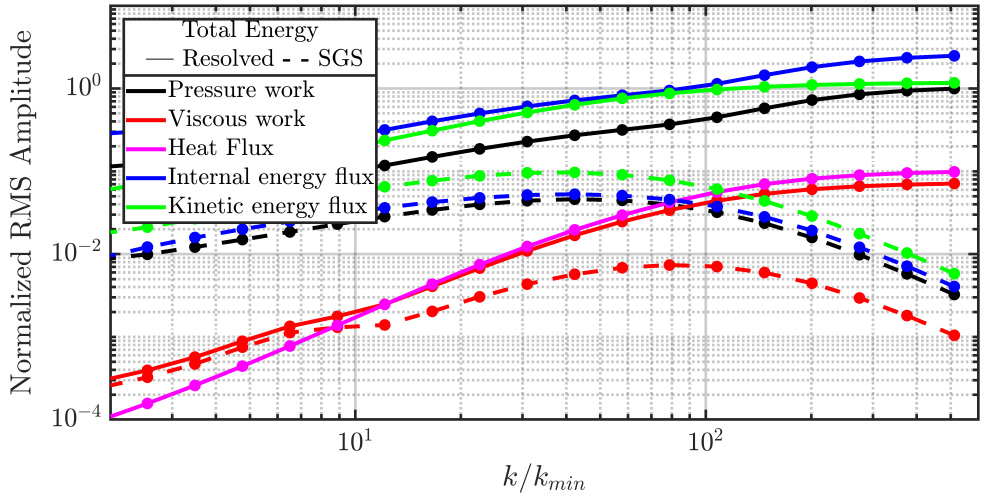

$M_c = 0.1$

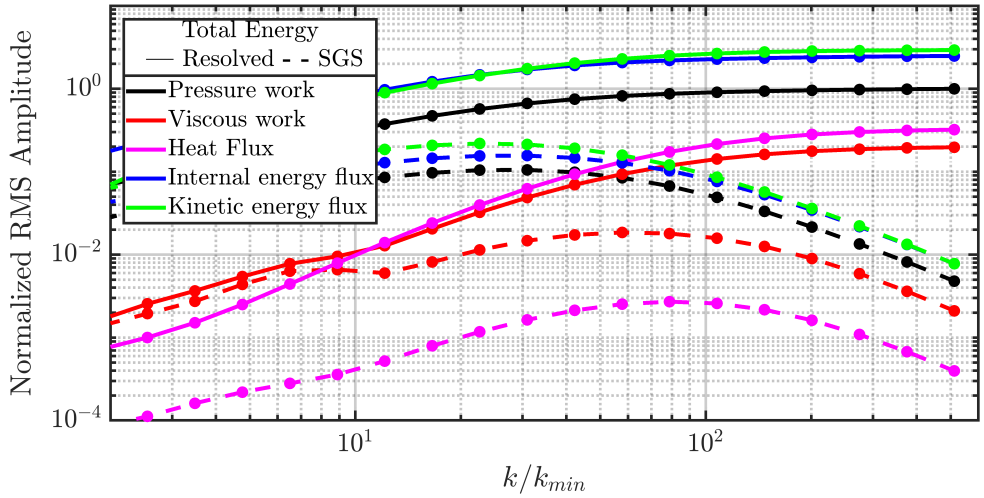

$M_c = 1.1$

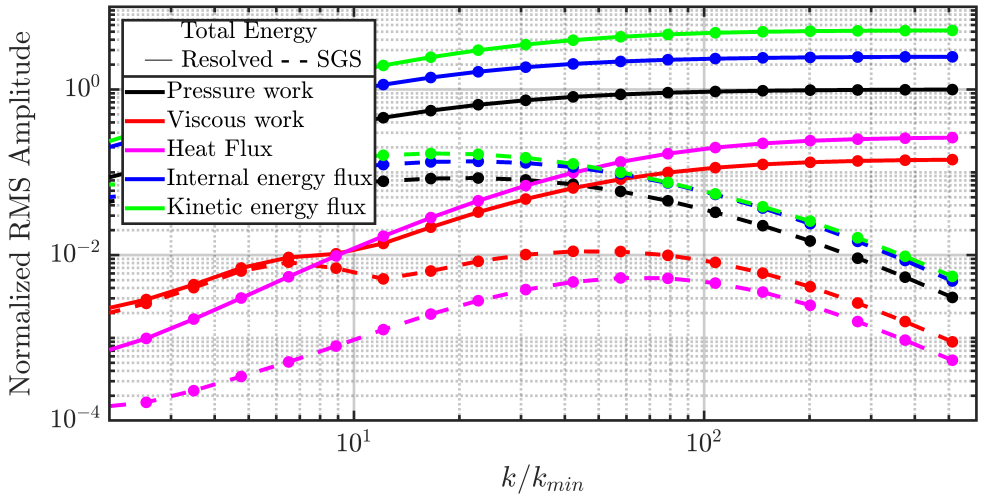

s

$M_c = 2.2$

Figure D.2: RMS amplitude of terms in the filtered total energy equation (Equation (2.48)) for the perfect gas mixing layer at $M_c = 0.1 - 1.1 - 2.2$ (top-middle-bottom). Results are averaged over the domain and over the self-similar period growth phase of the mixing layer. The turbulent Mach numbers averaged over the centerplane are respectively equal to $0.05 - 0.38 - 0.67$.

Appendix E

Principal Component Analysis (PCA)

The principal component analysis (PCA) consists in a transformation of a set of variables into an uncorrelated set of principal components also named modes (Jolliffe, 2005). The method can be reduced to a problem of matrix diagonalization. The aim is to find new axes, using linear combinations of inputs, such that the variance of point clouds around these axes is maximal. Eigenvalues can be seen as energy coefficients. The PCA aims at evaluating the redundant information among variables and can therefore be used to reduce the number of inputs before the ANN training. By reducing this number of variables, the PCA enables to represent data with a minimum number of directions.

The first PCA are separately performed over the three different cases. Figure E.1 displays the cumulative variance rates for each PCA mode. It symbolizes the cumulative amount of energy present in the modes. For the three cases, the first PCA mode contains more than 40% of the information contained in the 15 inputs. This rate increases to approximately 70% selecting the first two modes. In order to keep 95% of the information, one needs to select at least the first five PCA modes for the mixing layers and the first six modes for the HIT. The three PCA show here the redundancy of the 15 inputs which could be simplified into approximately five variables. The complexity of the problem, which is related to the number of modes required to represent the data, tends to increase with the compressibility effects, likely because the variance of physical variables usually increases which the turbulent Mach number.

Figures E.2 and E.3 respectively investigate the composition of the first two modes representing more than 70% of the information, that is the contribution of the input variables to these 2 dominant modes. Since PCA modes are constructed from a linear combination of input variables, the contribution values given in Figures E.2 and E.3 corresponds to the coefficients associated to each input variable for respectively the mode 1 and the mode 2. For the first mode, the three plots corresponding to the forced HIT and the mixing layers are very close. The contribution of the thermodynamic variables ($\bar{\rho}$, T, $\widehat{p}$, $\bar{\rho}\widetilde{E}$) and their Laplacians is identical between the three cases and between the variables. The contribution of the gradients is not the same for the 3 configurations. The mixing layer at $M_c = 1.1$ is very different from the one at $M_c = 2.2$ and the forced HIT. It is surprising to notice that the projection of the mixing layer at $M_c = 2.2$ is closer to the forced HIT than the mixing layer at $M_c = 1.1$. It is likely that the representation of modes is also related to the compressibility of the flow. Turbulent Mach numbers are indeed closer between the mixing layer at $M_c = 2.2$ ($M_t = 0.67$) and the forced HIT ($M_t = 0.8$) than with the mixing layer at $M_c = 1.1$ ($M_t = 0.38$).

Looking at the second mode shows in particular a contribution of input variables to this mode which changes significantly from one configuration to another, while this contribution was quite similar for the 3 configurations when analyzing mode 1. The practical consequence

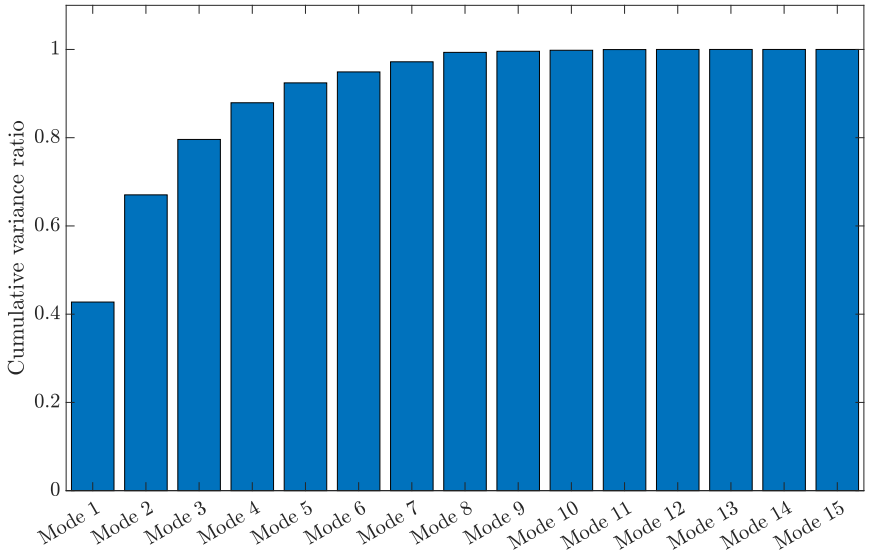

Forced HIT

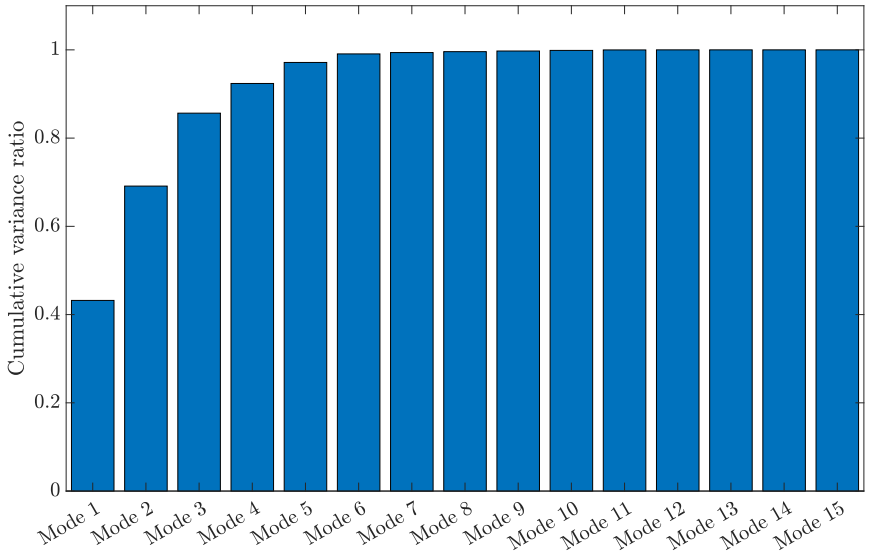

$M_c = 1.1$

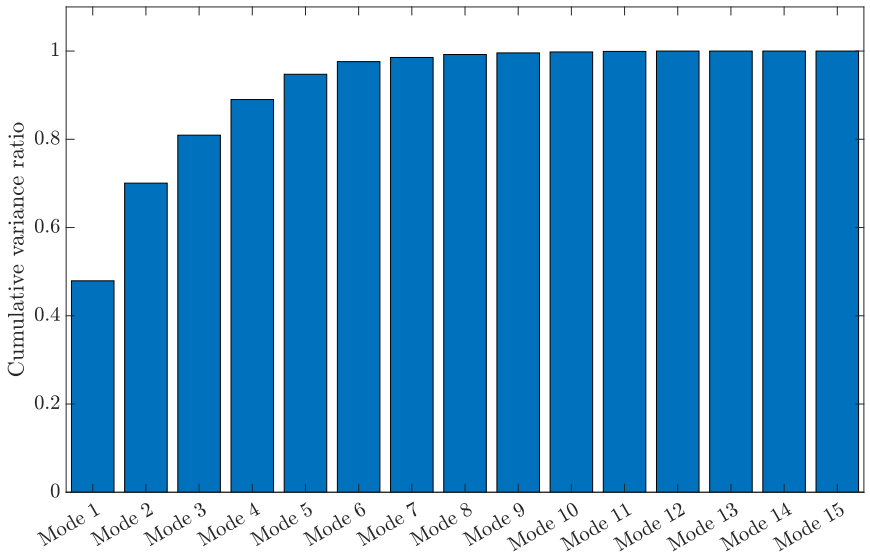

$M_c = 2.2$

Figure E.1: Cumulative variance rates are plotted for each PCA mode for the forced HIT (top) and for the mixing layers at $M_c = 1.1$ (middle) and at $M_c = 2.2$ (bottom).

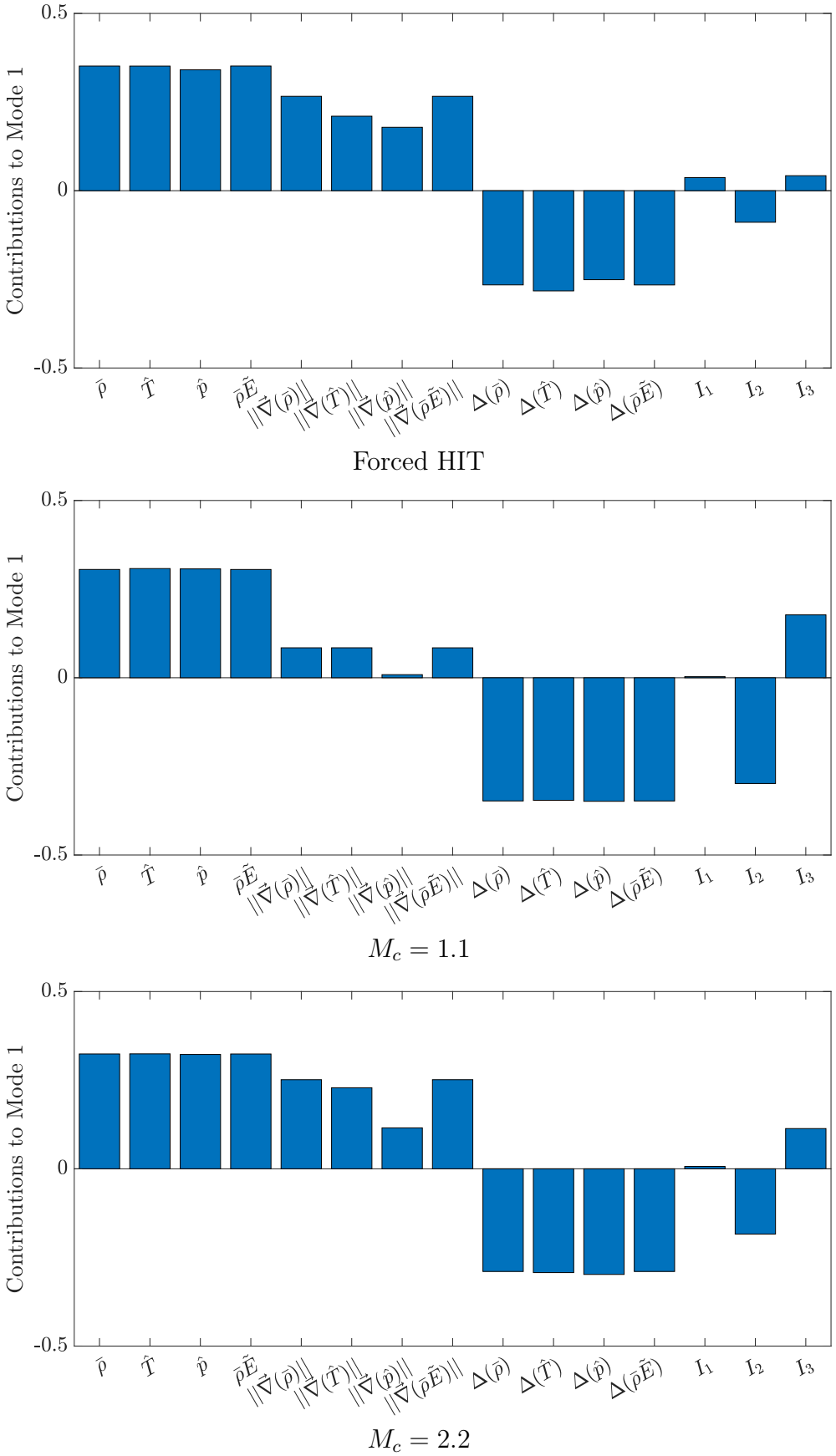

Figure E.2: Projection of mode 1 in the inputs space for the forced HIT (top) and for the mixing layers at $M_c = 1.1$ (middle) and at $M_c = 2.2$ (bottom). The mode 1 represents more than 40% of the information.

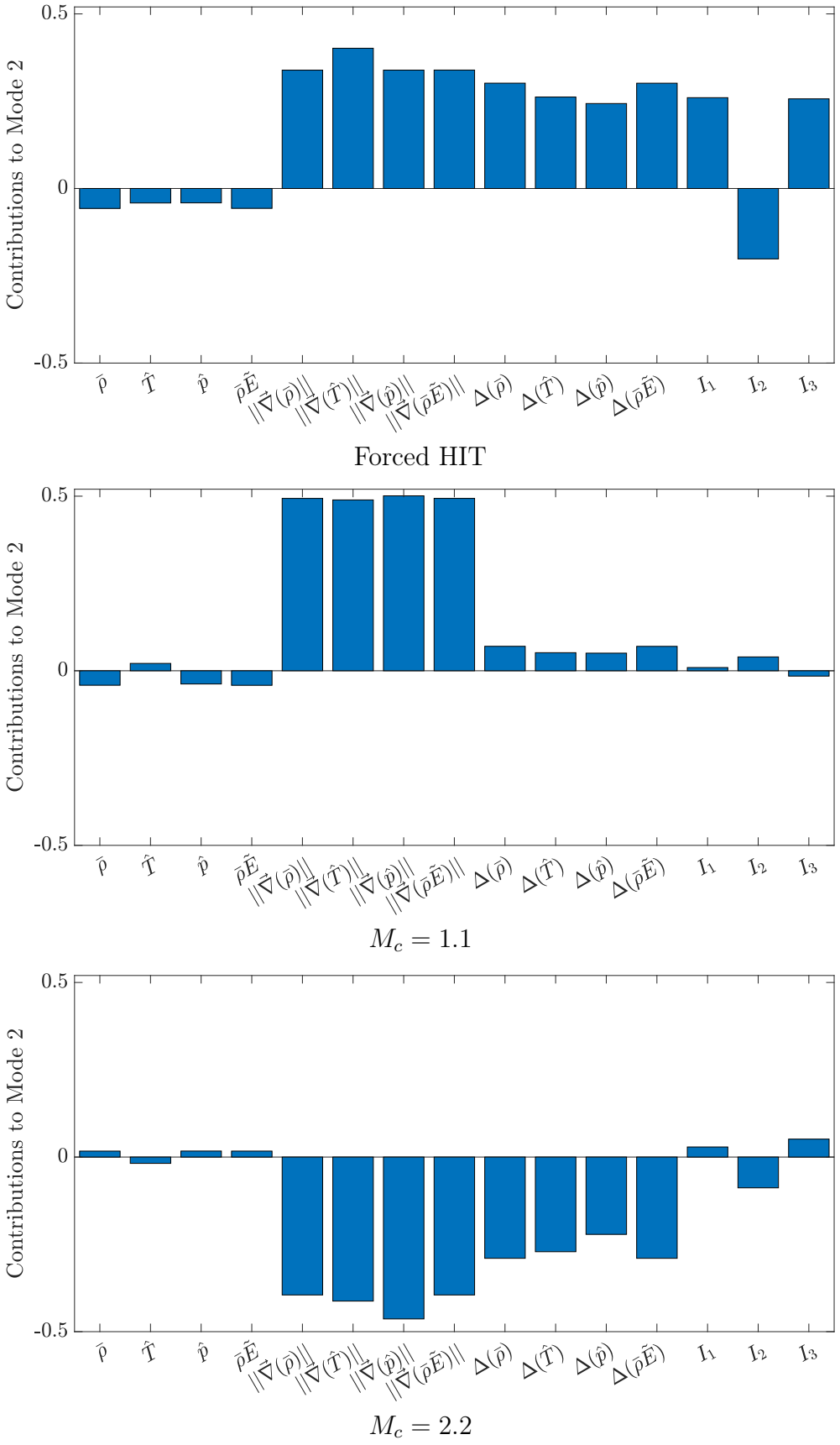

Figure E.3: Projection of mode 2 in the inputs space for the forced HIT (top) and for the mixing layers at $M_c = 1.1$ (middle) and at $M_c = 2.2$ (bottom). The mode 2 represents more than 22% of the information.

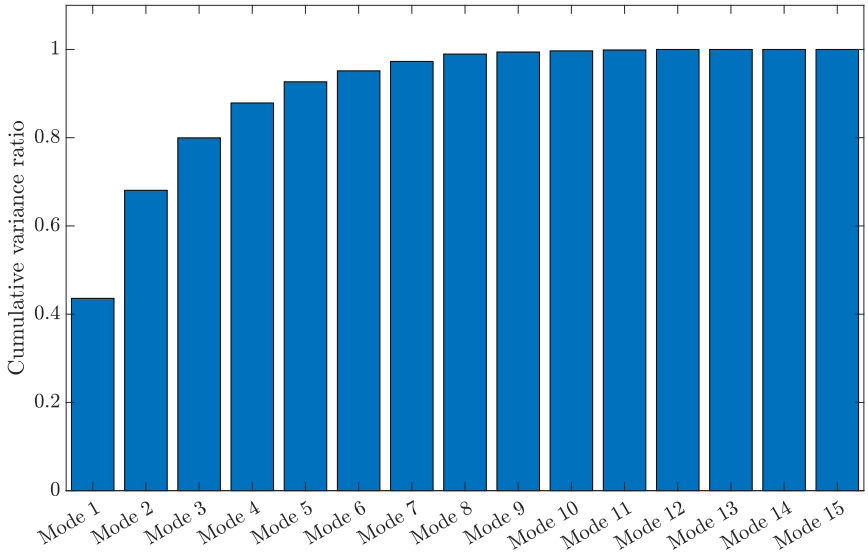

Figure E.4: Cumulative variance rates are plotted for each mode for the PCA performed simultaneously over the forced HIT and the mixing layers at $M_c = 1.1$ and at $M_c = 2.2$.

of this observation is that it would be probably more useful to perform a PCA for the dataset gathering simultaneously the forced HIT and the mixing layers at $M_c = 1.1$ and at $M_c = 2.2$. Indeed, the expected contribution of the PCA is a unique simplification or reduction of the set of input variables and not a simplified set which would be specific to a given flow configuration.

The results obtained for this "global" PCA are first displayed in Figure E.4, with the cumulative variance rates for each mode. Similarly to the three previous PCA performed separately for each flow configuration, the first mode represents more than 40% of the information and one needs to select at least six modes to represent 95% of the information. The decomposition of the first two modes of this "global" PCA (see Figure E.5) is found to be very close to the decomposition of the first two modes for the PCA applied to the forced HIT only (see respectively the top plot of Figure E.2 for the first mode and the top plot of Figure E.3 for the second mode). This comparison shows the strong influence of the HIT configuration with respect to the mixing layer configurations, which could be due to the larger number of elements in the HIT database: about $307M$ against $134M$ for each mixing layer (see Table 6.1).

Even though it remains difficult to relate the projection over the mathematical PCA modes to a precise physical understanding of the flow features, PCA modes can be used to visualize the data. Figure E.6 shows the projection of the data onto the first two modes space containing more than 70% of the information. Both mixing layers point clouds are included in the forced HIT one. As compressiblity effects increase, the point clouds spread in the (Mode 1,Mode 2) space. PDF are also displayed for both modes along axis. Consistently with the PDF of the SGS pressure (see Figure 6.5), distributions are wider for the HIT. **The overlapping of the databases could lead to think that using only the forced HIT is enough to train the ANN. Note however that modes** 1 **and** 2 **are actually not the same for each configuration so this would be a misinterpretation.** Generalization tests performed in Section 6.4.2 actually show the necessity to add the mixing layers to the database exploited by the ANN training process.

Following the present analysis, and even though it was observed from Figure E.4 that about 6 modes only could be selected to represent significant inputs to the model (instead of the

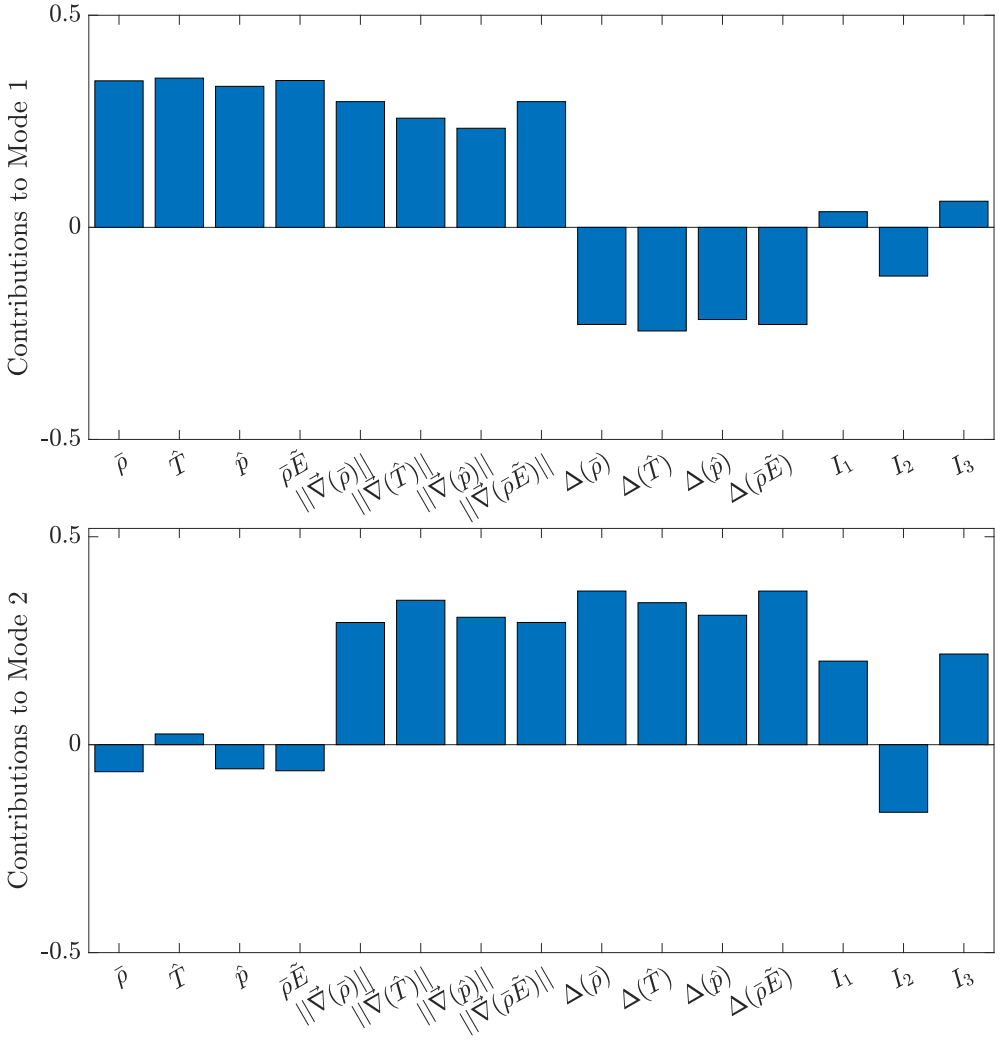

Figure E.5: Projection of modes 1 (top) and 2 (bottom) in the inputs space for the PCA performed simultaneously over the forced HIT and the mixing layers at $M_c = 1.1$ and at $M_c = 2.2$. The mode 1 and 2 represents respectively about 44% and 25% of the information.

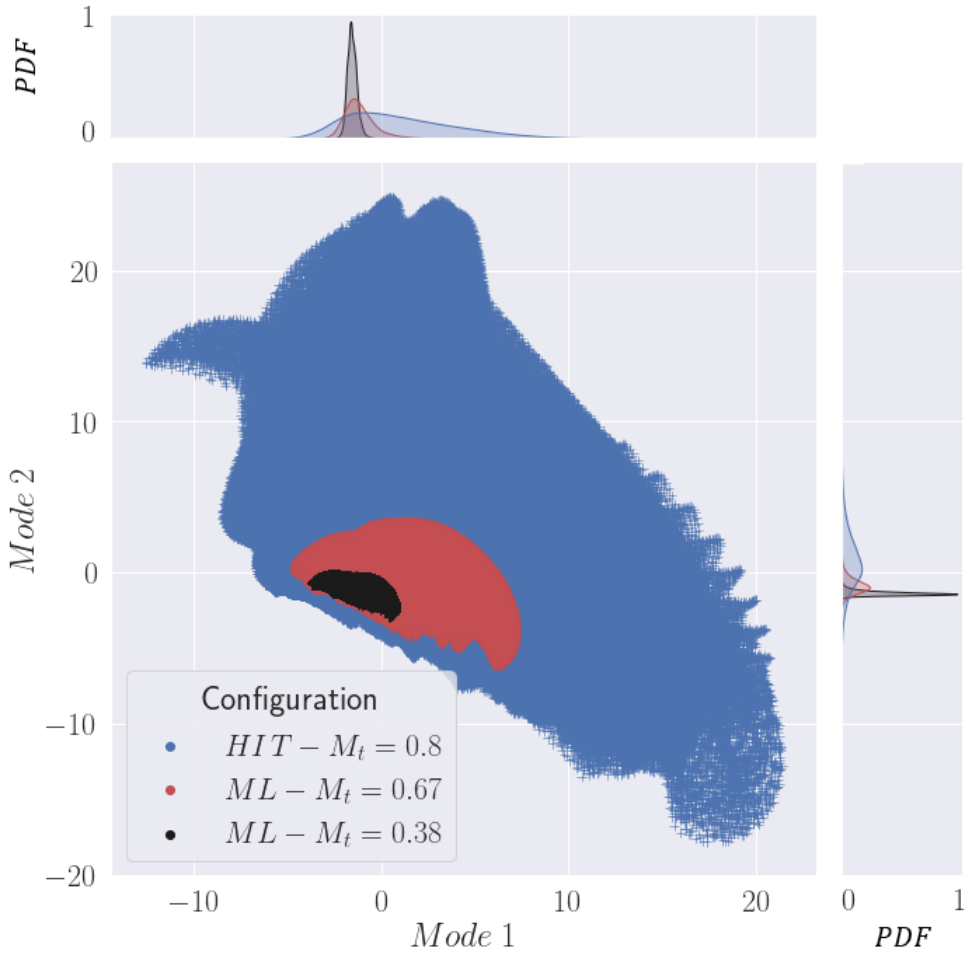

Figure E.6: (Top) Projection of the data for the forced HIT and the mixing layers into the first two PCA modes containing more than 70% of the information. The normalized PDF is also given for each mode along axis.

initial set of 15 variables), it was eventually decided to stick with the initial set of 15 variables. The motivation for this choice was to consider that accelerating the training of the ANN with a reduced set of modes had however to be paid in the *a posteriori* application of the model since the mathematical PCA modes must be reconstructed from the available physical variables each time the model is applied. This might prove expensive and also make the physical interpretation of the model even more delicate.

Appendix F

HSIC validation

As mentioned in Section 6.3.2, when applied to hyperparameters grid search results, Hilbert-Schmidt Independence Criterion (HSIC) coefficients are used to measure the independence between two probability distributions: the probability distribution of hyperparameters among arms randomly selected by the hyperparameters search method and the probability distribution of hyperparameters among the best decile ANN (the 10% of the best ANN) (Novello *et al.*, 2021).

The problem of hyperparameters optimization consists in finding the best combination of n hyperparameters among the n_s tested combinations to get the most effective ANN f such that:

$$f(\boldsymbol{X_1}, ..., \boldsymbol{X_n}) = \boldsymbol{Y} \tag{F.1}$$

where $\boldsymbol{X_i} = \begin{pmatrix} x_{i,1} \\ ... \\ x_{i,n_s} \end{pmatrix}$ denotes the i^{th} hyperparameter vector and $\boldsymbol{Y} = \begin{pmatrix} y_1 \\ ... \\ y_{n_s} \end{pmatrix}$ is the output vector containing the score or the error of the tested ANN. The sub-vector of $\boldsymbol{Y}$ containing the best decile is denoted $\boldsymbol{Y_{10\%}}$. A new random variable $\boldsymbol{Z} = \begin{pmatrix} z_1 \\ ... \\ z_{n_s} \end{pmatrix} = \mathbb{1}_{y_j \in \boldsymbol{Y_{10\%}}}$, which is equal to unity when the ANN is among the best decile and zero otherwise, is introduced. $S(\boldsymbol{X_i}, \boldsymbol{Y_{10\%}})$ is a measure of the distance between the distribution of X_i and the distribution of X_i conditioned to $\boldsymbol{Z} = \boldsymbol{1}$, denoted $(\boldsymbol{X_i}|(\boldsymbol{Z} = \boldsymbol{1}))$:

$$\begin{aligned} S(\boldsymbol{X_i}, \boldsymbol{Y_{10\%}}) \;=\; & (P(\boldsymbol{Z} = \boldsymbol{1}))^2 \left[\frac{1}{m^2} \sum_{j=1}^{n_s} \sum_{l=1}^{n_s} k(x_{i,j}, x_{i,l}) \delta(z_j = 1) \delta(z_l = 1) \right. \\ & \left. + \frac{1}{n_s^2} \sum_{j=1}^{n_s} \sum_{l=1}^{n_s} k(x_{i,j}, x_{i,l}) - \frac{2}{n_s m} \sum_{j=1}^{n_s} \sum_{l=1}^{n_s} k(x_{i,j}, x_{i,l}) \delta(z_l = 1) \right] \end{aligned} \tag{F.2}$$

where $\delta(z_l = 1) = \begin{cases} 1, & \text{if } z_l = 1. \\ 0, & \text{otherwise.} \end{cases}$ is the Kronecker delta, $m = n_s \times P(\boldsymbol{Z} = \boldsymbol{1})$ is the number of ANN among the best decile, and $k(x, y) = \exp\left(-\frac{\|x-y\|^2}{2h^2}\right)$ is the Gaussian radial basis function. The parameter h is selected as to maximize HSIC values. Since we choose the best decile to select the most effective ANN, $P(\boldsymbol{Z} = \boldsymbol{1}) = 0.10$.

	$S_{\boldsymbol{X_1},\boldsymbol{Y_{10\%}}}$	$S_{\boldsymbol{X_2},\boldsymbol{Y_{10\%}}}$	$S_{\boldsymbol{U_1},\boldsymbol{Y_{10\%}}}$	$S_{\boldsymbol{U_2},\boldsymbol{Y_{10\%}}}$
$n_s = 500$	$2.6.10^{-3}$	$2.8.10^{-3}$	$3.3.10^{-3}$	$2.9.10^{-3}$
$n_s = 1000$	$1.9.10^{-3}$	$2.4.10^{-3}$	$2.5.10^{-3}$	$2.4.10^{-3}$
$n_s = 2000$	$2.0.10^{-3}$	$2.7.10^{-3}$	$2.4.10^{-3}$	$2.8.10^{-3}$
$n_s = 10000$	$2.0.10^{-3}$	$2.6.10^{-3}$	$2.6.10^{-3}$	$2.7.10^{-3}$
$n_s = 10000$ Novello *et al.* (2021)	$3.7.10^{-3}$	$4.8.10^{-3}$	$4.8.10^{-3}$	$4.8.10^{-3}$

Table F.1: HSIC coefficients for Example 1 varying the number of test sets n_s.

Normalization of the hyperparameters space

Hyperparameters can be defined in very different mathematical spaces. For example, the type of activation function is a categorical variable, whereas the batch size is a positive integer number and the α parameter for L2 regression is a real number. Moreover, the type of distribution (uniform or normal) impacts the HSIC computation. The first following example (extracted from Novello *et al.* (2021)) illustrates this effect.

Example 1

Let $f : [0, 2]^2 \to 0, 1$ such that:

$$f(X_1, X_2) = \begin{cases} 1, & \text{if } X_1 \in [0, 1] \text{ and } X_2 \in [0, 1], \\ 0, & \text{otherwise} \end{cases} \tag{F.3}$$

According to the definition of f, X_1 and X_2 have the same effect over the value of $f(X_1, X_2)$. Their HSIC should therefore be identical. Let X_1 be a normal distribution of mean 1 and variance 0.1, truncated between 0 and 2 and X_2 be a uniform distribution between 0 and 2. The values of $S_{\boldsymbol{X_1},\boldsymbol{Y_{10\%}}}$ and $S_{\boldsymbol{X_2},\boldsymbol{Y_{10\%}}}$ are given in Table F.1 for n_s varying from 500 to 10000. The convergence is obtained between $n_s = 2000$ and $n_s = 10000$. Contrary to what is expected from the definition of f, HSIC are found different between X_1 and X_2. To tackle this issue, Novello *et al.* (2021) propose to transform X_i into U_i as $\phi_i(X_i) = U_i$ where ϕ_i is the cumulative distribution function (CDF) of X_i. As a result, U_i follows a uniform distribution over $[0, 1]$ according to the property of the CDF. The methodology is thoroughly explained in Novello *et al.* (2021) for discrete hyperparameters.

The HSIC related to the transformed variables U_1 and U_2 are displayed in Table F.1. $S_{\boldsymbol{U_1},\boldsymbol{Y_{10\%}}}$ and $S_{\boldsymbol{U_2},\boldsymbol{Y_{10\%}}}$ are now found identical as expected from the definition of f. Results show the relevance of the normalization of hyperparameters space when distributions are different. Note that the numerical results we obtained differ from those given in Novello *et al.* (2021). After verification of the code and a thorough discussion with the authors, the present results can be considered as validated. In the following, X_i is always normalized into U_i to compute HSIC.

	$S_{\boldsymbol{U_1},\boldsymbol{Y_{10\%}}}$	$S_{\boldsymbol{U_2},\boldsymbol{Y_{10\%}}}$	$S_{\boldsymbol{U_3},\boldsymbol{Y_{10\%}}}$	$S_{(\boldsymbol{U_2},\boldsymbol{U_3}),\boldsymbol{Y_{10\%}}}$	$S_{(\boldsymbol{U_4},\boldsymbol{U_5}),\boldsymbol{Y_{10\%}}}$
$n_s = 500$	$2.5.10^{-3}$	$2.1.10^{-3}$	$2.2.10^{-4}$	$6.5.10^{-4}$	$2.0.10^{-4}$
$n_s = 1000$	$2.8.10^{-3}$	$6.8.10^{-5}$	$1.2.10^{-4}$	$8.6.10^{-4}$	$9.1.10^{-5}$
$n_s = 2000$	$2.7.10^{-3}$	$4.2.10^{-5}$	$3.2.10^{-5}$	$7.0.10^{-4}$	$4.9.10^{-5}$
$n_s = 10000$	$2.8.10^{-3}$	$9.7.10^{-6}$	$9.4.10^{-6}$	$6.8.10^{-4}$	$9.7.10^{-6}$
$n_s = 10000$ Novello *et al.* (2021)	$5.8.10^{-3}$	$2.4.10^{-5}$	$1.8.10^{-5}$	$1.4.10^{-3}$	$2.0.10^{-5}$

Table F.2: HSIC coefficients for Example 2 varying the number of test sets n_s.

Interaction between hyperparameters

Even though the HSIC value of X_i is low, X_i may actually have an impact due to its interactions with the other hyperparameters. The following example illustrates this effect.

Example 2

Let $f : [0, 2]^3 \to 0, 1$ such that:

$$f(X_1, X_2, X_3) = \begin{cases} 1, & \text{if } X_1 \in [0,1], X_2 \in [1,2] \text{ and } X_3 \in [0,1] \\ 1, & \text{if } X_1 \in [0,1], X_2 \in [0,1] \text{ and } X_3 \in [1,2] \\ 0, & \text{otherwise} \end{cases} \tag{F.4}$$

When evaluated separately, the HSIC values of X_2 and X_3 do not show an influence over the value of $f(X_1, X_2, X_3)$. There is indeed no difference between the probability distributions of X_2 and $(X_2|(Z = 1))$. Yet, X_2 and X_3 have a combined effect over $f(X_1, X_2, X_3)$. Table F.2 gathers the results for X_1, X_2, X_3, (X_2, X_3) and (X_4, X_5) where X_4 and X_5 are two dummy variables, uniformly distributed, used to have a reference of comparison for (X_2, X_3). Note that HSIC are computed using the CDF transformation presented in Example 1.

Results show a good convergence for $S_{\boldsymbol{U_1},\boldsymbol{Y_{10\%}}}$ but much less for other HSIC. For $n_s = 10000$, HSIC values are yet consistent, $S_{\boldsymbol{U_2},\boldsymbol{Y_{10\%}}}$ and $S_{\boldsymbol{U_3},\boldsymbol{Y_{10\%}}}$ are almost identical consistently with the definition of Example 2. Both values are very low and close to the one of $S_{(\boldsymbol{U_4},\boldsymbol{U_5}),\boldsymbol{Y_{10\%}}}$ which have no effect on $f(X_1, X_2, X_3)$. Even though the values of $S_{\boldsymbol{U_2},\boldsymbol{Y_{10\%}}}$ and $S_{\boldsymbol{U_3},\boldsymbol{Y_{10\%}}}$ indicate that there is not effect of these variables on the output, the combined HSIC $S_{(\boldsymbol{U_2},\boldsymbol{U_3}),\boldsymbol{Y_{10\%}}}$ is important. It is one order of magnitude smaller than $S_{\boldsymbol{U_1},\boldsymbol{Y_{10\%}}}$ but two orders of magnitude larger than $S_{(\boldsymbol{U_4},\boldsymbol{U_5}),\boldsymbol{Y_{10\%}}}$. Once again, values are different from Novello *et al.* (2021) but after verification of the code and discussions with the authors, the present results can be considered as validated.

Figure F.1 displays interaction HSIC between variables. The most influential variable X_1 is also the one that interacts the most with other variables. Consistently with Table F.2, even though X_2 and X_3 are not very influential, their interaction HSIC is much larger. This kind of representation enables a visualization of interactions at stake between hyperparameters.

Moreover, one can notice that :

$$S_{\boldsymbol{U_i},\boldsymbol{Y_{10\%}}} = S_{(\boldsymbol{U_i},\boldsymbol{U_i}),\boldsymbol{Y_{10\%}}} \tag{F.5}$$

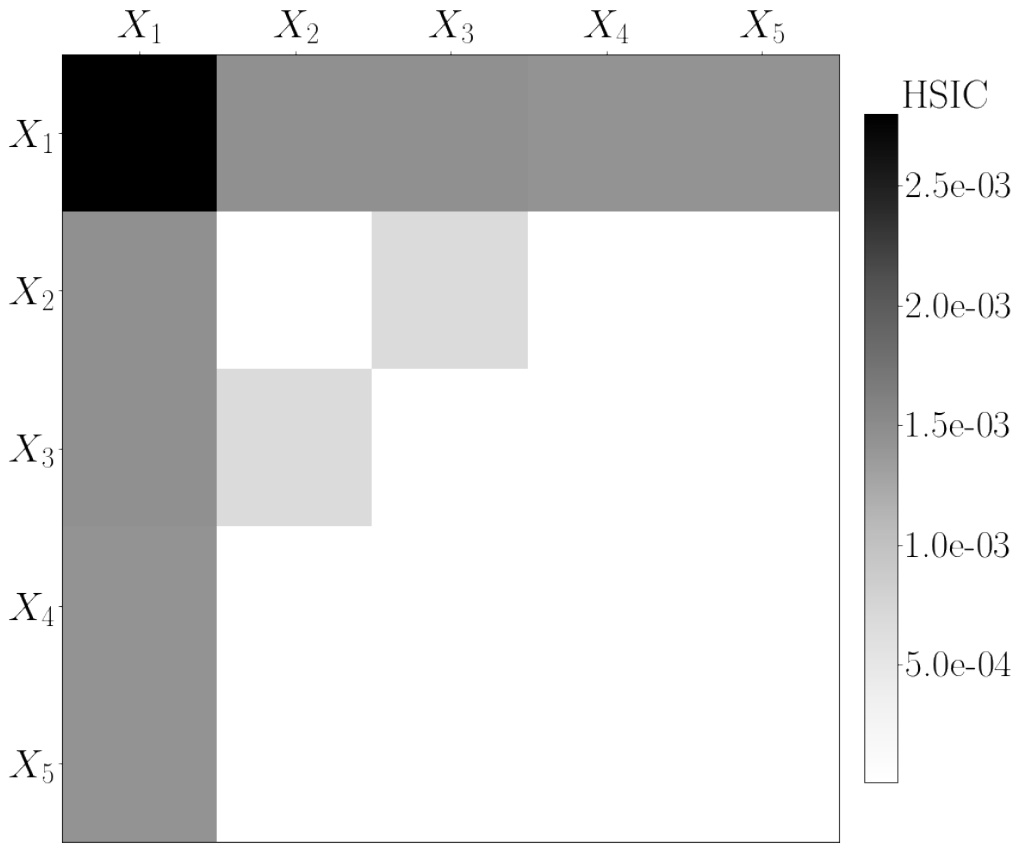

Figure F.1: Representation of HSIC interactions for Exemple 2.

This relation can be mathematically demonstrated using Equation (F.2) (not shown here) and constitutes an additional proof of the proper computation of HSIC.

dernière page de la thèse

AUTORISATION DE SOUTENANCE

Vu les dispositions de l'arrêté du 25 mai 2016,

Vu la demande du directeur de thèse

Monsieur C. CORRE

et les rapports de

M. G. BALARAC
Professeur - Laboratoire des Ecoulements Géophysiques et industriels (LEGI)
Domaine Universitaire - CS 40700 - 38058 Grenoble cedex 9

et de

M. G. IACCARINO
Professeur - Institute for Computational & Mathematical Engineering - Stanford University
Huang Engineering Building - 475 Via Ortega - Suite B060 - Stanford - CA 94305 - USA

Monsieur VADROT Aurélien

est autorisé à soutenir une thèse pour l'obtention du grade de **DOCTEUR**

Ecole doctorale Mécanique, Energétique, Génie Civil et Acoustique

Fait à Ecully, le 19 octobre 2021

P/Le directeur de l'E.C.L.
Le directeur des Formations

Grégory VIAL

ECOLE CENTRALE DE LYON
Service Scolarité
ECULLY